Dissipative dynamics of a qubit-oscillator system in the ultrastrong coupling and driving regimes

DISSERTATION

zur Erlangung des
DOKTORGRADES DER NATURWISSENSCHAFTEN (DR. RER. NAT.)
der Naturwissenschaftlichen Fakultät II - Physik
der Universität Regensburg

vorgelegt von

Johannes Hausinger
aus
Offenberg

im Jahr 2010

Das Promotionsgesuch wurde am 30.06.2010 eingereicht.
Das Kolloquium fand am 27.10.2010 statt.

Die Arbeit wurde von Prof. Dr. Milena Grifoni angeleitet.

Prüfungsausschuß:

Vorsitzender:	Prof. Dr. D. Bougeard
1. Gutachter:	Prof. Dr. M. Grifoni
2. Gutachter:	Prof. Dr. S. Kohler
weiterer Prüfer:	Prof. Dr. A. Schäfer

Contents

1 Introduction

Most phenomena of our daily life seem to be governed completely by classical physics. The trajectory of an apple falling from a tree is fairly well described by Newtonian physics. Even events involving much smaller objects, like the Brownian motion of a small particle in a drop of water, obey classical laws [1]. Similar to the theory of general and special relativity, which on the first glimpse seems to play a role only in the realms of free space and at velocities beyond human capabilities, quantum mechanics might yield the impression to be of importance only in the regime of microscopic scales. Surely, we all have accepted that both theories play a non-negligible role in our modern world. Let us just think, for instance, of the Global Positioning System, which needs indeed to take into account relativistic effects on the atomic clocks in its satellites in order to accurately determine a position on earth [2]. Also quantum mechanics entered our daily life through various technical gadgets. For example, the laser finds application in many different devices; transistors play an important role in modern computers; ferromagnetism makes storage of information possible; the photoelectric effect is used for energy production, etc. All these applications are based on quantum mechanical effects. Nevertheless, they seem to take place only on a level which is not perceptible to our human eye, not having a direct influence on our macroscopic world. One of these effects is the superposition of physical states. As a student one encounters usually at the beginning of a lecture on quantum mechanics the famous gedankenexperiment of Schrödinger's cat [3]. In the beginning it is a very puzzling idea that the condition (or state if one wishes) of a cat, which is hidden in a box from the observer's eyes and subject to a lethal device obeying the laws of radioactive decay and thus of quantum mechanics, is not well defined, but - said in a sloppy way - rather a superposition of life and dead. The idea looses a big deal of its fascination and seems to be of more philosophical nature, when we take into account that under observation, i.e., by opening the box and examining the cat, its state becomes determinate. It seems that we have no means to find out how the cat's state was before the measurement. For microscopic objects the superposition principle has been confirmed in various cases, see, e.g., the interference experiments on electrons by Jönsson [4] and Tonomura et al. [5]. Quite naturally the question arises if the superposition principle and other quantum mechanical laws can be extended into macroscopic realms. This issue was put forward by Leggett in the early 80s [6, 7]. At this point it is important to define what is meant by "macroscopic quantum effects". Let us consider for example the Josephson effect [8]: even with no voltage applied a resistiveless current is measured through two superconducting electrodes which are separated by a thin oxide layer. This is a macroscopic effect in the sense that the current consists of many electronic degrees of freedom. It is a quantum effect, as the current results from the tunneling of pairs of electrons, so-called Cooper-pairs, whose wavefunction consists of a superposition of pairs being localized on either side of the barrier. However, the effect relies not on the superposition of two macroscopic degrees of freedom like in the example of Schrödinger's cat. Rather it can be seen as collective behavior of many microscopic degrees of freedom experiencing quantum effects on the microscopic scale.

To test quantum mechanics acting on macroscopic degrees of freedom, Leggett suggested to investigate the effects of “macroscopic quantum tunneling” (MQT) and “macroscopic quantum coherence” (MQC) in a superconducting ring interrupted by a Josephson junction, a so-called “radio frequency superconducting quantum interference device” (rf-SQUID). In this system, the phase difference across the Josephson junction or the corresponding magnetic flux through the ring[1] can be seen as macroscopic parameter. For a high enough self-inductance of the loop, it behaves like a particle being trapped in one of the minima of a double-well potential. Under certain conditions tunneling out of the well (MQT) and even coherent quantum oscillations (MQC) between the two minima were predicted theoretically. The main obstacles to observe these effects consist in thermal escape from the well (a too high temperature also makes a distinction of the separate quantum levels impossible) and coupling of the macroscopic degree of freedom to microscopic ones, which act on the system of interest like a constant measurement and thus destroy quantum coherence. When Leggett wrote his articles, at least the first problem seemed to be feasible, owed to big achievements in cooling techniques. Concerning the second one, superconducting devices seemed to be most promising candidates being less sensitive to dissipative effects. Caldeira and Leggett [11] could theoretically show that dissipation leads merely to a reduction in the tunneling rate, and indeed MQT could already be experimentally realized soon after Leggett's proposal (see, e.g., [1, 12] and references therein). However, as pointed out in [6], MQT is *not* a sufficient proof for the superposition of macroscopic states, because it would work as well for a mixture of particles. It was only in 1999, when Nakamura et al. observed for the first time MQC in a superconducting Cooper-pair Box [13]. The main element in their experiment was also a Josephson junction, but instead of the phase the role of the macroscopic degree of freedom was taken by the excess charge resulting on one of the electrodes due to Cooper-pair tunneling. They managed to visualize coherent oscillations between the zero and one excess Cooper-pair state.

Almost at the same time when Leggett asked his question about the relevance of quantum mechanics for macroscopic objects, the idea of quantum computation was born [14]. There, the quantum mechanical superposition of several degrees of freedom - not necessarily macroscopic ones - plays a crucial role: The linear combination of the two logical states of a bit, forming a so-called quantum bit (qubit), is one of the key ingredients of a quantum computer. In the beginning single atoms, ions or spins – that is, microscopic degrees of freedom – in combination with optical systems formed the workhorse, providing quite naturally a two-level system representing the logical states of the qubit. Experience with manipulating quantum states of those systems had already been at hand from various experiments. Furthermore, those qubits can be well isolated from spurious environmental degrees of freedom, thus providing long decoherence times. On the other hand, fabricating them at a large scale and implementing them in computational architectures bears some difficulties. Therefore, it seemed natural to look for qubit concepts which were based on electronic degrees of freedom, taking advantage on the knowledge of integrated circuit design from ordinary computers. With the Nakamura experiment the first solid-state realization of a qubit had been born and several other were soon to follow. Despite of the advanced experimental experience on optical systems, superconducting qubits proved to be successful in the implementation

---

[1] The relation between the phase difference and the flux Φ through the ring is, see [9] and [10]: $\gamma_J = 2\pi\Phi/\Phi_0(\text{mod}2\pi)$ with the elementary flux quantum $\Phi_0 = h/2e$. The flux $\Phi = \Phi_{\text{ext}} + LI$ consists of the externally applied flux Φ_{ext} and the flux induced by the supercurrent I in the ring of inductance L.

of simple quantum gates in quite a short time after their discovery. The discussion of advantages and disadvantages of the various qubit designs is still a hot topic and we will not follow this line [14]. Fact is that, like in an ordinary computer, solid-state systems with their many degrees of freedom couple most naturally to the electric circuit environment and thus are easily manipulated, read-out and implemented at large scales. Unfortunately, this brings again the drawback of being most sensitive to environmental influences.
For the physical implementation of a qubit, it is important to have a discrete energy spectrum, and that the two states representing its logical entities $|0\rangle$ and $|1\rangle$ are energetically well separated from all the other states in the device. For instance, the nth and $(n+1)$th orbital of a Rydberg atom can fullfill those criteria. The challenge is now to form such a two-level system out of electronic devices or in other words to build artificial atoms. In Sec. 1.1, we describe how artificial atoms can be formed using superconducting circuits. In order to couple different qubits with each other or transport information between them, photons seem to be promising candidates just like for systems based on real atoms. Depending on the kind of superconducting qubit various schemes have been suggested to establish qubit-photon coupling leading to the field of circuit quantum electrodynamics (circuit QED), on which we give a short overview in Sec. 1.2.

1.1 Superconducting qubits

Concerning an electronical realization of a qubit one can, for example, think of using the ground- and first excited state of a simple quantum LC-circuit, which can be described by a quantum harmonic oscillator. However, due to the linear nature of the potential, a transition from the first to the second excited level would be as probable as a transition between the two qubit states itself, so that one could not speak of a bit anymore. This problem can be circumvented by replacing the linear LC-circuit by a nonlinear one, which is most naturally provided by a circuit containing a Josephson tunneling junction. Such a junction consists of two superconducting electrodes typically separated by a thin oxide layer. In 1962, B. D. Josephson predicted a zero-voltage, direct supercurrent flowing through the junction [8], which results from Cooper-pairs tunneling through the insulating layer and can be described by

$$I_S = I_C \sin\gamma_J. \tag{1.1}$$

Here, γ_J is the gauge invariant phase difference across the junction between the two global wavefunctions, describing the Cooper-pairs in the superconducting electrodes, and I_C is the critical current determined by the geometry of the tunneling layer. Josephson further showed that a finite voltage V over the contact yields an alternating current, and that the phase difference obeys

$$\frac{d\gamma_J}{dt} = \frac{2\pi V}{\Phi_0}, \tag{1.2}$$

with $\Phi_0 = h/2e$ being the elementary flux quantum. Combining Eqs. (1.1) and (1.2), we obtain

$$V = L_J(\gamma_J)\frac{\partial I_S}{\partial t}, \tag{1.3}$$

where we defined the nonlinear Josephson inductance $L_J(\gamma_J) = \Phi_0/2\pi I_C \cos\gamma_J$. From this, we see that the Josephson tunneling element can be understood as an LC-circuit, where the linear inductance is replaced by a nonlinear one, and the two electrodes build the capacitative element. We can calculate the energy stored in the junction by using Eqs. (1.1) and (1.2). Assuming that the starting phase-difference is $\gamma_J(0) = \pi/2$ and the final one $\gamma_J(t) = \gamma_J$,[2] we get

$$U(\gamma_J) = \int_0^t I_S(t')V(t')dt' = -E_J \cos\gamma_J \tag{1.4}$$

with the so-called Josephson energy $E_J = \Phi_0 I_C/2\pi$. Instead of the parabolic potential found for the ordinary LC-circuit with a linear inductance, the Josephson element has the shape of a cosine washboard. A more detailed discussion of this potential can be found, e.g., in [10]. Taking into account the excess charge Q stored on the capacitor, we get for the total energy

$$E_T = \frac{Q^2}{2C_J} + U(\gamma_J), \tag{1.5}$$

where C_J is the capacitance of the junction. In order to examine the quantum dynamical behavior of the Josephson junction, we introduce the conjugate operators, $\hat{\gamma}_J$ and $\hat{N} \equiv \hat{Q}/2e$. The latter corresponds to the number of Cooper-pairs having tunneled through the junctions, and the two operators obey the commutator relation $[\hat{\gamma}_J, \hat{N}] = \mathrm{i}$. The Hamiltonian of the junction then reads

$$H_J = E_C\hat{N}^2 + U(\hat{\gamma}_J) = -E_C\frac{\partial^2}{\partial\hat{\gamma}_J^2} + U(\hat{\gamma}_J), \tag{1.6}$$

where $E_C = (2e)^2/2C_J$ is the charging energy of one Cooper-pair on the junction. As pointed out in [9] the residual offset charge on the capacitor should be considered as well by replacing $\hat{N}$ with $\hat{N} - Q_r/2e$. For simplicity we neglect this term. Besides, we assume in the above considerations temperatures low enough to neglect the effect of fermionic quasiparticle tunneling. An estimate of this temperature can be found in [9]: there it is argued that the energy of thermal fluctuations must be much smaller than the qubit transition frequency between states $|0\rangle$ and $|1\rangle$ so that $k_BT \ll \hbar\omega_{01}$. Moreover, the energy gap of the superconductor has to be large compared to the transition frequency, $\omega_{01} \ll \Delta_c$. Typically the latter lies for superconducting qubits in the range from 5-20 GHz, which corresponds to temperatures around 1K.

For further considerations the ratio E_C/E_J is important. For $E_C/E_J \gg 1$, the influence of the potential $U(\hat{\gamma}_J)$ in the junction Hamiltonian is very weak, and thus all values of $\hat{\gamma}_J$ appear with nearly equal probability - the phase is delocalized, while the charge degree of freedom is strongly localized. Thus, we speak of the "charging regime". The contrary case, $E_C/E_J \ll 1$, is denoted as the "phase" or "flux regime".

1.1.1 Charge qubits

We concentrate first on the case $E_C/E_J \gg 1$, where we use as basis states the number of Cooper-pair charges $|N\rangle$ – with $\hat{N}|N\rangle = N|N\rangle$ – having passed through the junction and forming an excess charge on one of the superconducting electrodes. A simple realization of these so-called charge qubits is the Cooper-pair box, Fig. 1.1 (for a detailed review see, e.g., [9, 12, 15]). Through an external bias applied to the Josephson element, the tunneling of Cooper-pairs from the reservoir electrode to the superconducting island, which is connected

---

[2] A different starting condition for the phase like for example $\gamma_J(0) = 0$ just yields an overall shift of the potential energy of E_J.

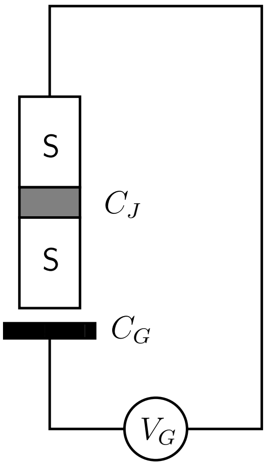

Figure 1.1: Sketch of a Cooper-pair box (after [15]). A superconducting island is connected by a Josephson tunnel junction of capacitance C_J to a superconducting reservoir. An external gate voltage V_G controls the tunneling of Cooper-pairs from the reservoir to the island.

by the capacitor C_g to the gate voltage V_g, can be controlled; it results in an excess or lack of Cooper-pairs on the island.[3] The Hamiltonian of the Cooper-pair box reads [16]

$$H_{CPB} = E_C(\hat{N} - N_g)^2 - E_J \cos \hat{\gamma}_J. \tag{1.7}$$

Here, $E_C = (2e)^2/2(C_J + C_g)$ is the single Cooper-pair charging energy and $N_g = C_g V_g/2e$ the dimensionless gate charge. In the charge state representation Eq. (1.7) becomes

$$H_{CPB} = \sum_N \left\{ E_C(N - N_g)^2 |N\rangle\langle N| - \frac{1}{2} E_J(|N\rangle\langle N+1| + |N+1\rangle\langle N|) \right\}. \tag{1.8}$$

For $E_J = 0$, the charge states form an eigenbasis, and whenever N_g is a half-integer, two neighboring charge states are degenerate, see the eigenenergy spectrum in Fig. 1.2. At higher energies also degeneracies between non-adjacent charge states can be observed. We will ignore them in the following discussion. As shown in Fig. 1.2, the degeneracies are lifted for finite Josephson energies. Further, we can limit our considerations due to the periodicity of the spectrum to the interval $0 < N_G < 1$. At $N_G = 0.5$ and small E_J, the eigenstates will be approximately a symmetric and antisymmetric superposition of the states $|N = 0\rangle$ and $|N = 1\rangle$. For temperatures $k_B T \ll E_C$, we can ignore all other charge states, as they have a much higher energy. Therefore, the Cooper-pair box Hamiltonian can effectively be described by a two-level system (TLS):

$$H_{\mathrm{TLS}} = -\frac{\hbar}{2}(\varepsilon \sigma_z + \Delta \sigma_x), \tag{1.9}$$

where σ_z and σ_x are the Pauli-spin matrices. The Hamiltonian is represented in the so-called localized basis, $\{|\uparrow\rangle, |\downarrow\rangle\}$. For the Cooper-pair box, the spin-up and spin-down state correspond to the charge states $|N = 0\rangle$ and $|N = 1\rangle$, respectively. They are eigenstates of the σ_z-Pauli matrix with $\sigma_z|\uparrow / \downarrow\rangle = \pm|\uparrow / \downarrow\rangle$. We further define the bias parameter $\varepsilon = E_C(1 - 2N_G)/\hbar$, by which the number of Cooper-pairs in the box can be controlled via the gate charge. For $\varepsilon = 0$, one says that the qubit is operated at the "degeneracy point" or "sweet spot". For this value, it is most robust against external noise induced by charge fluctuations. Furthermore, the Josephson tunneling element $\Delta = E_J/\hbar$ gives the minimum

---

[3] As a side-effect, also the residual offset charge Q_r is compensated by the gate voltage.

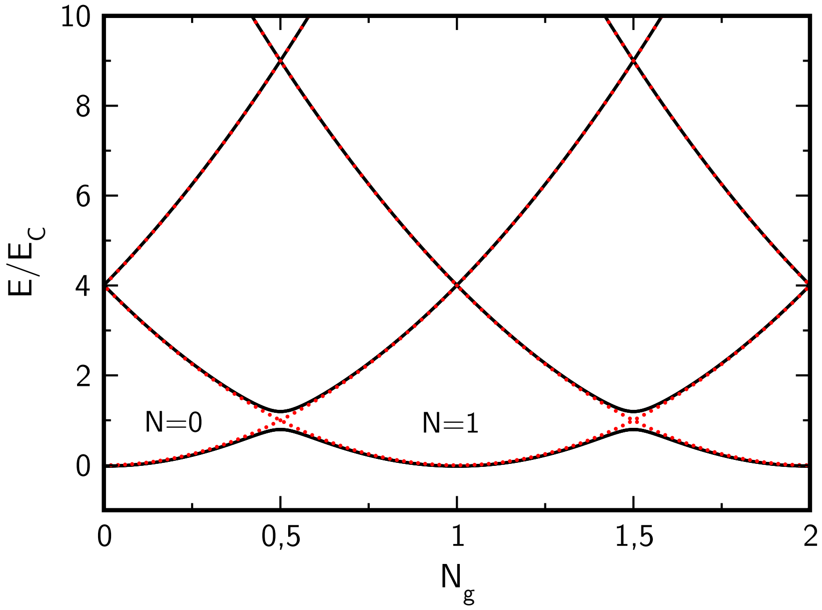

Figure 1.2: The energy spectrum of the Cooper-pair box against the dimensionless gate charge N_g. For $E_J = 0$ the charge states form an eigenbasis of the Cooper-pair box Hamiltonian and the corresponding eigenvalues show a parabolic behavior, see red dotted line. Whenever N_G is a half-integer, two adjacent charge states are degenerate. For $E_C/E_J = 0.1$, black solid line, the degeneracies are lifted.

energy splitting of the qubit.

The Cooper-pair box was first described theoretically by Büttiker [16], and a superposition of its charge states was experimentally realized by Bouchiat et al. [15] in 1998. One year later, Nakamura et al. [13] performed a groundbreaking experiment using the Cooper-pair box: Although its charge states involve a large number of conduction electrons, and thus clearly represent a macroscopic system,[4] Nakamura et al. succeeded to observe *and* to control coherent quantum oscillations between the $|N = 0\rangle$ and $|N = 1\rangle$ states. Apart from its fundamental significance, this experiment also paved the way to solid-state realizations of qubits. Until that time, the two logical qubit states had only been implemented using microscopic degrees of freedom.

1.1.2 Flux qubits

In the opposite regime of $E_C/E_J \ll 1$ the charges are fluctuating strongly, whereas the phase over the Josephson element and the corresponding magnetic flux are strongly localized and thus serve as the relevant degree of freedom. The most simple realization of such a flux qubit is the radio-frequency superconducting interference device (rf-SQUID), which consists of a superconducting ring being interrupted by a single Josephson junction [1]. Already in the early 80s, it was suggested as a candidate to investigate quantum effects in macroscopic systems, such as "macroscopic quantum tunneling" (or "decay") (MQT) and "macroscopic quantum coherence" (MQC) [6, 7]. Concerning the latter effect, which is of uttermost importance for quantum computing, the Cooper-pair box made the race with the Nakamura

---

[4] Macroscopic in this sense means that the charge states really act like a single degree of freedom and not just consists of a coherent superposition of many microscopic degrees of freedom.

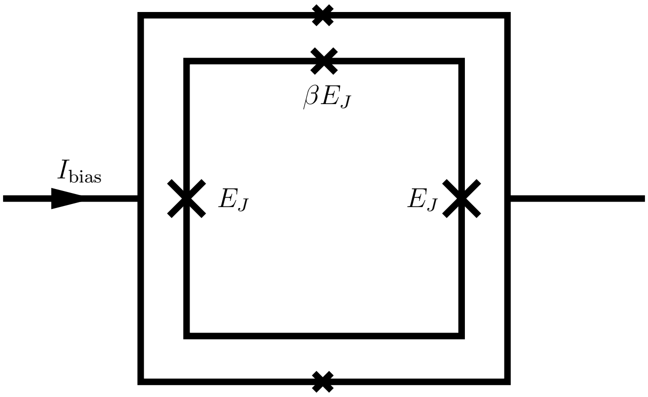

Figure 1.3: Sketch of a 3-junction persistent current qubit together with a biased dc-SQUID after [19]. The inner superconducting loop builds the qubit. It is interrupted by three Josephson junctions. Two junctions have the same Josephson energy E_J, while the third one is slightly smaller, βE_J. For $\beta > 0.5$ a double-well potential is formed. The outer, two-junction ring builds a dc-SQUID, which is coupled inductively to the qubit for read-out.

experiment of 1999. The flux state of the rf-SQUID turned out to be harder to control and due to the relatively large loop size[5] more sensitive to environmental influences [1]. Not before 2000, Friedman et al. [17] could measure an avoided level crossing in the energy spectrum of the rf-SQUID. Thereby, they made the superposition of two macroscopic flux states possible – a first hint of MQC. The breaktrough came 2003 with the experiment of Chiorescu et al. [18], who realized a proposal from Mooij and coworkers [19] to use a 3-junction persistent-current qubit instead of the single-junction rf-SQUID, by which the size of the superconducting loop and consequently the coupling to the environment could be strongly reduced, and the control of the flux states was improved. By this, they were able to measure for the first time MQC in flux qubits. Before, van der Wal et al. had used this setup to demonstrate the coherent superposition of two persistent current states [20] in an experiment similar to that of Friedman et al..

In this section, we discuss the physics behind the 3-junction persistent-current flux qubit. Two of the three Josephson junctions interrupting the loop have the same Josephson energy E_J, whereas the third one is slightly smaller, βE_J, with $0.5 < \beta < 1$, see Fig. 1.3. From the energy of a single junction, Eq. (1.4), we can calculate the total energy stored in the 3-junction qubit as

$$U/E_J = -\cos\gamma_1 - \cos\gamma_2 - \beta\cos\gamma_3, \tag{1.10}$$

where γ_i is the phase difference across junction i and the index J has been dropped for convenience. We further assume that an external flux $\Phi_{\text{ext}} = f\Phi_0$ penetrates the loop, where the dimensionless number f is the so-called frustration. The external flux induces a persistent current I_p, which flows clockwise or counter-clockwise through the loop, and itself results in an additional flux of size LI_P with L being the self-inductance of the loop. Typical values for the inductance and the persistent current are $L \sim 5\,\text{pH}$ and $I_p \sim 200\,\text{nA}$ [12, 21] resulting in a flux of about $10^{-3}\Phi_0$. This flux is big enough to be detected by read-out devices but can be disregarded in the further calculation so that the total flux Φ in the loop is equal to the external one. In order to eliminate one parameter in Eq. (1.10), we use the concept of fluxoid quantization around a superconducting ring [10],

$$\gamma_1 - \gamma_2 + \gamma_3 = -2\pi f + 2\pi n, \tag{1.11}$$

so that

$$U/E_J = -\cos\gamma_1 - \cos\gamma_2 - \beta\cos(2\pi f + \gamma_1 - \gamma_2). \tag{1.12}$$

---

[5] For a high self-inductance, a large ring size is needed for the rf-SQUID. Only a high self-inductance yields a double-well potential for the rf-SQUID dynamics, which is necessary for qubit realization [12].

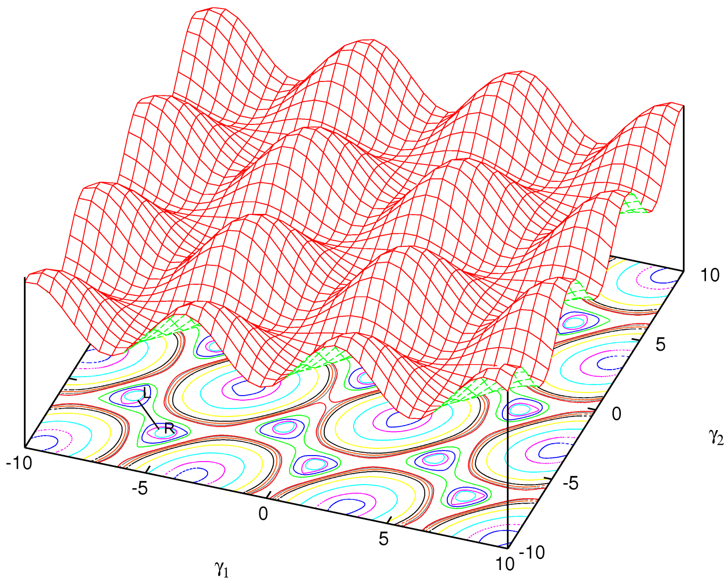

Figure 1.4: The potential $U(\gamma_1, \gamma_2)$ shown as a 3d and a contour plot. For this plot we used $\beta = 0.9$ and $f = 0.5$. As long as $\beta > 0.5$ one finds a periodic pattern in phase space with two degenerate minima in each unit-cell, L and R (the degeneracy is due to $f = 0.5$). Tunneling between this left and right minimum is possible, while intercell tunneling is hindered by high potential barriers.

For $\beta > 0.5$ the potential $U(\gamma_1, \gamma_2)$ results in a grid of double-well potentials in the γ_1, γ_2-phase-space, shown in Fig. 1.4. The barrier-height between the two minima of each of those double-wells is determined by β, and such can be engineered in the fabrication process. Replacing the third junction by a dc-SQUID, it can be even varied in situ [19, 21]. For $f = 0.5$, the two minima are energetically degenerate, and the qubit is at the sweet spot. We notice that the frustration f takes the role of the control parameter in the flux qubit, just like the dimensionless gate charge N_g did in the case of the charge qubit. Intercell tunneling between different double-wells has to be suppressed by appropriately chosen parameters, so that charge fluctuations have no influence on the qubit coherence [19]. Now, we concentrate on a single double-well and plot in Fig. 1.5 the energy U_J along the shortest connection between the two minima. The left and right well correspond to a clockwise and counter-clockwise supercurrent in the loop, and we denote the states as $|L\rangle$ and $|R\rangle$, or $|\downarrow\rangle$ and $|\uparrow\rangle$ in the qubit picture. The classical energies of these states are [20]

$$\pm \frac{\hbar}{2}\varepsilon = \pm I_p(\Phi_{\text{ext}} - \frac{1}{2}\Phi_0). \tag{1.13}$$

Hereby, the amplitude I_p of the persistent current is very close to the critical current of the weakest junction. If we do not take into account higher energy states, the Hamiltonian of the flux qubit is $H_{\text{FQ}} = -\hbar\varepsilon\sigma_z/2$. If further the separation between the two minima of the double well is small enough and the barrier is not too high, quantum mechanical tunneling is possible between the wells. We thus introduce in the above Hamiltonian the tunneling matrix element Δ and find

$$H_{\text{FQ}} = -\frac{\hbar}{2}(\varepsilon\sigma_z + \Delta\sigma_x). \tag{1.14}$$

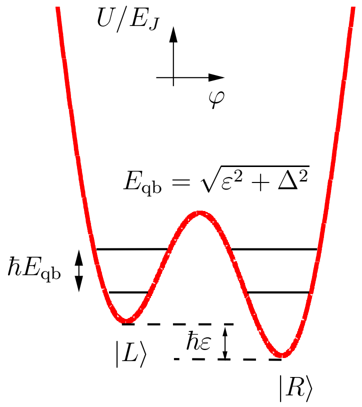

Figure 1.5: The potential $U(\gamma_1, \gamma_2)$ plotted against the line φ which connects the two minima of a double-well in Fig. 1.4. Those minima correspond to clockwise and counter-clockwise persistent currents in the qubit loop. For a small distance between the minima and a not too high barrier tunneling is possible. The energy eigenstates form a symmetric and antisymmetric superposition of the macroscopic current states. The lowest two energy levels are indicated by the horizontal lines. For $f \neq 0.5$, we have a finite energy difference $\hbar\varepsilon$ between the minima.

Like for the charge qubit, we can describe the flux qubit by a two-level system.
The qubit loop in Fig. 1.3 is surrounded by another superconducting ring interrupted by two smaller Josephson junctions. This latter loop is a so-called dc-SQUID [10], which acts as a very sensitive magnetometer and is able to detect even smallest changes of the magnetic flux in the qubit. Also the flux induced by the persistent currents flowing in the qubit loop can be measured. In practice, a bias current is ramped through the SQUID, and the value for which the SQUID switches to the finite-voltage state is registered. The latter depends on the flux, and through a series of repeated measurements the state of the qubit can be determined with great preciseness. A detailed description of the read-out process is given in [22, 23].

1.2 Qubit-oscillator systems

Since qubits in real life will always be subjected to dissipation and decoherence effects due to the coupling to environmental degrees of freedom, see Chapter 3, and therefore loose their quantum mechanical nature, it is necessary to store the information they contain in auxiliary systems. Furthermore, in order to perform algorithms of quantum information theory, coherent communication between different qubits is needed.

1.2.1 Cavity quantum electrodynamics

For qubits built from real atoms, photons have been proposed as potential information carriers [24]. In order to control and store the photon energy, the atoms are placed inside a mirror resonator. Such a setup is commonly known as “cavity quantum electrodynamics” [25–27]. Assuming that the atom couples through its dipole moment to a single mode of the electromagnetic field in the cavity and can be modeled as a simple two-level system, the corresponding Hamiltonian is, see, e.g., [27, 28],

$$H_{\text{TLS-osc}} = H_{\text{TLS}} + H_{\text{int}} + H_{\text{osc}}, \tag{1.15}$$

with the cavity field being described by a harmonic oscillator of frequency Ω, $H_{\rm osc} = \hbar\Omega B^\dagger B$, where we neglected the zero point energy, and denoted by B and $B^\dagger$ the annihilation and creation operators acting on the oscillator quanta. The coupling between the atom and the oscillator is accounted for through the interaction term $H_{\rm int} = \hbar g \sigma_z (B + B^\dagger)$. Interesting hereby is the regime of strong coupling g, which means that a photon being emitted from the atom to the cavity can be reabsorbed by the atom and emitted again, the whole circle repeating several times before loss processes occur like escape through the cavity mirrors, relaxation to other atomic levels or into different photon modes, or decay due to fluctuations in the qubit's control parameter induced by the environment [29]. Summarizing all the different loss effects – no matter if being related to the atom or the cavity – by a single rate constant γ, the condition for strong coupling reads $g \gg \gamma$.

In order to give a picture of the involved dynamics, let us consider the atom and the cavity being initially prepared in the state $|0, \mathrm{e}\rangle \equiv |0\rangle \otimes |\mathrm{e}\rangle$; i.e., the excited TLS interacts with an empty cavity. Allowing free evolution of the system and neglecting dissipative effects, coherent oscillations of frequency $2g$ between the states $|0, \mathrm{e}\rangle$ and $|1, \mathrm{g}\rangle$ can be observed, so-called vacuum Rabi oscillations, where $|\mathrm{g}\rangle$ stands for the energy groundstate of the qubit. Placing a second atom inside the cavity, information between the two atoms can be transferred with the help of the photon.

Under the dipole approximation, which is also applied in the derivation of the Hamiltonian (1.15), the strength of the coupling is directly proportional to the dipole moment d of the atom and the vacuum electric field E_{el} at the position of the atom in the cavity, where E_{el} scales inversely with the cavity volume V_c [27, 28]:

$$\hbar g = -dE_{\mathrm{el}} = -d\sqrt{\frac{\hbar\Omega}{2\varepsilon_0 V_c}}, \tag{1.16}$$

with ε_0 being the permittivity of the vacuum. For a hydrogenic Rydberg atom placed in a three-dimensional resonator, the dimensionless coupling strength g/Ω can be estimated as [30]

$$\frac{g}{\Omega} \sim \frac{\alpha^{3/2}}{\sqrt{8V_c/\lambda^3}}, \tag{1.17}$$

with α being the fine structure constant and λ the resonator wavelength. Furthermore, it was assumed that the oscillator frequency Ω equals the qubit transition frequency. Thus, we see that a natural upper bound for the coupling strength is given by the size of the cavity. In experiments with optical or microwave cavities, g/Ω is found to be of the order 10^{-6}. Even with this small value, the strong coupling regime can be achieved, because of the sharpness of the atomic transitions (few losses due to spontaneous emission to other atomic levels) and high cavity quality factors.

1.2.2 Circuit quantum electrodynamics

Inspired by the beautiful experiments in quantum optical systems, demonstrating the interaction between matter and light, proposals to use the ideas of cavity quantum electrodynamics also in solid-state setups emerged. There, photons being emitted from artificial atoms, like those being introduced in Sec. 1.1, are coupled to the quantized excitations of an electromagnetic oscillator, like a transmission-line resonator or a simple LC-circuit. As we will see in the following, experiments were soon to follow these theoretical concepts giving raise to the field of circuit quantum electrodynamics. The coupling strengths known from cavity QED could be excelled by far in these new setups, making today's solid-state qubits to another top candidates for quantum computing.

Circuit QED with a transmission-line resonator

In 2004, Blais et al. [29] suggested to place an artificial atom – in their case a Cooper-pair box – into a transmission-line resonator, see Fig 1.6. The resonator consists of a central conductor between two ground planes. The role of the cavity mirrors is taken by the two gaps in the central conductor, which are separated by about a resonator wavelength. In the shown proposal the qubit is located in between one of the ground planes and the central waveguide. A gate voltage can be applied to the Cooper-pair box by biasing the center conductor. This gate voltage consists of a dc-part and many oscillatory modes. Placed in the middle of the cavity the qubit couples to the mode which is maximal there. At low temperatures, it is sufficient to take only one these modes into account, and the resonator can be modeled as a simple LC-circuit of frequency $\Omega = 1/\sqrt{LC}$ so that we end up again with Eq. (1.15), the Hamiltonian of a qubit-oscillator system. The transition dipole moment of the Cooper-pair box can be derived as $d_{\mathrm{CPB}} = e\, s\, C_g/(C_g + C_J)$, where s is the spacing between the center plane and the groundplane, C_J the capacitance of the Josephson junction and C_g stands for the gate capacitor of the box (see Fig. 1.1). For experimentally realistic values of $C_g/(C_g + C_J) = 0.1$ and $s = 10\mu$m [29, 31], one finds a transition dipole moment of $d_{\mathrm{CPB}} \sim 2 \times 10^4\, ea_0$.[6] This is about four orders of magnitude larger than the one in real atoms. Apart from the enhanced dipole moment also the geometry of the cavity plays a decisive role, see Eqs. (1.16) and (1.17). Contrary to a 3D-cavity, the volume can be confined very tightly in the transverse directions only limited by the qubit size, which can be made much smaller than the resonator wavelength λ so that we can speak of a quasi-1D cavity ($V_{1D} \approx 10^{-6}$cm^3 versus $V_{3D} \approx 1$cm^3 [32]). It can be shown [30, 33] that the upper limit of the dimensionless coupling strength for such a setup scales like $g/\Omega \sim \alpha^{1/2}$, which is a

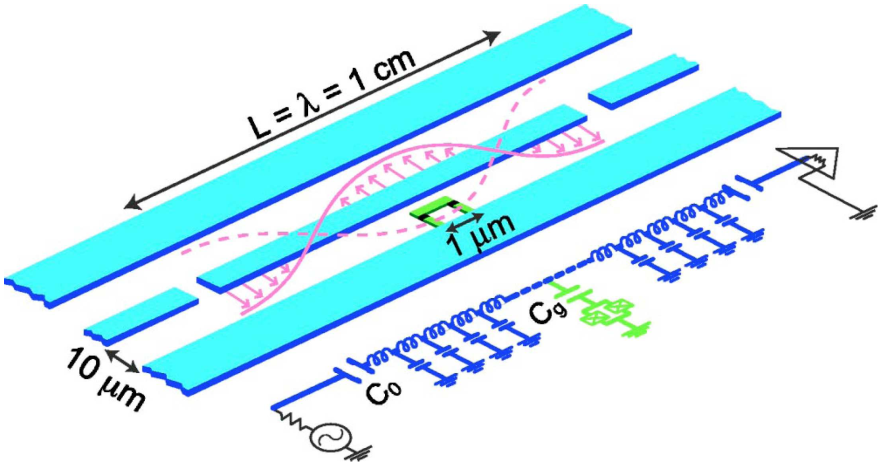

Figure 1.6: Circuit QED setup: A Cooper-pair box is placed in a one-dimensional cavity. The cavity is a so-called transmission-line resonator. It consists of a center conductor between two ground planes. The central line is interrupted by two gaps of capacity C_0 acting like mirrors in conventional cavities. Through an external voltage an electric field can be applied to the central line, forming standing waves in the cavity. The qubit is strongly coupled to one of these modes by electric dipole interaction. Lower figure: corresponding circuit representation. Reprinted figure with permission from [29]. Copyright (2004) by the American Physical Society.

---

[6] The Bohr radius is given by a_0.

clear improvement to the cavities used for real atoms and can lead in realistic experimental situations to coupling strengths of a few percent [29, 30], making it easier to reach the strong coupling limit. Another advantage compared to real atom experiments is that the parameters of the artificial atoms can be adjusted during the fabrication process or even be modified in situ [31]. Furthermore, the location of the atom is fixed, yielding a stable coupling constant g. Comparing to other qubit-oscillator setups, like a flux-qubit coupled to an LC-circuit, a benefit of the transmission-line setup is that the qubit can be fabricated inside the cavity, so that the resonator when being detuned from the qubit's transition frequency acts like an effective shielding of environmental influences, as we will see later in Chapter 4. Furthermore, photons traveling along the waveguide allow to connect even distant, non-neighboring qubits [34].

In [31], strong coupling between an artificial atom and a single photon could be observed for the first time in a solid-state device using the above setup. The resonator frequency measured by Wallraff et al. was $\Omega = 2\pi\, 6.044\,\mathrm{GHz}$, which corresponds to a temperature of about $\hbar\Omega/k_B \approx 300\,\mathrm{mK}$. By operating the system at a temperature $T < 100\,\mathrm{mK}$, the oscillator remains mainly in its groundstate $j = 0$, making transitions between the dressed states $|0, \mathrm{e}\rangle$ and $|1, \mathrm{g}\rangle$ most probable. Indeed, a splitting in the transmission spectrum of this qubit-oscillator system equivalent to a vacuum Rabi frequency of about 11.6 MHz could be observed.

Circuit QED with SQUIDS and LC-oscillators

Simultaneously to the experiment of the Yale group, demonstrating strong coupling between a Cooper-pair box and a transmission-line resonator, Chiorescu et al. could induce oscillations between the dressed qubit-oscillator states $|0, \mathrm{g}\rangle$ and $|1, \mathrm{e}\rangle$ (blue sideband) or $|1, \mathrm{g}\rangle$ and $|0, \mathrm{e}\rangle$ (red sideband) by applying an external driving [35]. In their experiment, they used the setup of Fig. 1.3, where the dc-SQUID in parallel with an external shunt capacitance can be modeled as harmonic oscillator [22, 23] of plasma frequency $\Omega = 1/\sqrt{(L_J + L_{sl})C_{sh}}$ with L_J being the inductance of the Josephson junctions of the SQUID, L_{sl} its self-inductance and C_{sh} the shunt capacitance.[7] The coupling between the TLS and the oscillator is inductively mediated by the supercurrent in the shared qubit and SQUID branches giving rise to a coupling strength of $g \approx 0.2\,\mathrm{GHz}$. Chiorescu et al. also performed measurements by applying a strong, resonant microwave radiation directly to the qubit, which corresponds to a *classical* electromagnetic field involving many photons. Also for this case of a driven TLS, which we will discuss in more detail in Chapter 5, induced Rabi oscillations were observed. However, notice, that these "driven" Rabi oscillations are different from the vacuum ones, as, first, the former involve a classical rather than a quantum oscillator, and thus the qubit oscillates between its energy eigenstates $|\mathrm{g/e}\rangle$, while for the latter the oscillation takes place between the states $|0, \mathrm{e}\rangle$ and $|1, \mathrm{g}\rangle$, which are not eigenstates of the total Hamiltonian. Second, for the driven case, the Rabi frequency depends linearly on the microwave amplitude, whereas the vacuum Rabi frequency only depends on intrinsic system parameters [35, 37, 38].

In the slightly different setup of Johansson et al. [38], the flux qubit and SQUID are additionally enclosed by a larger loop forming an LC-circuit of frequency $\Omega = 1/\sqrt{LC}$, which again can be described as a harmonic oscillator. The SQUID in this setup is just used for

---

[7] If the SQUID is biased with a current close to the switching current the harmonic oscillator model is not valid anymore and nonlinear effects must be taken into account, see [36].

readout purposes and thus can be neglected in the total Hamiltonian, so that we end up again with Eq. (1.15) for the qubit-oscillator system. By preparing the system in the state $|0, \mathrm{e}\rangle$ and bringing the qubit through an external flux pulse in resonance with the LC-circuit, coherent vacuum Rabi oscillations could be observed.

Up to now, many experiments have been performed in the field of circuit QED differing more or less strongly from the setups introduced above but proving the feasibility of the principle idea of using solid-state systems for quantum computing. For instance, Houck and colleagues made the transmission-line resonator penetrable at one end so that photons being emitted from a transmon qubit, which is an optimized version of the Cooper-pair box with tuneable transition frequency, can leave the cavity, travel along the wave-guide and transport with them the information about the state of the emitting artificial atom – so-called *flying qubits* [39]. Coherent state transfer was demonstrated between two Josephson phase qubits [40] (large superconducting loops interrupted by just a single Josephson junction) or transmon qubits [34] which were coupled to the ends of a transmission-line resonator.

Crucial for all these experiments is that the qubit and the oscillator are in the strong coupling regime. However, the dimensionless coupling constant g/Ω remains small enough so that for theoretical investigations the Jaynes-Cummings model (JCM) [41] is still applicable. This model is based on a rotating-wave approximation (RWA) and neglects transitions between nonresonant terms. It works for small coupling strengths $g/\Omega \ll E_{\mathrm{qb}}, \Omega$ and around resonance $E_{\mathrm{qb}} \approx \Omega$. For a more detailed discussion see Sec. 2.1.

While in the original transmission-line experiment of Wallraff et al. a coupling strength of $g/\Omega \sim 10^{-3}$ was observed, in more recent setups couplings up to a few percent, $g/\Omega \lesssim 0.025$, have been reported [34, 40, 42–44], reaching the upper limit possible for electric dipole coupling [30, 33], whereas in cavity QED one finds typically $g/\Omega \sim 10^{-6}$ [25]. Already with coupling strengths getting closer to $g/\Omega = 0.1$, an application of the JCM is questionable. Thus, in Section 2.2, we will present the effect of taking higher orders in the coupling g into account and consider also counter-rotating terms. However, for even higher coupling strengths approaches are needed which are nonperturbative in g. In the next section, we will introduce the regime of ultrastrong coupling, where the JCM breaks down.

1.2.3 The ultrastrong coupling regime

So far we have assumed for the qubit-transmission-line experiment that the artificial atom is placed in between the center conductor and the groundplane. Devoret et al. analyzed theoretically the change in the coupling strength if instead the Cooper-pair box interrupts the central conductor (direct coupling) [30]. Then, the predominant coupling mechanism is a magnetic instead of an electric one, since the qubit couples to the current in the cavity, and coupling strengths of $g/\Omega \sim \alpha^{-\frac{1}{2}}$ or for reasonable experimental values up to $g/\Omega \simeq 20$ are predicted. To our knowledge the Devoret proposal, which is based on charge qubits, has not been realized experimentally yet. In 2009, Bourassa et al. [45] proposed a setup where a Josephson flux qubit is placed within the center line of an inhomogeneous cavity.[8] The coupling strength depends on the length of the shared qubit-resonator element and thus is not dependent on the total area of the qubit loop so that also qubits with a smaller inductance can couple effectively, while spurious flux noise is avoided. Dimensionless coupling strengths of a several tens of percent have been predicted and, indeed, $g/\Omega \approx 0.12$ was measured just recently by Niemczyk and colleagues [46] in a beautiful experiment, where they could

---

[8] Note that for the description of an inhomogeneous cavity a single mode is not sufficient anymore.

even show in direct observation the failure of the JCM. For a flux-qubit coupled galvanically to an LC-circuit, Forn-Díaz et al. measured the Bloch-Siegert shift at a coupling strength $g/\Omega \approx 0.09$ [47], a phenomenon which cannot be explained by the JCM neither, see Eq. (2.20), and much stronger couplings seem to be in reach in those systems [48].

In semiconductor systems the ultrastrong coupling regime has been proposed for intersubband cavity polaritons in the far infrared [49] and been recently reached experimentally [50, 51]. Furthermore, the ultrastrong coupling regime has been predicted for qubits coupled to a nanomechanical resonator [52].

1.3 Thesis outline

The recent advances of both theoretical and experimental nature which have been introduced in this chapter ask for analytical techniques to treat the qubit-oscillator system beyond the rotating-wave approximation. Therefore, we present in Chapter 2 two approaches which fullfill this demand: one of them relies on a perturbative treatment with respect to the coupling between qubit and oscillator and thus is still restricted to intermediate coupling strengths, while the other one considers the tunneling matrix as small parameter and allows for a treatment of ultrastrong coupling. We compare both of them to the Jaynes-Cummings model.

In order to treat environmental influences on the qubit, we give in Chapter 3 a short review on the concept of quantum master equations. In particular, we discuss the Caldeira-Leggett model and sketch how it leads under certain approximations to the Bloch-Redfield master equation, by which the time evolution of the density operator for a system coupled to a thermal bath of harmonic oscillators can be calculated.

In Chapter 4, we apply the master equation approach to obtain the dissipative dynamics of the qubit-oscillator system. We use different approximations for solving analytically the underlying differential equations and compare our results to numerical calculations and the dissipative Jaynes-Cummings model.

In the limit of high photon numbers the quantized harmonic oscillator can be treated classically, leading together with the coupling to the environment to the driven spin-boson model. In a first step, we demonstrate in Chapter 5, how the nondissipative dynamics of this model can be obtained by a combination of Floquet theory and Van Vleck perturbation theory contrasting it to a rotating-wave treatment of the external driving. Then, we include dissipative effects by considering the Floquet-Born-Markov master equation. We give a detailed discussion of the relaxation and dephasing rates of the TLS. Moreover, coherent destruction of tunneling and driving-induced oscillations are examined.

Chapter 6 combines the concepts introduced in Chapter 2 and 5: we investigate a driven TLS coupled to quantized harmonic oscillator. We introduce the dressed Floquet state basis and calculate the quasienergy spectrum of the qubit-oscillator system perturbatively in the tunneling matrix element. We close the chapter with a discussion on the dynamics of the reduced density operator of the qubit.

The major results of this thesis are summarized in Chapter 7, where also an outlook to future work is provided.

2 Analytical methods beyond the rotating-wave approximation

Parts of this chapter have been published in collaboration with M. Grifoni [53], [54].

As already pointed out in the previous section, the Jaynes-Cummings model (JCM) is usually invoked to explain cavity and circuit QED experiments for coupling strengths with $g \ll E_{\rm qb}, \Omega$. Going beyond those coupling strengths and especially in the ultrastrong coupling regime, the rotating-wave approximation and thus the JCM is *not* satisfied anymore. After giving a more detailed explanation of the JCM in Sec. 2.1, we will present in this chapter two different approaches to treat also stronger coupling: The first one relies on a perturbative treatment with respect to g, and we will calculate the energy spectrum and eigenstates of the qubit-oscillator Hamiltonian up to second order in Sec. 2.2. By this, we can treat couplings like they occur in the experiments of Niemczyk et al. [46] and Forn-Díaz et al. [47]. The second method takes all orders of the coupling strength into account and thus also works in the deep ultrastrong coupling regime. It relies on a perturbative approach in the modified tunneling matrix element, which we will introduce in Sec. 2.3. Both approaches will be found to work well in different parameter regimes and thus can explain, if used together, the behavior of the qubit-oscillator system for the whole coupling range. We will examine further the nondissipative dynamics of the qubit using both approaches. That means, we will calculate the population difference

$$P(t) = \langle \sigma_z(t) \rangle = \mathrm{Tr}_{\rm TLS}\{\sigma_z \rho_{\rm red}(t)\} = 2\langle \uparrow | \rho_{\rm red}(t) | \uparrow \rangle - 1 \tag{2.1}$$

between the $| \uparrow\rangle$ and $| \downarrow\rangle$ states of the qubit. The reduced density operator of the TLS $\rho_{\rm red}(t) = \mathrm{Tr}_{\rm osc}\{\rho(t)\}$ is found after tracing out the oscillator degrees of freedom from the qubit-oscillator density operator ρ. As starting conditions, we assume the qubit and the oscillator to be uncoupled for $t < 0$, and the first to be prepared in the spin-up state, while the oscillator being in thermal equilibrium obeying a Boltzmann distribution:

$$\rho(0) = | \uparrow\rangle\langle \uparrow | \otimes \sum_j \frac{1}{Z} \mathrm{e}^{-\hbar\beta j \Omega} |j\rangle\langle j|, \tag{2.2}$$

where Z is the partition function of the harmonic oscillator, and $\beta = (k_B T)^{-1}$ the inverse temperature. In order to determine the time evolution of the density operator, we have to express it in the eigenbasis of the qubit-oscillator Hamiltonian. Thus, in the following we will diagonalize this Hamiltonian approximately, calculating its eigenstates and the corresponding eigenenergies. In both approaches we will use Van Vleck perturbation theory (VVP). Originally this method was used to treat modifications on diatomic molecules caused by vibrations and rotations of the nuclei [55]. Since then, the formalism has found many applications in both chemistry and physics and experienced various modifications; see, for example, [56–59]. The main idea behind these different variants is, however, always the same: a unitary transformation T is applied in order to construct an effective Hamiltonian which exhibits, to a certain order in the perturbation, the same eigenenergies as the original Hamiltonian but only connects almost degenerate levels. In this work we choose for the transformation the form $T = \exp(\mathrm{i}S)$, which was originally proposed by Kemble in [60] and is described in more detail in [28] and Appendix A.

2.1 Rotating-wave approximation and Jaynes-Cummings model

The workhorse of cavity quantum electrodynamics is the so-called Jaynes-Cummings model (JCM). The Hamiltonian for the qubit-oscillator system as it is written down in Eq. (1.15) cannot be diagonalized analytically. However, for not too strong coupling strengths, $g \ll E_{\mathrm{qb}}, \Omega$, a simplification can be invoked. To this end, we consider the TLS Hamiltonian H_{TLS} in its energy eigenbasis, defined by the ground and excited states,

$$|\mathrm{g}\rangle = \cos(\Theta/2)|\uparrow\rangle - \sin(\Theta/2)|\downarrow\rangle \quad \text{and} \quad |\mathrm{e}\rangle = \sin(\Theta/2)|\uparrow\rangle + \cos(\Theta/2)|\downarrow\rangle, \tag{2.3}$$

with the mixing angle $\tan\Theta = -\Delta/\varepsilon$ for $-\pi/2 \leq 0 < \pi/2$. In this basis we find, $H'_{\mathrm{TLS}} = -\hbar E_{\mathrm{qb}}\sigma'_z/2$, where $E_{\mathrm{qb}} = \sqrt{\varepsilon^2 + \Delta^2}$ is the qubit transition frequency, and $\sigma'_z|\mathrm{g/e}\rangle = \pm|\mathrm{g/e}\rangle$. As basis for the qubit-oscillator system we use now $|j, \mathrm{g/e}\rangle \equiv |j\rangle \otimes |\mathrm{g/e}\rangle$, where $|j\rangle$ is a Fock-number state of the harmonic oscillator. The Hamiltonian (1.15), becomes

$$H'_{\text{TLS-osc}} = -\frac{\hbar}{2}E_{\mathrm{qb}}\sigma'_z + \hbar\Omega B^\dagger B + \hbar g\left(\frac{\varepsilon}{E_{\mathrm{qb}}}\sigma'_z - \frac{\Delta}{E_{\mathrm{qb}}}\sigma'_x\right)(B + B^\dagger). \tag{2.4}$$

For the case of zero static bias ($\varepsilon = 0$),[1] and by introducing the qubit raising and lowering operators $\sigma'_\pm = \frac{1}{2}(\sigma'_x \pm \mathrm{i}\sigma'_y)$, the interaction part can be written as

$$H'_{\mathrm{int}} = H'_{\mathrm{R}} + H'_{\mathrm{NR}} = -\hbar g(\sigma'_+ B + \sigma'_- B^\dagger) - \hbar g(\sigma'_- B + \sigma'_+ B^\dagger). \tag{2.5}$$

Hereby, H'_{R} describes resonant processes, where, for instance, the atom is excited while an oscillator quantum is annihilated, whereas H'_{NR} stands for nonresonant processes, in which the atom and the field are excited or deexcited simultaneously, so that the total number of excitations in the system is changed. The latter contributions are also often called counter-rotating terms, because, if we assume the qubit and the oscillator being at or close to resonance ($E_{\mathrm{qb}} \approx \Omega$) and transform the Hamiltonian into the rotating frame [27], those terms are oscillating fast and are usually neglected – a procedure which is known as the rotating-wave approximation (RWA). This leads to the Jaynes-Cummings Hamiltonian [41]:

$$H^{\mathrm{JCM}} = -\hbar\frac{\Delta}{2}\sigma'_z + \hbar\Omega B^\dagger B - \hbar g(\sigma'_+ B + \sigma'_- B^\dagger), \tag{2.6}$$

which is commonly used in quantum optics to describe interaction of matter and light.[2] This Hamiltonian can be diagonalized exactly. The energy of the groundstate $|0\rangle^{\mathrm{JCM}} = |0, \mathrm{g}\rangle$ is $E_0^{\mathrm{JCM}} = -\hbar E_{\mathrm{qb}}/2$. For the higher states we get

$$|2j+1\rangle^{\mathrm{JCM}} = \cos\left(\alpha_j^{\mathrm{JCM}}/2\right)|(j+1), \mathrm{g}\rangle + \sin\left(\alpha_j^{\mathrm{JCM}}/2\right)|j, \mathrm{e}\rangle, \tag{2.7}$$

$$|2j+2\rangle^{\mathrm{JCM}} = -\sin\left(\alpha_j^{\mathrm{JCM}}/2\right)|(j+1), \mathrm{g}\rangle + \cos\left(\alpha_j^{\mathrm{JCM}}/2\right)|j, \mathrm{e}\rangle, \tag{2.8}$$

---

[1] Note that in cavity QED experiments the static bias ε is usually zero. In superconducting qubits, however, it can be tuned easily also to nonzero values.

[2] For $\varepsilon \neq 0$ a term proportional to $(B + B^\dagger)(|\mathrm{e}\rangle\langle\mathrm{e}| - |\mathrm{g}\rangle\langle\mathrm{g}|)$ is neglected within the RWA as well [61].

corresponding to the eigenenergies

$$\hbar E^{\mathrm{JCM}}_{2j+1/2j+2} = \hbar \left[(j+\frac{1}{2})\Omega \mp \frac{1}{2}\sqrt{\delta^2 + 4(j+1)g^2} \right] , \tag{2.9}$$

with $\delta = \Delta - \Omega$ and $\tan \alpha^{\mathrm{JCM}}_j = 2\sqrt{j+1}g/\delta$. Except for the groundstate, the eigenstates of the JCM are built from superpositions of two states, namely $|j+1, \mathrm{g}\rangle$ and $|j, \mathrm{e}\rangle$. At qubit-oscillator resonance ($\Omega = \Delta$), those doublets build for vanishing coupling, $g = 0$, a two-fold degenerate subspace, see Fig. 2.1. For finite g, the degeneracy in those subspaces is lifted, and the corresponding eigenenergies are split by $2\hbar g\sqrt{j+1}$, see Eq. (2.9). For the lowest doublet, we get the vacuum Rabi-splitting of $2g$. For strong detuning, $|\delta| \gg 0$, and/or stronger coupling, $g/\Omega \gtrsim 10^{-1}$, the JCM is not a valid approximation anymore. We will see in the later part of this work, how higher order corrections in the coupling play an important role and the picture of the JCM can be improved. We will, however, also in these schemes always try to identify manifolds of two-dimensional subspaces, which we can diagonalize easily.

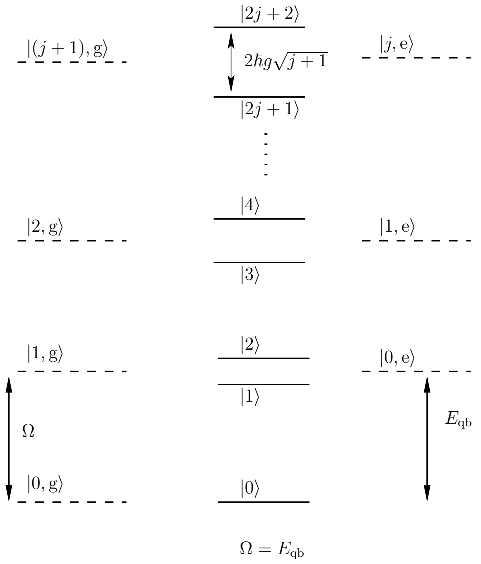

Figure 2.1: Energy spectrum of a qubit-oscillator system at resonance ($\Omega = E_{\mathrm{qb}}$). The two outer columns show the uncoupled case ($g = 0$). On the left side, qubit-oscillator states involving the TLS groundstate are shown; on the right side, the excited TLS states. At resonance the states $|j+1, \mathrm{g}\rangle$ and $|j, \mathrm{e}\rangle$ are degenerate and form a two-dimensional subspace or manifold. In the middle column the so-called Jaynes-Cummings ladder [42] can be seen: for finite coupling g the degeneracy in the subspaces is lifted, and the energy levels split by $2\hbar g\sqrt{j+1}$.

2.2 Perturbation theory in g

In this first approach the coupling strength g is assumed to be small compared to the qubit transition frequency E_{qb} and the oscillator frequency Ω. We show how to find the eigenvalues of the unperturbed qubit-oscillator Hamiltonian $H_{\text{TLS-osc}}$ approximately by using Van Vleck perturbation theory (VVP). The idea is to take advantage of the doublet structure of the energy spectrum of the uncoupled ($g = 0$) qubit-oscillator system near resonance, e.g., around $E_{\mathrm{qb}} \approx \Omega$. Then, as long as the perturbation is small compared to the energy separation of the different doublets, the full Hamiltonian will exhibit a similar spectrum of bundled energy levels.

2.2.1 Energy spectrum and eigenstates

The eigenenergies of the uncoupled qubit-oscillator system ($g = 0$) are easily found as $\mp\hbar E_{\mathrm{qb}}/2 + \hbar j\Omega$ belonging to the eigenstates $|j, \mathrm{g/e}\rangle$. The dashed lines in Fig. 2.2 show

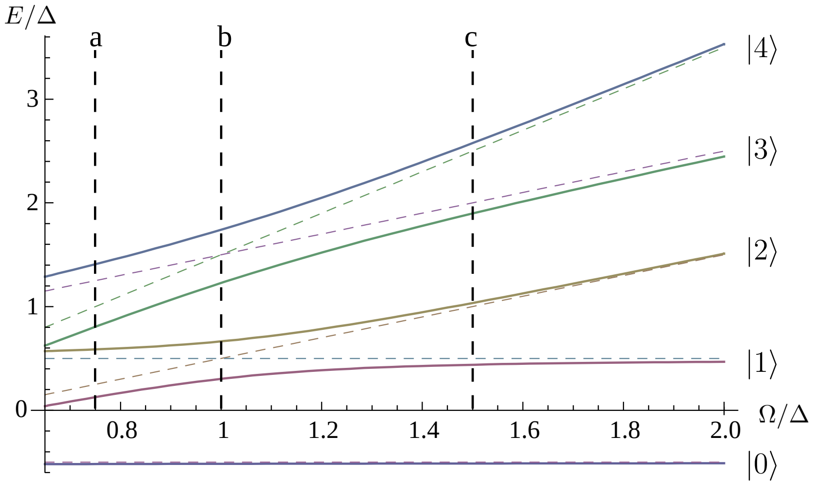

Figure 2.2: Energy spectrum of the coupled qubit-oscillator system against the oscillator frequency Ω. Solid lines show the energy levels for the five lowest energy states with the coupling being switched on ($g/\Delta = 0.18$) and the TLS being unbiased ($\varepsilon/\Delta = 0$). For comparison the energy levels for the uncoupled case are also given (dashed lines). At resonance ($\Omega/\Delta = 1$) the spectrum exhibits avoided crossings, whereas it approaches the uncoupled case away from resonance. The vertical dashed lines visualize three different situations: the positively detuned regime (a), the resonant case (b) and the negatively detuned regime (c).

the corresponding energy spectrum against the oscillator frequency Ω for the five lowest eigenstates. Except for the groundstate, $|0, \mathrm{g}\rangle$, the states $|j+1, \mathrm{g}\rangle$ and $|j, \mathrm{e}\rangle$ are degenerate in the resonant case ($\Omega = E_{\mathrm{qb}}$). Close to resonance the spectrum exhibits a doublet structure. In the following, we work in the energy basis of the qubit-oscillator system, $|j, \mathrm{g/e}\rangle$; i.e., we consider the Hamiltonian $H'_{\text{TLS-osc}}$, Eq. (2.4). In order to diagonalize it, we consider H'_{int} as a small perturbation, which is reasonable as long as $g \ll E_{\mathrm{qb}}, \Omega$. Applying VVP, we construct an effective Hamiltonian,

$$H'_{\mathrm{eff}} = \mathrm{e}^{\mathrm{i}S} H'_{\text{TLS-osc}} \mathrm{e}^{-\mathrm{i}S}, \tag{2.10}$$

having the same eigenvalues as $H'_{\text{TLS-osc}}$ but no matrix elements connecting states which are far off from degeneracy. Thus, H'_{eff} is block-diagonal with all quasidegenerate energy levels being in one common block. As in our case always two states are nearly degenerate, each block of H'_{eff} builds a 2 by 2 matrix. This matrix can be easily diagonalized in order to determine the eigenstates. Following [28, 58] we calculate the transformation matrix S up to second order in g. The general formulae for both an arbitrary Hamiltonian and $H'_{\text{TLS-osc}}$ are given in Appendix A. The only surviving matrix elements of the effective Hamiltonian, apart from the ones being of zeroth order in g, are

$$\left(H'_{\mathrm{eff}}\right)^{(1)}_{j\mathrm{e};(j+1)\mathrm{g}} = \left(H'_{\mathrm{eff}}\right)^{(1)}_{(j+1)\mathrm{g};j\mathrm{e}} = \hbar\tilde{\Delta}\sqrt{j+1} \quad \text{with} \quad \tilde{\Delta} = -\frac{g\Delta}{E_{\mathrm{qb}}}, \tag{2.11}$$

and

$$\left(H'_{\mathrm{eff}}\right)^{(2)}_{j\mathrm{e};j\mathrm{e}} = -\frac{\hbar\varepsilon^2}{E_{\mathrm{qb}}^2\Omega}g^2 + j\frac{\hbar\Delta^2}{E_{\mathrm{qb}}^2(E_{\mathrm{qb}}+\Omega)}g^2 \equiv \hbar(W_1 - jW_0), \tag{2.12}$$

$$\left(H'_{\mathrm{eff}}\right)^{(2)}_{j\mathrm{g};j\mathrm{g}} = \hbar[W_1 + (j+1)W_0]. \tag{2.13}$$

Thus, $H'_{\mathrm{eff}} = (H'_{\mathrm{eff}})^{(0)} + (H'_{\mathrm{eff}})^{(1)} + (H'_{\mathrm{eff}})^{(2)}$ has the matrix structure

$$H'_{\mathrm{eff}} = \hbar \left(\begin{array}{c|cc|c} \ddots & & & \\ \hline & \frac{E_{\mathrm{qb}}}{2} + j\Omega + W_1 - jW_0 & \sqrt{j+1}\tilde{\Delta} & \\ & \sqrt{j+1}\tilde{\Delta} & -\frac{E_{\mathrm{qb}}}{2} + (j+1)\Omega + W_1 + (j+2)W_0 & \\ \hline & & & \ddots \end{array} \right), \tag{2.14}$$

where the section shown corresponds to the basis states $|j, \mathrm{e}\rangle$ and $|j+1, \mathrm{g}\rangle$. From this form it is easy to calculate the eigenstates and eigenenergies. The groundstate $|0\rangle_{\mathrm{eff}} \equiv |0, \mathrm{g}\rangle$, which is an eigenstate of H'_{eff}, has the eigenenergy

$$\hbar E_0 = \hbar \left(-\frac{E_{\mathrm{qb}}}{2} + W_0 + W_1 \right). \tag{2.15}$$

The other eigenstates of H'_{eff} are, $j \geq 0$,

$$|2j+1\rangle_{\mathrm{eff}} = \cos(\alpha_j/2)\,|j+1, \mathrm{g}\rangle + \sin(\alpha_j/2)\,|j, \mathrm{e}\rangle, \tag{2.16a}$$

$$|2j+2\rangle_{\mathrm{eff}} = -\sin(\alpha_j/2)\,|j+1, \mathrm{g}\rangle + \cos(\alpha_j/2)\,|j, \mathrm{e}\rangle, \tag{2.16b}$$

corresponding to the eigenenergies

$$\begin{aligned} \hbar E_{2j+1/2j+2} =& \hbar \left[(j + \frac{1}{2})\Omega + W_1 + W_0 \mp \frac{\delta_j}{2\cos\alpha_j} \right] \\ =& \hbar \left[(j + \frac{1}{2})\Omega + W_1 + W_0 \mp \frac{1}{2}\sqrt{\delta_j^2 + 4(j+1)|\tilde{\Delta}|^2} \right], \end{aligned} \tag{2.17}$$

with $\delta_j = E_{\mathrm{qb}} - \Omega - 2(j+1)W_0$, $\tan\alpha_j = 2\sqrt{j+1}|\tilde{\Delta}|/\delta_j$ and $0 \leq \alpha_j < \pi$. By construction these are also eigenenergies of $H'_{\text{TLS-osc}}$. Using the transformation (2.10) we get the eigenvectors of $H'_{\text{TLS-osc}}$ as

$$|0\rangle = \mathrm{e}^{-\mathrm{i}S}|0\rangle_{\mathrm{eff}}, \quad |2j+1\rangle = \mathrm{e}^{-\mathrm{i}S}|2j+1\rangle_{\mathrm{eff}} \quad \text{and} \quad |2j+2\rangle = \mathrm{e}^{-\mathrm{i}S}|2j+2\rangle_{\mathrm{eff}}. \tag{2.18}$$

The energy spectrum of $H'_{\text{TLS-osc}}$ is shown in Fig. 2.2 for the case of an unbiased TLS ($\varepsilon = 0$). We want to emphasize that our findings are also valid for the more general case $\varepsilon \neq 0$. At resonance, where the spectrum for the uncoupled case is degenerated, avoided crossings can be seen. The gap between two formerly degenerated levels for $\Omega = E_{\mathrm{qb}}$ is

$$E_{2j+2} - E_{2j+1} = 2\sqrt{j+1}g + \mathcal{O}(g^3), \tag{2.19}$$

which is as predicted by the Jaynes-Cummings model [41, 62].
Comparing the Van Vleck eigenstates and eigenenergies to the ones found by the JCM, Eqs. (2.7), (2.8) and (2.9), we see that the counter-rotating terms yield second-order corrections in g not present in the Jaynes-Cummings Hamiltonian. These corrections give rise to a very prominent effect concerning the resonance condition between the TLS and the oscillator. From δ_{JC} we find the TLS being in resonance with the oscillator for $\Omega = E_{\mathrm{qb}}$. Considering δ_j from the calculations above, this resonance condition is shifted to

$$\Omega = E_{\mathrm{qb}}\sqrt{1 + 2(j+1)\frac{\Delta^2}{E_{\mathrm{qb}}^4}g^2} \approx E_{\mathrm{qb}}\left[1 + (j+1)\frac{\Delta^2}{E_{\mathrm{qb}}^4}g^2 + \mathcal{O}(g^3)\right]. \tag{2.20}$$

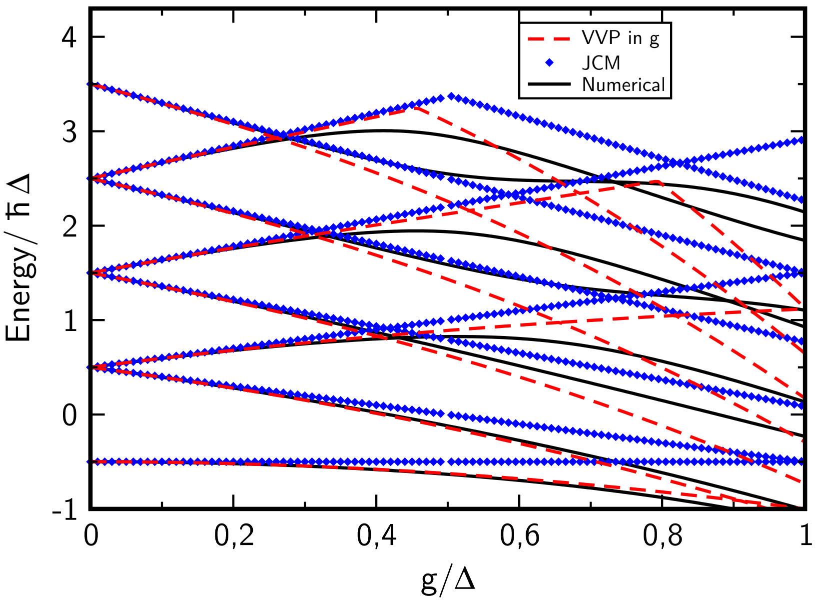

Figure 2.3: Energy spectrum of the qubit-oscillator system against coupling strength g at zero bias ($\varepsilon/\Delta = 0$) and for zero detuning ($\Delta = \Omega$), see line b) in Fig. 2.2. We compare results obtained from numerical diagonalization to the JCM and VVP to second order in g. For the lower energy levels VVP shows better agreement with the numerics than JCM, while the latter seems to work better for the 6th and 8th level. For coupling strengths $g/\Delta \gtrsim 0.3$, deviations for both analytical methods increase.

This second-order correction to the resonance frequency due to counter-rotating terms is known as Bloch-Siegert shift [63]. The eigenstates of the JCM, Eqs. (2.7) and (2.8), are always a superposition of two basis states of the unperturbed system. This is like for the eigenstates (2.16a) and (2.16b) of the effective Hamiltonian (2.10). However, in order to find the eigenstates $|n\rangle$ of $H_{\text{TLS-osc}}$ we had to apply the transformation $\exp(-\mathrm{i}S)$ on the effective eigenstates so that $|n\rangle$ is in the end a superpostion of *several* states of the basis $\{|j, \mathrm{g}\rangle; |j, \mathrm{e}\rangle\}$. The Bloch-Siegert shift in a qubit-oscillator system has just recently been measured in [47] for a coupling of $g/\Omega = 0.09$.

In Figs. 2.3, 2.4 and 2.5, the energy spectrum of the qubit-oscillator model is shown for zero, positive and negative detuning of the qubit, respectively, at zero static bias ($\varepsilon = 0$) against the coupling strength g. We thereby compare VVP and the JCM against an exact numerical diagonalization. In all three cases, both VVP and the JCM agree well with the numerics for weak coupling, $g/\Delta \lesssim 0.3$. For higher coupling strength, VVP shows an improvement to the JCM for the lower energy levels, which will be especially important during the calculation of the dynamics at low temperature. The 6th and 8th energy level seem to be given even better by the JCM. However, no systematic improvement by the JCM compared to the VVP can be seen for higher energy levels in general. Surprisingly, for the case of negative detuning, $\Omega/\Delta = 1.5$, VVP yields almost exact results for the lowest two energy levels up to a coupling strength to $g/\Delta = 1.0$. Strictly speaking, for such a strong detuning, the states $|j+1, \mathrm{g}\rangle$ and $|j, \mathrm{e}\rangle$ do not build a degenerate subspace anymore. Still, VVP seems to work well.

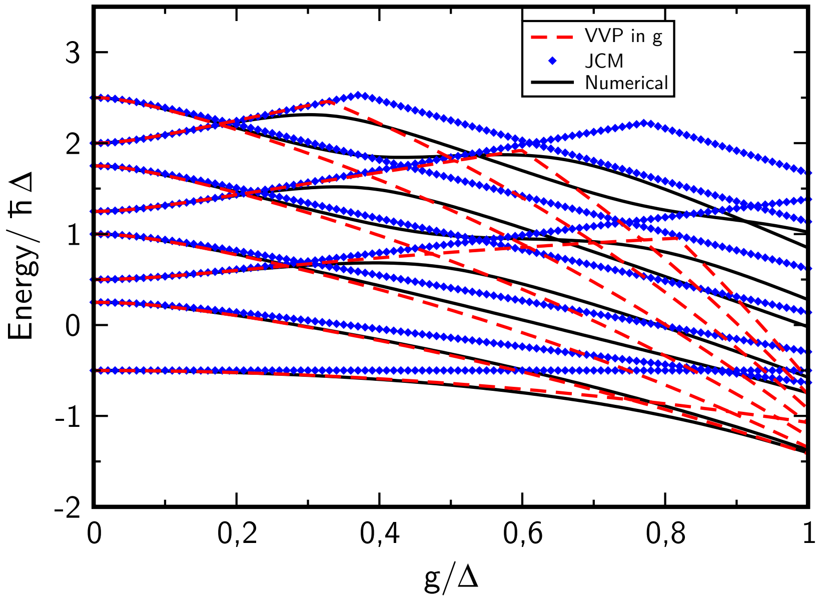

Figure 2.4: Same as in Fig. 2.3 but for positive detuning ($\Omega/\Delta = 0.75$), see line a) in Fig. 2.2. For the lower energy levels, again VVP shows a better agreement with the numerics than the JCM, while both get less reliable for coupling strengths of $g/\Delta \gtrsim 0.3$.

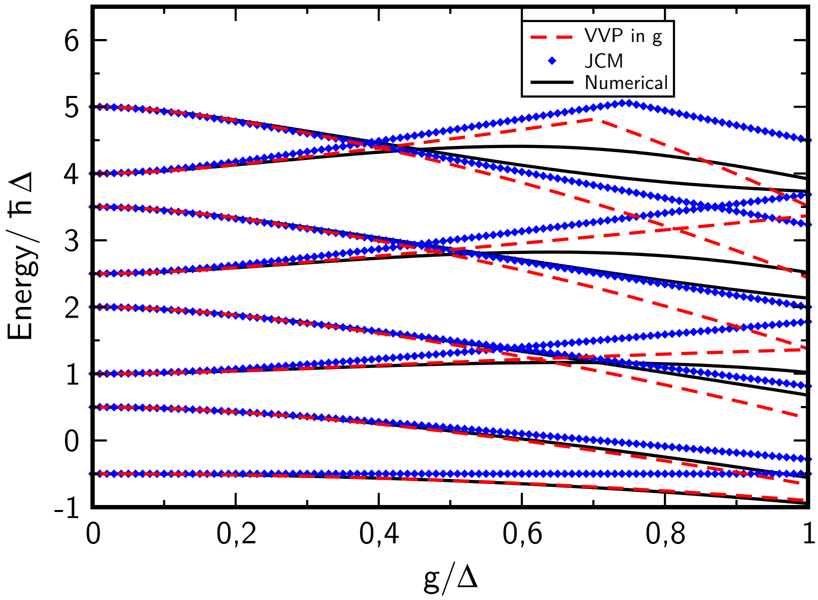

Figure 2.5: Same as in Fig. 2.3 but for negative detuning ($\Omega/\Delta = 1.5$), see line c) in Fig. 2.2. For the first two levels, VVP returns the numerical results even up to $g/\Delta = 1$, while the JCM fails for $g/\Delta \gtrsim 0.4$. Also for the higher energy levels, the agreement between VVP and the numerics is enhanced.

2.2.2 Nondissipative dynamics

Having calculated the eigenstates and eigenenergies of the qubit-oscillator system, we examine now the dynamics of the TLS; i.e., we turn our attention to formula (2.1) for the population difference. After some algebra, illustrated in more detail in B.1, we arrive at an expression for $P(t)$, given in terms of diagonal and off-diagonal elements of $\rho(t)$ in the TLS-qubit energy eigenbasis $\{|n\rangle\}$. It reads

$$P(t) = \sum_n p_{nn}(t) + \sum_{\substack{n,m \\ n>m}} p_{nm}(t) \tag{2.21}$$

where

$$p_{nn}(t) = \sum_j \left\{ \cos\Theta \left[\langle j,\mathrm{g}|n\rangle^2 - \langle j,\mathrm{e}|n\rangle^2 \right] + 2\sin\Theta \langle j,\mathrm{g}|n\rangle\langle j,\mathrm{e}|n\rangle \right\} \rho_{nn}(t), \tag{2.22a}$$

$$\begin{aligned} p_{nm}(t) = 2\sum_j \Big\{ & \cos\Theta \left[\langle j,\mathrm{g}|n\rangle\langle m|j,\mathrm{g}\rangle - \langle j,\mathrm{e}|n\rangle\langle m|j,\mathrm{e}\rangle \right] \\ & + \sin\Theta \left[\langle j,\mathrm{e}|n\rangle\langle m|j,\mathrm{g}\rangle + \langle j,\mathrm{e}|m\rangle\langle n|j,\mathrm{g}\rangle \right] \Big\} \mathrm{Re}\{\rho_{nm}(t)\} \end{aligned} \tag{2.22b}$$

with $\rho_{nm}(t) = \langle n|\rho(t)|m\rangle$. Equation (2.21) is valid quite generally both in the dissipative and nondissipative case. All we have to know are the matrix elements of the density operator and its behavior with time. With qubit and oscillator forming a closed system, the time evolution of the density operator is given by $\rho(t) = \mathrm{e}^{-(\mathrm{i}/\hbar)H_{\text{TLS-osc}}t}\rho(0)\mathrm{e}^{(\mathrm{i}/\hbar)H_{\text{TLS-osc}}t}$ and consequently

$$\rho_{nm}(t) = \langle n|\rho(t)|m\rangle = \mathrm{e}^{-\mathrm{i}\omega_{nm}t}\rho_{nm}(0) \tag{2.23}$$

with $\omega_{nm} = \frac{1}{\hbar}(E_n - E_m)$. With that Eq. (2.21) becomes

$$P(t) = p_0 + \sum_{\substack{n,m \\ n>m}} p_{nm}(0)\cos\omega_{nm}t, \tag{2.24}$$

where we defined $p_0 \equiv \sum_n p_{nn}(0)$. From Eq. (2.24) we notice that the dynamics of the qubit is characterized by an infinite number of oscillation frequencies. This is a consequence of the coupling to the oscillator.

Low temperature approximation

With Eq. (2.24) we found a formula which describes the nondissipative dynamics up to second order in g, thereby taking into account all oscillator levels. Thus, we still have to deal with an infinite Hilbert space. Typical experiments, see, e.g., [31, 35], run in a temperature regime for which $\beta^{-1} \lesssim \hbar\Omega, \hbar E_{\mathrm{qb}}$. In the following, we will consider $\beta = 10(\hbar\Delta)^{-1}$. For tunneling elements in the GHz regime, this corresponds to a temperature of several mK. Since we consider a thermal occupation for the harmonic oscillator, it is sufficient to assume only its lower levels to be occupied at such a small temperature. However, it will turn out later that this holds only true for not too strong coupling values g. For the following analytical calculation, it will be sufficient to concentrate on eigenstates of $H_{\text{TLS-osc}}$ up to $|4\rangle$. This truncation leaves us with ten possible oscillation frequencies ω_{nm}, where $n, m = 0, 1, \ldots, 4$ and $n > m$.

Dynamics for zero static bias ($\varepsilon = 0$)

As a first example we calculate the dynamics of an unbiased TLS ($\varepsilon = 0$). Here the coefficients p_0, $p_{30}(0)$, $p_{40}(0)$, $p_{21}(0)$ and $p_{43}(0)$ vanish due to symmetry, so that

$$\begin{aligned} P(t) =& p_{10}\cos(\omega_{10}t) + p_{20}\cos(\omega_{20}t) + p_{31}\cos(\omega_{31}t) + p_{41}\cos(\omega_{41}t) \\ &+ p_{32}\cos(\omega_{32}t) + p_{42}\cos(\omega_{42}t)\,. \end{aligned} \tag{2.25}$$

Additionally as a benchmark, we consider a case where the JCM is expected to still work fine, namely relatively weak coupling $g/\Delta = 0.18$ and qubit and oscillator being in resonance ($\Omega = \Delta$). In this case we find with Eq. (2.17) the transitions frequencies

$$\omega_{10} = \Delta_0 - g, \quad \omega_{20} = \Delta_0 + g, \tag{2.26a}$$

$$\omega_{31} = \Delta_0 + (1 - \sqrt{2})g, \quad \omega_{41} = \Delta_0 + (1 + \sqrt{2})g, \tag{2.26b}$$

$$\omega_{32} = \Delta_0 - (1 + \sqrt{2})g, \quad \omega_{42} = \Delta_0 - (1 - \sqrt{2})g. \tag{2.26c}$$

The dynamical quantity $P(t)$ and its Fourier transform,

$$F(\nu) := 2\int_0^\infty dt P(t)\cos(\nu t), \tag{2.27}$$

are shown in Fig. 2.6. Six different frequencies, which are in the Fourier spectrum symmetrically located around the point $\omega = \Delta_0$, are found. Among those frequencies ω_{10} and ω_{20} are dominating. They correspond to transitions between the first or second energy level of the qubit-oscillator system and its groundstate. Their weights are almost equal, and they give raise to the famous vacuum Rabi splitting of $2g$. We further notice that the JCM only returns those two frequencies. Nevertheless, one sees almost no difference between the JCM and VVP for $P(t)$. Thus, for the nondissipative, zero static bias case and a coupling of $g/\Delta = 0.18$, the JCM represents a good and sufficient approximation for the dynamics. However, this will change when we consider also dissipation in Chapter 4.

In Figs. 2.7, 2.8 and 2.9, we examine the dynamics for a stronger coupling $g/\Delta = 0.3$. We investigate zero ($\Omega/\Delta = 1$), positive ($\Omega/\Delta = 0.75$) and negative ($\Omega/\Delta = 1.5$) qubit-oscillator detuning. Both the JCM and VVP give a picture which corresponds qualitatively well to the numerical results. However, concerning the population difference $P(t)$, both approaches get slightly out of phase with time. In the resonant case in Fig. 2.7, the deviations of the JCM and VVP from the numerics are almost equally strong, albeit the JCM does not cover the small oscillation peaks ω_{32}, ω_{31}, ω_{42} and ω_{41}. The dominating frequencies ω_{10} and ω_{20} are for both methods almost exactly located as predicted by the numerics. For positive detuning, Fig. 2.8, the JCM gets a bit faster out of phase than the VVP graph. Here, the dominating frequency is ω_{20}. Stronger deviations from the two main frequencies than observed in Fig. 2.7 can be seen. For negative detuning in Fig. 2.9, ω_{10} dominates. We will explain later how the weights of the frequencies depend on the detuning. In contrast to the JCM, VVP agrees very well with the numerics for $\Omega > \Delta$. We could already notice such a behavior in the energy spectrum, see Fig. 2.5. We also examined higher coupling strengths using the methods introduced in this section. However, the deviations between the two analytical methods and exact numerical results increased fast. Also our simplification to use only the four lowest energy levels of the qubit-oscillator system turned out not to hold anymore at higher coupling.

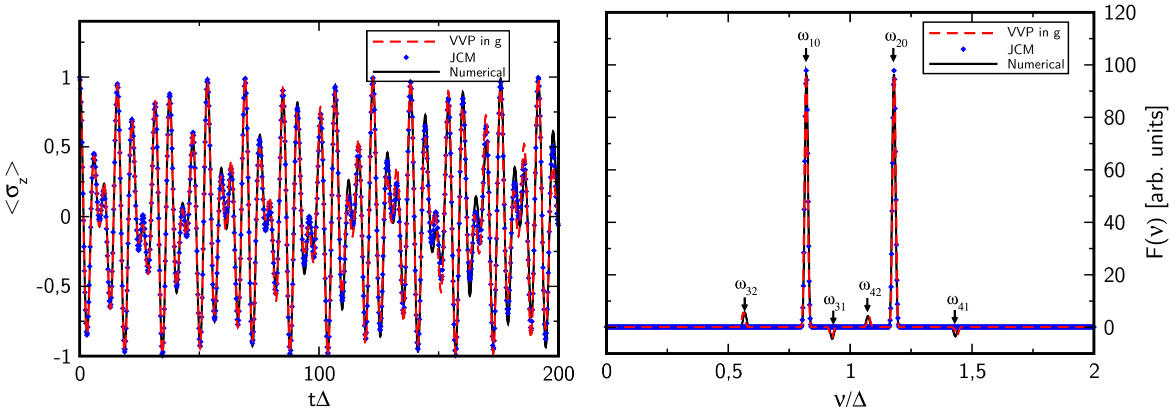

Figure 2.6: Left-hand graph: Dynamics of the population difference $P(t)$ for the unbiased qubit-oscillator system at resonance ($\Omega = \Delta$) with $g/\Delta = 0.18$ and $\hbar\beta\Delta = 10$. Right-hand graph: Fourier transform $F(\nu)$ of $P(t)$. Both the JCM and VVP agree well with the exact numerical results. The peaks in the Fourier spectrum are situated around $\omega = \Delta$ according to Eqs. (2.26a) - (2.26c). Clearly, ω_{10} and ω_{20} are the dominating frequencies. The JCM only returns those dominating peaks. In order to visualize the delta-functions, finite widths have been artificially introduced.

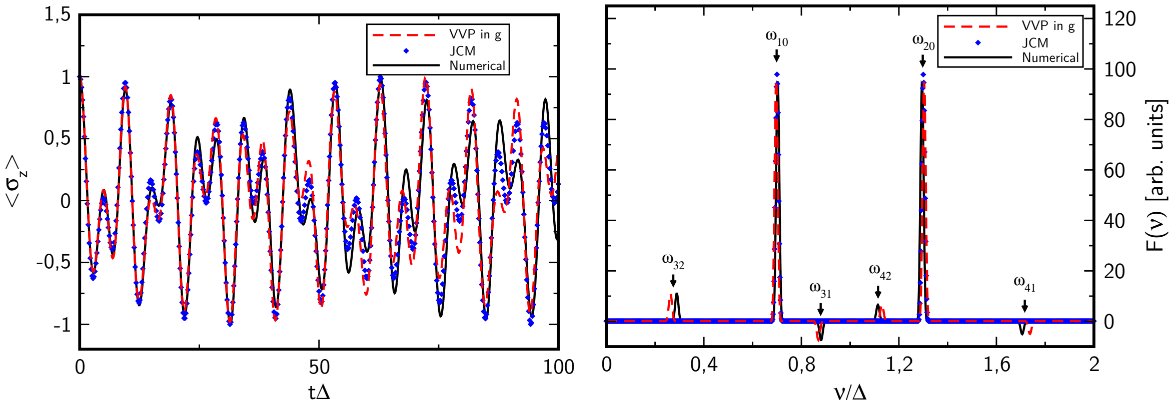

Figure 2.7: Population difference $P(t)$ and its Fourier transform $F(\nu)$ of an unbiased qubit-oscillator system at resonance ($\Omega = \Delta$) and a temperature $\hbar\beta\Delta = 10$. The coupling is with $g/\Delta = 0.3$ stronger than in Fig. 2.6. Concerning $P(t)$, both the JCM and VVP get slightly out of phase with time compared to the numerics. The main frequencies in the Fourier spectrum are correctly returned by both approaches. Van Vleck perturbation theory also covers the small frequencies peaks, which slightly deviate from the numerical results.

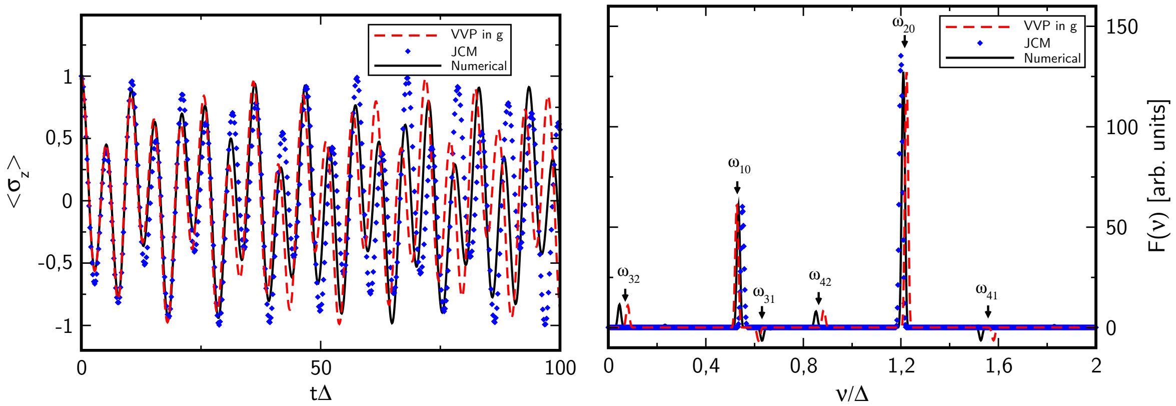

Figure 2.8: Same as in Fig. 2.7, but for positive detuning $\Omega/\Delta = 0.75$. Qualitatively, the agreement between numerics, the JCM and VVP is good, however, for long times the latter two get out of phase. Also the main frequencies, ω_{10} and ω_{20}, given by the JCM or VVP are slightly shifted from the numerical values. The frequency peak ω_{20} is dominating.

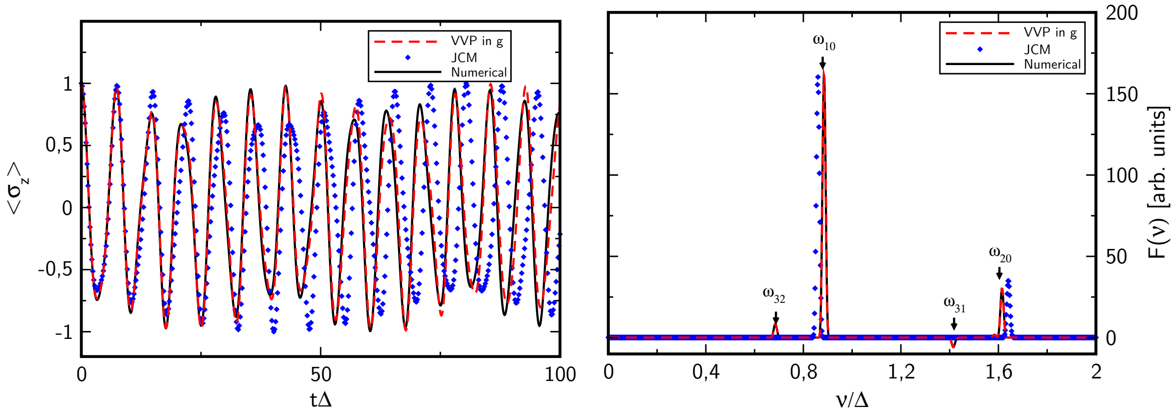

Figure 2.9: Same as in Fig. 2.7, but for negative detuning $\Omega/\Delta = 1.5$. Van Vleck perturbation theory agrees better with the numerical results than the JCM, which gets very fast out of phase. The latter shows also stronger deviations concerning the peaks ω_{10} and ω_{20}. The frequency peak ω_{10} is dominating. The peak ω_{42} is covered by ω_{20} and ω_{41} lies beyond the plotted frequency range.

We tested our results also for the nonzero static bias case and found good approximate results as long as we are not too far from resonance ($\Omega \approx E_{\mathrm{qb}}$), and/or $g \ll E_{\mathrm{qb}}, \Omega$ is valid. We will give a detailed analysis for finite bias when we study the dissipative dynamics.

To summarize, one notices that due to the coupling with the oscillator additional frequencies are induced into the qubit dynamics. Theoretically, the number of those frequencies is infinite. At low temperatures, however, transitions between the lower energy levels of the system are clearly dominating. For weak coupling, both the JCM and VVP work well. Here, the JCM is preferable due to its simplicity. However, for stronger couplings, one obtains already slightly better results using VVP, at least in the detuned case. This will become more evident, when we discuss the dissipative dynamics in Chapter 4. Another advantage of our VVP method is that it works both in the unbiased and biased case. We have to keep in mind, however, that the method presented here still relies on a perturbative approach in g. We go to second order in g, and the method starts to fail when we approach stronger couplings, in particular $g \sim \Omega, E_{\mathrm{qb}}$. We will see in the next section how such strong couplings can be treated analytically.

2.3 Perturbation theory in Δ

As we have seen in the previous sections, a perturbative treatment of the qubit-oscillator Hamiltonian (1.15) with respect to the coupling strength explains well the qubit's dynamics for weak or intermediate coupling but cannot go beyond into the ultrastrong coupling regime. In particular, it fails for a dimensionless coupling strength g/Ω which approaches unity, as described in Sec. 1.2.3 and predicted in [30, 33, 45]. In such a regime, theories being nonperturbatively in g become important. A couple of them can already be found in the literature: The adiabatic approximation (see [52] and references therein) relies on a polaron transformation and is derived under the assumption $\Omega \gg E_{\mathrm{qb}}$. It fails to return the limit of zero coupling $g \to 0$, where the JCM works well. An improvement to this theory is given by the generalized rotating-wave approximation (GRWA) [64], which is a combination of the adiabatic approximation and the standard RWA and works well in both regimes of zero and large qubit-oscillator detuning. Furthermore, it covers correctly the weak coupling limit. However, it has not been used yet to investigate the dynamics of the qubit-oscillator system. The NIBA calculations by Nesi et al. [65] treat analytically a two-level system coupled to an harmonic oscillator to all orders in the coupling strength g, taking environmental influences into account. Zueco et al. present a theory beyond the rotating-wave approximation in the strong dispersive regime [66].

However, all these theories are derived for an unbiased two-level system ($\varepsilon = 0$) or, in the terminology of cavity and circuit QED, for a qubit operated at the degeneracy point or sweet spot. We have learnt already in Sec. 1.1 that it is quite straightforward to vary the static bias ε of superconducting qubits by an external control parameter. Therefore, theories are necessary which treat the *biased* qubit-oscillator system in the ultrastrong coupling limit. Brito et al. used in [67] a slightly changed polaron transformation on the qubit-oscillator model and obtained by truncating the displaced harmonic oscillator to its first excited level an effective four-level model. Quite recently, the adiabatic approximation for a high-frequency oscillator was reviewed for a biased system [61]. Furthermore, the opposite regime of a high-frequency qubit has been examined there.

In this section, we present a theory which takes the static bias of the TLS into account and treats the qubit-oscillator system to all orders in the coupling strength by considering the qubit tunneling matrix element Δ as a small perturbation. For zero static bias, our approach can be seen as an extension of the adiabatic approximation by taking into account higher order terms of Δ using Van Vleck perturbation theory (VVP). We do not only examine the energy levels of the system but also calculate corrections to the displaced qubit-oscillator states, which we obtain using a polaron transformation on the unperturbed ($\Delta = 0$) case. Unlike in the adiabatic approximation discussed in [61], we take the qubit's static bias into account while identifying degenerate subspaces, thereby adjusting the renormalized frequency already in the first-order approach. Our results work very well for negative detuning ($E_{\mathrm{qb}} < \Omega$) for the whole range of coupling strength and even exceeds in accuracy results obtained from the GRWA for $\varepsilon = 0$. For not too weak coupling $g/\Omega \gtrsim 0.5$ and/or finite static bias, it agrees with numerical results even for the resonant $E_{\mathrm{qb}} = \Omega$ or positive detuning $E_{\mathrm{qb}} > \Omega$. With these observations we believe that our approach can close the parameter gap which cannot be treated by the JCM or the GRWA.

2.3.1 Diagonalization of the qubit-oscillator Hamiltonian

In the following, we demonstrate how the full Hamiltonian $H_{\text{TLS-osc}}$ can be diagonalized perturbatively to second order in Δ. Notice that in contrast to Sections 2.1 and 2.2, we express now $H_{\text{TLS-osc}}$ in the localized basis states $|\uparrow / \downarrow\rangle$. For a vanishing tunneling element, $\Delta = 0$, the polaron-like transformation

$$U = \exp\{g(B - B^{\dagger})\sigma_z/\Omega\} \tag{2.28}$$

brings $H_{\text{TLS-osc}}$ into a diagonal form.[3] Its eigenstates are $|\widetilde{j, \uparrow / \downarrow}\rangle = U|j, \uparrow / \downarrow\rangle$, where $|j, \uparrow / \downarrow\rangle$ are the eigenstates of the qubit-oscillator system for $\Delta = 0$ and $g = 0$. In detail, we get

$$|\widetilde{j,\uparrow}\rangle = \sum_{j'=0}^{\infty} [\mathrm{sign}\,(j - j')]^{|j'-j|}\,\Xi^{|j'-j|}_{\mathrm{Min}\{j,j'\}}(\alpha/4)|j',\uparrow\rangle, \tag{2.29}$$

$$|\widetilde{j,\downarrow}\rangle = \sum_{j'=0}^{\infty} [\mathrm{sign}\,(j' - j)]^{|j'-j|}\,\Xi^{|j'-j|}_{\mathrm{Min}\{j,j'\}}(\alpha/4)|j',\downarrow\rangle, \tag{2.30}$$

with

$$\Xi^{l}_{j}(x) = x^{l/2}\sqrt{\frac{j!}{(j+l)!}}\,\mathsf{L}^{l}_{j}(x)\mathrm{e}^{-\frac{x}{2}}, \tag{2.31}$$

$\alpha = (2g/\Omega)^2$, and where $\mathsf{L}^{l}_{j}(x)$ are the generalized Laguerre polynomials. Equations (2.29) and (2.30) correspond to the displaced oscillator states used, e.g., in [52, 68, 69], where the displacement depends on the qubit state, and form a so-called *dressed state basis* [28, 70–72], since they give rise to a dressing of the tunneling matrix element as we will see just below. The eigenvalues are

$$\hbar E^{0}_{j,\uparrow/\downarrow} = \mp\frac{\hbar}{2}\varepsilon + \hbar j\Omega - \hbar\frac{g^2}{\Omega}. \tag{2.32}$$

---

[3] In [67] it is pointed out that the simple polaron transformation fails in the limit of large tunneling elements $\Delta \gg \Omega$. For a flux-qubit this situation occurs for an applied external flux at which the qubit potential changes from a double-well to a single well, and thus the qubit eigenstates become delocalized. In our work, however, we do not aim at describing such a parameter regime.

For finite Δ, the perturbative matrix elements become in this basis [52, 61, 73]

$$\begin{aligned} -\frac{\hbar}{2}\Delta_j^{j'} &\equiv -\frac{\hbar}{2}\langle\widetilde{j,\downarrow}|\Delta\sigma_x|\widetilde{j',\uparrow}\rangle \\ &= -\frac{\hbar}{2}\Delta\left[\mathrm{sign}\left(j'-j\right)\right]^{|j'-j|}\Xi_{\mathrm{Min}\{j,j'\}}^{|j'-j|}(\alpha). \end{aligned} \tag{2.33}$$

This dressing by Laguerre polynomials becomes in the high-photon limit, $j, j' \to \infty$, and for finite $j' - j$ a dressing by Bessel functions, just like in the case of a classically driven TLS, see Sec. 5.2 and [68, 69, 71, 74–76].

For $\Delta = 0$ and $\varepsilon = l\Omega$, the unperturbed eigenstates $|\widetilde{j,\downarrow}\rangle$ and $|\widetilde{j+l,\uparrow}\rangle$ have the same energies, so that we can identify a two-fold degenerate subspace in the complete Hilbert space of the problem.[4] Again, we use VVP to determine the effective Hamiltonian $H_{\mathrm{eff}} = \exp(\mathrm{i}S)H\exp(-\mathrm{i}S)$. In contrast to the previous section, we perform now a perturbative approach with respect to Δ instead of g. The result is again an effective Hamiltonian consisting of 2 by 2 blocks of the shape

$$\hbar\begin{pmatrix} E_{j,\downarrow}^0 + \frac{1}{4}\varepsilon_{j,\downarrow}^{(2)} & -\frac{1}{2}\Delta_j^{j+l} \\ -\frac{1}{2}\Delta_j^{j+l} & E_{j+l,\uparrow}^0 - \frac{1}{4}\varepsilon_{j+l,\uparrow}^{(2)} \end{pmatrix}, \tag{2.34}$$

where we calculate the transformation matrix S to second order in Δ and define the diagonal corrections as

$$\varepsilon_{j,\downarrow/\uparrow}^{(2)} = \sum_{\substack{k=-j \\ k\neq\pm l}}^{\infty} \frac{\left(\Delta_j^{k+j}\right)^2}{\varepsilon \mp k\Omega}. \tag{2.35}$$

Notice that for zero bias, $\varepsilon = 0$, the degenerate subspace consists of oscillator states with equal quantum number j. If one neglects the second order corrections $\varepsilon^{(2)}$ the effective Hamiltonian reduces to the one obtained within the so-called "adiabatic approximation in the dispaced oscillator basis" in [52, see Eq. (9) there]. It is derived for the limit $\Omega \gg E_{\mathrm{qb}}$ and relies on a separation of timescales: In order to calculate the fast dynamics of the oscillator (fast compared to the qubit), the part in Eq. (1.15) coming from the TLS is neglected, so that one gets an effective Hamiltonian for the oscillator, reading

$$\hbar g\sigma_z(B^\dagger + B) + \hbar\Omega B^\dagger B. \tag{2.36}$$

Thus, depending on the state of the qubit the oscillator is displaced in opposite directions, while the energy for a fixed oscillator quantum number j remains the same, given by $\hbar j\Omega - \hbar g^2/\Omega^2$ [52]. By reintroducing the qubit contribution this degeneracy is lifted. However, as long as $E_{\mathrm{qb}} \ll \Omega$, the doublet structure is conserved. For an unbiased system, as treated in [52], the above condition translates to $\Delta \ll \Omega$, and the tunneling matrix element Δ can be treated as a small perturbation, leading in the end to an effective Hamiltonian consisting of 2 by 2 blocks, with a renormalized frequency on the off-diagonal. This adiabatic approximation is automatically enclosed in the method presented in this section. Furthermore, it is extended to nonzero bias, and also higher order corrections in Δ are included in Eq. (2.34). In [61], a finite bias ε is considered in the parameter regime where eigenstates with same oscillator

---

[4] Notice, that for $l > 0$ the first l spin-up states have no degenerate partner, while for $l < 0$ the first l spin-down states are unpaired.

quanta j remain quasidegenerate, so that the tunneling matrix element of a subspace remains dressed by a L_j^0 Laguerre polynomial. This is a valid approximation in the case that $\Omega \gg E_{\mathrm{qb}}$. On the contrary, when $\varepsilon \gtrsim \Omega$ and therefore also $E_{\mathrm{qb}} \gtrsim \Omega$, a dressing of higher order Laguerre polynomial occurs even in first order in Δ. Additionally, the opposite regime of a high-frequency qubit $E_{\mathrm{qb}} \gg \Omega$ has been treated in [61] analytically for certain special cases. This situation is also partly contained in our formalism.
The eigenenergies of Eq. (2.34) are

$$\hbar E_{j,\mp} = \hbar \left[\left(j + \frac{l}{2} \right) \Omega - \frac{g^2}{\Omega} + \frac{1}{8} \left(\varepsilon^{(2)}_{j,\downarrow} - \varepsilon^{(2)}_{j+l,\uparrow} \right) \mp \frac{1}{2} \Omega^l_j \right] \tag{2.37}$$

with the *dressed oscillation frequency*

$$\Omega^l_j = \sqrt{\left[\varepsilon - l\Omega + \frac{1}{4} \left(\varepsilon^{(2)}_{j,\downarrow} + \varepsilon^{(2)}_{j+l,\uparrow} \right) \right]^2 + \left(\Delta^{j+l}_j \right)^2}. \tag{2.38}$$

Notice that the quantum number j corresponds to a *mixture* of the oscillator levels j and l. Only for $\varepsilon = 0$ this mixing vanishes. We obtain the eigenstates of $H_{\text{TLS-osc}}$ by $|\Phi_{j,\pm}\rangle = \exp(-\mathrm{i}S)|\Phi^{(0)}_{j,\pm}\rangle$ with the eigenstates of Eq. (2.34) given by

$$|\Phi^{(0)}_{j,-}\rangle = -\sin\left(\Theta^l_j/2\right) |\widetilde{j,\downarrow}\rangle - \operatorname{sign}\left(\Delta^{j+l}_j\right) \cos\left(\Theta^l_j/2\right) |\widetilde{j+l,\uparrow}\rangle, \tag{2.39}$$

$$|\Phi^{(0)}_{j,+}\rangle = \cos\left(\Theta^l_j/2\right) |\widetilde{j,\downarrow}\rangle - \operatorname{sign}\left(\Delta^{j+l}_j\right) \sin\left(\Theta^l_j/2\right) |\widetilde{j+l,\uparrow}\rangle, \tag{2.40}$$

and the mixing angle

$$\tan\Theta^l_j = \frac{\left|\Delta^{j+l}_j\right|}{\varepsilon - l\Omega + \frac{1}{4}\left(\varepsilon^{(2)}_{\downarrow,j} + \varepsilon^{(2)}_{\uparrow,j+l}\right)} \tag{2.41}$$

for $0 < \Theta^l_j \leq \pi$. In App. A.2 the transformation is calculated to second order in Δ and applied to the effective states. By this we have all information we need to calculate the dynamics of the qubit-oscillator system.
Van Vleck perturbation theory yields good approximate results as long as the matrix elements connecting different nondegenerate subspaces with each other are much smaller than the energetical distance between those subspaces [28]. In our case this means

$$\left| \frac{1}{2} \Delta^{j+k}_j \right| \ll |\varepsilon - k\Omega| \quad \forall \quad k \neq l. \tag{2.42}$$

We will discuss the validity of our approach for the different cases below.

2.3.2 Energy spectrum in the ultrastrong coupling regime

In this section we examine the energy spectrum of the qubit-oscillator system as obtained from Eq. (2.37) and compare it to results found by exact numerical diagonalization. We check its robustness for variable coupling strength g and detuning $\delta = E_{\mathrm{qb}} - \Omega$ between the qubit energy splitting and oscillator frequency.

Zero static bias $\varepsilon = 0$

First, we concentrate on the regime of zero static bias. Equation (2.37) for the Van Vleck eigenenergies perturbative in Δ simplifies further for $\varepsilon = 0$:

$$\hbar E_{j,\mp} = \hbar\left[j\Omega - \frac{g^2}{\Omega} - \frac{1}{4}\sum_{\substack{k=-j \\ k\neq 0}}^{\infty} \frac{(\Delta_j^{k+j})^2}{k\Omega} \mp \frac{1}{2}|\Delta \mathsf{L}_j^0(\zeta)\mathrm{e}^{-\zeta/2}|\right]. \tag{2.43}$$

The semi-infinite sum in the above expression converges, and we show analytical expressions for the first four energy levels:

$$\hbar E_{0,\mp} = \hbar\left[-\frac{g^2}{\Omega} + \frac{\Delta^2\mathrm{e}^{-\alpha}}{4\Omega}[\Gamma(0,-\alpha) + \ln(-\alpha) + \gamma] \mp \frac{1}{2}|\Delta\mathrm{e}^{-\alpha/2}|\right], \tag{2.44}$$

$$\begin{aligned}\hbar E_{1,\mp} =& \hbar\left[\Omega - \frac{g^2}{\Omega} + \frac{\Delta^2\mathrm{e}^{-\alpha}}{4\Omega}\left\{1 + \gamma + \mathrm{e}^{\alpha}(\alpha-1) - \alpha[\alpha - \gamma(\alpha-2)]\right.\right.\\ &\left.\left. + (\alpha-1)^2[\Gamma(0,-\alpha) + \ln(-\alpha)]\right\} \mp \frac{1}{2}|\Delta(1-\alpha)\mathrm{e}^{-\alpha/2}|\right],\end{aligned} \tag{2.45}$$

where we used the Euler-Mascheroni constant γ and the incomplete Γ-function [77]. We will test our findings against the JCM, in particular Eq. (2.9). Furthermore, we can compare our results to the generalized rotating-wave approximation (GRWA) [64]. In that approach the total Hamiltonian (1.15) is expressed in the effective basis states (2.39) and (2.40), disregarding the second-order corrections in Δ. Taking into account that $\Delta_j^{j'} = (-1)^{|j-j'|}\Delta_{j'}^{j}$, the corresponding matrix is for the first six basis states $\{|\Phi_{j,\mp}^{(0)}\rangle\}$ with $j = 0, 1, 2$

$$\hbar\begin{pmatrix} E_{0,-} & 0 & 0 & \frac{1}{2}\Delta_0^1 & -\frac{1}{2}\Delta_0^2 & 0 & \dots \\ 0 & E_{0,+} & -\frac{1}{2}\Delta_0^1 & 0 & 0 & \frac{1}{2}\Delta_0^2 & \dots \\ 0 & -\frac{1}{2}\Delta_0^1 & E_{1,-} & 0 & 0 & \frac{1}{2}\Delta_1^2 & \dots \\ \frac{1}{2}\Delta_0^1 & 0 & 0 & E_{1,+} & -\frac{1}{2}\Delta_1^2 & 0 & \dots \\ -\frac{1}{2}\Delta_0^2 & 0 & 0 & -\frac{1}{2}\Delta_1^2 & E_{2,-} & 0 & \dots \\ 0 & \frac{1}{2}\Delta_0^2 & \frac{1}{2}\Delta_1^2 & 0 & 0 & E_{2,+} & \dots \\ \vdots & \vdots & \vdots & \vdots & \vdots & \vdots & \ddots \end{pmatrix}. \tag{2.46}$$

In this representation, the remote matrix elements, which turn out to yield fast rotating contributions for $\Delta \approx \Omega$, are neglected . A more elaborated justification is given in [64]. This procedure is quite similar to the standard rotating-wave approximation and one ends up again with a block-diagonal matrix,

$$\hbar \begin{pmatrix} E_{0,-} & 0 & 0 & 0 & 0 & 0 & \dots \\ 0 & E_{0,+} & -\frac{1}{2}\Delta_0^1 & 0 & 0 & 0 & \dots \\ 0 & -\frac{1}{2}\Delta_0^1 & E_{1,-} & 0 & 0 & 0 & \dots \\ 0 & 0 & 0 & E_{1,+} & -\frac{1}{2}\Delta_1^2 & 0 & \dots \\ 0 & 0 & 0 & -\frac{1}{2}\Delta_1^2 & E_{2,-} & 0 & \dots \\ 0 & 0 & 0 & 0 & 0 & E_{2,+} & \dots \\ \vdots & \vdots & \vdots & \vdots & \vdots & \vdots & \ddots \end{pmatrix}, \tag{2.47}$$

which is straightforwardly diagonalized and the energy of the groundstate remains unchanged, namely $\hbar E_{0,-}$. The remaining levels are given by

$$\begin{aligned} E_{j,\mp}^{\mathrm{GRWA}} =& (j+\frac{1}{2})\Omega - \frac{g^2}{\Omega} + \frac{\Delta}{4}\mathrm{e}^{-\alpha/2}(|\mathsf{L}_j^0(\alpha)| - |\mathsf{L}_{j+1}^0(\alpha)|) \\ & \mp \left\{ \left[\frac{\Omega}{2} - \frac{\Delta}{4}\mathrm{e}^{-\alpha/2}(|\mathsf{L}_j^0(\alpha)| + |\mathsf{L}_{j+1}^0(\alpha)|) \right]^2 + \frac{\Delta^2}{4}\frac{\alpha}{j+1}\mathrm{e}^{-\alpha}[\mathsf{L}_j^1(\alpha)]^2 \right\}^{\frac{1}{2}} . \end{aligned} \tag{2.48}$$

The GRWA uses the advantages of the adiabatic approximation, namely its ability to go to strong coupling strengths and to treat detuned systems, and also gives reliable results in the weak coupling regime of the JCM.

As a first test of our method, we compare in Fig. 2.10 the obtained energy levels for a weak coupling strength of $g/\Omega = 0.1$ and for varying qubit-oscillator detuning $\delta \equiv \Delta - \Omega$ to the GRWA and the JCM model. Both are known to work well in this regime. We find that VVP gives only valid results for negative detuning, $\Delta < \Omega$. This was expected as it relies on a perturbative approach in Δ, and we know already from the adiabatic approximation that it fails for $\Delta \gtrsim \Omega$ and simultaneously small g/Ω. In this regime of weak coupling, the JCM or GRWA are clearly preferable to our method. For an intermediate coupling strength, the same discussion is presented in Fig. 2.11. We do not show the Jaynes-Cummings energy levels in this regime anymore, because they fail completely to return the correct energy spectrum. Van Vleck perturbation theory and the GRWA yield good results for negative detuning $\delta < 0$, but also at resonance, $\Delta = \Omega$, they agree well with the numerics. At positive detuning both deviate strongly from the exact solution. With a coupling strength of $g/\Omega = 1.0$ in Fig. 2.12, we are already deep in the ultrastrong coupling regime. Those high values have not been observed experimentally yet. They are, however, predicted to be realizable [30]. Again, we compare to the exact numerics. For negative detuning, GRWA and VVP show a good agreement with the numerics. However, approaching zero detuning or going beyond to positive one, the GRWA fails in particular for the two lowest states, which will turn out to be important for the calculations of the dynamics. In order to explain this failure, we also show in Fig. 2.12 the adiabatic approximation. As pointed out, the GRWA is a combination of the ordinary RWA, and thus works well for weak coupling, and of the adiabatic approximation, which works very well for strong negative detuning, $\Omega \gg \Delta$, for all values of the coupling.

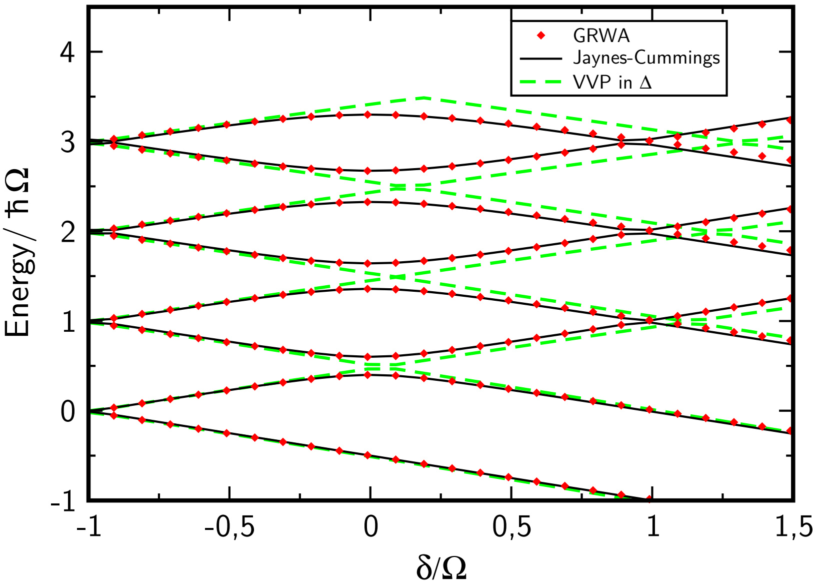

Figure 2.10: Energy levels against detuning $\delta = \Delta - \Omega$ for $\varepsilon/\Omega = 0$, $g/\Omega = 0.1$. Our VVP solution is compared to the GRWA and the JCM. The latter agree both well with numerical calculations for the whole detuning range (not shown), while VVP yields only reliable results for negative detuning, $\Delta < \Omega$.

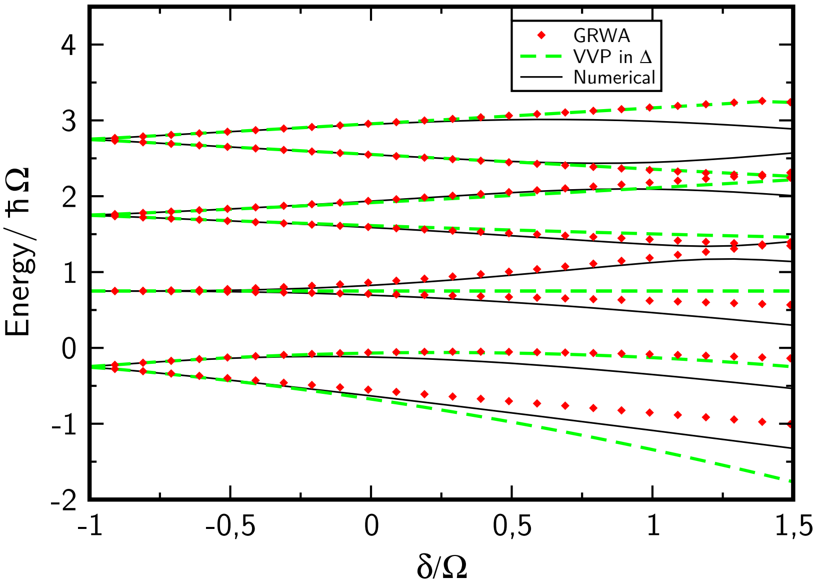

Figure 2.11: Energy levels against detuning $\delta = \Delta - \Omega$ for $\varepsilon/\Omega = 0$, $g/\Omega = 0.5$. The JCM fails already completely for such a coupling strength (not shown). We compare VVP and the GRWA against numerical calculations. Both agree well with the numerics for negative detuning and even at resonance. For stronger positive detuning they both fail. The strongest deviations can be seen for the lower energy levels.

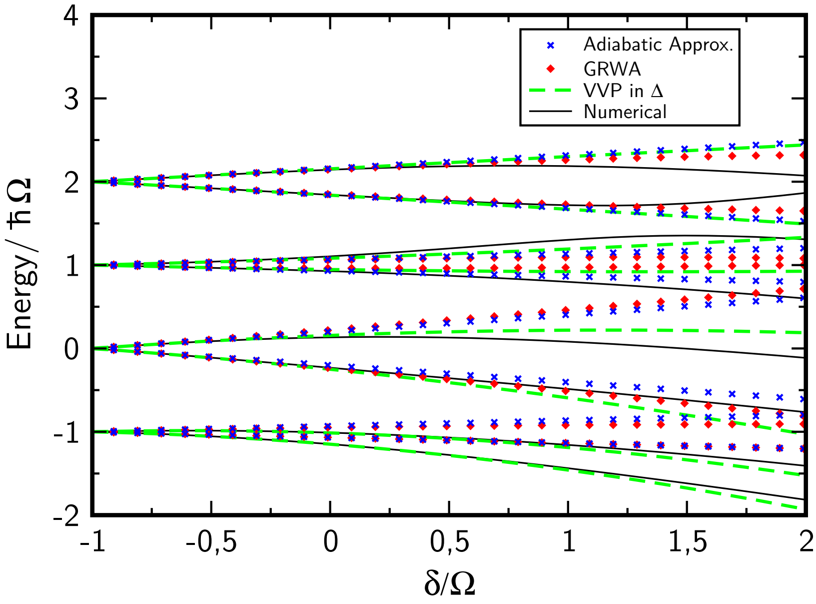

Figure 2.12: Energy levels against detuning $\delta = \Delta - \Omega$ for $\varepsilon/\Omega = 0$, $g/\Omega = 1.0$. We compare VVP, the adiabatic approximation and GRWA against a numerical calculation. For a negative detuning all three approaches agree very well with the exact numerics. However, for zero and positive detuning deviations occur. In particular, the ground level and the first excited level are not described correctly by the adiabatic approximation and the GRWA for strong positive detuning, while VVP yields good results.

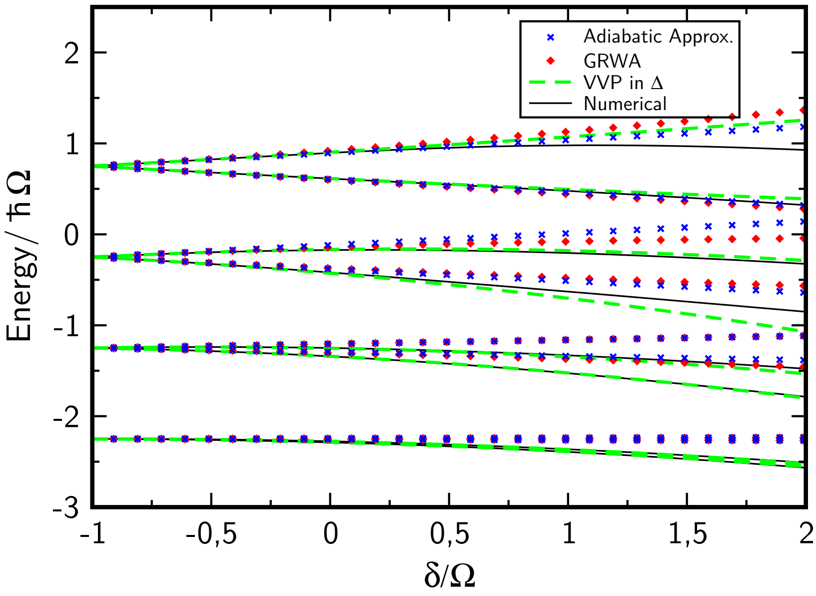

Figure 2.13: Energy levels against detuning. Same as in Fig. 2.12, but for a coupling strength of $g/\Omega = 1.5$. Again, adiabatic approximation and GRWA fail for zero and positive detuning, while VVP gives the first four energy levels correctly even up to a detuning of $\delta/\Omega = 2.0$. And also for the higher energy levels it yields good results beyond the resonance case.

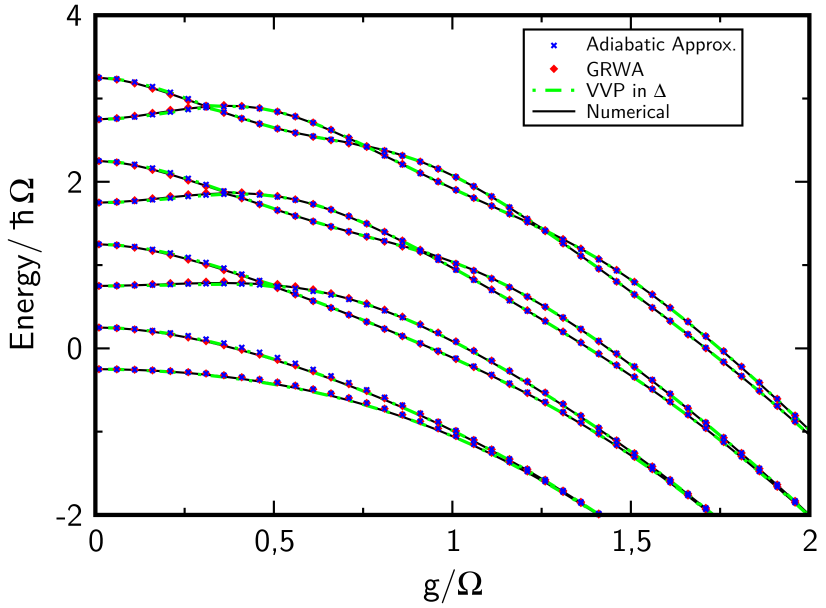

Figure 2.14: Energy levels against coupling strength g/Ω for negative detuning ($\delta/\Omega = -0.5$). Numerical results are compared with the adiabatic approximation, GRWA and VVP. All three approaches show only slight deviations.

At resonance or at positive detuning, the adiabatic approximation shows deviations from the exact solution for a coupling strength $g/\Omega = 1.0$. This coupling strength is, however, already too strong to be treated correctly by the RWA. Thus, we are in a kind of intermediate regime, which is also not covered by the GRWA, but can be important in experimental applications. On the contrary, VVP shows a good agreement with the numerical data for negative detuning and even up to exact resonance. Only for positive detuning, deviations start to occur. This becomes even more distinct for stronger coupling strengths, like $g/\Omega = 1.5$ in Fig. 2.13. While the adiabatic approximation and also the GRWA fail for zero and positive detuning, VVP agrees surprisingly well with the numerical results up to $\delta = 2.0$ for the first four energy levels; i.e., we have $\Delta/\Omega = 3$. Also for the higher levels we still find a good agreement for not too strong positive detuning. This improvement is due to the fact that VVP also takes into account connections between nondegenerate subspaces and therefore higher-order corrections in the dressed tunneling matrix element. To show this in more detail, we discuss in the following the first eight energy levels depending on the coupling strength for negative, zero and positive detuning. In Fig. 2.14, the case $\Delta/\Omega = 0.5$ or $\delta/\Omega = -0.5$ is given. All three approaches, the adiabatic approximation, the GRWA and VVP, show very good agreement with the numerical results for the whole range of g/Ω. At resonance, $\Delta/\Omega = 1.0$, in Fig. 2.15, we have to distinguish between different parameter regimes: For smaller values of the coupling, $g/\Omega \lesssim 0.5$, the adiabatic approximation and VVP show deviations from the numerical results apart from the ground level, as they do not take into account correctly the zero coupling resonance [64], while the GRWA on the other hand works well. For higher couplings strengths, VVP exhibits a slight improvement to the GRWA and the adiabatic approximation for the first two energy levels, as could already be seen from Figs. 2.12 and 2.13. This improvement becomes more evident for stronger positive detuning, $\delta/\Omega = 0.5$, as shown in Fig. 2.16. Van Vleck perturbation theory agrees well with the numerical results for $g/\Omega \gtrsim 0.75$, while the adiabatic approximation and GRWA do partly deviate from the

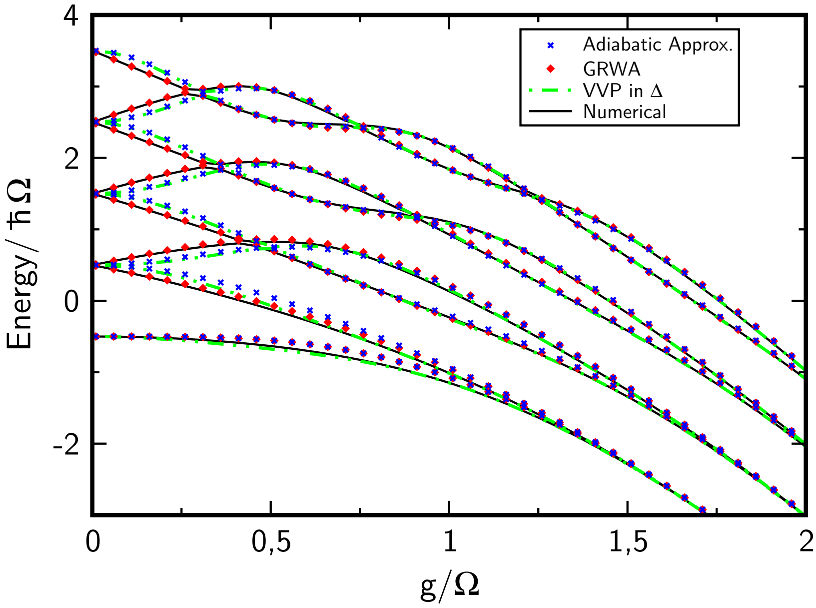

Figure 2.15: Energy levels against coupling strength at resonance ($\delta/\Omega = 0$). For small coupling strength, the adiabatic approximation and VVP show small deviations from the correct values (see especially the higher energy levels). The GRWA works well in this regime. For stronger coupling strength, all three approaches agree well with the numerical results.

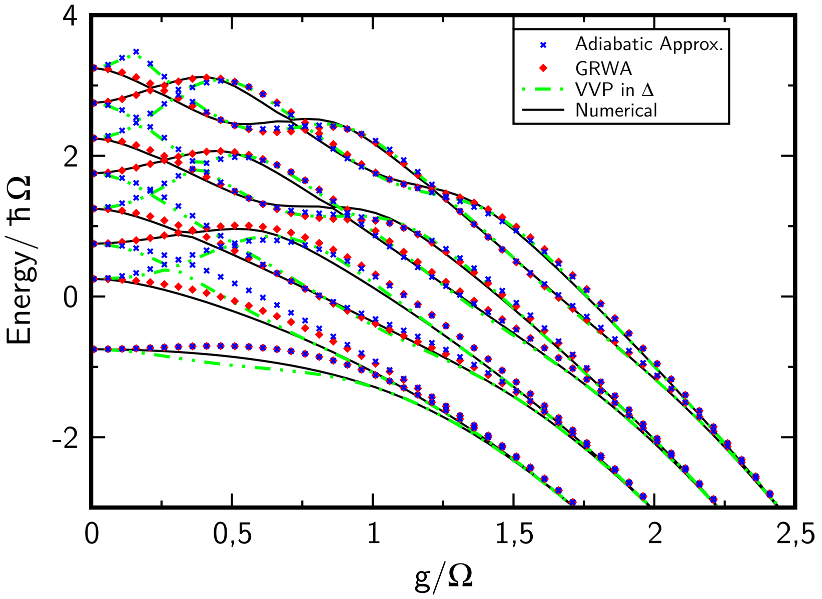

Figure 2.16: Energy levels against coupling strength for positive detuning ($\delta/\Omega = 0.5$). For coupling strengths with $g/\Omega \gtrsim 0.75$, VVP exhibits the best agreement with numerical results, while for smaller coupling and higher energy levels, the GRWA should be used.

numerical results. However, for $g/\Omega < 0.75$ and the lower energy levels, the results from all three approaches are not very satisfying. The adiabatic approximation and VVP even predict unphysical crossings, while the GRWA at least yields the correct weak coupling limit. To summarize: For weak coupling up to a few percent, the JCM and GRWA are the methods of choice when it comes to the calculation of the energy levels, because they reproduce correctly this limit, while the adiabatic approximation and VVP cannot cover this regime at resonance or positive detuning. Note, however, that the JCM also fails already for a coupling strength of about $g/\Omega \approx 0.12$, when a mixture of several oscillator modes is involved, because then the influence of the counter-rotating terms becomes important [46]. The GRWA remains valid for arbitrary coupling strength at negative detuning. For being close to or at resonance, the adiabatic approximation and VVP deviate for weak coupling from the numerical results for the higher energy levels, work, however, well for stronger couplings. For the groundstate, VVP represents even an improvement to both the adiabatic approximation and the GRWA for the whole coupling regime. It also exceeds the other methods in exactness at strong positive detuning and stronger coupling.

Why does VVP even work for $\Delta \geq \Omega$? We can explain this by looking at its validity for $\varepsilon = 0$. From condition (2.42), we get

$$\left|\frac{1}{2}\Delta_j^{j+k}\right| \ll |k\Omega| \quad \forall \quad k \neq 0. \tag{2.49}$$

From the definition of the dressed tunneling matrix element Δ_j^{j+k}, Eq. (2.33), we see that for small Δ/Ω – i.e., for negative detuning – this condition is fullfilled even for weak coupling. For stronger coupling $g/\Omega > 1$, the dressed tunneling matrix element, Δ_j^{j+k}, approaches zero independently of Δ/Ω, so that VVP even works for positive detuning.

Plotted against the coupling strength the energy levels exhibit some further peculiarities. Most interesting is the finding that for strong coupling two adjacent energy levels become degenerate, so that coherent oscillations between them become completely suppressed. We can understand that by considering expression (2.43), where we find that two energy levels with the same index j differ only in the sign of the dressed oscillation frequency, which vanishes for large g. For the higher energy levels, degeneracies also occur for lower g/Ω values, happening at the zeros of the Laguerre polynomials. These phenomena are discussed in more detail in [52, 61, 64] and we come back to them when presenting the dynamics.

Finite static bias $\varepsilon \neq 0$

In this section we discuss the energy spectrum for the case of finite static bias. We compare our VVP calculation to an exact numerical diagonalization. We further show in certain cases calculations disregarding connections between the different manifolds, that is second-order corrections in Δ, which would be the natural extension of the adiabatic approximation to finite bias. We do not compare to the GRWA, as it exists so far just for the zero bias case. To start, we show in Fig. 2.17 the energy levels against the static bias for a coupling strength of $g/\Omega = 1.0$ and no detuning in the zero bias case ($\Delta = \Omega$). For such a coupling strength, we find a very good agreement between our VVP calculations and numerically obtained results. Most remarkably, this agreement holds even away from the resonant points, $\varepsilon = l\Omega$, for which our approximation has been performed. We also checked the effect on the spectrum when neglecting the second order corrections in Δ. The qualitative behavior remains the same; however, quantitative deviations occur (not shown in Fig. 2.17). For negative detuning,

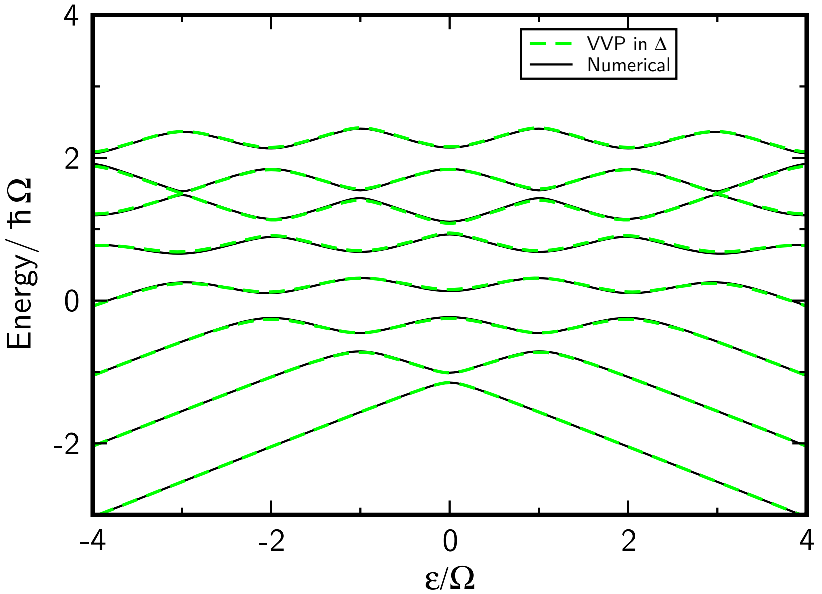

Figure 2.17: Energy levels against static bias ε for $g/\Omega = 1.0$ at resonance $\Delta/\Omega = 1.0$. Van Vleck perturbation theory is compared to a numerical diagonalization of the Hamiltonian.

$\Delta < \Omega$, the agreement between analytical and numerical results is even enhanced, while for positive detuning up to $\Delta/\Omega = 1.5$ only slight deviations occur. The accuracy of VVP becomes less good entering the weak coupling regime, as we could already observe for the zero static bias case and we will show in the following. Before, we want to consider some general features of the spectrum at nonzero static bias. We pointed out while identifying the degenerate subspaces in Eq. (2.34) that for $\varepsilon = l\Omega$ with $l \neq 0$ certain unperturbed energy levels have no degenerate partner. Without loss of generality, we assume $l > 0$, that means that the first l energy levels corresponding to a spin-up state have no degenerate partner, and their energy is simply given by $\hbar E^0_{j,\uparrow} - \frac{\hbar}{4}\varepsilon^{(2)}_{\uparrow,j}$ with $j = 0, 1, 2, ...l-1$. Of course, also the corresponding effective eigenstates are simply $|\widetilde{j,\uparrow}\rangle$, and we cannot observe avoided crossings or superposition of states. For instance, in Fig. 2.17 at $\varepsilon/\Omega = 1$, we observe the lowest energy level being without partner, while the higher ones form avoided crossings with the adjacent level. For $\varepsilon/\Omega = 2$, the two lowest levels are "free" etc..

In Figures 2.18, 2.19 and 2.20, we present the dependence of the energy spectrum on the coupling strength g/Ω for the case of $\varepsilon/\Omega = 1.0$ and $\Delta/\Omega = 0.5$, $\Delta/\Omega = 1.0$ and $\Delta/\Omega = 1.5$, respectively. Just like in the zero static bias case, VVP yields best results for $\Delta/\Omega < 1$, because there the condition for a perturbative approach is most satisfied. Also, the extended adiabatic approach yields very convincing results, only for $g/\Omega \to 0$ one can notice slight deviations. For $\Delta/\Omega = 1.0$ in Fig. 2.19, VVP still shows an almost exact agreement with the numerical results, whereas the adiabatic approximation fails for weak coupling. This failure of the latter becomes more evident going to positive detuning like $\Delta/\Omega = 1.5$ in Fig. 2.20. But there also the VVP exhibits strong deviations for coupling strengths $g/\Omega \lesssim 0.75$. We also tested for static bias values being no multiples of Ω and found a confirmation of the above findings. For stronger static bias, VVP describes the lower energy levels well even for positive detuning, see, e.g., the case $\varepsilon/\Omega = 3.0$ in Fig. 2.21. Here, the three lowest energy levels are without degenerate partner and therefore can be described by the corrected unperturbed energy. The influence of the mixing to other energy levels is less strong.

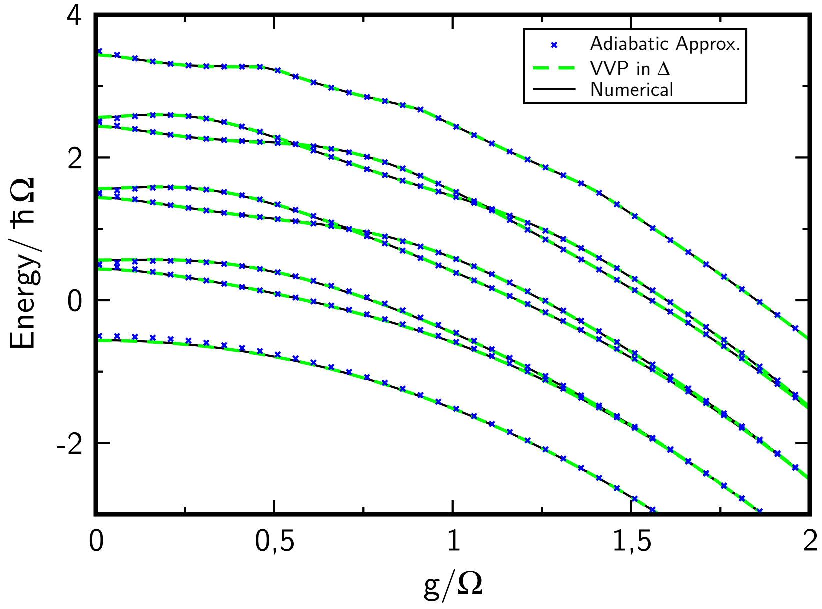

Figure 2.18: Energy levels against coupling g/Ω for $\varepsilon/\Omega = 1.0$ and $\Delta/\Omega = 0.5$. The adiabatic approximation and VVP agree almost perfectly with numerical results. Slight deviations can be seen for the adiabatic approximation at $g/\Omega \to 0$.

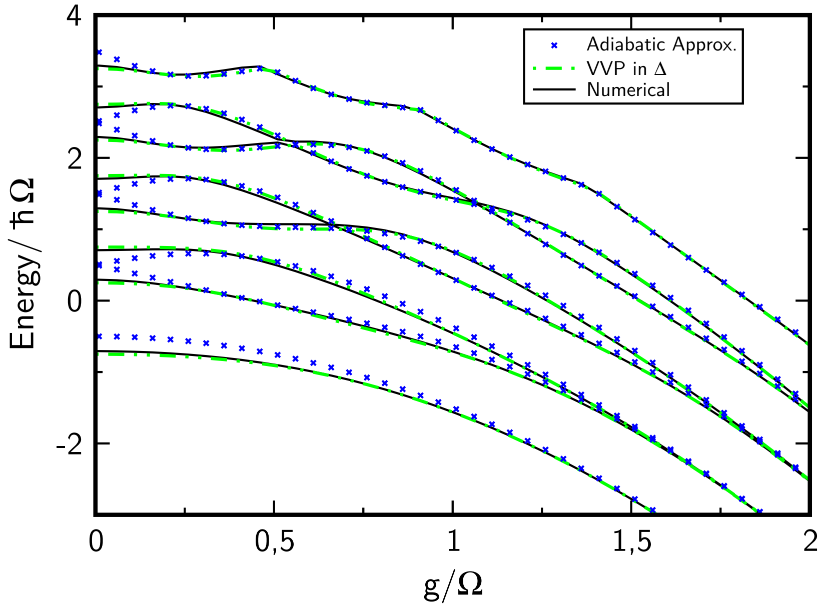

Figure 2.19: Energy levels against coupling g/Ω for $\varepsilon/\Omega = 1.0$ and $\Delta/\Omega = 1.0$. Van Vleck perturbation theory still holds against numerical results, while the adiabatic approximation fails specifically for weak coupling strengths.

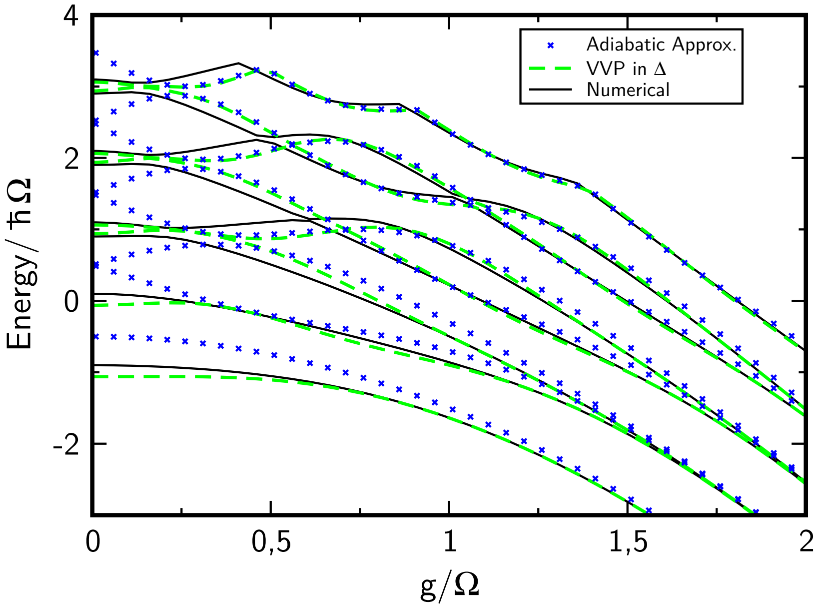

Figure 2.20: Energy levels against coupling g/Ω for $\varepsilon/\Omega = 1.0$ and $\Delta/\Omega = 1.5$. In this regime, also VVP shows deviations from the numerical results for $g/\Omega \lesssim 0.75$ especially for the higher energy levels. It agrees well for stronger coupling.

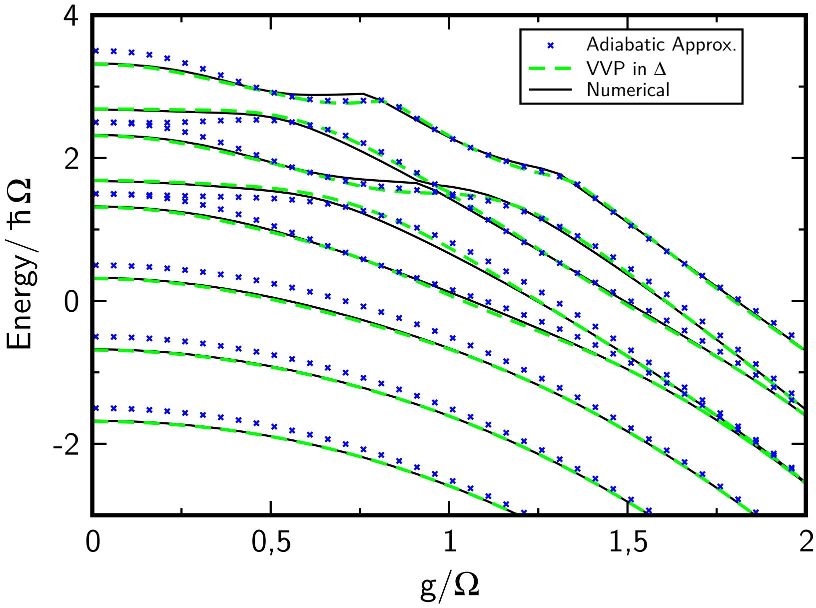

Figure 2.21: Energy levels against coupling g/Ω for $\varepsilon/\Omega = 3.0$ and $\Delta/\Omega = 1.5$. The three lowest energy levels have no "degenerate" partner. Despite the high value of Δ, VVP still gives reliable results, while the adiabatic approximation differs from the numerical values even for the low energy levels.

2.3.3 Dynamics of the qubit in the ultrastrong coupling regime

We are interested in determining the population difference between the two qubit states; i.e., we calculate

$$\langle\sigma_z(t)\rangle = \mathrm{Tr}_{\mathrm{TLS}}\{\sigma_z\rho_{\mathrm{red}}(t)\} = 2\langle\uparrow|\rho_{\mathrm{red}}(t)|\uparrow\rangle - 1, \tag{2.50}$$

where $\rho_{\mathrm{red}}(t)$ is obtained after tracing out the oscillator degrees of freedom from the qubit-oscillator density operator ρ. The matrix elements of the latter read in the system's energy eigenbasis $\{|\Phi_\alpha\rangle\}$

$$\rho_{\alpha\beta}(t) = \langle\Phi_\alpha|\rho(t)|\Phi_\beta\rangle = \rho_{\alpha\beta}(0)\mathrm{e}^{-\mathrm{i}\omega_{\alpha\beta}t}, \tag{2.51}$$

where $\alpha, \beta \,\epsilon\, \{\pm, j\}$ or $\{\uparrow / \downarrow, j\}$. As starting conditions we use Eq. (2.2) and again assume low temperatures, $\hbar\beta\Omega = 10$, at which mainly the lower oscillator levels are of importance. The dynamics for higher oscillator occupation numbers at zero static bias have been investigated in [52].

The transition frequencies are defined as $\omega_{\alpha\beta} = E_\alpha - E_\beta$, where E_α stands either for $E_{j,\mp}$ in the case of two-fold degenerate subspaces or $E^0_{j,\uparrow/\downarrow} \mp \frac{1}{4}\varepsilon^{(2)}_{j,\uparrow/\downarrow}$ for one-dimensional subspaces. We further can distinguish between two different timescales: large oscillatory contributions are resulting from different oscillator quanta j, while the difference in dressed oscillation frequencies Ω^l_j acts on a much longer timescale, and its contribution vanishes for large coupling strengths g/Ω.

In the following subsections we will investigate the dynamics for the unbiased and biased case. Again, we will compare exact numerical results to VVP and the adiabatic approximation. Apart from the energy levels, also the eigenstates become now important. In particular, we will find that away from the condition $\varepsilon = l\Omega$, the higher-order corrections are crucial to give the correct dynamics.

Dynamics for zero static bias $\varepsilon = 0$

For zero static bias, we first examine a regime where we expect our approximation to work well. We thus consider a not too strong tunneling matrix element, $\Delta/\Omega = 0.5$, and a coupling strength of $g/\Omega = 1.0$. Figures 2.22 and 2.23 show the population difference $\langle\sigma_z(t)\rangle$ and its Fourier transform,

$$F(\nu) := 2\int_0^\infty dt\langle\sigma_z(t)\rangle\cos(\nu t), \tag{2.52}$$

respectively. Concerning the population difference, we see a relatively good agreement between the numerical calculation and VVP for short timescales. In particular, VVP also correctly returns the small overlaid oscillations. For longer timescales, the two curves get out of phase. The adiabatic approximation only can reproduce the coarse-grained dynamics. The fast oscillations are completely missed. To understand this better, we turn our attention to the Fourier transform in Fig. 2.23. There, we find several groups of frequencies located around $\nu/\Omega = 0$, $\nu/\Omega = 1.0$, $\nu/\Omega = 2.0$ and $\nu/\Omega = 3.0$. This can be explained by considering the transition frequencies in more detail. We have from Eq. (2.37),

$$\omega^l_{\mp k,\mp j} = \hbar[(k-j)\Omega + \epsilon^l_{k,j} \pm \frac{1}{2}(\Omega^l_j - \Omega^l_k)], \tag{2.53}$$

and

$$\omega^l_{\mp k,\pm j} = \hbar[(k-j)\Omega + \epsilon^l_{k,j} \mp \frac{1}{2}(\Omega^l_j + \Omega^l_k)], \tag{2.54}$$

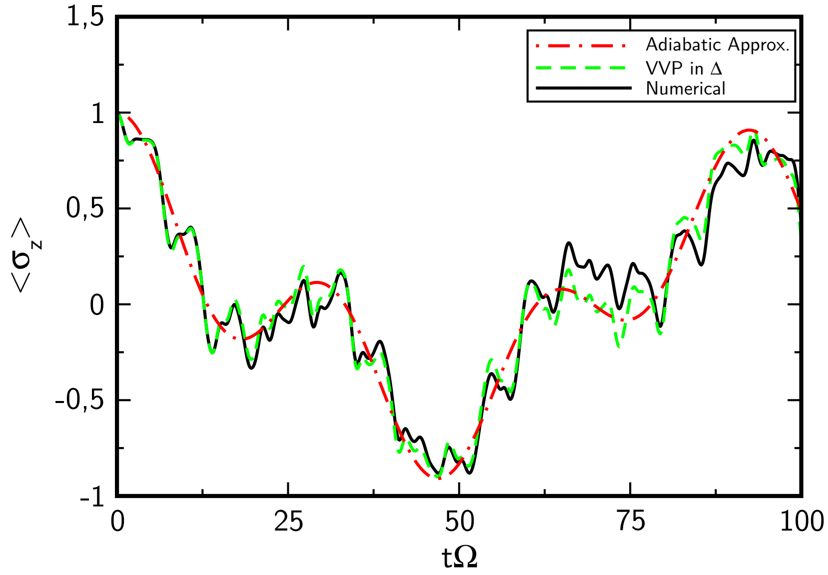

Figure 2.22: Population difference for zero static bias. Further parameters are $\Delta/\Omega = 0.5$, $\hbar\beta\Omega = 10$ and $g/\Omega = 1.0$. The adiabatic approximation and VVP are compared to numerical results. The first covers only the longscale dynamics, while VVP also returns the fast oscillations. With increasing time small differences between numerical results and VVP become more pronounced.

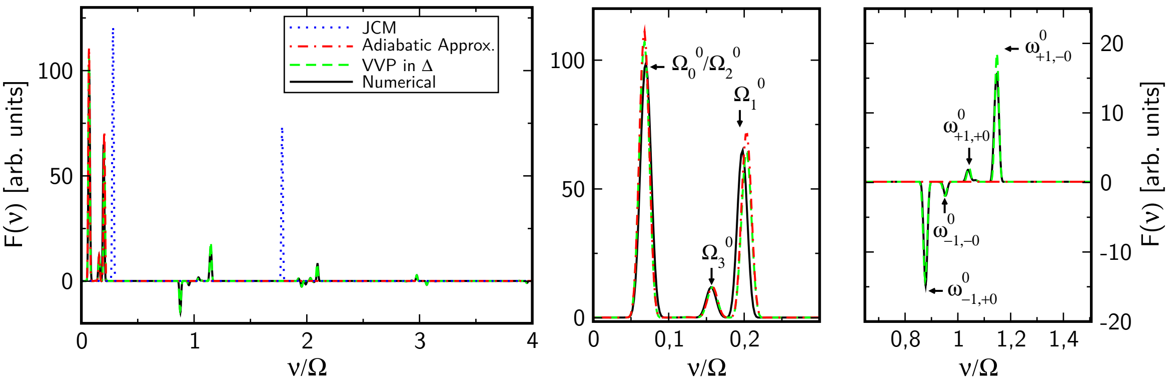

Figure 2.23: Fourier transform of the population difference in Fig. 2.22. The left-hand graph shows the whole frequency range. The lowest frequency peaks originate from transitions between levels within a degenerate subspace and are determined through the dressed oscillation frequency Ω_j^0. Numerical calculations and VVP predict groups of peaks located around $\nu/\Omega = 0, 1, 2, 3$. The first group at $\nu/\Omega = 0$ is shown in the middle graph. One can identify frequencies Ω_0^0 and Ω_2^0, which fall together, and Ω_1^0. The small peak comes from the frequency Ω_3^0. This first group of peaks is also covered by the adiabatic approximation. The other groups come from transitions between different manifolds. The adiabatic approximation does not take them into account, while VVP does. A blow-up of the peaks coming from transitions between neighboring manifolds is given in the right-hand graph. In the left-hand graph additionally the Jaynes-Cummings peaks are shown, which, however, fail completely.

with $\epsilon^{l}_{k,j} = \frac{1}{8}\left(\varepsilon^{(2)}_{k,\downarrow} - \varepsilon^{(2)}_{j,\downarrow} + \varepsilon^{(2)}_{j+l,\uparrow} - \varepsilon^{(2)}_{k+l,\uparrow}\right)$ being the second-order corrections. The term $(k-j)\Omega$ determines to which group of peaks a frequency belongs, and Ω^{l}_{j} is its relative position within this group. The dynamics is dominated by the peaks belonging to transitions between the same subspace, $k-j=0$, while the next group with $k-j=1$ yields already faster oscillations. Theoretically, infinite many peaks belong to each group. However, since we operate the system at low temperature, only those with a small oscillator number play a role. For the used parameter regime, the adiabatic approximation does not take into account the connections between different manifolds. It therefore covers only the first group of peaks with $k-j=0$, providing the long-scale dynamics. For $\varepsilon = 0$, the dominating frequencies in this first group are given by $\Omega^0_0 = |\Delta \mathrm{e}^{-\alpha/2}|$, $\Omega^0_1 = |\Delta(1-\alpha)\mathrm{e}^{-\alpha/2}|$ and $\Omega^0_2 = |\Delta \mathsf{L}^0_2(\alpha)\mathrm{e}^{-\alpha/2}|$, where Ω^0_0 and Ω^0_2 coincide. A small peak at $\Omega^0_3 = |\Delta \mathsf{L}^0_3(\alpha)\mathrm{e}^{-\alpha/2}|$ can also be seen. Ω^0_j has Δ as an upper bound so that the range over which the peaks are spread within a group increases with Δ. Notice that for certain coupling strengths some peaks vanish; like, for example, choosing a coupling strength of $g/\Omega = 0.5$ makes the peak at Ω^0_1 disappearing completely, independent of Δ, and the Ω^0_0 and Ω^0_2 peaks split. The JCM yields two oscillation peaks determined by the Rabi splitting and fails completely to give the correct dynamics, see the left-hand graph in Fig. 2.23.

Now, we proceed to an even stronger coupling, $g/\Omega = 2.0$, where we also expect the adiabatic approximation to work better [52]. From Fig. 2.14, we notice that at such a coupling strength, the lowest energy levels are degenerate within a subspace. Only for oscillator numbers like $j = 3$, we see that a small splitting arises. This splitting becomes larger for higher levels. Thus, only this and higher manifolds can give significant contributions to the long time dynamics; that is, they can yield low frequency peaks. By looking at Figs. 2.24 and 2.25, we notice that both the adiabatic approximation and VVP agree quite well with the numerics. Especially the first group of Fourier peaks in Fig. 2.25 is also covered almost correctly by the adiabatic approximation. The first manifolds we can identify with those peaks are the ones with $j = 3$ and $j = 4$. This is a clear indication that even at low temperatures higher oscillator quanta are involved due to the large coupling strength. Also frequencies coming from transitions between the energy levels from neighboring manifolds are shown enlarged in Fig. 2.25. The adiabatic approximation and VVP can cover the main structure of the peaks involved there, while the former shows stronger deviations.

If we go to higher values $\Delta/\Omega \gtrsim 1$, the peaks in the individual groups become more spread out in frequency space, and for the population difference dephasing already occurs at a shorter timescale. For $\Delta/\Omega = 1$, at least VVP yields still acceptable results in Fourier space but gets fast out of phase for the population difference.

Dynamics for finite static bias $\varepsilon \neq 0$

As a first case, we consider in Fig. 2.26 a weakly biased qubit ($\varepsilon/\Omega = \sqrt{0.5}$) being at resonance with the oscillator ($E_{\mathrm{qb}} = \Omega$). For a coupling strength of $g/\Omega = 1.0$, we find a good agreement between the numerics and VVP. The adiabatic approximation, however, conveys a different picture: Looking at the time evolution it reveals collapse and rebirth of oscillations after a certain interval. This feature does not survive for the exact dynamics. Like in the unbiased case, the adiabatic approximation gives only the first group of frequencies between the quasidegenerate subspaces, and thus yields a wrong picture of the dynamics. In order to cover the higher frequency groups, we need again to go to higher-order corrections by using VVP.

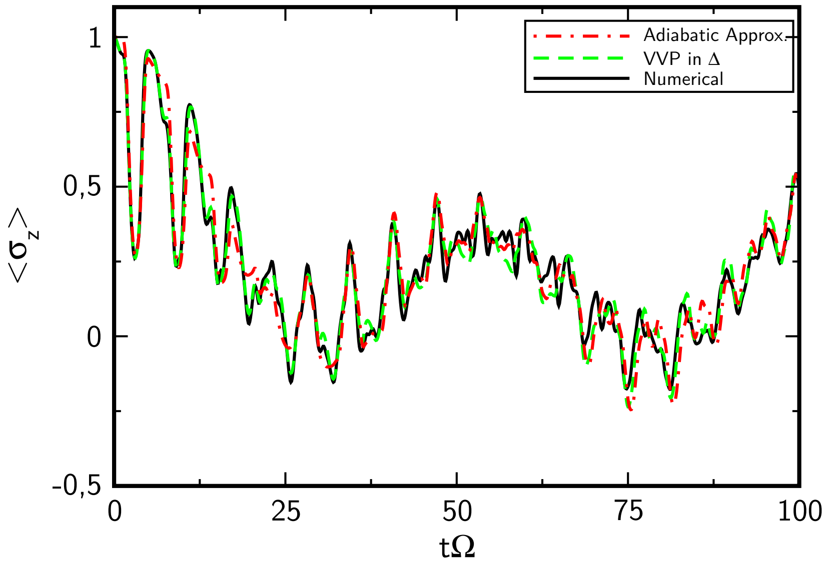

Figure 2.24: Population difference for zero static bias. Same parameters as in Fig. 2.22 but for a coupling strength of $g/\Omega = 2.0$. Both the adiabatic approximation and VVP agree well with the numerics, but show slight dephasing on a longer timescale.

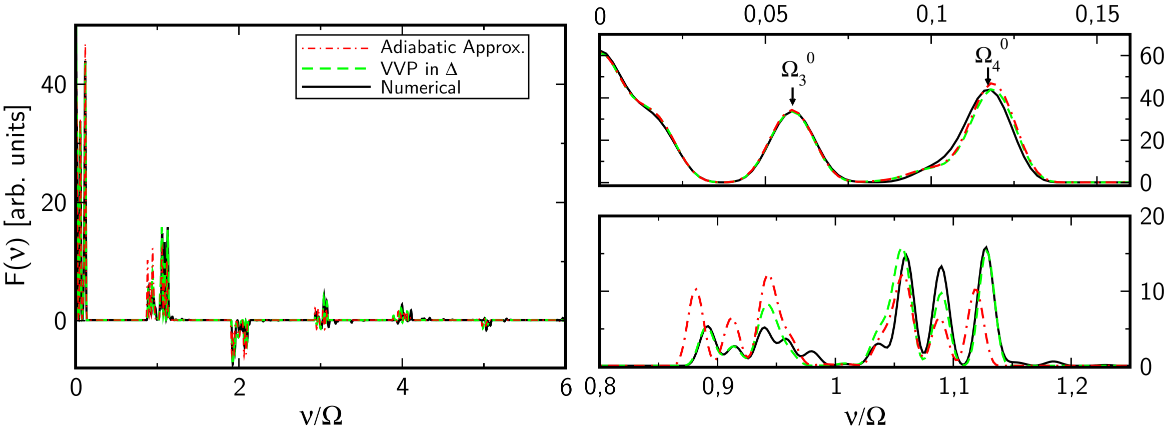

Figure 2.25: Fourier spectrum of the population difference in Fig. 2.24. In the left-hand graph a large frequency range is covered. Peaks are located around $\nu/\Omega = 0$, 1.0, 2.0, 3.0 etc. Even the adiabatic approximation exhibits the higher frequencies. The upper right-hand graph shows the first group close to $\nu/\Omega = 0$. The two main peaks come from Ω_3^0 and Ω_4^0 and higher degenerate manifolds. Frequencies from lower manifolds contribute to the peak at zero. The adiabatic approximation and VVP agree well with the numerics. The lower right-hand graph shows the second group of peaks around $\nu/\Omega = 1.0$. This group is also predicted by the adiabatic approximation and VVP, but they do not fully return the detailed structure of the numerics. Interestingly, there is no peak exactly at $\nu/\Omega = 1.0$ indicating no nearest neighbor transition between the low degenerate levels.

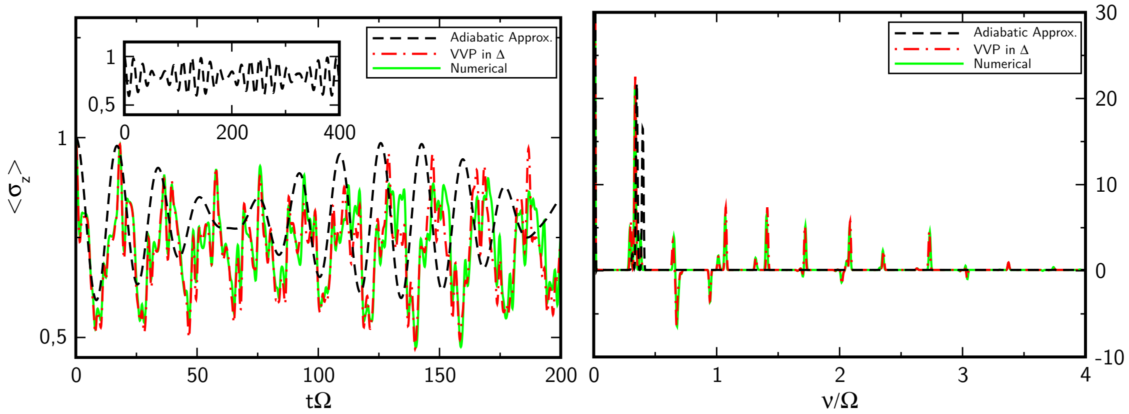

Figure 2.26: Population difference and Fourier spectrum for a biased qubit ($\varepsilon/\Omega = \sqrt{0.5}$) at resonance with the oscillator ($E_{\mathrm{qb}} = \Omega$) in the ultrastrong coupling regime ($g/\Omega = 1.0$). Concerning the time evolution VVP agrees well with numerical results. Only for long time weak dephasing occurs. The inset in the left-hand figure shows the adiabatic approximation only. It exhibits death and revival of oscillations which are not confirmed by the numerics. For the Fourier spectrum, VVP covers the various frequency peaks, which are gathered into groups like for the unbiased case. The adiabatic approximation only returns the first group.

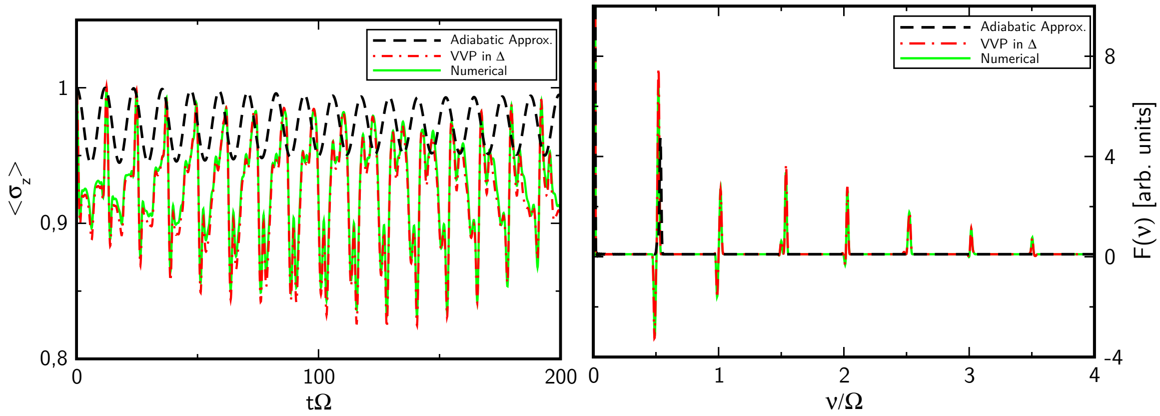

Figure 2.27: Population difference and Fourier spectrum for $\varepsilon/\Omega = 1.5$, $\Delta/\Omega = 0.5$ and $g/\Omega = 1.0$. Van Vleck perturbation theory is confirmed by numerical calculations, while results obtained from the adiabatic approximation deviate strongly. In Fourier space, we find pairs of frequency peaks coming from the two dressed oscillation frequencies Ω_j^1 and Ω_j^2. The spacings in between those pairs is about 0.5Ω. The adiabatic approximation only returns one of those dressed frequencies in the first pair.

The case of ε being not a multiple of the oscillator frequency Ω is also of special interest, since we used for the derivation of our approximate analytical results that we were able to identify degenerate subspaces for the unperturbed case $\Delta = 0$. For $\varepsilon = l\Omega$, we found that the levels $E^0_{j,\downarrow}$ and $E^0_{j+l,\uparrow}$ form a degenerate doublet, which dominates the long-scale dynamics through the dressed oscillations frequency Ω^l_j. For l being not an integer those doublets cannot be identified unambiguously anymore. For instance, we examine the case $\varepsilon/\Omega = 1.5$ in Fig. 2.27. Here, it is not clear which levels should be gathered into one subspace: j and $j+1$ or j and $j+2$. Both the dressed oscillation frequencies Ω^1_j and Ω^2_j influence the longtime dynamics. In Fig. 2.27, we chose $l = 2$ for our approximate method. Surprisingly, VVP gives a very accurate picture for both the dynamics and the Fourier spectrum. For $l = 1$ we obtained the same result (not shown here). Independent of the choice of l, VVP covers all relevant frequencies because of taking into account connections between different manifolds. We always find pairs of frequencies resulting from Ω^1_j and Ω^2_j. Those pairs are separated approximately by 0.5Ω, which is the smallest distance between the unperturbed energy levels (only the single levels are separated by a larger distance). For a bias of $\varepsilon/\Omega = 2.5$, for example, one would detect the same separation between the different groups of peaks. The adiabatic approximation extended to nonzero static bias fails in such a situation, because it only considers one of the two frequencies, as can be also seen by looking at the dynamics in Fig. 2.27. Furthermore, as we saw already in the unbiased case, it neglects the higher frequencies for intermediate coupling.

2.4 Summary

To summarize this chapter, we want to give a short overview of the different approaches we introduced and their regime of validity. We started in Sec. 2.1 with the Jaynes-Cummings model (JCM). It is derived for zero static bias ε under the assumption of weak coupling strength $g \ll \Delta, \Omega$ and that the TLS and the oscillator are close to resonance. This two conditions allow us to perform a rotating-wave approximation (RWA) and to neglect non-resonant terms so that the resulting Hamiltonian can be diagonalized exactly. Despite its simplicity, the JCM can explain many phenomena in cavity QED, which made it a very successful approach. For stronger coupling and detuning the RWA breaks down. Furthermore, in order to explain effects like the Bloch-Siegert shift, the counter-rotating terms are needed even in the weak coupling regime. Thus, we presented in Section 2.2 a new approach taking explicitly those terms into account. It relies on a perturbative treatment of the full Hamiltonian with respect to the coupling strength g and thus is like the Jaynes-Cummings model limited to not too strong coupling. We included terms up to the second order in g. It also was derived assuming $E_{\text{qb}} \approx \Omega$. However, it turned out that it works well also for strong negative detuning, see, e.g., Fig. 2.9. Furthermore, the case of a finite static bias ε is included.

Motivated by recent experimental achievements in the area of ultrastrong qubit-oscillator coupling, which was introduced in Sec. 1.2.3, we discussed in Sec. 2.3 an approach which treats the qubit-oscillator system to all orders in g. The price we had to pay was to make some restriction on the tunneling matrix element Δ and thus the qubit transition frequency E_{qb} compared to the oscillator frequency Ω. In detail, we followed a perturbative approach with respect to the dressed tunneling element Δ^l_j. However, since especially for strong coupling this dressed element becomes suppressed by a Gaussian, and by using Van Vleck perturbation theory to include also higher orders, we could go beyond the limit $\Delta \ll \Omega$ of an adiabatically fast oscillator [52, 61]. For zero bias, we compared the energy spectrum obtained by VVP in Δ and the adiabatic approximation to the generalized rotating-wave approximation in [64]. For $\Delta/\Omega < 1$ all approaches agree well with numerical results for the whole coupling range, while at resonance and slight positive detuning the GRWA was found to be preferable at weak coupling $g \to 0$, since it returns correctly the Jaynes-Cummings limit. For strong coupling and small positive detuning VVP in Δ even showed slightly better results than the GRWA.

We investigated in detail the dynamics of the qubit in the zero bias case both in the weak to intermediate and the ultrastrong coupling regime at low temperature. In the former regime the JCM and VVP with respect to g are the methods of choice. For ultrastrong coupling the adiabatic approximation gives a coarse-grained picture of the time evolution of the population difference, while VVP in Δ also covers the higher frequencies agreeing well with numerical results.

The two new approaches we introduced in this chapter also work in the case of a biased qubit, and the adiabatic approximation was extended to that regime so that also qubits which are not operated at their symmetry point can be discussed almost for the whole coupling regime.

3

Dissipation and the quantum master equation

In the previous chapters we considered the TLS and the oscillator as closed systems. In reality the situation is quite different. Reading-out the qubit or oscillator state exposes it to environmental influences, which in turn leads to dissipation and decoherence effects in the system's dynamics. Our goal in this chapter is to provide a realistic picture of those influences and to take them into account in our calculations. A quite successful way to include the environment is the system-bath model: a system with few degrees of freedom is coupled to a heat bath with many or even infinite degrees of freedom. Such an open system cannot be described anymore by a unitary time evolution, since the heat bath causes a modification of the equations of motion of the conservative system, adding a damping term and a randomly fluctuating force. These new equations of motion are called Langevin equations. In the following sections we will first show their classical version. Then, the so-called Caldeira-Leggett model is introduced: the bath is described by an infinite number of quantized harmonic oscillators. This is quite a natural assumption in the case of circuit QED experiments, where the environment is the electromagnetic field of the surrounding circuitry, which is exactly described by the oscillator model. We will show how the Caldeira-Leggett model leads to a quantum version of the classical Langevin equation. Finally, we will derive from this approach the Born-Markov master equation for the density operator of the system.

3.1 The classical Langevin equation

In classical mechanics the movement of a particle of mass M experiencing friction and a rapidly fluctuating force ξ is described by the Langevin equation [78],

$$M\ddot{X}(t) + M\gamma\dot{X}(t) = \xi(t). \tag{3.1}$$

Langevin found Eq. (3.1) trying to describe a Brownian particle moving through a liquid. The position of the particle is given by $X(t)$, friction is represented by the term $\gamma\dot{X}(t)$, and $\xi(t)$ is the force the particle feels being hit by the molecules in the liquid. The latter is assumed to be independent of X and, since the collisions with the molecules are practically instantaneous, it varies much faster than $X(t)$. In the case of a heat reservoir at temperature T with zero memory time the latter yields [1, 78]

$$\langle\xi(t)\xi(t')\rangle = 2M\gamma k_{\mathrm{B}}T\delta(t-t'), \tag{3.2}$$

where t and t' are distinct times. Any force $\xi(t)$ fulfilling (3.2) is called *white* or *δ-correlated noise*. One further assumes that $\langle\xi(t)\rangle = 0$. It is not straightforward to find a quantized equation corresponding to the classical form (3.1) and there have been several different attempts. The most successful one is introduced in the next section.

3.2 The Caldeira-Leggett model

In their work on quantum mechanical tunneling [11, 79] Caldeira and Leggett describe the open quantum system together with its environment as a closed system - the so-called system-plus-reservoir approach - and establish the Hamiltonian H of the entire model as:[1]

$$H = H_{\mathrm{S}} + H_{\mathrm{B}} + H_{\text{S-B}}. \tag{3.3}$$

H_{B} describes the environmental bath and $H_{\text{S-B}}$ the interaction between system and bath. Dissipation in such a model works as follows: energy from the system is transferred to the environment via the interaction term. By assuming the environment to consist of a huge number of degrees of freedom, the probability that this energy returns back to the system tends to be zero - the relevant system suffers from dissipation. It is further implied that any individual degree of freedom of the bath is coupled weakly to the system which is a reasonable assumption for a macroscopic environment. Because of the weak perturbation of an individual degree of freedom, the bath can be modeled as a set of simple harmonic oscillators, and $H_{\text{S-B}}$ is a linear function of the bath coordinates. However, Caldeira and Leggett emphasize that a weak coupling between the system and an individual bath mode does not mean that the overall interaction between system and environment is weak, since the latter consists of a large number of individual modes, and their coupling strengths add up.

We will specify now the individual parts of H. For simplicity, we consider for the open system a particle of mass M moving in the potential V:

$$H_{\mathrm{S}} = \frac{P^2}{2M} + V(X). \tag{3.4}$$

Later, this can be generalized easily to the qubit Hamiltonian. The Hamiltonian of the bath reads:

$$H_{\mathrm{B}} = \sum_{k=1}^{N} \left(\frac{p_k^2}{2m_k} + \frac{1}{2} m_k \omega_k^2 x_k^2 \right), \tag{3.5}$$

with m_k and ω_k being the mass and frequency of an individual oscillator. For now, we consider a finite but very large number N of harmonic oscillators. The interaction term,

$$H_{\text{S-B}} = -\sum_{k=1}^{N} F_k(X) x_k + \Delta V(X), \tag{3.6}$$

requires a closer look. So far we have just used that it is linear in the bath coordinates x_k. The dependence on X is determined by $F(X)$. Additionally, there is the counter- or renormalization term

$$\Delta V(X) = \sum_{k=1}^{N} \frac{F_k^2(X)}{2 m_k \omega_k^2}. \tag{3.7}$$

In order to explain that term, we introduce the effective potential of the global system as

$$V_{\mathrm{eff}}(X, x_k) = V(X) + \sum_{k=1}^{N} \frac{1}{2} m_k \omega_k^2 x_k^2 - \sum_{k=1}^{N} F_k(X) x_k + \Delta V(X). \tag{3.8}$$

---

[1] Pioneering work has been earlier performed by Ullersma [80] and Zwanzig [81].

Now, we determine the minimum of this potential with respect to the bath coordinate x_k^*; i.e., we solve

$$\frac{\partial}{\partial x_k} V_{\text{eff}}(X, x_k)\bigg|_{x_k = x_k^*} = 0 \tag{3.9}$$

and obtain $x_k^* = F_k(X)/m_k\omega_k^2$. At this point the effective potential becomes

$$V_{\text{eff}}(X, x_k^*) = V(X) - \sum_{k=1}^{N} \frac{F_k^2(X)}{2m_k\omega_k^2} + \Delta V(X). \tag{3.10}$$

If we set $\Delta V(X) = 0$, the effective potential can even sink below the original value $V(X)$. In order to avoid this potential-shift the counter-term $\Delta V(X)$ in Eq. (3.6) is introduced. Since it is a function of the system coordinates only, it is often included in H_{S}. However, we want to avoid a redefinition of the system Hamiltonian, and further because it will cancel some spurious terms in the derivation of the master equation, we consider the renormalization term explicitly.

In the following, we will concentrate on the special case of a separable interaction:

$$F_k(X) = c_k F(X), \tag{3.11}$$

where c_k is the coupling constant for an individual mode. If $F(X)$ is a nonlinear function of the position coordinate, we get a state-dependent dissipation process. We will simplify the interaction even further and restrict our model to

$$F_k(X) = c_k X. \tag{3.12}$$

That is, we consider a bilinear coupling between system and environment, leading to a state-independent dissipation process. With these conditions, the total Hamiltonian becomes:

$$H = \frac{P^2}{2M} + V(X) + \frac{1}{2}\sum_{k=1}^{N}\left[\frac{p_k^2}{m_k} + m_k\omega_k^2\left(x_k - \frac{c_k}{m_k\omega_k^2}X\right)^2\right]. \tag{3.13}$$

3.3 Elimination of the heat bath

We are going to show now that the above Hamiltonian (3.13) indeed leads to a Langevin equation for the system coordinate X. To see that, we have to eliminate the environmental degrees of freedom. In the Heisenberg picture, the time evolution of an operator $\mathcal{O}$ is given by

$$\frac{d\mathcal{O}}{dt} = \frac{i}{\hbar}[H, \mathcal{O}]. \tag{3.14}$$

With that, we find for the system coordinates:

$$\dot{X} = \frac{P}{M} \quad \text{and} \quad \dot{P} = -\frac{\partial V}{\partial X} + \sum_{k=1}^{N} c_k\left(x_k - \frac{c_k}{m_k\omega_k^2}X\right), \tag{3.15}$$

and for the bath coordinates:

$$\dot{x}_k = \frac{p_k}{m_k} \quad \text{and} \quad \dot{p}_k = -m_k\omega_k^2 x_k + c_k X, \tag{3.16}$$

which enables us to determine the equations of motion for the system and the bath. Equation (3.15) yields

$$M\ddot{X} + \frac{\partial V}{\partial X} + \sum_{k=1}^{N} \frac{c_k^2}{m_k \omega_k^2} X = \sum_{k=1}^{N} c_k x_k \tag{3.17}$$

for the system, and Eq. (3.16) yields

$$m_k \ddot{x}_k + m_k \omega_k^2 x_k = c_k X \tag{3.18}$$

for a single bath degree of freedom. A solution for Eq. (3.18) is given by

$$x_k(t) = x_k(0)\cos(\omega_k t) + \frac{p_k(0)}{m_k \omega_k}\sin(\omega_k t) + \frac{c_k}{m_k \omega_k}\int_0^t dt' \sin(\omega_k(t-t'))X(t'). \tag{3.19}$$

After integration by parts this becomes

$$\begin{aligned} x_k(t) = x_k(0)\cos(\omega_k t) + \frac{p_k(0)}{m_k \omega_k}\sin(\omega_k t) + \frac{c_k}{m_k \omega_k^2}\Bigg[& X(t) - \cos(\omega_k t)X(0) \\ & - \int_0^t dt' \cos(\omega_k(t-t'))\dot{X}(t')\Bigg]. \end{aligned} \tag{3.20}$$

In order to remove the bath degrees of freedom from Eq. (3.17), we insert the equation for $x_k(t)$ into it and arrive at

$$M\ddot{X} + \frac{\partial V}{\partial X} + M\int_0^t dt' \gamma(t-t')\dot{X}(t') + M\gamma(t)X(0) = \zeta(t), \tag{3.21}$$

where we introduced the damping kernel

$$\gamma(t) = \frac{1}{M}\sum_{k=1}^{N} \frac{c_k^2}{m_k \omega_k^2}\cos(\omega_k t) \tag{3.22}$$

and the fluctuating force

$$\zeta(t) = \sum_{k=1}^{N} c_k \left[x_k(0)\cos(\omega_k t) + \frac{p_k(0)}{m_k \omega_k}\sin(\omega_k t)\right]. \tag{3.23}$$

Equation (3.21) is the generalized quantum Langevin equation, analogous to the classical form (3.1). It consists of the damping kernel $\gamma(t)$, which is no longer time independent but exhibits memory effects, yielding colored noise, and of the fluctuating force $\zeta(t)$. So far, our discussion of the system-plus-reservoir approach has been quite general concerning the bath. In the following we will assume the most common case of a heat bath, and therefore calculate averages of the force-force correlation function with respect to the thermal equilibrium distribution of the bath. We further notice an additional term in Eq. (3.21), which is a transient depending on the initial coordinate $X(0)$. To deal with this transient term, the introduction of a shifted stochastic force is recommended [1], namely

$$\xi(t) = \zeta(t) - M\gamma(t)X(0). \tag{3.24}$$

Using this shifted force, the thermal average should be calculated with respect to the bath Hamiltonian H_{B} *and* the interaction term $H_{\text{S-B}}$; i.e., we assume that the initial states of the reservoir are shifted by the coupling to the system, and find

$$\langle \xi(t) \rangle_{\mathrm{B,int}} = \frac{\mathrm{Tr_B}\left[\xi(t) \exp\left(-\beta(H_{\mathrm{B}} + H_{\text{S-B}})\right)\right]}{\mathrm{Tr_B}\left[\exp\left(-\beta(H_{\mathrm{B}} + H_{\text{S-B}})\right)\right]} = 0. \tag{3.25}$$

However, in the later derivation of the master equation, it is very useful to assume that the bath is initially decoupled from the system. Thus, we will neglect the initial slippage [82], which is an artefact from a factorized starting condition [1], and accounts for the time needed to build up the initially neglected correlations between system and bath. This can be considered a good approximation if $\gamma(t)$ is a rapidly decaying function, and we are not interested in times t being too close to the initial time. As we will further assume that the damping kernel $\gamma(t)$ has the form of a δ-distribution and invoke a Markov approximation, we will follow this second approach and assume an unshifted bath, so that the thermal average is taken over the environment alone:

$$\langle \zeta(t) \rangle_{\mathrm{B}} = \frac{\mathrm{Tr_B}\left[\zeta(t) \exp\left(-\beta H_{\mathrm{B}}\right)\right]}{\mathrm{Tr_B}\left[\exp\left(-\beta H_{\mathrm{B}}\right)\right]} = 0. \tag{3.26}$$

For the correlation function we get

$$\langle \zeta(t)\zeta(0) \rangle_{\mathrm{B}} = \sum_{k=1}^{N} \frac{\hbar c_k^2}{2 m_k \omega_k} \left[\coth\left(\frac{\hbar\beta\omega_k}{2}\right) \cos(\omega_k t) - i \sin(\omega_k t)\right]. \tag{3.27}$$

Considering the limit ($\hbar \to 0$) and using the formula (3.22) for $\gamma(t)$, we recover the classical expression for a colored noise source:

$$\lim_{\hbar \to 0} \langle \zeta(t)\zeta(0) \rangle_{\mathrm{B}} = M k_{\mathrm{B}} T \gamma(t). \tag{3.28}$$

In this limit, the quantum Langevin equation is equivalent to the classical Langevin equation.

3.4 Spectral density

In order to characterize the bath, we would have to specify m_k, ω_k and c_k for each oscillator. It would be convenient to have a single parameter including all these variables. We therefore introduce the spectral density of the bath,

$$J(\omega) = \frac{\pi}{2} \sum_{k=1}^{N} \frac{c_k^2}{m_k \omega_k} \delta(\omega - \omega_k). \tag{3.29}$$

With this definition, the damping kernel becomes

$$\gamma(t) = \frac{1}{M} \frac{2}{\pi} \int_0^\infty d\omega \, \frac{J(\omega)}{\omega} \cos(\omega t), \tag{3.30}$$

and the force-force correlation function reads

$$\langle \zeta(t)\zeta(0) \rangle_{\mathrm{B}} = \frac{\hbar}{\pi} \int_0^\infty d\omega \, J(\omega) \left[\coth\left(\frac{\hbar\beta\omega}{2}\right) \cos(\omega t) - i \sin(\omega t)\right]. \tag{3.31}$$

All the effects of the bath are now included in the spectral density, and, in principle, it is enough to know $J(\omega)$ to predict the influence of the bath on the dynamics of the system. For a large number of bath oscillators, the sum in $J(\omega)$ can be replaced by an integral, and the spectral density becomes continuous in ω.

A special type of spectral density, on which a lot of work can be found in the literature, is the so-called Ohmic spectral density:

$$J(\omega) = M\gamma\omega. \tag{3.32}$$

Putting this into Eq. (3.30) yields

$$\gamma(t) = 2\gamma\delta(t). \tag{3.33}$$

Equation (3.33) inserted in the quantum Langevin equation (3.21) leads to damping term $M\gamma\dot{X}(t)$ like in the classical Langevin equation (3.1), and therefore resembles Ohm's law. In this case, we have a memory-free damping and white noise. Unfortunately, for $J(\omega)$ - as it is given in Eq. (3.32) - the force-force correlation function would diverge for high frequencies leading to unphysical results [1]. Therefore, a high-frequency cutoff is introduced:

$$J(\omega) = M\gamma\omega e^{-\omega/\omega_c}. \tag{3.34}$$

This cutoff leads again to memory effects, and can, in certain situations, also be connected to a physical meaning [82]: let us consider, e.g., a Josephson junction which is inductively coupled to the environmental degrees of freedom. As soon as the wavelengths of that external noise get smaller than the size of the Josephson junction, a local theory is not applicable anymore; i.e., we cannot treat the junction as a lumped circuit element. A high frequency cutoff avoids this problem. In our further calculations, we will choose the cutoff frequency ω_c high enough to make sure that for the long time behavior $t \gg \omega_c^{-1}$ the Ohmic case is dominant, and the value of ω_c has no direct influence on the dynamics.

Besides the Ohmic spectral density, there are also different models like the one for a structured bath introduced in Chapter 4.

3.5 The master equation

In the previous section we saw that the Caldeira-Leggett model leads indeed to a quantum Langevin equation for the open system, which corresponds closely, in the limit $\hbar \to 0$, to the classical Langevin equation, and takes into account damping and dissipation effects that the open system experiences through its coupling to a heat bath with many degrees of freedom. We will, however, not use the Langevin equation to examine the dynamics of the open system, but rather are interested in an appropriate equation of motion for its density operator. We therefore will derive in this section the quantum master equation of the reduced operator of the open system. We will start from the Liouville-von Neumann equation for the density operator of the whole closed system, and invoke several approximations, which we will carefully keep track of, and arrive finally at the desired master equation.

3.5.1 The Born-Markov approximation

Before we use the Caldeira-Leggett model and describe the reservoir as an ensemble of thermal oscillators, we consider the closed system in its most general form with no specification on the bath:

$$H = H_{\text{S}}(t) + H_{\text{B}} + H_{\text{S-B}} \tag{3.35}$$

Furthermore, we allow the system Hamiltonian $H_{\text{S}}(t)$ to be explicitly time dependent. Thus, the time evolution operator of the system is

$$U_{\text{S}}(t,0) = \top \exp\left\{-\frac{\mathrm{i}}{\hbar}\int_0^t dt'\, H_{\text{S}}(t')\right\}, \tag{3.36}$$

where $\top$ is the time-ordering operator. Further, we define

$$U_0(t,0) = U_{\text{S}}(t,0)U_{\text{B}}(t,0) \tag{3.37}$$

with

$$U_B(t,0) = \mathrm{e}^{-\frac{\mathrm{i}}{\hbar}H_{\text{B}}(t-0)}, \tag{3.38}$$

where we assumed that the bath Hamiltonian is not time dependent. The Liouville-von Neumann equation, which determines the time evolution of the density operator $W(t)$ of the total system, reads in the interaction picture [83]

$$\mathrm{i}\hbar\partial_t W(t)_I = [H_{\text{S-B}}(t)_I, W(t)_I], \tag{3.39}$$

with $H_{\text{S-B}}(t)_I = U_0(t,0)^\dagger H_{\text{S-B}}(t)U_0(t,0)$. A formal integration of Eq. (3.39), and setting $t_0 = 0$, yields

$$W(t)_I = W(0)_I - \frac{\mathrm{i}}{\hbar}\int_0^t dt'\, [H_{\text{S-B}}(t')_I, W(t')_I]. \tag{3.40}$$

Inserting this back into Eq. (3.39), we get an integro-differential equation for the full density matrix:

$$\dot{W}(t)_I = -\frac{\mathrm{i}}{\hbar}[H_{\text{S-B}}(t)_I, W(0)_I] - \left(\frac{1}{\hbar}\right)^2 \int_0^t dt'\, [H_{\text{S-B}}(t)_I, [H_{\text{S-B}}(t')_I, W(t')_I]]. \tag{3.41}$$

Because we are interested only in the dynamics of the open system, we trace out the bath degrees of freedom and thus arrive at

$$\dot{\rho}_{\text{S}}(t)_I = -\frac{\mathrm{i}}{\hbar}\mathrm{Tr}_{\text{B}}\{[H_{\text{S-B}}(t)_I, W(0)_I]\} - \left(\frac{1}{\hbar}\right)^2 \int_0^t dt'\, \mathrm{Tr}_{\text{B}}\{[H_{\text{S-B}}(t)_I, [H_{\text{S-B}}(t')_I, W(t')_I]]\}, \tag{3.42}$$

where $\rho_{\text{S}}(t)_I = \mathrm{Tr}_{\text{B}}\{W(t)_I\}$ is the reduced density operator of the open system in the interaction picture. The first term on the r.h.s of Eq. (3.42) is usually set to zero. This can be done when the interaction term has no diagonal elements in the representation in which H_{B} is diagonal. If it has diagonal terms, like, e.g., the renormalization term in the Caldeira-Leggett model, they can be usually included in the system Hamiltonian H_{S}. However, we will not do this in the following. The exact master equation (3.42) still depends on the density operator of the total system. In order to eliminate $W(t)$, we invoke a first approximation:

The Born approximation In the Born approximation, we assume a weak coupling between system and bath, in the sense that the bath density operator is not significantly changed by the interaction with the system, which allows us to write[2]

$$W(t)_I \approx \rho_\mathrm{S}(t)_I \rho_\mathrm{B}(0). \tag{3.43}$$

In fact, for a bilinear coupling term between system and bath, like $X \cdot x_k$, it is enough to assume that [82]

$$\mathrm{Tr}_B\{[x_k(t),[x_k(t'),W(t')_I]]\} \approx \rho_\mathrm{S}(t')_I \otimes \mathrm{Tr}_\mathrm{B}\{[x_k(t),[x_k(t'),\rho_\mathrm{B}(0)]]\}, \tag{3.44}$$

i.e., we assume that the bath correlation times are much shorter than the time interval during which we examine the system, and thus the bath correlation functions are not significantly changed by the interaction. This is justified for a bath consisting of infinite degrees of freedom so that the effects of the interaction with the system dissipate away quickly and do not react back on it. With that, the master equation for the reduced density operator becomes

$$\begin{aligned}\dot{\rho_\mathrm{S}}(t)_I =& -\frac{i}{\hbar}\mathrm{Tr}_B\{[H_\mathrm{S}(t)_I,\rho_\mathrm{S}(0)\rho_\mathrm{B}(0)]\}\\ &-\left(\frac{1}{\hbar}\right)^2\int_0^t dt'\mathrm{Tr}_B\{[H_\text{S-B}(t)_I,\left[H_\text{S-B}(t')_I,\rho_\mathrm{S}(t')_I\rho_\mathrm{B}(0)\right]]\}.\end{aligned} \tag{3.45}$$

A final step to have a first-order differential equation for the reduced density operator is to perform one approximation more:

The Markov approximation The correlation times of a thermal bath, like it will be considered in the next section, are comparable with the thermal correlation time

$$\tau_\mathrm{T} = \frac{\hbar}{2\pi k_B T}, \tag{3.46}$$

where T is the temperature of the bath.[3] A typical timescale of the open system is its relaxation time $\tau_\mathrm{R} = \gamma^{-1}$. For

$$\tau_\mathrm{T} \ll \tau_\mathrm{R}, \tag{3.47}$$

the reduced density operator $\rho_\mathrm{S}(t')$ is changing only weakly during the time in which the bath correlation functions vanish, and thus we can set $\rho_\mathrm{S}(t') \to \rho_\mathrm{S}(t)$. Further for times $t \gg \tau_\mathrm{T}$ we can set the limit in the integration in Eq. (3.45) to infinity. Upon substituting $t' = t - t''$, we find,

$$\begin{aligned}\dot{\rho_\mathrm{S}}(t)_I =& -\frac{i}{\hbar}\mathrm{Tr}_B\{[H_\mathrm{S}(t)_I,\rho_\mathrm{S}(0)\rho_\mathrm{B}(0)]\}\\ &-\left(\frac{1}{\hbar}\right)^2\int_0^\infty dt''\mathrm{Tr}_B\{[H_\text{S-B}(t)_I,\left[H_\text{S-B}(t-t'')_I,\rho_\mathrm{S}(t)_I\rho_\mathrm{B}(0)\right]]\}.\end{aligned} \tag{3.48}$$

This is the famous Born-Markov master equation. We have to emphasize that it underlies certain restrictions. First of all, it is only valid for weak coupling between bath and system.

---

[2] The assumption of weak coupling also allows us to stop the series expansion in Eq. (3.42) after second order in the coupling Hamiltonian.

[3] Typical bath temperatures as used in this work yield a thermal correlation time $\tau_\mathrm{T} < 1\,\mathrm{ns}$.

Besides, it gives us no correct information about the system for times being in the order of the bath correlation time τ_T. In particular, we see from Eq. (3.46) that, in the case of zero bath temperature, the Markov assumption is not valid anymore. For finite temperature, however, the Born-Markov master equation is quite a powerful prescription to simulate the dynamics of a damped system being subjected to dissipation.

3.5.2 The Caldeira-Leggett master equation

Depending on the specific system under consideration, various further approximations can be involved to simplify the Born-Markov master equation (3.48). For example, in the case of a quantum optical system, inverse differences $|\omega - \omega'|^{-1}$ of transition frequencies are usually small compared to the relaxation time, which means that the coherent dynamics of the open system goes through many cycles before it decays [83]; we have

$$\tau_\mathrm{S} \ll \tau_\mathrm{R}, \tag{3.49}$$

where $\tau_\mathrm{S} \sim |\omega - \omega'|^{-1}$ is the timescale of the open system's evolution. In this case, frequency differences are neglected within a rotating-wave approximation, which brings the Born-Markov master equation in Linblad form, thereby guaranteeing positivity of the density operator, which is not a necessary feature of Eq. (3.48) per se [1, 82, 83]. Those Linblad master equations are due to their simplicity often also used in solid-state systems. This is not always clearly justified, because there one often encounters stronger system-environment couplings and therefore faster relaxation times than in optical systems, so that condition (3.49) does not hold anymore. Furthermore, the above described rotating-wave approximation breaks down at low temperatures. If the characteristic timescale of the open system becomes even smaller than the bath correlation times, also the Markov approximation breaks down, and one has to use other techniques, like, e.g., the exact treatment of the non-Markovian effects within the Feynman-Vernon influence functional approach [1].

Another simplification can be invoked when we are only interested in the steady state of the dynamics, as it is often the case in transport calculations. Then the differential equation (3.48) becomes a linear system of equations, which can be solved exactly. In this regime of infinite times the Markov approximation yields exact results.

In this work the full Born-Markov master equation is taken into account. For the reservoir, we consider a thermal bath consisting of an infinite number of oscillators, the Caldeira-Leggett model. We express the bath operator in second quantization, using the definitions

$$x_k = \sqrt{\frac{\hbar}{2m_k\omega_k}}(b_k^\dagger + b_k), \quad p_k = \mathrm{i}\sqrt{\frac{\hbar m_k\omega_k}{2}}(b_k^\dagger - b_k). \tag{3.50}$$

In view of later calculations on the TLS we define also the dimensionless system coordinate $\tilde{X} \equiv X/x_0$, where x_0 is a scaling parameter of dimension of X. Finally, by redefinition of the coupling constant as $\nu_k = -x_0 c_k/\sqrt{2\hbar m_k\omega_k}$ and by dropping the zero point energy of the bath oscillators, we arrive at

$$H = H_\mathrm{S}(t) + H_\mathrm{B} + H_\text{S-B}, \tag{3.51}$$

with the bath Hamiltonian

$$H_\mathrm{B} = \sum_k \hbar\omega_k b_k^\dagger b_k, \tag{3.52}$$

and the interaction

$$H_{\text{S-B}} = \tilde{X}\sum_k \hbar\nu_k(b_k^\dagger + b_k) + \tilde{X}^2\sum_k \hbar\frac{\nu_k^2}{\omega_k}. \tag{3.53}$$

Moreover, like in Sec. 3.3, we consider the environment to be a thermal heat bath with the canonical equilibrium distribution

$$\rho_{\text{B}}(0) = \frac{\exp(-\beta H_{\text{B}})}{\text{Tr}_{\text{B}}\{\exp(-\beta H_{\text{B}})\}}. \tag{3.54}$$

We can use those definitions to perform the trace over the bath degrees of freedom in Eq. (3.48), and arrive at

$$\begin{aligned}\dot{\rho_{\text{S}}}(t)_I =& -i\sum_k \frac{\nu_k^2}{\omega_k}\left[\tilde{X}(t)^2, \rho_{\text{S}}(0)\right]\\ &-\sum_k \nu_k^2\int_0^\infty dt'\,\left[\tilde{X}(t), [\tilde{X}(t-t'), \rho_{\text{S}}(t)_I]\right]\cos\left(\omega_k t'\right)\coth\left(\frac{\hbar\beta\omega_k}{2}\right)\\ &+\mathrm{i}\sum_k \nu_k^2\int_0^\infty dt'\,\left[\tilde{X}(t), [\tilde{X}(t-t'), \rho_{\text{S}}(t)_I]_+\right]\sin\left(\omega_k t'\right)\end{aligned} \tag{3.55}$$

with

$$\tilde{X}(t) = U_{\text{S}}^\dagger(t,0)\tilde{X}U_{\text{S}}(t,0). \tag{3.56}$$

The quadratic term in the first line of the above formula comes from the renormalization term in the coupling Hamiltonian $H_{\text{S-B}}$. By integrating the remaining terms in Eq. (3.55) by parts and neglecting the initial slip term similarly to the discussion in Sec. 3.3, this term is canceled by the coupling to the bath and we obtain

$$\begin{aligned}\dot{\rho_{\text{S}}}(t)_{\text{I}} =& -\sum \nu_k^2\int_0^\infty dt'\,\left[\tilde{X}(t), \left[\tilde{X}(t-t'), \rho_{\text{S}}(t)_{\text{I}}\right]\right]\cos(\omega_k t')\coth(\hbar\beta\omega_k/2)\\ &+\mathrm{i}\sum_k \frac{\nu_k^2}{\omega_k}\int_0^\infty dt'\left[\tilde{X}(t), \left[\frac{\partial}{\partial t'}\tilde{X}(t-t'), \rho_{\text{S}}(t)_{\text{I}}\right]_+\right]\cos(\omega_k t').\end{aligned} \tag{3.57}$$

Finally, in the Schrödinger picture this becomes

$$\begin{aligned}\dot{\rho_{\text{S}}}(t) =& -\frac{\mathrm{i}}{\hbar}\left[H_{\text{S}}(t), \rho_{\text{S}}(t)\right]\\ &-\sum_k \nu_k^2\int_0^\infty dt'\,\left[\tilde{X}, \left[U_{\text{S}}^\dagger(t-t',t)\tilde{X}U_{\text{S}}(t-t',t), \rho_{\text{S}}(t)\right]\right]\cos(\omega_k t')\coth(\hbar\beta\omega_k/2)\\ &+\mathrm{i}\sum_k \frac{\nu_k^2}{\omega_k}\int_0^\infty dt'\left[\tilde{X}, \left[\frac{\mathrm{i}}{\hbar}U_{\text{S}}^\dagger(t-t',t)\left[\tilde{X}, H_{\text{S}}(t)\right]U_{\text{S}}(t-t',t), \rho_{\text{S}}(t)\right]_+\right]\cos(\omega_k t')\\ \equiv& -\frac{\mathrm{i}}{\hbar}\left[H_{\text{S}}(t), \rho_{\text{S}}(t)\right] + \mathcal{L}_{\text{Diss}}(t)\rho_{\text{S}}(t).\end{aligned} \tag{3.58}$$

Defining the spectral density as

$$G(\omega) = \sum_k \nu_k^2\delta(\omega-\omega_k) = (x_0^2/\hbar\pi)J(\omega), \tag{3.59}$$

and together with Eq. (3.30), we get for the dissipative part

$$\mathcal{L}_{\text{Diss}}(t) = \mathcal{L}_{\text{friction}}(t) + \mathcal{L}_{\text{noise}}(t), \tag{3.60}$$

where

$$\begin{aligned}\mathcal{L}_{\text{noise}}\rho_{\text{S}}(t) = &-\int_0^\infty dt' \left[\tilde{X}, \left[U_{\text{S}}^\dagger(t-t',t)\tilde{X}U_{\text{S}}(t-t',t), \rho_{\text{S}}(t)\right]\right] \\ &\times \int_0^\infty d\omega\, G(\omega)\cos(\omega t')\coth(\hbar\beta\omega/2)\end{aligned} \tag{3.61}$$

depends on the temperature of the bath and describes thermal fluctuations. It is the source of decoherence the system suffers through its coupling to the environment [83], while the friction term

$$\mathcal{L}_{\text{friction}}\rho_{\text{S}}(t) = -\int_0^\infty dt' \frac{Mx_0^2}{2\hbar^2}\gamma(t') \left[\tilde{X}, \left[U_{\text{S}}^\dagger(t-t',t)\left[\tilde{X}, H_{\text{S}}(t)\right]U_{\text{S}}(t-t',t), \rho_{\text{S}}(t)\right]_+\right] \tag{3.62}$$

depends on the damping kernel $\gamma(t)$.

Bloch-Redfield master equation for a time independent Hamiltonian

We assume now that the system Hamiltonian H_{S} is *not* explicitly time dependent, and that we have a discrete and complete eigenbasis of this Hamiltonian with

$$H_{\text{S}}|n\rangle = \hbar E_n|n\rangle. \tag{3.63}$$

We define further

$$\begin{aligned}Q_{nm} &= \int_0^\infty d\tau\, \langle n|U_{\text{S}}^\dagger(t-\tau,t)\tilde{X}U_{\text{S}}(t-\tau,t)|n\rangle \int_0^\infty d\omega\, G(\omega)\cos(\omega\tau)\coth\left(\frac{\hbar\beta\omega}{2}\right) \\ &= \int_0^\infty d\tau \int_0^\infty d\omega\, G(\omega)\cos(\omega\tau)\coth\left(\frac{\hbar\beta\omega}{2}\right)\mathrm{e}^{-\mathrm{i}\omega_{nm}\tau}\tilde{X}_{nm},\end{aligned} \tag{3.64}$$

and

$$\begin{aligned}P_{nm} &= -\frac{1}{\hbar}\int_0^\infty d\tau\, \langle n|U_{\text{S}}^\dagger(t-\tau,t)\left[\tilde{X}, H_{\text{S}}\right]U_{\text{S}}(t-\tau,t)|m\rangle \int_0^\infty d\omega\, \frac{G(\omega)}{\omega}\cos(\omega\tau) \\ &=\omega_{nm}\int_0^\infty d\tau \int_0^\infty d\omega\, \frac{G(\omega)}{\omega}\cos(\omega\tau)\mathrm{e}^{-\mathrm{i}\omega_{nm}\tau}\tilde{X}_{nm}\end{aligned} \tag{3.65}$$

with $\tilde{X}_{nm} = \langle n|\tilde{X}|m\rangle$ and $\omega_{nm} = (E_n - E_m)$. The integral over τ can be evaluated by using

$$\int_0^\infty d\tau\, \mathrm{e}^{\mathrm{i}\omega\tau} = \pi\delta(\omega) + \mathrm{i}\mathcal{P}(1/\omega), \tag{3.66}$$

where $\mathcal{P}$ is the principal part. We can thus see that the noise term leads to a temperature dependent frequency shift, which is usually denoted as Stark shift, while the friction term induces a so-called Lamb shift, which is not vanishing even for zero temperature and stems from vacuum fluctuations. In the following we will neglect those frequency shifts, so that we get

$$Q_{nm} \approx \frac{\pi}{2}G(\omega_{nm})\coth\left[\frac{\hbar\beta\omega_{nm}}{2}\right]\tilde{X}_{nm} \tag{3.67}$$

and

$$P_{nm} \approx \frac{\pi}{2} G(\omega_{nm}) \tilde{X}_{nm}. \tag{3.68}$$

Using those results in Eq. (3.58) and after slightly rearranging the terms, we find a first-order differential equation for the matrix elements of the density operator ρ_{S} in the eigenbasis of the time independent Hamiltonian H_{S}, the so-called *Bloch-Redfield master equation*:

$$\dot{\rho}_{nm}(t) = -i\omega_{nm}\rho_{nm}(t) + \pi \sum_{kl} \mathcal{L}_{nm,kl}\rho_{kl}(t), \tag{3.69}$$

where have dropped the index "S" of the density operator for convenience. The free dynamics of the system is given by the first term of the sum in the above equation. The rate coefficients are defined as

$$\begin{aligned} \mathcal{L}_{nm,kl} = {} & \left[G(\omega_{nk})N_{nk} - G(\omega_{lm})N_{ml}\right] \tilde{X}_{nk}\tilde{X}_{lm} \\ & - \delta_{ml} \sum_{l'} G(\omega_{l'k})N_{l'k}\tilde{X}_{nl'}\tilde{X}_{l'm} \\ & + \delta_{nk} \sum_{k'} G(\omega_{lk'})N_{k'l}\tilde{X}_{lk'}\tilde{X}_{k'm} \end{aligned} \tag{3.70}$$

with

$$N_{nm} = \frac{1}{2}\left[\coth\left(\frac{\hbar\beta\omega_{nm}}{2}\right) - 1\right]. \tag{3.71}$$

The above calculations are valid for an arbitrary spectral density. For an Ohmic spectral density with the cutoff set to infinity; i.e.,

$$G(\omega) = \kappa\omega = (x_0^2/\hbar\pi)M\gamma\omega, \tag{3.72}$$

the following useful relations can be found

$$G(\omega_{mn}) = -G(\omega_{nm}), \quad G(\omega_{mn})N_{mn} = G(\omega_{nm})N_{nm} + G(\omega_{nm}), \tag{3.73}$$

and

$$\lim_{\omega_{nm}\to 0} G(\omega_{nm})N_{nm} = \frac{\kappa}{\hbar\beta}, \tag{3.74}$$

$$\lim_{\omega_{nm}\to 0} G(\omega_{nm})N_{mn} = -\frac{\kappa}{\hbar\beta}. \tag{3.75}$$

The case of a explicitly time dependent Hamiltonian will be discussed in Sec. 5.1.3 in the framework of Floquet theory.

With the quantum master equation (3.69) we have now the tool to include environmental effects into the discussion of the qubit's time evolution. In the next chapter we will use the qubit-oscillator Hamiltonian for H_{S} in Eq. (3.3) and solve the master equation for the corresponding density matrix in order to obtain the relaxation and dephasing rates for the qubit. However, we have to keep in mind the various approximations we have made in this chapter. First of all, we considered a bath consisting of an infinite number of *linear* oscillators. Besides, we assumed that the coupling between system and bath is weak, allowing to invoke the Born approximation. Moreover, we applied the Markov approximation, thereby neglecting transient terms which result from the assumed initial conditions for the system and bath and play a role on the scale of the bath correlation time. In particular, the Markov approximation breaks down for a bath temperature of $T \to 0$.

4

The dissipative qubit-oscillator system

Parts of this chapter have been published in collaboration with M. Grifoni in [53].

The considerations in the previous chapter were quite general: we did not specify the Hamiltonian H_{S} of the system being in contact with the reservoir. In this work we will concentrate on the models introduced in Chapter 1 and therefore consider as open system the two-level Hamiltonian H_{TLS}. In combination with a bath of harmonic oscillators one speaks of the so-called spin-boson model [1, 84]. Its Hamiltonian is

$$H_{\mathrm{SB}} = -\frac{\hbar}{2}(\varepsilon\sigma_z + \Delta\sigma_x) + \frac{\sigma_z}{2}\sum_k \hbar\nu_k(b_k^\dagger + b_k) + \sum_k \hbar\frac{\nu_k^2}{4\omega_k} + \sum_k \hbar\omega_k b_k^\dagger b_k, \tag{4.1}$$

where we used the general Hamiltonian (3.51) and inserted for the system coordinate $\tilde{X} = \sigma_z/2$. This model has been applied successfully on many different physical and chemical systems, for which the dynamics can be effectively described by the tunneling between the two localized states of a TLS, and environmental influences can be modeled by a bosonic bath. It can be used to explain dissipative and decoherence effects in charge and persistent-current qubits induced through voltage and flux fluctuations in the surrounding circuitry and measurement apparatus [1, 12, 22, 23]. Apart from these external sources, there exist also other mechanisms and origins of decoherence and dissipation, like quasiparticle tunneling in Josephson junctions, $1/f$ noise from background charges, interaction with nuclear spin degrees of freedom, excitation beyond the two states of the qubit etc. (for an overview see [1]). However, in this work we will not consider these latter influences.

Crucial for the effect of the environment on the dynamics of the TLS is the shape of the spectral density of the harmonic bath. It is common to assume an Ohmic spectral density, which is linear in the continuous bath modes. For instance, it describes the fluctuations in a charge qubit which is directly coupled to an electromagnetic environment represented by an Ohmic resistor [12]. A special situation occurs when we use as open system the qubit-oscillator Hamiltonian $H_{\text{TLS-osc}}$, where the oscillator feels the influence of the Ohmic bath. It has been shown in [85] that there exists an exact mapping between this case and the spin-boson model with a structured bath featuring an effective spectral density which is Ohmic at low frequencies but exhibits a Lorentzian-shaped peak at the oscillator frequency Ω. This model describes, for instance, a Josephson flux qubit read-out by a dc-SQUID, where environmental influences from the electric circuitry are transferred via the SQUID to the qubit [22, 23].

The spin-boson model can be formally solved using, e.g., real-time path integral methods [1, 84]. However, in order to get closed-form analytical results, approximations must be invoked. A quite common one is the so-called weak coupling approximation (WCA), which is perturbative in the bath spectral density [1]. It has, for example, been used in [22, 23] to give a first estimate on the relaxation and dephasing time of the qubit-SQUID system. However, for strong qubit-oscillator coupling $g \gg \Gamma$, where Γ is the width of the damped oscillator, and for small detuning $\delta = E_{\mathrm{qb}} - \Omega$ such an approximation breaks down [86], as coherent exchange processes between TLS and oscillator are disregarded. For an unbiased qubit the non-interacting blip approximation (NIBA) used in [65, 87–89] circumvents this problem as it is nonperturbative in the coupling g and therefore takes correctly into account the influence of the oscillator on the TLS. Moreover, it allows an analytic treatment of the dynamics. However, the NIBA is known to fail for a biased qubit at low temperatures [1, 84]. Another approach, which treats the system nonperturbatively in the bath, is the flow-equation renormalization method [90, 91], where the spin-boson Hamiltonian is diagonalized using infinitesimal unitary transformations. However, within this approach analytical solutions are difficult to find. Recently, a polaron transformation was used by Huang et al. to obtain analytically the population dynamics and confirm Shiba's relation for an unbiased TLS [92]. In the case in which the qubit and the oscillator are considered as the central quantum system being coupled to an Ohmic bath, the numerical, ab-initio quasiadiabatic propagator path-integral method (QUAPI) [93, 94] is a nice tool as it enables to cover both the resonant regime, where the oscillator frequency is close to the qubit energy splitting, and the dispersive regime with the oscillator being far detuned from the qubit [86, 88, 89]. Moreover, it can be applied to a biased as well as to an unbiased TLS and therefore be used as a testbed for analytical results. By considering the qubit-oscillator system in the representation of displaced oscillator states, Brito et al. were able to truncate the infinite Hilbert space of this system without loosing the effects of the oscillator on the TLS dynamics [95]. However, so far none of these works could provide an analytical expression for the dynamics of the dissipative qubit being valid for zero as well as nonzero detuning and for both a biased and unbiased TLS.

In this chapter an analytic expression for the dissipative dynamics of the qubit, including the effects of a finite detuning and of a static bias, is derived. We solve the Born-Markov master equation for the reduced density matrix of the qubit-oscillator system in the eigenbasis derived in Sec. 2.2 using Van Vleck perturbation theory up to second order in the coupling g. Thereby, we also include effects beyond the rotating-wave approximation.

4.1 The qubit-oscillator-bath system

In this section we consider the qubit-oscillator Hamiltonian, which was introduced in Sec. 1.2, Eq. (1.15), and which we repeat here:

$$H_{\text{TLS-osc}} = H_{\text{TLS}} + H_{\text{int}} + H_{\text{osc}}, \tag{4.2}$$

with

$$H_{\text{TLS}} = -\frac{\hbar}{2}(\varepsilon\sigma_z + \Delta\sigma_x), \quad H_{\text{int}} = \hbar g \sigma_z (B^\dagger + B), \quad H_{\text{osc}} = \hbar\Omega B^\dagger B. \tag{4.3}$$

In order to mimic dissipative effects on this system, we use $H_{\text{TLS-osc}}$ as system Hamiltonian in the Caldeira-Legget model, Eq. (3.51). We assume that the bath couples directly to the oscillator coordinate, so that $\tilde{X} = (B^\dagger + B)$, and the interaction Hamiltonian between system and bath becomes

$$H_{\text{SB}} = (B^\dagger + B)\sum_k \hbar\nu_k(b_k^\dagger + b_k) + (B^\dagger + B)^2 \sum_k \hbar\frac{\nu_k^2}{\omega_k}. \tag{4.4}$$

Furthermore, we consider the spectral density of the bath to be Ohmic

$$G_{\mathrm{Ohm}}(\omega) = \sum_k \nu_k^2 \delta(\omega - \omega_k) = \kappa\omega. \tag{4.5}$$

In [85] it is shown that the above model is equivalent to that of a TLS being coupled directly to a harmonic bath including the single oscillator of frequency Ω; i.e., a spin-boson model with a peaked effective spectral density,

$$G_{\mathrm{eff}}(\omega) = \frac{2\alpha\omega\Omega^4}{(\Omega^2 - \omega^2)^2 + (\Gamma\omega)^2}. \tag{4.6}$$

The width of the Lorentzian-shaped peak is given by $\Gamma = 2\pi\kappa\Omega$. The relation between α and the coupling parameter g between qubit and oscillator is $g = \Omega\sqrt{\alpha/(8\kappa)}$ [20, 22]. This second perspective is suitable for calculating the dynamics of the qubit using a path-integral approach, as it was done for example in [65] for the case of an unbiased qubit ($\varepsilon = 0$). The approach in [65], however, being based on the NIBA [1], is not suitable to investigate the low temperature dynamics of a biased TLS. Thus, in this chapter we will consider the qubit and the single oscillator as central quantum system.

4.2 Dissipative dynamics

Like in the nondissipative case, we want to calculate the population difference of the qubit states taking the influence of the bath into account. We follow the lines in Sec. 3.5.2 and express the Bloch-Redfield master equation, Eqs. (3.69) and (3.70),

$$\dot{\rho}_{nm}(t) = -i\omega_{nm}\rho_{nm}(t) + \pi \sum_{kl} \mathcal{L}_{nm,kl}\rho_{kl}(t), \tag{4.7}$$

in terms of the eigenstates and eigenenergies of the qubit-oscillator system derived in Sec. 2.2 within VVP in g. We will present in the following several approximation schemes to solve this master equation analytically and compare them to numerical results.

4.2.1 Position matrix elements

As a first step we have to determine the Bloch-Redfield tensor $\mathcal{L}_{nm,kl}$. For this we need the position matrix elements X_{nm} in the qubit-oscillator eigenbasis.[1] By use of Eqs. (2.16a), (2.16b) and (2.18) those states are expressed in the basis $\{|j,\mathrm{g}\rangle; |j,\mathrm{e}\rangle\}$. We define the operator $X' = \mathrm{e}^{\mathrm{i}S}\left(B^\dagger + B\right)\mathrm{e}^{-\mathrm{i}S}$. Four different situations can be distinguished. There are matrix elements were neither the oscillator nor the qubit state are changed, namely $\langle j,\mathrm{g}|X'|j,\mathrm{g}\rangle = -2L_0$ and $\langle j,\mathrm{e}|X'|j,\mathrm{e}\rangle = 2L_0$ with $L_0 = \varepsilon g/E_{\mathrm{qb}}\Omega$. We see that those elements are independent of j, the occupation number of the oscillator. Next, we look at the case where we have a change of a single oscillator quantum and get $\langle j,\mathrm{g}|X'|j+1,\mathrm{g}\rangle = \sqrt{j+1}(1 + L_{\mathrm{osc}})$ and $\langle j,\mathrm{e}|X'|j+1,\mathrm{e}\rangle = \sqrt{j+1}(1 - L_{\mathrm{osc}})$ with

$$L_{\mathrm{osc}} = \frac{(2E_{\mathrm{qb}} + 3\Omega)\Delta^2}{E_{\mathrm{qb}}^2\Omega(E_{\mathrm{qb}} + \Omega)^2} g^2. \tag{4.8}$$

---

[1] We drop the tilde in X_{nm} for convenience.

For a change of the qubit state, we have $\langle j,\mathrm{g}|X'|j,\mathrm{e}\rangle = \Delta g/E_{\mathrm{qb}}(E_{\mathrm{qb}}+\Omega) \equiv L_{\mathrm{q}}$. And finally, if the qubit and the oscillator state are changed simultaneously, one obtains $\langle j,\mathrm{g}|X'|j{+}1,\mathrm{e}\rangle = \sqrt{j+1}L^{+}_{\mathrm{q,osc}}$ and $\langle j,\mathrm{e}|X'|j+1,\mathrm{g}\rangle = \sqrt{j+1}L^{-}_{\mathrm{q,osc}}$,

$$\text{where}\quad L^{+}_{\mathrm{q,osc}} = \frac{4\varepsilon\Delta}{E^2_{\mathrm{qb}}(E_{\mathrm{qb}}+\Omega)(E_{\mathrm{qb}}+2\Omega)}g^2 \quad\text{and}\quad L^{-}_{\mathrm{q,osc}} = \frac{-4\varepsilon\Delta}{E^2_{\mathrm{qb}}\Omega(E_{\mathrm{qb}}-2\Omega)}g^2. \tag{4.9}$$

Comparing the magnitude of the transition terms, we notice that those consisting in changes of the oscillator occupation only are the dominant ones, as they have a part which is of zeroth order in g. Further, for the case in which the qubit is operated at the degeneracy point L_0 and $L^{+/-}_{\mathrm{q,osc}}$ vanish. With those results we can calculate the matrix elements X_{nm}. They are given in Appendix C.1.

4.2.2 Analytical solution of the master equation

Like in Sec. 2.2.2 we assume the system to be operated at low temperatures and thus take as highest qubit-oscillator state the eigenstate $|4\rangle$. To determine the population difference $P(t)$, formulae (2.1), (2.21), (2.22a) and (2.22b) can be used. Unlike in the nondissipative case, $\rho(t)$ is not given anymore by the simple expression Eq. (2.23). Rather, we have to solve a system of coupled differential equations, namely Eq. (4.7). To do this analytically we will follow three different approaches and compare them finally to the numerical solution of Eq. (4.7). We start by introducing

$$\rho_{nm}(t) = \mathrm{e}^{-\mathrm{i}\omega_{nm}t}\sigma_{nm}(t), \tag{4.10}$$

which yields the set of differential equations for σ_{nm} :

$$\dot{\sigma}_{nm}(t) = \pi\sum_{kl}\mathcal{L}_{nm,kl}\mathrm{e}^{\mathrm{i}(\omega_{nm}-\omega_{kl})t}\sigma_{kl}(t). \tag{4.11}$$

Full secular approximation (FSA):

As a first approach we make the full secular approximation; i.e., we neglect fast rotating terms in Eq. (4.11) and keep only contributions where $\omega_{nm}-\omega_{kl}$ vanishes. In this way the off-diagonal elements of σ_{nm} are decoupled from the diagonal ones so that

$$\dot{\sigma}_{nn}(t) = \pi\sum_{k}\mathcal{L}_{nn,kk}\sigma_{kk}(t), \tag{4.12}$$

$$\dot{\sigma}_{nm}(t) = \pi\mathcal{L}_{nm,nm}\sigma_{nm}(t) \quad \text{for} \quad n \neq m. \tag{4.13}$$

The equation for the off-diagonal elements is then

$$\sigma_{nm}(t) = \sigma^0_{nm}e^{\pi\mathcal{L}_{nm,nm}t}, \tag{4.14}$$

which becomes with Eq. (4.10)

$$\rho_{nm}(t) = \rho^0_{nm}e^{\pi\mathcal{L}_{nm,nm}t}e^{-\mathrm{i}\omega_{nm}t}. \tag{4.15}$$

As through the FSA the oscillatory motion of the dynamics is separated from the relaxation one we can divide Eq. (2.21) into two parts,

$$P(t) = P_{\mathrm{relax.}}(t) + P_{\mathrm{dephas.}}(t), \tag{4.16}$$

where $P_{\text{relax.}}(t) = \sum_n p_{nn}(t)$ describes the relaxation and $P_{\text{dephas.}}(t) = \sum_{n>m} p_{nm}(t)$ the dephasing part of the dynamics. With Eq. (4.15) the latter takes the form

$$P_{\text{dephas.}}(t) = \sum_{n>m} p_{nm}(0)\mathrm{e}^{-\Gamma_{nm}t}\cos(\omega_{nm}t) \tag{4.17}$$

with the dephasing rates $\Gamma_{nm} \equiv -\pi\mathcal{L}_{nm,nm}$. Expressions for the dephasing coefficients $\mathcal{L}_{nm,nm}$ can be found in Appendix C.2. As initial conditions $\rho^0_{nm} = \sigma^0_{nm} = \rho_{nm}(0)$ we assume again the qubit to be in the spin-up state and the oscillator in thermal equilibrium, see Eq. (2.2). The diagonal elements are more difficult to obtain, as one has to solve a system of coupled differential equations, Eq. (4.12). Calculating the corresponding rate coefficients of this system for the five lowest eigenstates, we find that there are only eight independent ones, namely $\mathcal{L}_{00,11}$, $\mathcal{L}_{00,22}$, $\mathcal{L}_{11,22}$, $\mathcal{L}_{11,33}$, $\mathcal{L}_{11,44}$, $\mathcal{L}_{22,33}$, $\mathcal{L}_{22,44}$ and $\mathcal{L}_{33,44}$. They are given by

$$\mathcal{L}_{jj,kk} = 2G(\omega_{jk})N_{jk}X^2_{jk} \quad \text{with} \quad j < k, \tag{4.18}$$

where j and k adopt the above values. Furthermore, $\mathcal{L}_{00,33}$, $\mathcal{L}_{00,44}$, $\mathcal{L}_{33,00}$ and $\mathcal{L}_{44,00}$ vanish. The remaining rate coefficients are combinations of the above. We find that

$$\mathcal{L}_{kk,jj} = \mathcal{L}_{jj,kk} + 2G(\omega_{jk})X^2_{jk} = (N_{jk}+1)2G(\omega_{jk})X^2_{jk} \tag{4.19}$$

and

$$\begin{aligned}
\mathcal{L}_{00,00} &= -\mathcal{L}_{11,00} - \mathcal{L}_{22,00}, && \text{(4.20a)}\\
\mathcal{L}_{11,11} &= -\mathcal{L}_{00,11} - \mathcal{L}_{22,11} - \mathcal{L}_{33,11} - \mathcal{L}_{44,11}, && \text{(4.20b)}\\
\mathcal{L}_{22,22} &= -\mathcal{L}_{00,22} - \mathcal{L}_{11,22} - \mathcal{L}_{33,22} - \mathcal{L}_{44,22}, && \text{(4.20c)}\\
\mathcal{L}_{33,33} &= -\mathcal{L}_{11,33} - \mathcal{L}_{22,33} - \mathcal{L}_{44,33}, && \text{(4.20d)}\\
\mathcal{L}_{44,44} &= -\mathcal{L}_{11,44} - \mathcal{L}_{22,44} - \mathcal{L}_{33,44}. && \text{(4.20e)}
\end{aligned}$$

However, the system Eq. (4.12) is still too complicated to be solved analytically. Thus, we invoke a further approximation: we consider the factor $N_{nm} + 1 = \frac{1}{2}[\coth(\hbar\beta\omega_{nm}/2) + 1]$ with $n < m$ in Eq. (4.19) and use that $\lim_{\omega\to-\infty}\coth(\hbar\beta\omega_{nm}/2) = -1$. It depends strongly on the temperature β for which value of ω_{nm} this limit is reached approximately. For the parameters we are working with one usually is in the region where $(N_{nm}+1) \ll 1$. Thus, we will neglect in the following terms containing the factor $(N_{nm}+1)$. Furthermore, one sees from Eq. (2.19) that $\omega_{12} \backsim g$ and $\omega_{34} \backsim g$. With that $\mathcal{L}_{11,22} = \mathcal{O}(g^3)$ and $\mathcal{L}_{33,44} = \mathcal{O}(g^3)$ can be neglected. Using Eqs. (4.20a) – (4.20e) the matrix of the system (4.12) becomes

$$\mathcal{L}_{\text{relax.}} = \begin{pmatrix}
0 & \mathcal{L}_{00,11} & \mathcal{L}_{00,22} & 0 & 0\\
0 & -\mathcal{L}_{00,11} & 0 & \mathcal{L}_{11,33} & \mathcal{L}_{11,44}\\
0 & 0 & -\mathcal{L}_{00,22} & \mathcal{L}_{22,33} & \mathcal{L}_{22,44}\\
0 & 0 & 0 & -\mathcal{L}_{11,33}-\mathcal{L}_{22,33} & 0\\
0 & 0 & 0 & 0 & -\mathcal{L}_{11,44}-\mathcal{L}_{22,44}
\end{pmatrix}. \tag{4.21}$$

The eigenvalues and eigenvectors of this matrix and the associated time evolution of the elements $\sigma_{nn}(t)$ are given in Eqs. (C.18) – (C.22) of Appendix C.3. Unlike for the dephasing part Eq. (4.17), we cannot extract a simple analytical expression for the relaxation rate as $P_{\text{relax.}}(t) = \sum_n p_{nn}(t)$ now consists of a sum of several exponential functions. But still we are able to provide an analytical formula for $P(t)$ using Eq. (4.16).

An ansatz for the long-time dynamics:

In order to obtain a simple expression for the relaxation part, we consider the long-time dynamics of the system. In other words, rather than looking at the many relaxation contributions to the populations $\sigma_{nn}(t)$, we focus on the eigenvalue of the rate matrix, which has the smallest absolute value, because it will dominate at long times. Further, we consider only the three lowest qubit-oscillator eigenstates, $|0\rangle$, $|1\rangle$ and $|2\rangle$ in Eq. (4.12), and obtain with Eqs. (4.20a) - (4.20c) that

$$\mathcal{L}_{\text{relax.}} = \begin{pmatrix} -\mathcal{L}_{11,00} - \mathcal{L}_{22,00} & \mathcal{L}_{00,11} & \mathcal{L}_{00,22} \\ \mathcal{L}_{11,00} & -\mathcal{L}_{00,11} - \mathcal{L}_{22,11} & \mathcal{L}_{11,22} \\ \mathcal{L}_{22,00} & \mathcal{L}_{22,11} & -\mathcal{L}_{00,22} - \mathcal{L}_{11,22} \end{pmatrix}. \tag{4.22}$$

Here, we have not neglected the rate coefficients containing the term $(N_{nm} + 1)$ and further took $\mathcal{L}_{11,22}$ into account despite of being of third order in g as those contributions remove the degeneracy between the two lowest eigenvalues at resonance, cf. inset in Fig. 4.1. The smallest contribution to the relaxation process reads

$$\begin{aligned} \Gamma_{\text{r}} \equiv -\frac{\pi}{2}\Bigg\{ -\sum_{n\neq m} \mathcal{L}_{nn,mm} + \Bigg[\Bigg(\sum_{n\neq m} \mathcal{L}_{nn,mm} \Bigg)^2 - 4(\mathcal{L}_{00,11}\mathcal{L}_{00,22} + \mathcal{L}_{11,00}\mathcal{L}_{00,22} \\ + \mathcal{L}_{00,11}\mathcal{L}_{11,22} + \mathcal{L}_{11,00}\mathcal{L}_{11,22} + \mathcal{L}_{00,11}\mathcal{L}_{22,00} + \mathcal{L}_{11,22}\mathcal{L}_{22,00} \\ + \mathcal{L}_{22,11}\mathcal{L}_{00,22} + \mathcal{L}_{11,00}\mathcal{L}_{22,11} + \mathcal{L}_{22,00}\mathcal{L}_{22,11}) \Bigg]^{1/2} \Bigg\}. \end{aligned} \tag{4.23}$$

With the system being detuned this expression can be simplified further, namely

$$\Gamma_{\text{r}} \approx \pi \mathcal{L}_{00,22} \quad \text{for} \quad \Omega < E_{\text{qb}}; \quad \Gamma_{\text{r}} \approx \pi \mathcal{L}_{00,11} \quad \text{for} \quad \Omega > E_{\text{qb}}. \tag{4.24}$$

In Fig. 4.1 the relaxation rate Γ_{r} as obtained from Eq. (4.23) is shown as a function of the oscillator frequency Ω. It is maximal close to resonance ($\Omega \approx E_{\text{qb}}$), however, not at exact resonance as one would expect using the formulae obtained by a path-integral approach based on the assumption of weak coupling between TLS and structured bath, as it was done, e.g., in [22, 23]. This point of maximal relaxation rate is of great interest for statistical measurement setups where a repeated read-out and therefore fast relaxation to the equilibrium state is needed. If Ω is detuned from the resonance, Γ_{r} decays. This effect has already been predicted by Blais et al. [29]. As the qubit is not directly coupled to the bath but rather through the oscillator, the latter being detuned filters out the environmental noise at the qubit transition frequency. Additionally, we show the second smallest contribution in Fig. 4.1. We notice that there is an avoided crossing close to the resonant point. Finally, we find that

$$P_{\text{relax.}}(t) = (p_0 - p_\infty)\mathrm{e}^{-\Gamma_{\text{r}} t} + p_\infty, \tag{4.25}$$

where $p_0 \equiv \sum_n p_{nn}(0)$. For getting p_∞ we have in principle to find the steady-state solution of Eq. (4.12). Here, we just assume for $t \to \infty$ a Boltzmann distribution for the qubit-oscillator system, so that $\rho_{nn}(\infty) = Z^{-1}\mathrm{e}^{-\beta E_n}$ with $Z = \sum_n \mathrm{e}^{-\beta E_n}$. Thus, with Eq. (2.22a),

$$p_\infty = \sum_n \sum_i \Big\{ \cos\Theta \Big[\langle j\mathrm{g}|n\rangle^2 - \langle j\mathrm{e}|n\rangle^2 \Big] + 2\sin\Theta \langle j\mathrm{g}|n\rangle\langle j\mathrm{e}|n\rangle \Big\} \rho_{nn}(\infty). \tag{4.26}$$

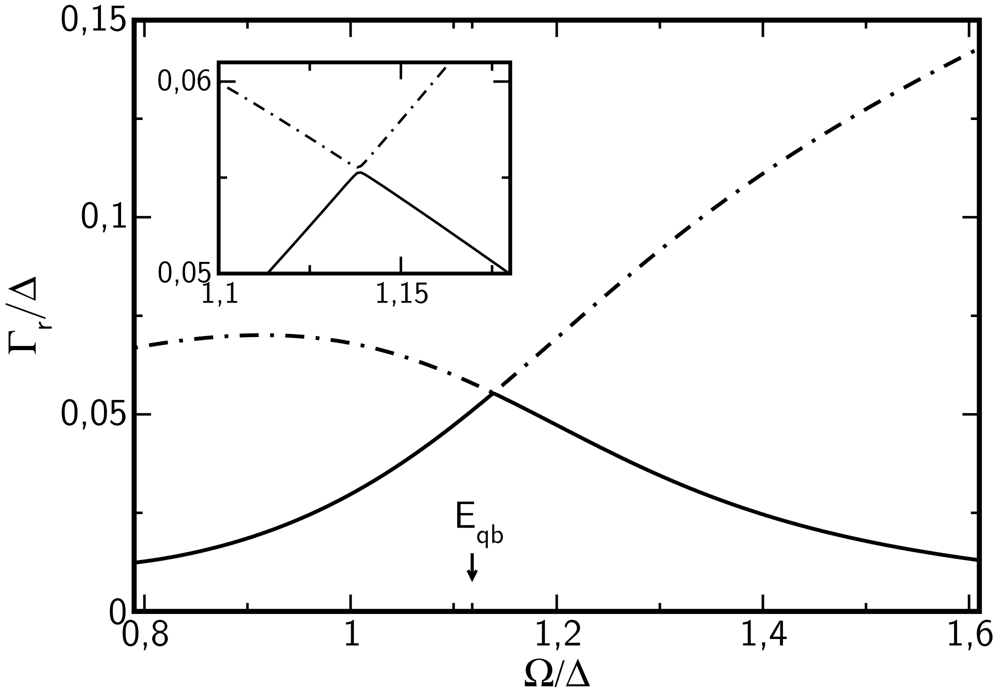

Figure 4.1: The relaxation rate Γ_r as it is given in Eq. (4.23) drawn against the oscillator frequency Ω (solid line). Used values are $\varepsilon = 0.5\Delta$, corresponding to a frequency splitting $E_\mathrm{qb} = 1.118\Delta$, and coupling $g = 0.18\Delta$. Moreover, the damping constant is $\kappa = 0.0154$ ($\alpha = 4 \times 10^{-3}$ at $\Omega = \Delta$) and $\beta = 10(\hbar\Delta)^{-1}$. Close to resonance ($\Omega \approx E_\mathrm{qb}$) Γ_r is maximal. For a comparison also the second smallest eigenvalue is plotted (dotted-dashed line). The inset shows the two eigenvalues close to resonance.

The formula for the long-time dynamics is obtained as

$$P(t) = (p_0 - p_\infty)e^{-\Gamma_\mathrm{r}t} + p_\infty + \sum_{n>m} p_{nm}(0)e^{-\Gamma_{nm}t}\cos(\omega_{nm}t). \tag{4.27}$$

To get further insight on the dominant frequencies we evaluate the Fourier transform of Eq. (4.27) according to

$$F(\nu) = 2\int_0^\infty dt P(t)\cos\nu t, \tag{4.28}$$

yielding

$$\begin{aligned} F(\nu) =& 2(p_0 - p_\infty)\frac{\Gamma_\mathrm{r}}{\omega^2 + \Gamma_\mathrm{r}^2} + 2\pi p_\infty \delta(\nu) \\ &+ \sum_{n<m} p_{nm}\Gamma_{mn}\left[\frac{1}{\Gamma_{mn}^2 + (\omega_{mn}+\nu)^2} + \frac{1}{\Gamma_{mn}^2 + (\omega_{mn}-\nu)^2}\right]. \end{aligned} \tag{4.29}$$

Partial secular approximation (PSA):

An improvement to the FSA is to take into account certain nonvanishing contributions of $\omega_{nm} - \omega_{kl}$. We have to keep in mind, that there are quasidegenerate levels close to resonance. In our case the first with second energy level and the third with fourth one build a doublet, meaning that they are close together in energy space. The level spacing is approximately proportional to g for the former and $\sqrt{2}g$ for the latter. Because of that and as the transitions from level three and four are less probable, we will in the following only consider the first and second level as being almost degenerate. Taking this into account in Eq. (4.11) we arrive for the diagonal elements at

$$\dot{\sigma}_{nn}(t) = \pi \sum_{k} \mathcal{L}_{nn,kk}\sigma_{kk}(t) + \pi\mathcal{L}_{nn,12}\sigma_{12}(t)\mathrm{e}^{-\mathrm{i}\omega_{12}t} + \pi\mathcal{L}_{nn,21}\sigma_{21}(t)\mathrm{e}^{-\mathrm{i}\omega_{21}t}. \tag{4.30}$$

A numerical analysis shows that the effect of the last two terms on the right-hand side of the above equation will in the worst case lead to very small, fast oscillations in $\sigma_{nn}(t)$ and play no role in $P(t)$. Thus, we finally write

$$\dot{\sigma}_{nn}(t) \cong \pi \sum_{k} \mathcal{L}_{nn,kk}\sigma_{kk}(t), \tag{4.31}$$

which is the same equation as we got in the FSA approach. However, the off-diagonal contributions σ_{01}, σ_{02}, σ_{13}, σ_{23}, σ_{14} and σ_{24} have to be examined more carefully. From (4.11) we find that one has to solve the equations

$$\begin{aligned}
\dot{\rho}_{nm}(t) =& (-\mathrm{i}\omega_{nm} + \pi\mathcal{L}_{nm,nm})\rho_{nm}(t) + \pi\mathcal{L}_{nm,jk}\rho_{jk}(t), && (4.32)\\
\dot{\rho}_{jk}(t) =& \pi\mathcal{L}_{jk,nm}\rho_{nm}(t) + (-\mathrm{i}\omega_{jk} + \pi\mathcal{L}_{jk,jk})\rho_{jk}(t) && (4.33)
\end{aligned}$$

with $\{(nm),(jk)\} = \{(01);(02)\}$,$\{(13);(23)\}$ or $\{(14);(24)\}$. As solution one gets

$$\begin{aligned}
\rho_{nm} =& c^{(+)}_{nm,jk} v^{(+)}_{nm,jk} \mathrm{e}^{\lambda^{(+)}_{nm,jk}t} + c^{(-)}_{nm,jk} v^{(-)}_{nm,jk} \mathrm{e}^{\lambda^{(-)}_{nm,jk}t}, && (4.34)\\
\rho_{jk} =& c^{(+)}_{nm,jk} \mathrm{e}^{\lambda^{(+)}_{nm,jk}t} + c^{(-)}_{nm,jk} \mathrm{e}^{\lambda^{(-)}_{nm,jk}t}. && (4.35)
\end{aligned}$$

Here, the oscillation frequencies and the decay of the off-diagonal elements are given by

$$\lambda^{(+/-)}_{nm,jk} = \frac{1}{2}\left[\pi(\mathcal{L}_{nm,nm} + \mathcal{L}_{jk,jk}) - \mathrm{i}(\omega_{nm} + \omega_{jk}) \pm R_{nm,jk}\right] \tag{4.36}$$

with

$$R_{nm,jk} = \sqrt{\left[\pi(\mathcal{L}_{nm,nm} - \mathcal{L}_{jk,jk}) - \mathrm{i}(\omega_{nm} - \omega_{jk})\right]^2 + 4\pi^2\mathcal{L}_{nm,jk}\mathcal{L}_{jk,nm}}. \tag{4.37}$$

The amplitudes of the oscillations are given through the coefficients

$$c^{(+/-)}_{nm,jk} = \pm\frac{2\pi\mathcal{L}_{jk,nm}\rho^0_{nm} - \rho^0_{jk}\left[\pi(\mathcal{L}_{nm,nm} - \mathcal{L}_{jk,jk}) - \mathrm{i}(\omega_{nm} - \omega_{jk}) \mp R_{nm,jk}\right]}{2R_{nm,jk}} \tag{4.38}$$

and

$$v^{(+/-)}_{nm,jk} = \frac{1}{2\pi\mathcal{L}_{jk,nm}}\left[\pi(\mathcal{L}_{nm,nm} - \mathcal{L}_{jk,jk}) - \mathrm{i}(\omega_{nm} - \omega_{jk}) \pm R_{nm,jk}\right]. \tag{4.39}$$

Thus, we have again all ingredients to calculate analytically the relaxation and dephasing part of Eq. (4.16). For the PSA we cannot provide a simple expression for the dephasing rates as in the FSA, where we had $\Gamma_{nm} = -\pi\mathcal{L}_{nm,nm}$. As one can see from Eqs. (4.34) and (4.35), ρ_{01} and ρ_{02} are a mixture of contributions decaying with $\mathrm{Re}\{\lambda^{(+)}_{01,02}\}$ and $\mathrm{Re}\{\lambda^{(-)}_{01,02}\}$. Similar to our findings for the relaxation rate, also here the smallest eigenvalue will dominate the

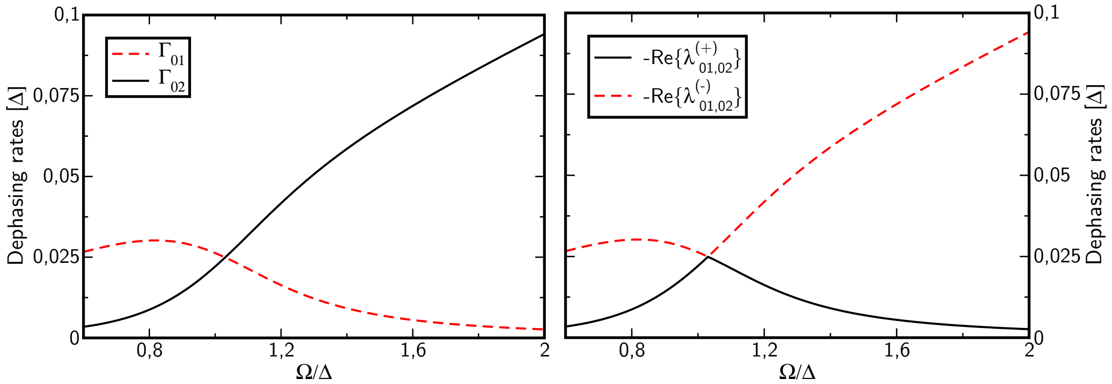

Figure 4.2: Comparison between the dephasing rates of the two dominant frequencies as they are obtained using the FSA or the PSA, respectively. On the left: the FSA rates $\Gamma_{01} \equiv -\pi\mathcal{L}_{01,01}$ (dashed red line) and $\Gamma_{02} \equiv -\pi\mathcal{L}_{02,02}$ (solid black line). On the right: the real part of $\lambda^{(-)}_{01,02}$ (red dashed line) and $\lambda^{(+)}_{01,02}$ (black solid line) as given by Eq. (4.36) is shown. The rate dominating the dephasing behavior is defined as $\Gamma^{(+)}_{12} \equiv -\mathrm{Re}\{\lambda^{(+)}_{01,02}\}$. For $\Omega < \Delta$ we see that $\Gamma^{(+)}_{12}$ is approximated by the FSA rate Γ_{02}, while for $\Omega > \Delta$ by Γ_{01}. Used values are $\varepsilon = 0$, $g = 0.18\Delta$, $\kappa = 0.0154$ and $\beta = 10(\hbar\Delta)^{-1}$.

dephasing behavior. From the right graph in Fig. 4.2 we find that this is $\mathrm{Re}\{\lambda^{(+)}_{01,02}\} \equiv -\Gamma^{(+)}_{12}$. Comparing it with the dephasing rates we got using the FSA, left graph in Fig. 4.2, we see that for positive detuning ($\Omega < E_{\mathrm{qb}}$) the rate $\Gamma_{02} = -\pi\mathcal{L}_{02,02}$ approximates $\Gamma^{(+)}_{12}$, whereas for negative detuning ($\Omega > E_{\mathrm{qb}}$) this is done by $\Gamma_{01} = -\pi\mathcal{L}_{01,01}$. In the FSA Γ_{02} and Γ_{01} correspond to the frequencies ω_{20} and ω_{10}, respectively. In the PSA the frequency $\omega^{(+)}_{12} \equiv \mathrm{Im}\{\lambda^{(+)}_{01,02}\}$ is given by $\omega^{(+)}_{12} = \omega_{20}$ for $\Omega < E_{\mathrm{qb}}$ and $\omega^{(+)}_{12} = \omega_{10}$ for $\Omega > E_{\mathrm{qb}}$. Hence, for positive detuning oscillations with frequency ω_{20} will dominate the dynamics, while those with ω_{10} will almost vanish. For negative detuning it is the other way round. In Eqs. (4.34) and (4.35) this behavior is reflected by the coefficients $c^{(+/-)}_{nm,jk}$ and $v^{(+/-)}_{nm,jk}$. Around resonance ($\Omega \approx E_{\mathrm{qb}}$) the dephasing rates and frequencies are a mixture of Γ_{01} and Γ_{02} or ω_{10} and ω_{20}, respectively. From the left graph in Fig. 4.2 one notices further that the FSA rate Γ_{02} grows monotonically with Ω for negative detuning. However, as the weight of the corresponding frequency ω_{20} will be almost zero, Γ_{02} will give no relevant contribution to $P_{\mathrm{dephas.}}(t)$ in this regime but the dephasing will rather be associated to the FSA rate Γ_{01}. Hence, out of resonance the FSA will still fairly well describe the dynamics of $P(t)$. Comparing the expressions for $\mathcal{L}_{01,01}$ and $\mathcal{L}_{02,02}$ given in Appendix C.2 by Eqs. (C.1) and (C.2) with the approximative expressions for the relaxation rate at negative and positive detuning Eq. (4.24), we see that for zero bias ($\varepsilon = 0$) the PSA dephasing rate is equal to $\Gamma_{\mathrm{r}}/2$. For a biased system an additional term is added depending on the spectral density of the bath at $\omega = 0$. In Fig. 4.3 we compare the three analytical solutions described above to the numerical solution of the master equation for the case of an unbiased TLS being at resonance with the oscillator. Concerning both the dynamics of $P(t)$ and its Fourier spectrum we see a good agreement between the different solutions. The one being closest to the numerical solution is the PSA solution. We also want to mention that going to stronger damping κ, the FSA results start to show deviations from the numerical solution. Here, one should use the PSA only. However, for the parameter regime used in the following, we will mainly apply Eq. (4.27) due to its simple, analytical form.

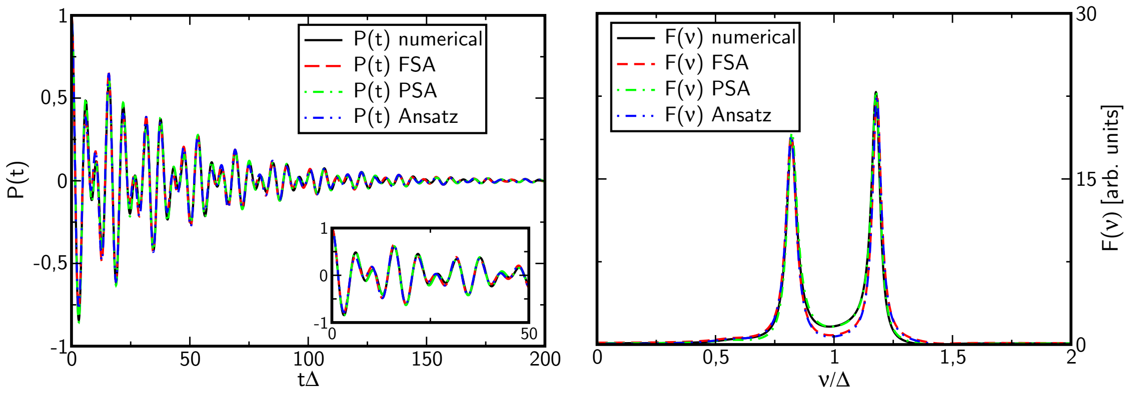

Figure 4.3: Comparison between the behavior of $P(t)$ and its Fourier transform $F(\nu)$ as obtained from the numerically exact solution (black solid curve) of the Eq. (4.7) and the three analytical approximations discussed in the text. The red dashed curve is the full secular approximation (FSA) solution, the green dotted-dashed curve the partial secular approximation (PSA) solution and the blue double-dotted-dashed curve the analytical expressions Eqs (4.27) and (4.29). The parameters are $\varepsilon = 0$, $\Omega = \Delta$, $g = 0.18\Delta$, $\kappa = 0.0154$ and $\beta = 10(\hbar\Delta)^{-1}$. For the chosen regime of parameters differences between numerical and analytical results are barely visible.

4.3 Discussion of the results

Having solved the master equation (4.7) analytically and numerically we can examine the dynamics of the system and its Fourier transform for different situations. First, we will look at a qubit operated at the degeneracy point ($\varepsilon = 0$) being in and out of resonance with the oscillator. Then, we will concentrate on the biased qubit in the same regime of parameters.

4.3.1 The unbiased qubit

For unbiased qubits we can compare our predictions with the analytical results obtained in [65] by starting from a spin-boson model with the effective spectral density Eq. (4.6). In [65] a so-called weak damping approximation (WDA) based on the non-interacting blip approximation (NIBA) is applied. The WDA allows for a nonperturbative treatment of the coupling between the TLS and oscillator and hence can reproduce the occurrence of two dominating frequencies as expected, e.g., from exact QUAPI calculations [86]. The NIBA, and hence the WDA, however, become not reliable for a biased TLS. We find that the overall agreement between our approach and the WDA is very good. However, in the WDA solution the frequencies are slightly shifted compared to the ones obtained from our master equation. This may result from the perturbative expansion we have performed with respect to g by applying the Van Vleck perturbation theory.
First, we look at the resonant case shown in Fig. 4.4. In agreement with previous works [65, 86], we find that the dynamics is dominated by two frequencies corresponding to ω_{10} and ω_{20} with separation being approximately $2g$. The weight of the latter is a bit larger. The reason for the bigger weight is that at resonance ($\Omega = \Delta$) the qubit-oscillator eigenstate $|j\rangle$ is not a symmetric superposition of the states $|j, \mathrm{e}\rangle$ and $|j+1, \mathrm{g}\rangle$ unlike it is predicted by the Janyes-Cummings model, see Sec. 2.1. We notice that the two unequal peaks have indeed been experimentally observed in [31] (see Fig. 4b therein). Considering the states $|1\rangle_{\mathrm{eff}}$ and $|2\rangle_{\mathrm{eff}}$ in Eqs. (2.16a) and (2.16b), one already sees that for a symmetric superposition of

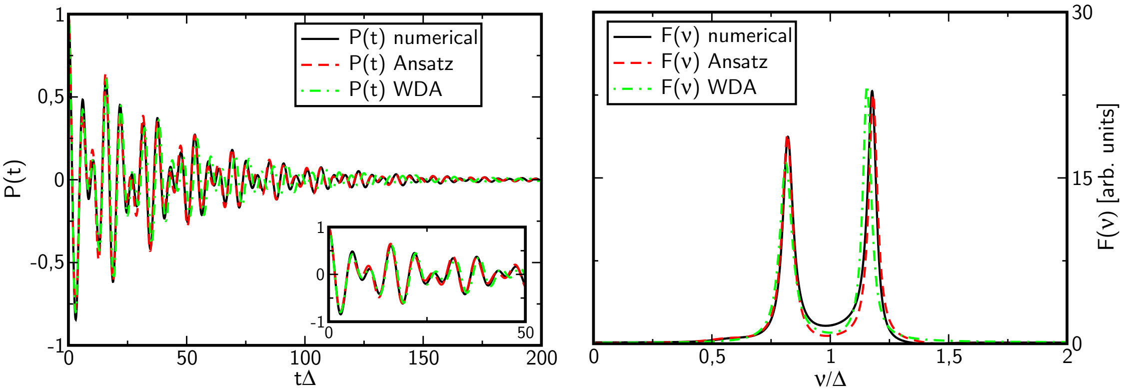

Figure 4.4: Dynamics of the population difference $P(t)$ (left-hand side) and its Fourier transform $F(\nu)$ (right-hand side) for an unbiased TLS being in resonance with the oscillator ($\Omega = \Delta$). The numerical solution of the master equation (black solid line) is compared with the analytical expressions (4.27) and (4.29) (red dashed line) and the weak damping approximation (WDA) from [65] (green dotted-dashed line). The parameters are $\varepsilon = 0$, $\Omega = \Delta$, $g = 0.18\Delta$, $\kappa = 0.0154$ and $\beta = 10(\hbar\Delta)^{-1}$. From the Fourier transform one sees that two frequencies are dominating the dynamics. The separation of those two peaks is approximately $2g$. The nondissipative dynamics is shown for comparison in Fig. 2.6.

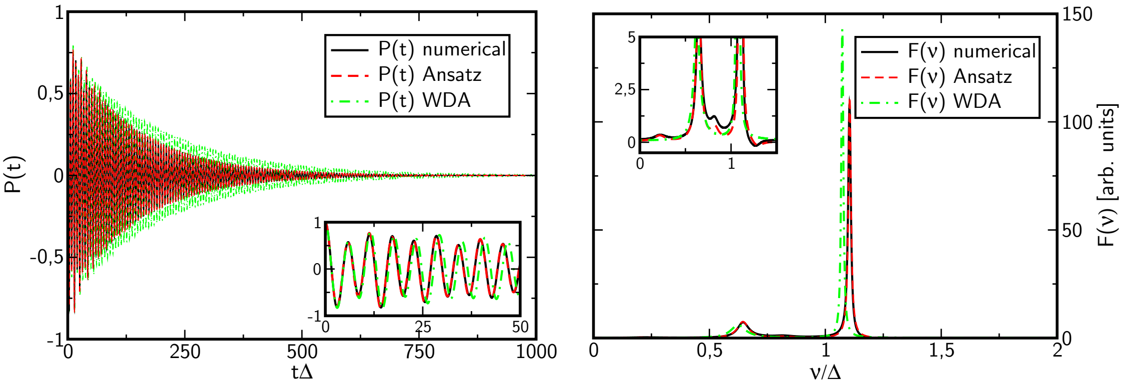

Figure 4.5: Dynamics of $P(t)$ and its Fourier transform $F(\nu)$ for positive detuning ($\Omega < \Delta$) and for $\varepsilon = 0$. Same parameters as in Fig. 4.4 are used except that now $\Omega = 0.75\Delta$. The frequency ω_{20} dominates the dynamics. The inset on the right graph shows a zoom into the Fourier transform. The numerical solution and the analytical expression Eq. (4.29) exhibit besides the main peaks at ω_{10} and ω_{20} two additional peaks, corresponding to the frequencies ω_{24} (between the two main peaks) and ω_{23} (on the left of the first main peak). The two dips come from ω_{13} and ω_{14}.

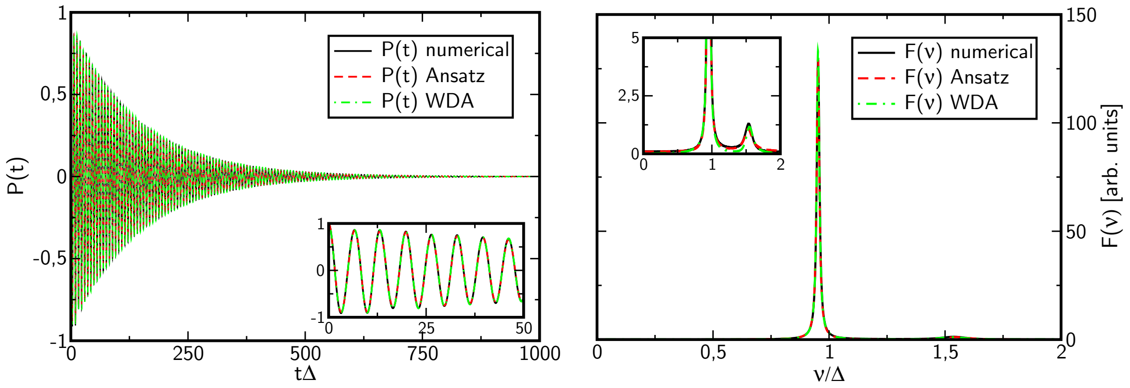

Figure 4.6: Dynamics of $P(t)$ and its Fourier transform $F(\nu)$ for negative detuning ($\Omega > \Delta$), for $\varepsilon = 0$ and $\Omega = 1.5\Delta$. The peak at ω_{10} dominates. No additional peaks are found. A very good agreement between all approaches discussed in the text is found. Remaining parameters are as in Fig. 4.4.

these states we need that δ_0 vanishes or that $\Omega = [(E_{\mathrm{qb}}^4 + 2g^2\Delta^2)/E_{\mathrm{qb}}^2]^{\frac{1}{2}}$ [cf. Eq. (2.20)]. Besides, in order to get the qubit-oscillator eigenstates one still has to perform the Van Vleck transformation, which adds contributions to $|1\rangle$ and $|2\rangle$ from states corresponding to oscillator levels higher than $j = 1$. Thus, our system behaves for $\Omega = \Delta$ as if being positively detuned, which means that the peak belonging to the higher frequency dominates, as we will show below. Slightly increasing Ω will give a stronger weight to the peak at ω_{10}. This effect is not very pronounced for the nondissipative dynamics of the unbiased qubit (Fig. 2.6), because there the two frequencies are still almost equally weighted. Looking, however, at the Fourier transform of the dissipative dynamics, Eq. (4.29), one notices that the dephasing rates also contribute to the weight of the peaks with a prefactor Γ_{nm}^{-1}. As for a positive detuned system Γ_{01} is slightly bigger than Γ_{02}, the difference between the two peaks becomes more clear in the dissipative case. For $\varepsilon \neq 0$ the effect can already be noticed in the nondissipative case.

Next, we consider in Fig. 4.5 the case of positive detuning, where $\Omega < \Delta$. No matter which approach one is looking at, clearly the frequency ω_{20} is dominating. Furthermore, paying attention to the timescale of the dynamics, one notices that the relaxation time is *enhanced* compared to the one we found for the resonant system. This behavior was already explained by the formula (4.23) for the relaxation rate. Again, the numerical and the solution obtained by using the long-time ansatz in Sec. 4.2.2 agree quite well with each other, whereas the amplitude of the oscillation with frequency ω_{20} is stronger in the WDA approach. Also remarkable is the fact that looking at the Fourier transform in Fig. 4.5 one sees in the inset already small contributions of the higher oscillator levels. The transitions corresponding to ω_{24} and ω_{23} give raise to small additional peaks, while the contributions of ω_{13} and ω_{14} are negatively weighted and cause dips. The WDA approach does not show this additional contributions. They are, however, confirmed by the numerical QUAPI calculations in [86] (see figure 2 therein). In the case of negative detuning ($\Omega > \Delta$) shown in Fig. 4.6 we find a quite good agreement between all three approaches. Also for negative detuning the relaxation time is enhanced compared to the resonant case. Contrary to the positively detuned situation the additional peaks have vanished. Besides, now the frequency ω_{10} is dominating the dynamics. This behavior, namely that for positive detuning ω_{20} and for

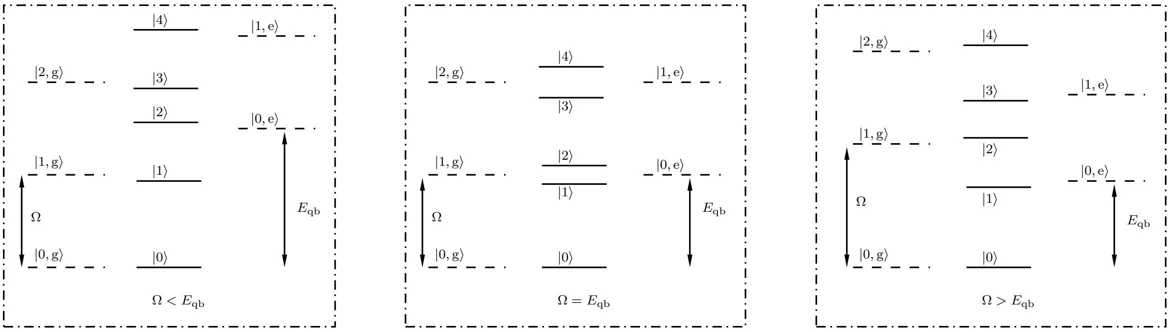

Figure 4.7: Schematic energy spectrum for three different situations. From left to right: positive detuning ($\Omega < E_{\mathrm{qb}}$), resonant case ($\Omega = E_{\mathrm{qb}}$) and negative detuning ($\Omega > E_{\mathrm{qb}}$). The dashed lines show the energy levels for the uncoupled qubit-oscillator system ($g = 0$). The solid lines depict the eigenstates obtained by Van Vleck perturbation theory in g.

negative detuning ω_{10} is dominating, was already found in [86].

We will briefly show how this observation can be explained. For this we look at Fig. 4.7. For a detuned system ($\Omega \neq E_{\mathrm{qb}}$) the qubit-oscillator eigenstates are not symmetric superpositions of the states $|j,\mathrm{g}\rangle$ and $|j,\mathrm{e}\rangle$. They rather asymptotically approach the eigenstates of the uncoupled qubit-oscillator Hamiltonian. In Fig. 2.2 we see that for a positively detuned system (line a) the qubit-oscillator eigenstate $|2j+1\rangle$ approaches the state $|(j+1),\mathrm{g}\rangle$, whereas the main contribution to the state $|2j+2\rangle$ will come from the state $|j,\mathrm{e}\rangle$. From the left diagram in Fig. 4.7 we see that the state $|2\rangle$ is energetically higher than the state $|1\rangle$. However, due to the Boltzmann distributed occupation of the oscillator, the state $|0,\mathrm{e}\rangle$ will be more populated than the state $|1,\mathrm{g}\rangle$ and consequently also $|2\rangle$ will exhibit a larger population than $|1\rangle$, as the latter only feels a small contribution from the state $|0,\mathrm{e}\rangle$. Thus, transitions from $|2\rangle$ to the groundstate are more likely to occur than those from $|1\rangle$ to the groundstate. This explains the dominance of ω_{20} in Fig. 4.5 and Fig. 4.9. In this case the frequency $\omega_{20} \approx E_{\mathrm{qb}}$ and $\omega_{10} \approx \Omega$. Minor peaks from transitions to the levels lying in between can be also seen.

For negative detuning (line c in Fig. 2.2) $|2j+1\rangle$ approaches $|j,\mathrm{e}\rangle$, while $|2j+2\rangle$ is close to $|(j+1),\mathrm{g}\rangle$. From the right graph in Fig. 4.7 we see that the state $|1\rangle$, being lowest in energy apart from the groundstate, is now also more probable to be occupied than $|2\rangle$. Therefore, as confirmed by Fig. 4.6 and Fig. 4.10, the frequency ω_{10} is dominating whereas ω_{20} is represented only by a small peak in the Fourier spectrum. Furthermore, as there are no additional energy levels between the state $|1\rangle$, which is most probably to be populated, and the ground level, other transitions than those corresponding to ω_{10} or ω_{20} are very unlikely to occur. In Fig. 4.10 the dip corresponding to ω_{21} appears only very faintly.

4.3.2 The biased qubit

We will now examine a qubit being operated at finite bias. We consider the case $\varepsilon > 0$. For negative bias-offset the behavior is analogous. Again three different situations are taken into account: the qubit being in resonance with the oscillator ($E_{\mathrm{qb}} = \Omega$), positive ($\Omega < E_{\mathrm{qb}}$) and negative ($\Omega > E_{\mathrm{qb}}$) detuning.

For the resonant case ($\Omega = E_{\mathrm{qb}}$) depicted in Fig. 4.8 we see a similar behavior as for the

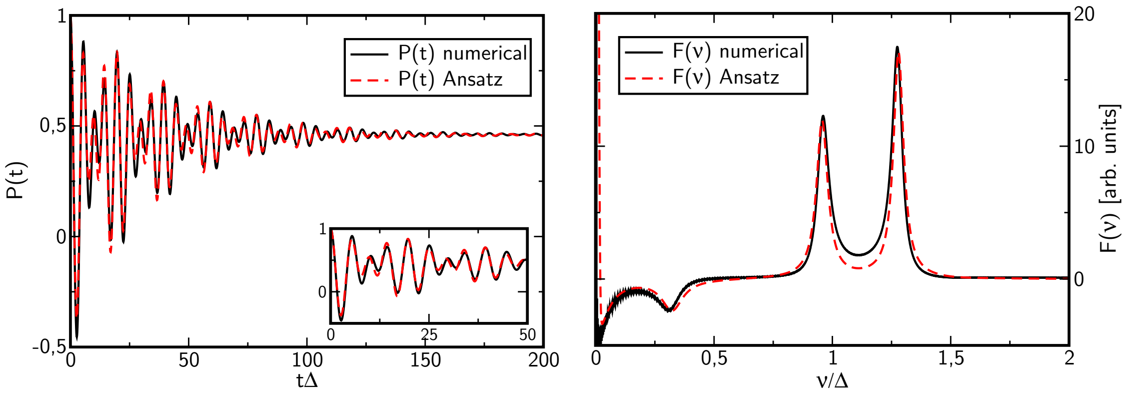

Figure 4.8: Dynamics of $P(t)$ and its Fourier transform $F(\nu)$ for the biased qubit being in resonance with the oscillator. Here, $\varepsilon = 0.5\Delta$ and $\Omega = E_{\mathrm{qb}}$. The remaining parameters are the same as for the unbiased qubit. In the Fourier spectrum the frequencies ω_{10} and ω_{20} dominate. At frequency ω_{21} a small dip can be seen. At $\nu = 0$ the spectrum exhibits a relaxation peak.

unbiased qubit. Again two frequencies, ω_{10} and ω_{20}, are dominating the dynamics. Left to the peak at ω_{10} a small dip can be found in the Fourier spectrum. This corresponds to the transition ω_{21}. For infinite time the dynamics relaxes to an equilibrium value which is nonzero in contrast to the unbiased case. This can be seen in the Fourier spectrum through a relaxation peak at $\nu = 0$. The peak arises because of the term

$$2(p_0 - p_\infty)\frac{\Gamma_{\mathrm{r}}}{\nu^2 + \Gamma_{\mathrm{r}}^2} + 2\pi p_\infty \delta(\nu) \tag{4.40}$$

in Eq. (4.29). The first part of this sum gives rise to the negative shift of this peak. The reason that for the analytical solution the peak is not as strongly shifted as for the numerical one is technical: in order to plot the delta function in Eq. (4.40) we gave it a finite width, which suppresses the negative contribution of the first term in Eq. (4.40). Like for the unbiased qubit the highest energy level playing a role for the dynamics is E_2; i.e., only the ground and first excited level of the oscillator are of importance. In Fig. 4.9 the dynamics and its Fourier transform for a positively detuned qubit-oscillator system with $\varepsilon \neq 0$ are shown. Like for the unbiased case detuning gives raise to longer relaxation times for the qubit. Also in agreement with the unbiased case is the dominance of the frequency ω_{20}. We see that for small t the long-time solution Eq. (4.27) slightly overestimates the maxima of the oscillations and underestimates its minima. Furthermore, we get here the unphysical situation that the maximum of the third oscillation in $P(t)$ exceeds the value of one. The reason for that behavior is that, by construction, we underestimate with Eq. (4.27) the relaxation at short times. For certain parameters the term $(p_0 - p_\infty)$ in Eq. (4.27) becomes negative. In this case the relaxation term yields a contribution to $P(t)$ which increases with time. Thus, a too small relaxation rate Γ_{r} means a too fast approach of the equilibrium value. On a longer timescale both graphs agree quite well. For the case of negative detuning ($\Omega > E_{\mathrm{qb}}$), which is presented in Fig. 4.10, the upward shift of the dynamics obtained from Eqs. (4.27) and (4.29) compared to the numerical graph of $P(t)$ at small times is even stronger. To visualize that it is not a failure of the FSA approach we show in Figures (4.9) and (4.10) additionally the analytical FSA solution of Eqs. (4.12) and (4.13). The latter agrees very well with the numerical solution. At long time scales and for the Fourier

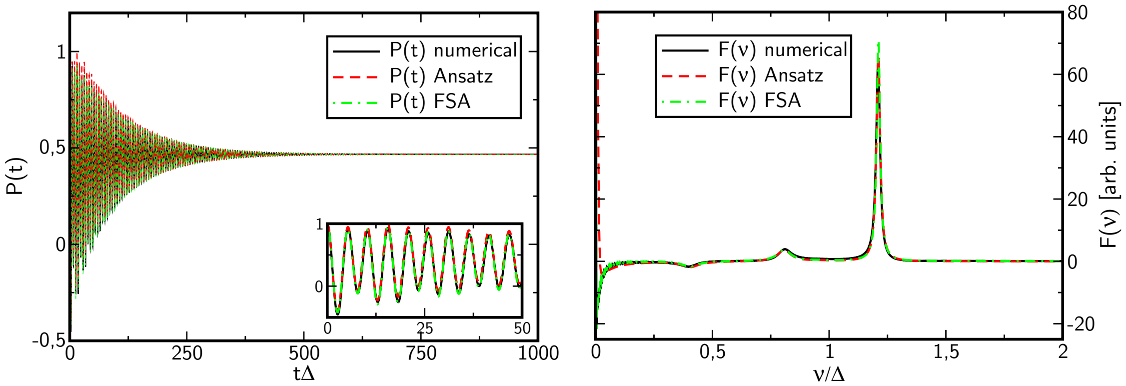

Figure 4.9: Dynamics of $P(t)$ and its Fourier transform $F(\nu)$ for positive detuning ($\Omega < E_{\mathrm{qb}}$) with $\Omega = 0.9\Delta$ and $\varepsilon = 0.5\Delta$. Next to the numerical solution (black solid curve) of the full master equation and the long time ansatz Eqs. (4.27) and (4.29) (red dashed curve), also the FSA solution of Eqs. (4.12) and (4.13) (green dotted-dashed curve) are shown. The dynamics is dominated by ω_{20}. The peak at ω_{10} is much weaker. Like for the resonant, biased qubit a dip is found at ω_{21} and a relaxation peak at $\omega = 0$.

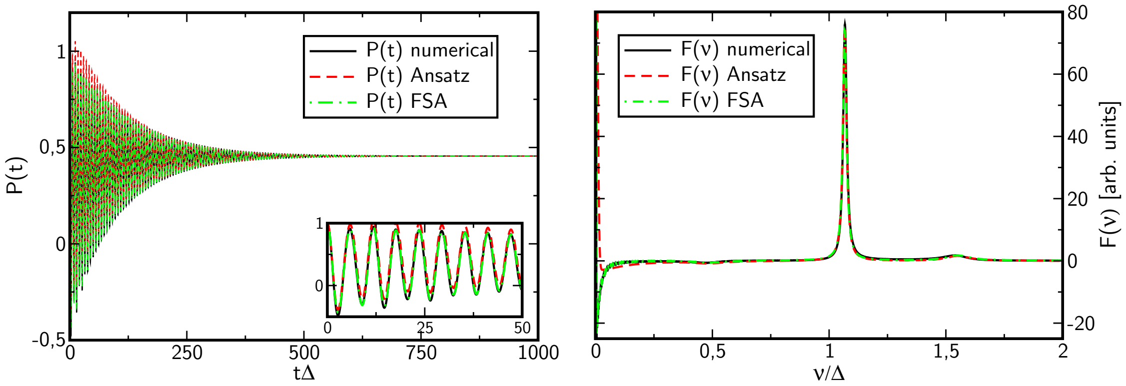

Figure 4.10: Dynamics and Fourier transform for negative detuning ($\Omega > E_{\mathrm{qb}}$) for $\Omega = 1.5\Delta$ and $\varepsilon = 0.5\Delta$. Like in Fig. 4.9 three different approaches are compared. In all three cases the frequency ω_{10} dominates.

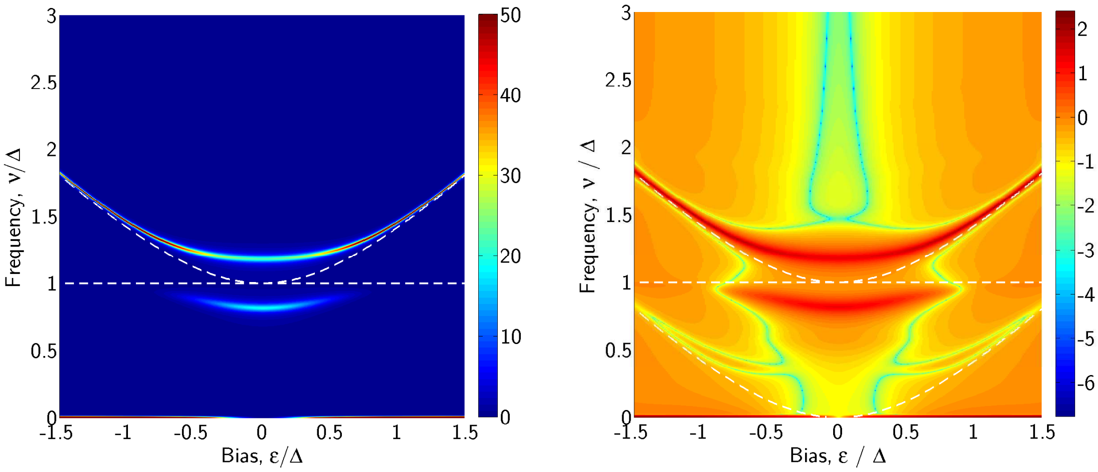

Figure 4.11: Fourier transform of the symmetrized correlation function plotted versus Fourier frequency ν and qubit bias ε. In the left-hand graph $S(\nu)$ is plotted in linear scale, in the right-hand graph $|S(\nu)|$ in logarithmic scale. The parameters are: $\Omega = \Delta$, $g = 0.18\Delta$, $\kappa = 0.0154$ and $\beta = 10(\hbar\Delta)^{-1}$. The white dashed, horizontal line indicates the oscillator frequency $\nu = \Omega$. The other two dashed white lines correspond to $\nu = E_{\mathrm{qb}}$ and $\nu = E_{\mathrm{qb}} - \Omega$.

spectrum all three approaches match with each other very well.
To conclude this paragraph we want to mention that all the results found both for the unbiased and the biased qubit confirm the numerical QUAPI results in [86].

4.3.3 Symmetrized correlation function

So far we have always considered the qubit for certain values of ε and finite or zero detuning. In this section, we fix the oscillator frequency at $\Omega = \Delta$. That means that an unbiased qubit will be at resonance with the oscillator. Changing the bias to positive or negative values will always lead to positive detuning, as $E_{\mathrm{qb}} \geq \Delta$. Figure 4.11 shows a density plot of the Fourier transform of the symmetrized correlation function against the bias of the qubit and the Fourier frequency ν. We consider this correlation function rather than $P(t)$, as it is symmetric in the bias ε. The symmetrized correlation function is defined as follows [1]:

$$S(t) = \frac{1}{2}\langle \sigma_{\mathrm{z}}(t)\sigma_{\mathrm{z}}(0) + \sigma_{\mathrm{z}}(0)\sigma_{\mathrm{z}}(t)\rangle - p_{\infty}^{2}, \tag{4.41}$$

where $\sigma_{\mathrm{z}}(t) = \mathrm{e}^{\mathrm{i}H_{\text{TLS-osc}}t/\hbar}\sigma_{\mathrm{z}}\mathrm{e}^{-\mathrm{i}H_{\text{TLS-osc}}t/\hbar}$. Expressed in terms of the population difference $P(t)$ this becomes,

$$S(t) = P_{\mathrm{s}}(t) + p_{\infty}(P_{\mathrm{a}}(t) - p_{\infty}), \tag{4.42}$$

with $P_{\mathrm{s}}(t)$ and $P_{\mathrm{a}}(t)$ being symmetric and antisymmetric in ε and $P(t) = P_{\mathrm{s}}(t) + P_{\mathrm{a}}(t)$. The Fourier transform of $S(t)$ is defined as

$$S(\nu) = 2\int_0^{\infty} dt \cos(\nu t) S(t). \tag{4.43}$$

Considering now Fig. 4.11 we see that for any bias the spectrum is dominated by two frequencies, namely ω_{10} and ω_{20}. Detuning the system ω_{20} gets more and more important, as we could already observe in the two previous sections for the positively detuned systems. Furthermore, the peaks are shifted to higher frequency values and at $\nu = 0$ the relaxation peak occurs. We want to compare these results to the circuit QED experiment performed by Wallraff et al. [31]. There the qubit is realized by a Cooper-pair box, which is coupled to a superconducting transmission line resonator, see Chapter 1. The properties of the system are determined by probing the resonator spectroscopically. The amplitude of a microwave probe beam transmitted through the resonator is measured versus the probe frequency and the gate charge of the Cooper-pair box (see figure 4 in [31]). Via the gate charge the qubit can be detuned in situ from the degeneracy point. The frequency of the resonator is chosen in such a way that it is in resonance with a qubit being operated at the degeneracy point. For the resonant case two dominating frequencies, being almost equally weighted and symmetrically positioned around the cavity frequency, are observed. Going away from the degeneracy point the system becomes detuned and the frequency of the cavity dominates. The behavior we observe in Fig. 4.11 is similar. However, as we are looking at the dynamics of the qubit, it corresponds to a spectroscopic measurement on the TLS rather than on the oscillator. As explained above the two lowest excited states of the coupled qubit-oscillator system, namely $|1\rangle$ and $|2\rangle$, evolve from an almost symmetric superposition of basis states $\{|j,\mathrm{g}\rangle, |j,\mathrm{e}\rangle\}$ at resonance ($\varepsilon = 0$) to the states $|1,\mathrm{g}\rangle$ and $|0,\mathrm{e}\rangle$ (cf the left graph in Fig. 4.7). For $\varepsilon = 0$ the two peaks of the Rabi splitting are observed. For $\varepsilon \neq 0$, which means positive detuning in this case, the peak with the lower frequency corresponding to ω_{10} approaches more and more the frequency Ω of the oscillator, as the state $|1\rangle$ becomes $|1,\mathrm{g}\rangle$ for large detuning and then $\omega_{10} \approx E_{|1,\mathrm{g}\rangle} - E_{|0,\mathrm{g}\rangle} = \Omega$. Furthermore, the transition peak for ω_{10} gets weaker as also the occupation probability of $|1\rangle$ decreases. At $\varepsilon \approx \pm 0.8\Delta$ the absolute value of the symmetrized correlation function vanishes at ω_{10} and increases again for higher values of $|\varepsilon|$, see right-hand graph in Fig. 4.11. Here, the amplitude p_{10} in $P(t)$ changes its sign. In contrast the peak at ω_{20} becomes stronger with the detuning and approaches more and more the qubit splitting energy $\hbar E_{\mathrm{qb}}$, as $|2\rangle$ approaches $|0,\mathrm{e}\rangle$ and then $\omega_{20} \approx E_{|0,\mathrm{e}\rangle} - E_{|0,\mathrm{g}\rangle} = E_{\mathrm{qb}}$. Additionally, looking at the logarithmic plot one sees around $\nu = 0.4\Delta$ a peak appearing, which corresponds to the frequency ω_{21} and is zero at $\varepsilon = 0$. For large detuning it arises from transitions from $|0,\mathrm{e}\rangle$ to $|1,\mathrm{g}\rangle$ and therefore has the value $\omega_{21} \approx E_{\mathrm{qb}} - \Omega$. The amplitude of this peak is very small compared to the peaks at ω_{10} and ω_{20} and is not resolved in the experiment of Wallraff et al. .

4.4 Comparison with the Jaynes-Cummings model

As we did in Sec. 2.2.2 for the nondissipative dynamics, we want to compare in this section the results we obtained for the dissipative case using Van Vleck perturbation theory in g against the Jaynes-Cummings model (JCM). In both situations we use the eigenstates and eigenvalues, Eqs. (2.15) – (2.18) for Van Vleck perturbation theory in g and Eqs. (2.7) – (2.9) for the JCM, in the Born-Markov master equation (4.7) and solve the resulting system of differential equations numerically. The fixed parameters we use are: $\varepsilon = 0$, $g/\Delta = 0.18$, $\kappa = 0.0154$ and $\hbar\beta\Delta = 10$. The oscillator frequency Ω is varied. For all the three possible cases (negative, positive and zero detuning) one notices from Figures 4.12 – 4.14 that the Jaynes-Cummings approach *underestimates* the dephasing rate Γ_{10} (means a larger peak at frequency ω_{10}) and *overestimates* the rate Γ_{20} (smaller peak at ω_{20}) compared to the approach with the full Hamiltonian $H_{\text{TLS-osc}}$.

The case of negative detuning ($\Omega > \Delta$) is shown in Fig. 4.12. As here the dynamics is

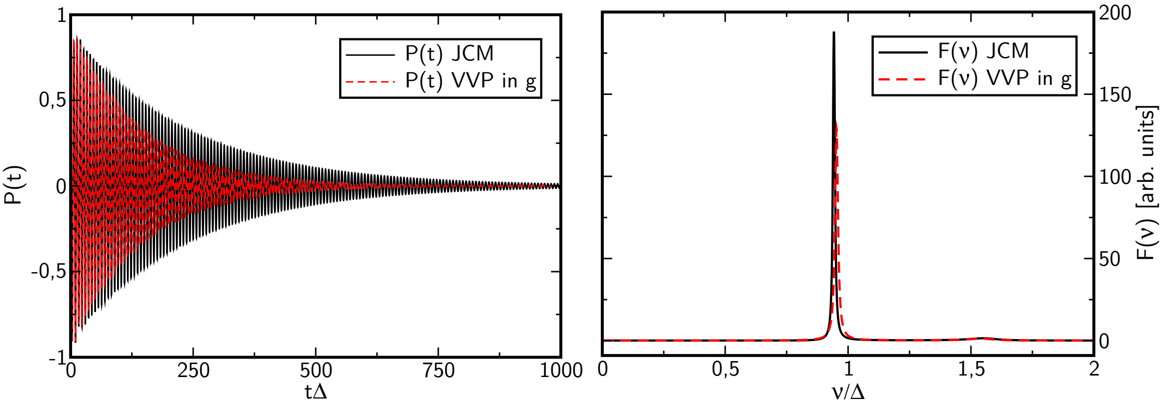

Figure 4.12: Dynamics $P(t)$ of the population difference and its Fourier transform $F(\nu)$ for negative detuning ($\Omega = 1.5\Delta$). The parameters are: $\varepsilon/\Delta = 0$, $g/\Delta = 0.18$, $\kappa = 0.0154$ and $\hbar\Delta\beta = 10$. The red dashed line shows the solution obtained numerically from the master equation using the eigenstates and eigenenergies obtained by VVP in g. The solid line shows the results obtained from the Jaynes-Cummings Hamiltonian.

dominated by the frequency ω_{10}, the equilibrium value is reached on a too long time scale using the Jaynes-Cummings Hamiltonian. On the contrary, for positive detuning ($\Omega < \Delta$), which is shown in Fig. 4.13, and where ω_{20} dominates, the equilibrium value is reached too fast within the JCM. Furthermore, considering the graph of the Fourier transform we find that small contributions which come from higher level transitions, and which have already been discussed in Sec. 4.3.1, are not covered by the JCM. For the resonant case ($\Omega = \Delta$) in Fig. 4.14, we find that the JCM predicts ω_{10} to be slightly dominating whereas if we consider the counter-rotating terms by using the Hamiltonian $H_{\text{TLS-osc}}$, then the frequency ω_{20} dominates. The reason for this discrepancy is that we have for $H_{\text{TLS-osc}}$ no symmetric or antisymmetric superposition of the unperturbed eigenstates at $\Omega = \Delta$ due to the counter-rotating terms in contrast to the JCM.

To conclude this section we can say that for an unbiased qubit-oscillator system the JCM gives a good insight in the qualitative behavior of $P(t)$ both for a slightly detuned and a nondetuned system. However, it under- or overestimates dephasing times for the system. Furthermore, we find taking into account counter-rotating terms in $H_{\text{TLS-osc}}$ that at $\Omega = E_{\text{qb}}$ the dressed eigenstates are not a symmetric or antisymmetric superposition of the uncoupled states. Moreover, the effects of transitions between states of different manifolds are neglected within the JCM.

4.5 Summary

In conclusion, we discussed in this chapter the dissipative dynamics of a qubit coupled through a harmonic oscillator to an environmental bath described by an Ohmic spectral density. In particular, we examined the regime of weak damping and moderate coupling between oscillator and TLS. An equivalent description of our system is provided by the spin-boson model with a structured spectral density. In contrast to many other works on this field, our starting point was not the Jaynes-Cummings Hamiltonian, but the full qubit-oscillator Hamiltonian, Eq. (4.2), where no initial rotating-wave approximation is applied. We provide two different approximations schemes to solve the Born-Markov master equation: The full

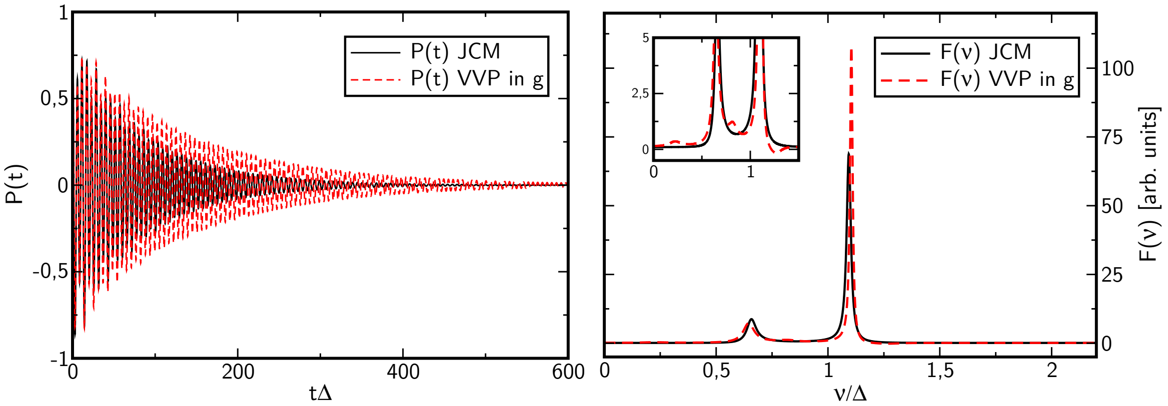

Figure 4.13: Dynamics $P(t)$ of the population difference and its Fourier transform $F(\nu)$ for positive detuning ($\Omega = 0.75\Delta$). The remaining parameters are the same as in Fig. 4.12. The red dashed line shows the solution obtained numerically from the master equation using the eigenstates and eigenenergies obtained by VVP in g. The solid line shows the results obtained from the Jaynes-Cummings Hamiltonian.

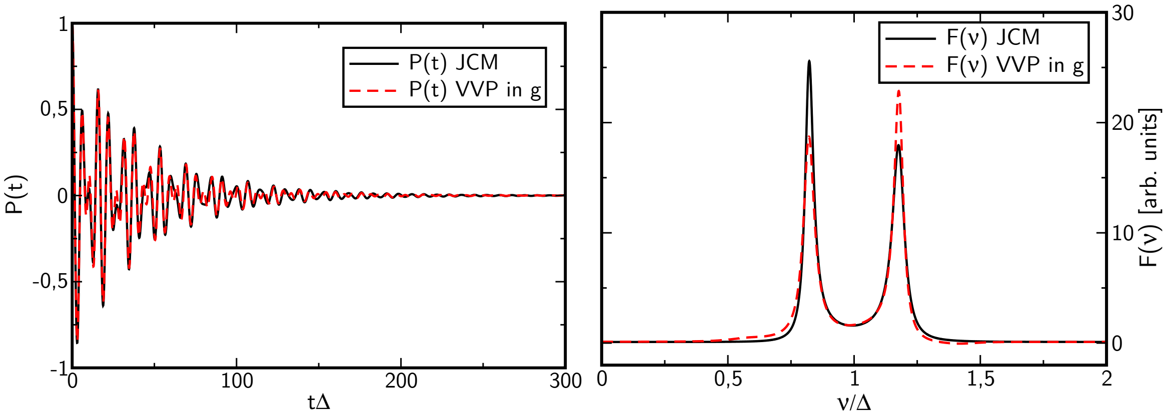

Figure 4.14: Dynamics $P(t)$ of the population difference and its Fourier transform $F(\nu)$ for the resonant case ($\Omega = \Delta$). The remaining parameters are the same as in Fig. 4.12. The red dashed line shows the solution obtained numerically from the master equation using the eigenstates and eigenenergies obtained by VVP in g. The solid line shows the results obtained from the Jaynes-Cummings Hamiltonian.

secular approximation completely decouples the coherences of the qubit-oscillator density matrix from the populations, thus leading to a simple expression for the dephasing part in the qubit's dynamics. Assuming again low temperatures also the relaxation part can be solved analytically. The resulting equations are, however, quite evolved, see Appendix C.3. To simplify these expressions further, we took only the smallest relaxatory contribution into account, yielding the closed analytical formula (4.27). Using as second approach a partial secular approximation we paid attention to the fact that the first two excited energy levels are almost degenerate for the parameters we are interested in, and transitions between them might yield nonnegligible contributions. We tested the different approximations against a numerical solution of the master equation and found a good overall agreement.

We showed that both relaxation and dephasing time are enhanced in the detuned regime. In particular, we found that the rates are not maximal exactly at resonance ($E_{\mathrm{qb}} = \Omega$) as would be expected from a standard weak coupling treatment of the spin-boson model with a structured environment.

The dynamics of both a biased and an unbiased qubit were intensively studied for zero and finite detuning in Sec. 4.3. The results also agree qualitatively with the numerical findings within the ab-initio QUAPI approach [86]. Besides, in Sec. 4.3.1 a good agreement with the results of the weak damping approximation performed in [65] for a symmetric spin-boson model was found. We further could explain the dominance of frequency ω_{20} in the case of positive detuning ($\Omega < E_{\mathrm{qb}}$) and of frequency ω_{10} for negative detuning ($\Omega > E_{\mathrm{qb}}$), respectively. Moreover, we showed that for large positive detuning ω_{20} approaches the energy splitting E_{qb} of the qubit, whereas ω_{10} approximates the oscillator frequency Ω. This behavior agrees nicely with spectroscopic experiments performed on the circuit QED architecture in [31].

In Sec. 4.4 we compared our results for an unbiased system to the ones obtained from the Jaynes-Cummings model. At resonance an initial RWA represents a good approximation and seems to be favorable as it is analytically exactly diagonalizable. For detuned systems, however, we find discrepancies concerning relaxation and dephasing times, and a RWA becomes less appropriate to give precise results. Thus, we think that our approach represents an improvement as it is valid in a wider parameter range avoiding an initial RWA. To our knowledge it provides for the first time analytical results for the dynamics of an unbiased *and* biased qubit coupled to a structured environment being valid simultaneously in the resonant *and* detuned regime. Furthermore, due to the generality of the qubit-oscillator model, we expect our results to be of interest for a wide range of experimental applications.

5

The dissipative, driven two-level system

Parts of this chapter have been published in collaboration with M. Grifoni in [76].

So far we have always considered a TLS coupled to a *quantized* harmonic oscillator, where the latter is occupied by a small number of photons and can also be seen as a weak driving acting on the qubit. Also for strong driving, the applied field can still be described by a quantized oscillator. We saw in Sec. 2.3.1 that for strong coupling the qubit-oscillator system is conveniently treated in the dressed state or displaced oscillator basis, leading to a dressing by Laguerre polynomials of the tunneling matrix, which becomes a Bessel function like dressing for high photon numbers [28, 68, 69, 72]. In this strong driving regime, a series of experiments and theoretical investigations has been performed recently on superconducting qubits examining Rabi oscillations in the multiphoton regime and the validity of the dressed state picture [70, 71, 75, 96–105]. To account for environmental effects, the latter is usually combined with the phenomenological Bloch equations [70, 71, 75, 96].

With the applied field being in a coherent state and for high photon numbers, an equivalent description consists in replacing the quantized oscillator by an external, classical driving [28, 106]. Already in the nondissipative case the driven TLS leads to a variety of phenomena like coherent destruction of tunneling (CDT) [107–109] or driving-induced tunneling oscillations (DITO) [70, 110–112]. Together with the coupling to a bath of harmonic oscillators, we arrive at the driven spin-boson model [1, 74, 112]. It is given by the undriven spin-boson Hamiltonian (4.1) in Chapter 4 simply with an external driving added to the TLS. In this work we will assume a sinusoidal modulation of the static bias, $\varepsilon(t) = \varepsilon + A\cos\omega_{\mathrm{ex}}t$, with A being the amplitude and ω_{ex} the frequency of the external driving. As for the undriven case various techniques have been applied to solve the driven spin-boson model. For example, the NIBA provides good approximate results for intermediate to high bath temperatures and/or strong damping of the system with arbitrary driving frequencies. However, there is the same drawback as already noted for the undriven case, namely that NIBA fails to reproduce the dynamics of a biased TLS correctly at low temperature. In [113–117] the polaron transformation leads to an integro-differential kinetic equation for the populations of the density matrix, which is equivalent to the generalized master equation under the NIBA. An alternative way to gain the dynamics of the driven spin-boson model for weak system-bath coupling and within the Markovian limit is to solve the underlying Bloch-Redfield equations. This is done numerically for weak damping in [111, 118, 119], while [111, 119] additionally provide an analytical examination of the dynamics in the high-frequency regime.

In this chapter we introduce a new approach to solve the dynamics of the monochromatically driven spin-boson model taking into account analytically the fast oscillations induced by the driving as well as the transient dynamics. In a first step, we combine Floquet theory [74, 106, 120] with Van Vleck perturbation theory (VVP) [28, 55] to derive the dynamics of the nondissipative system. This approach has recently been used also in [121] to evaluate the time-averaged transition probability of a nondissipative TLS. Going to second order in the tunneling matrix element, we derive expressions which include the fast oscillatory behavior of the Floquet states and are beyond the common rotating-wave results [99, 122] or perturbation theory in the driving strength [106, 123]. Further, to analyze dissipative effects, we consider the regime of weak damping and solve the corresponding Floquet-Born-Markov master equation applying a moderate rotating-wave approximation. While in [88, 89] a similar approach is used to study the asymptotic dynamics of the driven spin-boson model perturbatively in the driving strength, our approach treats the full time evolution of the system, to all orders in the driving amplitude, in the regime of moderate as well as high external frequencies and for arbitrary static bias. Specifically, we are able to give closed analytic expressions for both the relaxation and dephasing rates.

Our analysis enables us to shed light on the famous effects of CDT [107–109] and DITO [110–112]. Many investigations of those phenomena have been performed in the high-driving regime. This work treats them analytically also for moderate driving frequency and amplitude. We examine both the nondissipative and dissipative cases and compare them to a numerical solution of the problem.

In order to provide a toolbox to deal with periodically driven quantum systems, we will give in Sec. 5.1 a short overview of Floquet theory, the concept of the spatial Hilbert space extended to the time-domain and also introduce the Floquet-Born-Markov master equation. As a start we first examine in Sec. 5.2 the nondissipative, driven TLS by analyzing the quasienergy spectrum and eigenstates of the corresponding Floquet Hamiltonian applying a rotating-wave approximation (RWA) in Sec. 5.2.2. We can give an improved picture of the dynamics by using in Sec. 5.2.3 VVP to second order in the tunneling matrix element, whose validity is throughly tested for an extensive parameter range in Sec. 5.2.4. In Sec. 5.3 the driven spin-boson Hamiltonian is analyzed by solving the Floquet-Born-Markov master equation. We compare the analytical expressions for the relaxation and dephasing rates to the results obtained within the RWA and close the section with a discussion of CDT and DITO.

5.1 Driven quantum systems and Floquet theory

In this section, we will introduce the methods which we use to solve the periodically driven TLS. We mainly follow [106]. To start with, we assume an arbitrary, explicitly time dependent Hamiltonian imposing only the demand that it is periodic in time, namely $H(t+T) = H(t)$, where $T = 2\pi/\omega_{\mathrm{ex}}$, and ω_{ex} is the external driving frequency. We consider the time dependent Schrödinger equation

$$\mathrm{i}\hbar\partial_t|\psi_\beta(t)\rangle = H(t)|\psi_\beta(t)\rangle. \tag{5.1}$$

According to Floquet's theorem it can be solved by

$$|\psi_\beta(t)\rangle = |u_\beta(t)\rangle \mathrm{e}^{-\mathrm{i}\varepsilon_\beta t} \tag{5.2}$$

with the periodic function, $|u_\beta(t+T)\rangle = |u_\beta(t)\rangle$, and the so-called quasienergy[1] $\hbar\varepsilon_\beta$ for certain basis states $\{|\beta\rangle\}$. With $H(t)$ being Hermitian there exists a solution to (5.1) in which $|\psi_\beta(t)\rangle$ is unitary at all times and thus also $\hbar\varepsilon_\beta$ is real. Note that $u_{n,\beta}(t) \equiv \exp(-\mathrm{i}n\omega_{\mathrm{ex}}t)u_\beta(t)$

---

[1] In the literature ε_β is often also called characteristic exponent.

yields a solution of (5.1) identical to (5.2) but with the shifted quasienergy $\hbar\varepsilon_{n,\alpha} \equiv \hbar\varepsilon_\alpha - \hbar n\omega_{\rm ex}$.[2] We expand now the periodic functions in (5.1) in a Fourier series so that the components of $|\psi_\beta(t)\rangle$ read

$$\psi_{\alpha\beta}(t) \equiv \langle\alpha|\psi_\beta(t)\rangle = \sum_n u^{(n)}_{\alpha\beta} {\rm e}^{{\rm i}n\omega_{\rm ex}t} {\rm e}^{-{\rm i}\varepsilon_\beta t} \tag{5.3}$$

and for the Hamiltonian

$$H_{\alpha\beta}(t) = \sum_n H^{(n)}_{\alpha\beta} {\rm e}^{{\rm i}n\omega_{\rm ex}t}. \tag{5.4}$$

Using those two expansions in (5.1) we find

$$\sum_{\gamma,n,k} \left[H^{(n-k)}_{\alpha\gamma} + n\hbar\omega_{\rm ex}\delta_{\alpha,\gamma}\delta_{k,n}\right] {\rm e}^{{\rm i}n\omega_{\rm ex}t} u^{(k)}_{\gamma\beta} = \sum_n {\rm e}^{{\rm i}n\omega_{\rm ex}t} \hbar\varepsilon_\beta u^{(n)}_{\alpha\beta}. \tag{5.5}$$

Thus, for each Fourier coefficient $u^{(n)}_{\alpha\beta}$ there exists an equation

$$\sum_{\gamma,k} \left[H^{(n-k)}_{\alpha\gamma} + n\hbar\omega_{\rm ex}\delta_{\alpha,\gamma}\delta_{k,n}\right] u^{(k)}_{\gamma\beta} = \hbar\varepsilon_\beta u^{(n)}_{\alpha\beta}. \tag{5.6}$$

In order to interpret this equation, we consider $|u_\alpha(t)\rangle$ and its Fourier expansion,

$$|u_\alpha(t)\rangle = \sum_n {\rm e}^{{\rm i}n\omega_{\rm ex}t} |u^{(n)}_\alpha\rangle \tag{5.7}$$

so that $|u_\alpha(t)\rangle$ is automatically separated in a time dependent and time independent part. As basis for the time independent contributions we use the set $\{|\gamma\rangle\}$ representing a possible basis of $H(0)$. In this basis we get

$$|u_\alpha(t)\rangle = \sum_{\gamma,n} \langle\gamma|u^{(n)}_\alpha\rangle|\gamma\rangle {\rm e}^{{\rm i}n\omega_{\rm ex}t}. \tag{5.8}$$

5.1.1 Extended Hilbert space and periodicity relations

Now, we introduce the Hilbert space $\mathcal{T}$ of the T–periodic functions with the inner product defined as

$$(f,g) = \frac{1}{T}\int_0^T dt\, f^*(t)g(t). \tag{5.9}$$

The functions $(t|k) = \exp\{-{\rm i}k\omega_{\rm ex}t\}$ build an orthonormal and complete basis set of $\mathcal{T}$ [124]. Let us now consider the extended Hilbert or Sambe space $\mathcal{T}\otimes\mathcal{H}$ [120], where we define as a basis $|k,\gamma\rangle\rangle \equiv |k)\otimes|\gamma\rangle$ and the scalar product

$$\langle\langle\cdot|\cdot\rangle\rangle = \frac{1}{T}\int_0^T dt\,\langle\cdot|\cdot\rangle. \tag{5.10}$$

In this basis we find

$$\langle\langle k,\gamma|u_\alpha\rangle\rangle = (k|\langle\gamma|\sum_n|-n)|u^{(n)}_\alpha\rangle = \sum_n \delta_{k,-n}\langle\gamma|u^{(n)}_\alpha\rangle = \langle\gamma|u^{(-k)}_\alpha\rangle. \tag{5.11}$$

---

[2] We write the Floquet index $n = 0$ only in cases where it helps for understanding.

Thus, we know how to expand $|u_\alpha\rangle\rangle$ in the Floquet basis $\{|k,\gamma\rangle\rangle\}$:

$$|u_\alpha\rangle\rangle = \sum_{\gamma,k} \langle\gamma|u_\alpha^{(-k)}\rangle |k,\gamma\rangle\rangle. \tag{5.12}$$

The Fourier coefficients with negative index are the expansion coefficients. An equivalent way to derive the relation between the Fourier coefficients and the Floquet states can be achieved by considering the inverse Fourier transform:

$$\langle\gamma|u_\alpha^{(k)}\rangle = \frac{1}{T}\int_0^T dt \mathrm{e}^{-\mathrm{i}k\omega_{\mathrm{ex}}t}\langle\gamma|u_\alpha(t)\rangle = \frac{1}{T}\int_0^T dt \langle\gamma|u_{k,\alpha}(t)\rangle = \langle\langle\gamma|u_{k,\alpha}\rangle\rangle. \tag{5.13}$$

In the last step we used the definition of the internal product of the extended Hilbert space. Comparing Eq. (5.13) to (5.11) we find the relation

$$\langle\langle 0,\gamma|u_{k,\alpha}\rangle\rangle = \langle\langle -k,\gamma|u_{0,\alpha}\rangle\rangle. \tag{5.14}$$

Furthermore using Eq. (5.13) in (5.8) we obtain

$$|u_\alpha(t)\rangle = \sum_{\gamma,k} \mathrm{e}^{\mathrm{i}k\omega_{\mathrm{ex}}t}\langle\langle -k,\gamma|u_{0,\alpha}\rangle\rangle|\gamma\rangle. \tag{5.15}$$

Equation (5.6) therefore can be interpreted as a matrix equation for the Floquet Hamiltonian defined as

$$\mathcal{H} \equiv H(t) - \mathrm{i}\hbar\partial_t. \tag{5.16}$$

On the left-hand side of Eq. (5.6) the component $\langle\langle -k,\gamma|u_\beta\rangle\rangle$ of the vector $|u_\beta\rangle\rangle$ is applied to $\mathcal{H}$ and yields as an outcome the component $\langle\langle -n,\alpha|u_\beta\rangle\rangle$ multiplied with the eigenenergy $\hbar\varepsilon_\beta$. In the Floquet basis the matrix elements are then determined as

$$\langle\langle n,\alpha|\mathcal{H}|k,\gamma\rangle\rangle = H_{\alpha\gamma}^{k-n} - \hbar n\omega_{\mathrm{ex}}\delta_{\gamma,\alpha}\delta_{k,n}. \tag{5.17}$$

In the following we derive a useful periodicity relation among the components of the eigenvectors of $\mathcal{H}$, see [106, Eq. (11)]. We start with the eigenvalue equation for $|u_{m+p,\beta}\rangle\rangle$:

$$\mathcal{H}|u_{m+p,\beta}\rangle\rangle = \hbar(\varepsilon_{m,\beta} - p\omega_{\mathrm{ex}})|u_{m+p,\beta}\rangle\rangle. \tag{5.18}$$

Applying this equation on the state $|n+p,\alpha\rangle\rangle$ and looking to the left-hand side we get

$$\langle\langle n+p,\alpha|\mathcal{H}|u_{m+p,\beta}\rangle\rangle = \sum_{\gamma,j}\langle\langle n+p,\alpha|\mathcal{H}|j,\gamma\rangle\rangle\langle\langle j,\gamma|u_{m+p,\beta}\rangle\rangle. \tag{5.19}$$

With the help of Eq. (5.17) one finds

$$\sum_{\gamma,j}\left[\mathcal{H}_{\alpha\gamma}^{j-n-p} - \hbar(n+p)\omega_{\mathrm{ex}}\delta_{\alpha,\gamma}\delta_{n+p,j}\right]\langle\langle j,\gamma|u_{m+p,\beta}\rangle\rangle = \hbar(\varepsilon_{m,\beta} - p\omega_{\mathrm{ex}})\langle\langle n+p,\alpha|u_{m+p,\beta}\rangle\rangle, \tag{5.20}$$

which leads to

$$\sum_{\gamma,l}\left[\mathcal{H}_{\alpha\gamma}^{l-n} - \hbar n\omega_{\mathrm{ex}}\delta_{\alpha,\gamma}\delta_{n,l}\right]\langle\langle l+p,\gamma|u_{m+p,\beta}\rangle\rangle = \hbar\varepsilon_{m,\beta}\langle\langle n+p,\alpha|u_{m+p,\beta}\rangle\rangle. \tag{5.21}$$

Using again Eq. (5.17)

$$\sum_{\gamma,l} \langle\langle n,\alpha|\mathcal{H}|l,\gamma\rangle\rangle\langle\langle l+p,\gamma|u_{m+p,\beta}\rangle\rangle = \hbar\varepsilon_{m,\beta}\langle\langle n+p,\alpha|u_{m+p,\beta}\rangle\rangle. \tag{5.22}$$

As

$$\sum_{\gamma,l} |l,\gamma\rangle\rangle\langle\langle p+l,\gamma| = \delta_{p,0} \tag{5.23}$$

one arrives at

$$\langle\langle n,\alpha|\mathcal{H}|u_{m,\beta}\rangle\rangle = \hbar\varepsilon_{m,\beta}\langle\langle n+p,\alpha|u_{m+p,\beta}\rangle\rangle \tag{5.24}$$

or finally at

$$\langle\langle n,\alpha|u_{m,\beta}\rangle\rangle = \langle\langle n+p,\alpha|u_{m+p,\beta}\rangle\rangle. \tag{5.25}$$

Thus, it is enough to calculate the quasienergies and corresponding Floquet states in the interval $-\omega_{\mathrm{ex}}/2 < \varepsilon_{n,\alpha} \leq \omega_{\mathrm{ex}}/2$. For example, in order to calculate the vector $|u_\alpha(t)\rangle$ in the basis $\{|\gamma\rangle\}$ the individual components are determined by

$$\langle\gamma|u_\alpha(t)\rangle = \sum_k \langle\langle\gamma|u_{k,\alpha}\rangle\rangle \mathrm{e}^{\mathrm{i}k\omega_{\mathrm{ex}}t} = \sum_k \langle\langle -k,\gamma|u_{0,\alpha}\rangle\rangle \mathrm{e}^{\mathrm{i}k\omega_{\mathrm{ex}}t}, \tag{5.26}$$

so that we need in the end only the Floquet state $|u_{0,\alpha}\rangle\rangle$. This can be used to avoid certain problems occurring with a numerical calculation of the Floquet states: When diagonalizing the Floquet Hamiltonian numerically the eigenvectors obtain an arbitrary phase for different indices k. In case of real eigenvalues this arbitrary phase is either a plus or minus sign. Therefore, we perform the sum in the above Fourier transform over the basis states $|-k,\gamma\rangle\rangle$, for which we can control the phase by definition, rather than over the Floquet states $|u_{k,\alpha}\rangle\rangle$. Furthermore, as the infinite Hilbert space has to be truncated at a certain value $n_{\max}$ for a numerical calculation, the best choice for the Floquet state with fixed value of k is the one corresponding to the quasienergy lying in the "middle" of the Hilbert space, because the results belonging to eigenstates and eigenvalues lying at the edge suffer most from truncation effects.

5.1.2 Time evolution operator in the Floquet picture

The time evolution operator expressed in Floquet eigenstates of $H(t)$ is

$$U(t,t_0) = \sum_\gamma \mathrm{e}^{-\mathrm{i}\varepsilon_\gamma(t-t_0)}|u_\gamma(t)\rangle\langle u_\gamma(t_0)|. \tag{5.27}$$

Its matrix elements read

$$U_{\alpha,\beta}(t,t_0) \equiv \langle\alpha|U(t,t_0)|\beta\rangle = \sum_\gamma u_{\alpha\gamma}(t)u^*_{\beta\gamma}(t_0). \tag{5.28}$$

By using Eq. (5.15) we can express the time evolution operator in the extended Hilbert space and the Floquet states:

$$U_{\alpha,\beta}(t,t_0) = \sum_\gamma \sum_{k,l} \langle\langle -k,\alpha|u_{l,\gamma}\rangle\rangle\langle\langle u_{l,\gamma}|0,\beta\rangle\rangle \mathrm{e}^{-\mathrm{i}\varepsilon_{l,\gamma}(t-t_0)}\mathrm{e}^{\mathrm{i}k\omega_{\mathrm{ex}}t}. \tag{5.29}$$

As the states $\{|u_{l,\gamma}\rangle\rangle\}$ build a complete basis set in the extended Hilbert space and are eigenstates of the Floquet Hamiltonian (5.16) we can write

$$U_{\alpha,\beta}(t,t_0) = \sum_k \mathcal{U}^{(k)}_{\alpha,\beta} \mathrm{e}^{\mathrm{i}k\omega_{\mathrm{ex}}t} = \sum_k \langle\langle -k,\alpha| \exp[-\mathrm{i}\mathcal{H}(t-t_0)] |0,\beta\rangle\rangle \mathrm{e}^{\mathrm{i}k\omega_{\mathrm{ex}}t}. \tag{5.30}$$

This matrix element can be interpreted in the following ways:

1. $U_{\alpha,\beta}(t,t_0)$ gives the amplitude that a system which is at time t_0 in the state $|\beta\rangle$ evolves to the state $|\alpha\rangle$ at time t according to the *time dependent* Hamiltonian $H(t)$.
2. $\mathcal{U}^{(k)}_{\alpha,\beta}$ gives the amplitude that a system which is initially in the Floquet state $|0,\beta\rangle\rangle$ evolves to the Floquet state $|-k,\alpha\rangle\rangle$ according to the "*time independent*" Hamiltonian $\mathcal{H}$. Each of these amplitudes is weighted by a factor $\mathrm{e}^{\mathrm{i}k\omega_{\mathrm{ex}}t}$ and summing over all k gives the time dependent amplitude.

Thus, we expressed the evolution of a time dependent problem through a time independent one.

5.1.3 Floquet master equation

In order to take environmental influences into account, we consider in this section the Caldeira-Leggett model as introduced in Sec. 3.5.2 for a time dependent system Hamiltonian $H_{\mathrm{S}}(t)$. We assume further that $H_{\mathrm{S}}(t)$ is periodic in time, $H_{\mathrm{S}}(t+T) = H_{\mathrm{S}}(t)$, so that we can use Floquet theory. We want to calculate the time evolution of the matrix elements of the reduced density operator (3.58) in the basis of the periodic states introduced in Eq. (5.2):

$$\dot\rho_{\alpha\beta}(t) = \frac{\partial}{\partial t}\langle u_\alpha(t)|\rho_{\mathrm{S}}(t)|u_\beta(t)\rangle. \tag{5.31}$$

Using Eqs. (3.58) and (5.16) this can be written as

$$\begin{aligned}\dot\rho_{\alpha\beta}(t) =& -\frac{\mathrm{i}}{\hbar}\langle u_\alpha(t)|\left(\mathrm{i}\hbar\frac{\overleftarrow{\partial}}{\partial t} + H_{\mathrm{S}}(t)\right)\rho_{\mathrm{S}}(t)|u_\beta(t)\rangle + \frac{\mathrm{i}}{\hbar}\langle u_\alpha(t)|\rho_{\mathrm{S}}(t)\left(H_{\mathrm{S}}(t) - \mathrm{i}\hbar\frac{\overrightarrow{\partial}}{\partial t}\right)|u_\beta(t)\rangle \\ &+ \langle u_\alpha(t)|\mathcal{L}_{\mathrm{Diss}}\rho_{\mathrm{S}}(t)|u_\beta(t)\rangle \\ =& -\frac{\mathrm{i}}{\hbar}\langle u_\alpha(t)|\mathcal{H}^\dagger_{\mathrm{S}}(t)\rho_{\mathrm{S}}(t)|u_\beta(t)\rangle + \frac{\mathrm{i}}{\hbar}\langle u_\alpha(t)|\rho_{\mathrm{S}}(t)\mathcal{H}_{\mathrm{S}}(t)|u_\beta(t)\rangle + \langle u_\alpha(t)|\mathcal{L}_{\mathrm{Diss}}\rho_{\mathrm{S}}(t)|u_\beta(t)\rangle \\ =& -\mathrm{i}(\varepsilon_\alpha - \varepsilon_\beta)\rho_{\alpha\beta}(t) + \langle u_\alpha(t)|\mathcal{L}_{\mathrm{Diss}}\rho_{\mathrm{S}}(t)|u_\beta(t)\rangle.\end{aligned} \tag{5.32}$$

Analogous to Sec. 3.5.2, we define the now *time dependent* matrix elements of position and momentum operator as

$$\begin{aligned}Q_{\alpha\beta}(t) &= \int_0^\infty d\tau\,\langle u_\alpha(t)|U^\dagger_{\mathrm{S}}(t-\tau,t)\tilde X U_{\mathrm{S}}(t-\tau,t)|u_\beta(t)\rangle \int_0^\infty d\omega\,G(\omega)\cos(\omega\tau)\coth\left(\frac{\hbar\beta\omega}{2}\right) \\ &= \int_0^\infty d\tau \int_0^\infty d\omega\,G(\omega)\cos(\omega\tau)\coth\left(\frac{\hbar\beta\omega}{2}\right)\mathrm{e}^{-\mathrm{i}(\varepsilon_\alpha-\varepsilon_\beta)\tau}\langle u_\alpha(t-\tau)|\tilde X|u_\beta(t-\tau)\rangle,\end{aligned} \tag{5.33}$$

where we used Eq. (5.27) in the second step. Similarly,

$$
\begin{aligned}
P_{\alpha\beta}(t) =& -\frac{1}{\hbar}\int_0^\infty d\tau\, \langle u_\alpha(t)|U_\mathrm{S}^\dagger(t-\tau,t)\left[\tilde{X}, H_\mathrm{S}(t)\right] U_\mathrm{S}(t-\tau,t)|u_\beta(t)\rangle \\
&\times \int_0^\infty d\omega\, \frac{G(\omega)}{\omega}\cos(\omega\tau) \\
=& -\frac{1}{\hbar}\int_0^\infty d\tau \int_0^\infty d\omega\, \frac{G(\omega)}{\omega}\cos(\omega\tau)\mathrm{e}^{-\mathrm{i}(\varepsilon_\alpha-\varepsilon_\beta)\tau}\langle u_\alpha(t-\tau)|\left[\tilde{X}, H_\mathrm{S}(t)\right]|u_\beta(t-\tau)\rangle \\
=&(\varepsilon_\alpha-\varepsilon_\beta-\mathrm{i}\partial_t)\int_0^\infty d\tau \int_0^\infty d\omega\, \frac{G(\omega)}{\omega}\cos(\omega\tau)\mathrm{e}^{-\mathrm{i}(\varepsilon_\alpha-\varepsilon_\beta)\tau}\tilde{X}_{\alpha\beta}(t-\tau)
\end{aligned} \tag{5.34}
$$

and

$$
\tilde{X}_{\alpha\beta}(t) = \langle u_\alpha(t)|\tilde{X}|u_\beta(t)\rangle. \tag{5.35}
$$

Taking into account the periodicity of $|u_\alpha(t)\rangle$ we perform a Fourier expansion on the position matrix elements:

$$
\tilde{X}_{\alpha\beta}(t) = \sum_n \mathrm{e}^{\mathrm{i}n\omega_\mathrm{ex}t}\tilde{X}_{n,\alpha\beta}. \tag{5.36}
$$

With this Eq. (5.33) becomes

$$
\begin{aligned}
Q_{\alpha\beta}(t) =& \sum_n \mathrm{e}^{\mathrm{i}n\omega_\mathrm{ex}t}\tilde{X}_{n,\alpha\beta}\int_0^\infty d\tau \int_0^\infty d\omega\, G(\omega)\cos(\omega\tau)\coth\left(\frac{\hbar\beta\omega}{2}\right)\mathrm{e}^{-\mathrm{i}(\varepsilon_\alpha-\varepsilon_\beta+n\omega_\mathrm{ex})\tau} \\
=& \sum_n \mathrm{e}^{\mathrm{i}n\omega_\mathrm{ex}t}\tilde{X}_{n,\alpha\beta}\int_0^\infty d\omega\, G(\omega)\coth\left(\frac{\hbar\beta\omega}{2}\right)\frac{1}{2}\Bigg[\pi\delta\left(\omega-\varepsilon_\alpha+\varepsilon_\beta-n\omega_\mathrm{ex}\right) \\
&+\pi\delta\left(-\omega-\varepsilon_\alpha+\varepsilon_\beta-n\omega_\mathrm{ex}\right)+\mathrm{i}\mathcal{P}\left(\frac{1}{\omega-\varepsilon_\alpha+\varepsilon_\beta-n\omega_\mathrm{ex}}\right) \\
&+\mathrm{i}\mathcal{P}\left(\frac{1}{-\omega-\varepsilon_\alpha+\varepsilon_\beta-n\omega_\mathrm{ex}}\right)\Bigg].
\end{aligned} \tag{5.37}
$$

We neglect the contributions coming from the principal value $\mathcal{P}$, which would give again rise to Stark- and Lamb-shifted oscillation frequencies, and thus,

$$
Q_{\alpha\beta}(t) \approx \frac{\pi}{2}\sum_n \mathrm{e}^{\mathrm{i}n\omega_\mathrm{ex}t}G(\varepsilon_\alpha-\varepsilon_\beta+n\omega_\mathrm{ex})\coth\left[\frac{\hbar\beta(\varepsilon_\alpha-\varepsilon_\beta+n\omega_\mathrm{ex})}{2}\right]\tilde{X}_{n,\alpha\beta}. \tag{5.38}
$$

Also Eq. (5.34) is expanded into a Fourier series:

$$
\begin{aligned}
P_{\alpha\beta}(t) =& \sum_n \tilde{X}_{n,\alpha\beta}(\varepsilon_\alpha-\varepsilon_\beta+n\omega_\mathrm{ex})\mathrm{e}^{\mathrm{i}n\omega_\mathrm{ex}t}\int_0^\infty d\tau \int_0^\infty d\omega\, \frac{G(\omega)}{\omega}\cos(\omega\tau)\mathrm{e}^{-\mathrm{i}(\varepsilon_\alpha-\varepsilon_\beta+\omega_\mathrm{ex})\tau} \\
=& \sum_n \tilde{X}_{n,\alpha\beta}(\varepsilon_\alpha-\varepsilon_\beta+n\omega_\mathrm{ex})\mathrm{e}^{\mathrm{i}n\omega_\mathrm{ex}t}\int_0^\infty d\omega\, \frac{G(\omega)}{\omega}\frac{1}{2}\Bigg[\pi\delta\left(\omega-\varepsilon_\alpha+\varepsilon_\beta-n\omega_\mathrm{ex}\right) \\
&+\pi\delta\left(-\omega-\varepsilon_\alpha+\varepsilon_\beta-n\omega_\mathrm{ex}\right)+\mathrm{i}\mathcal{P}\left(\frac{1}{\omega-\varepsilon_\alpha+\varepsilon_\beta-n\omega_\mathrm{ex}}\right) \\
&+\mathrm{i}\mathcal{P}\left(\frac{1}{-\omega-\varepsilon_\alpha+\varepsilon_\beta-n\omega_\mathrm{ex}}\right)\Bigg].
\end{aligned} \tag{5.39}
$$

Neglecting again the principal value, we arrive at

$$P_{\alpha\beta}(t) \approx \frac{\pi}{2} \sum_n \mathrm{e}^{\mathrm{i}n\omega_{\mathrm{ex}}t} G(\varepsilon_\alpha - \varepsilon_\beta + n\omega_{\mathrm{ex}}) \tilde{X}_{n,\alpha\beta}. \tag{5.40}$$

Combining those results in Eq. (3.60), we find after some calculation

$$\begin{aligned} \langle u_\alpha(t)|\mathcal{L}_{\mathrm{Diss}}\rho_{\mathrm{S}}(t)|u_\beta(t)\rangle = \pi \sum_{\alpha',\beta'} \sum_{n,n'} \mathrm{e}^{\mathrm{i}(n+n')\omega_{\mathrm{ex}}t} \Big\{ & \left(N_{n,\alpha\alpha'} + N_{-n',\beta\beta'}\right) \tilde{X}_{n,\alpha\alpha'} \tilde{X}_{n',\beta'\beta} \\ - \delta_{\beta\beta'} \sum_{\beta''} \tilde{X}_{n',\alpha\beta''} N_{n,\beta''\alpha'} \tilde{X}_{n,\beta''\alpha'} - \delta_{\alpha\alpha'} \sum_{\alpha''} & N_{-n,\alpha''\beta'} \tilde{X}_{n,\beta'\alpha''} \tilde{X}_{n',\alpha''\beta} \Big\} \rho_{\alpha'\beta'}(t) \\ \equiv \pi \mathcal{L}_{\alpha\beta,\alpha'\beta'}(t)\rho_{\alpha'\beta'}(t) & \end{aligned} \tag{5.41}$$

with $N_{n,\alpha\beta} = N(\varepsilon_\alpha - \varepsilon_\beta + n\omega_{\mathrm{ex}})$, $N(\omega) = G(\omega)n_{\mathrm{th}}(\omega)$ and $n_{\mathrm{th}}(\omega) = \frac{1}{2}[\coth(\hbar\beta\omega/2) - 1]$. Finally, the master equation for the reduced density matrix becomes

$$\dot{\rho}_{\alpha\beta}(t) = -\mathrm{i}(\varepsilon_\alpha - \varepsilon_\beta)\rho_{\alpha\beta}(t) + \pi \sum_{\alpha'\beta'} \mathcal{L}_{\alpha\beta,\alpha'\beta'}(t)\rho_{\alpha'\beta'}(t). \tag{5.42}$$

This is the *Floquet-Born-Markov master equation* [125].

5.2 The nondissipative, driven two-level system

We consider now a specific example of a periodically driven quantum system. Again we investigate the two-level Hamiltonian introduced in Section 1.1, but now drive its longitudinal component, so that the Hamiltonian reads

$$H_{\mathrm{TLS}}(t) = -\frac{\hbar}{2}\left[\Delta\sigma_x + (\varepsilon + A\cos\omega_{\mathrm{ex}}t)\sigma_z\right]. \tag{5.43}$$

The coupling Δ between the two localized basis states $|\uparrow\rangle$ and $|\downarrow\rangle$ remains time independent, whereas the bias point consists of the static dc-component ε and a sinusoidal modulation of amplitude A and frequency ω_{ex}. Furthermore, for now we neglect environmental influences.

5.2.1 Floquet Hamiltonian

To resolve the dynamics of the driven system we consider the Floquet Hamiltonian $\mathcal{H}_{\mathrm{TLS}}(t) = H_{\mathrm{TLS}}(t) - \mathrm{i}\hbar\partial_t$, which has for $\Delta = 0$ the following set of eigenstates:

$$|u^0_{n,\uparrow/\downarrow}(t)\rangle = |\uparrow/\downarrow\rangle \exp\left[\pm\mathrm{i}\frac{A}{2\omega_{\mathrm{ex}}}\sin\omega_{\mathrm{ex}}t - \mathrm{i}n\omega_{\mathrm{ex}}t\right] = |\uparrow/\downarrow\rangle \sum_k \mathrm{e}^{\pm\mathrm{i}k\omega_{\mathrm{ex}}t} J_k\left(\frac{A}{2\omega_{\mathrm{ex}}}\right)\mathrm{e}^{-\mathrm{i}n\omega_{\mathrm{ex}}t} \tag{5.44}$$

with quasienergies $\hbar E^0_{n,\uparrow/\downarrow} = \mp\frac{\hbar}{2}\varepsilon - \hbar n\omega_{\mathrm{ex}}$. Here, $J_k(x)$ is the kth-order Bessel function. In the composite Hilbert space $\mathcal{T}\otimes\mathcal{H}$ [120] those states become

$$|u^0_{n,\uparrow/\downarrow}\rangle\rangle = |\uparrow/\downarrow\rangle \sum_l J_{\pm(n-l)}\left(\frac{A}{2\omega_{\mathrm{ex}}}\right)|l). \tag{5.45}$$

For the case of a finite tunneling matrix element Δ, the Floquet Hamiltonian $\mathcal{H}_{\text{TLS}}$ is nondiagonal in the above basis (5.45) and becomes in matrix representation

$$\hbar \left(\begin{array}{c|cccccc|c} \ddots & |u^0_{n,\uparrow}\rangle\rangle & |u^0_{n,\downarrow}\rangle\rangle & |u^0_{n+1,\uparrow}\rangle\rangle & |u^0_{n+1,\downarrow}\rangle\rangle & |u^0_{n+2,\uparrow}\rangle\rangle & |u^0_{n+2,\downarrow}\rangle\rangle & \\ \hline |u^0_{n,\uparrow}\rangle\rangle & E^0_{n,\uparrow} & -\frac{1}{2}\Delta_0 & 0 & -\frac{1}{2}\Delta_{-1} & 0 & -\frac{1}{2}\Delta_{-2} & \\ |u^0_{n,\downarrow}\rangle\rangle & -\frac{1}{2}\Delta_0 & E^0_{n,\downarrow} & -\frac{1}{2}\Delta_1 & 0 & -\frac{1}{2}\Delta_2 & 0 & \\ |u^0_{n+1,\uparrow}\rangle\rangle & 0 & -\frac{1}{2}\Delta_1 & E^0_{n+1,\uparrow} & -\frac{1}{2}\Delta_0 & 0 & -\frac{1}{2}\Delta_{-1} & \\ |u^0_{n+1,\downarrow}\rangle\rangle & -\frac{1}{2}\Delta_{-1} & 0 & -\frac{1}{2}\Delta_0 & E^0_{n+1,\downarrow} & -\frac{1}{2}\Delta_1 & 0 & \\ |u^0_{n+2,\uparrow}\rangle\rangle & 0 & -\frac{1}{2}\Delta_2 & 0 & -\frac{1}{2}\Delta_1 & E^0_{n+2,\uparrow} & -\frac{1}{2}\Delta_0 & \\ |u^0_{n+2,\downarrow}\rangle\rangle & -\frac{1}{2}\Delta_{-2} & 0 & -\frac{1}{2}\Delta_{-1} & 0 & -\frac{1}{2}\Delta_0 & E^0_{n+2,\downarrow} & \\ \hline & & & & & & & \ddots \end{array} \right) . \tag{5.46}$$

We defined

$$\Delta_{n-l} \equiv \Delta \langle\langle u^0_{n,\uparrow} | \sigma_x | u^0_{l,\downarrow} \rangle\rangle = J_{n-l}\left(\frac{A}{\omega_{\text{ex}}} \right) \Delta, \tag{5.47}$$

where we used the relation [126]

$$J_n(u \pm v) = \sum_{k=-\infty}^{\infty} J_{n \mp k}(u) J_k(v). \tag{5.48}$$

To find the dynamics of the system, we have to diagonalize the Floquet matrix. At this point, it is worth noticing that the dressed tunneling matrix elements introduced here, can be directly related to the ones we obtained in Sec. 2.3.1, Eq. (2.33), as the dressing by Laguerre polynomials becomes in the high photon limit of the quantized oscillator the Bessel function dressing we find here. Although working in the extended Hilbert space, the Floquet Hamiltonian exhibits a similar structure than the qubit-oscillator Hamiltonian $H_{\text{TLS-osc}}$ expressed in the basis of displaced oscillator states. Therefore in order to diagonalize the Hamiltonian, we can use similar approximation schemes as discussed in Sec. 2.3.1. A rotating-wave approximation scheme, which corresponds to the adiabatic approximation in Sec. 2.3.1, is applied in Sec. 5.2.2, while in Sec. 5.2.3 VVP in Δ is used. We also show that the RWA results can be obtained with VVP to lowest order in Δ.

5.2.2 Rotating-wave approximation

Let us look at the spectrum of the unperturbed problem ($\Delta = 0$). We notice that whenever the static bias fulfills the condition $\varepsilon = m\omega_{\text{ex}}$, the states $|u^0_{n,\uparrow}\rangle\rangle$ and $|u^0_{n+m,\downarrow}\rangle\rangle$ are degenerate, as then

$$E^0_{n+m,\downarrow} - E^0_{n,\uparrow} = \varepsilon - m\omega_{\text{ex}} = 0. \tag{5.49}$$

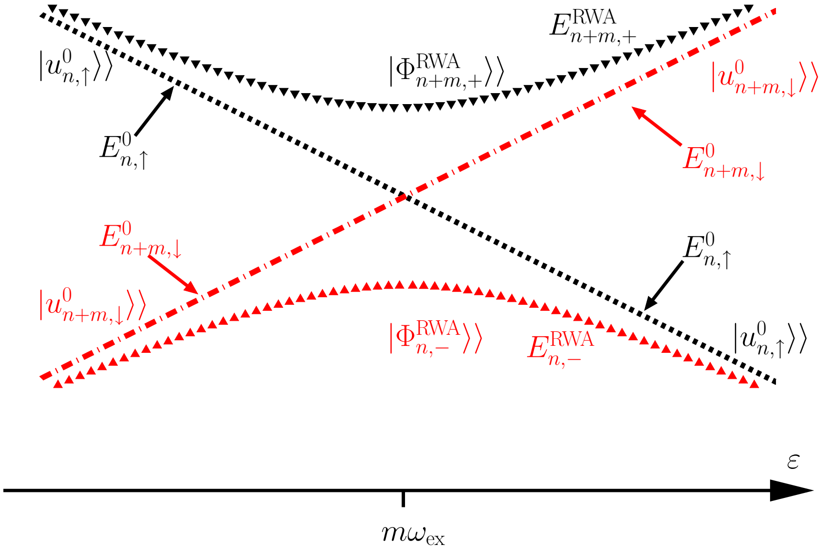

Figure 5.1: Quasienergies $\hbar E^{\mathrm{RWA}}_{n,-}$ and $\hbar E^{\mathrm{RWA}}_{n+m,+}$ (triangles) and unperturbed quasienergies $\hbar E^0_{n,\uparrow}$ and $\hbar E^0_{n+m,\downarrow}$ (dashed line and dotted-dashed line) for an m-photon resonance. The unperturbed quasienergies show an exact crossing at $\varepsilon = m\omega_{\mathrm{ex}}$ according to Eq. (5.49). The corresponding eigenstates are $|u^0_{n,\uparrow}\rangle\rangle$ and $|u^0_{n+m,\downarrow}\rangle\rangle$. For finite Δ an avoided crossing can be observed. The energy $\hbar E^{\mathrm{RWA}}_{n,-}$ and the corresponding eigenstate $|\Phi^{\mathrm{RWA}}_{n,-}\rangle\rangle$ are represented by red upward triangles, whereas $\hbar E^{\mathrm{RWA}}_{n+m,+}$ and $|\Phi^{\mathrm{RWA}}_{n+m,+}\rangle\rangle$ are shown by black downward triangles. For $\varepsilon > m\omega_{\mathrm{ex}}$ we find that $|\Phi^{\mathrm{RWA}}_{n,-}\rangle\rangle$ approaches $|u^0_{n,\uparrow}\rangle\rangle$, while $|\Phi^{\mathrm{RWA}}_{n+m,+}\rangle\rangle$ becomes $|u^0_{n+m,\downarrow}\rangle\rangle$ and vice versa for $\varepsilon < m\omega_{\mathrm{ex}}$. The labeling of the perturbed eigenstates and eigenenergies is chosen in a way that $E^{\mathrm{RWA}}_{n+m,+} \geq E^{\mathrm{RWA}}_{n,-}$ for all ε.

In this case, we speak of an m-photon resonance. As long as Δ is only a small perturbation, $\omega_{\mathrm{ex}} \gg \Delta$, then $\mathcal{H}_{\mathrm{TLS}}$ will exhibit a similar energy spectrum. The main corrections to the unperturbed Hamiltonian come from matrix elements connecting the (almost) degenerate levels. Thus, as a first approximation, we diagonalize an effective Hamiltonian, which consists of 2×2 blocks of the kind

$$\begin{pmatrix} \hbar E^0_{n,\uparrow} & -\frac{\hbar}{2}\Delta_{-m} \\ -\frac{\hbar}{2}\Delta_{-m} & \hbar E^0_{n+m,\downarrow} \end{pmatrix}, \tag{5.50}$$

and describes the energy states being connected by an m-photon resonance.
This result is also obtained within the RWA scheme as introduced in [99, 122]. In those works, the *time dependent* system Hamiltonian (5.43) is transformed to a rotating frame, and only terms fulfilling the resonance condition (5.49) are kept, while the fast-rotating components are neglected. This RWA is equivalent to the adiabatic approximation introduced in Sec. 2.3.1. The latter is *nonperturbative* in the qubit-oscillator coupling g and therefore has to be contrasted to the RWA used to derive the Jaynes-Cummings model in Sec. 2.1. In the case of a classical driving, the "Jaynes-Cummings RWA" translates to a so-called *Rabi rotating-wave approximation,* which is perturbative in the driving amplitude A, see, e.g., [28, 123], and becomes exact for circularly polarized radiation. In contrast, the RWA we are using here treats the driving amplitude nonperturbatively. Concerning the eigenenergies of the Floquet Hamiltonian for finite Δ, we notice that the exact crossing of the unperturbed energies ($\Delta = 0$) at $\varepsilon = m\omega_{\mathrm{ex}}$ becomes an avoided crossing (see Fig. 5.1), and the perturbed eigenstates are a mixture of the unperturbed ones. Those with higher eigenenergies are

labeled $|\Phi^{\mathrm{RWA}}_{n+m,+}\rangle\rangle$; those with lower energies $|\Phi^{\mathrm{RWA}}_{n,-}\rangle\rangle$.[3] They are defined below. In the far off-resonant case, $|\Phi^{\mathrm{RWA}}_{n+m,+}\rangle\rangle$ corresponds for $\varepsilon > m\omega_{\mathrm{ex}}$ to the unperturbed state $|u^0_{n+m,\downarrow}\rangle\rangle$, and $|\Phi^{\mathrm{RWA}}_{n,-}\rangle\rangle$ to $|u^0_{n,\uparrow}\rangle\rangle$. For $\varepsilon < m\omega_{\mathrm{ex}}$, the state $|\Phi^{\mathrm{RWA}}_{n+m,+}\rangle\rangle$ corresponds to $|u^0_{n,\uparrow}\rangle\rangle$, and $|\Phi^{\mathrm{RWA}}_{n,-}\rangle\rangle$ to $|u^0_{n+m,\downarrow}\rangle\rangle$. The eigenenergies are

$$\hbar E^{\mathrm{RWA}}_{n,-} = \hbar[(-n-\frac{1}{2}m)\omega_{\mathrm{ex}}-\frac{1}{2}\Omega^{\mathrm{RWA}}_m] \quad \text{and} \quad \hbar E^{\mathrm{RWA}}_{n+m,+} = \hbar[(-n-\frac{1}{2}m)\omega_{\mathrm{ex}}+\frac{1}{2}\Omega^{\mathrm{RWA}}_m] \tag{5.51}$$

with the dressed oscillation frequency

$$\Omega^{\mathrm{RWA}}_m \equiv \sqrt{(-\varepsilon+m\omega_{\mathrm{ex}})^2+\Delta^2_m}. \tag{5.52}$$

The corresponding eigenstates are

$$|\Phi^{\mathrm{RWA}}_{n,-}\rangle\rangle = -\sin\frac{\Theta^{\mathrm{RWA}}_m}{2}|u^0_{n,\uparrow}\rangle\rangle - \operatorname{sign}(\Delta_{-m})\cos\frac{\Theta^{\mathrm{RWA}}_m}{2}|u^0_{n+m,\downarrow}\rangle\rangle, \tag{5.53}$$

$$|\Phi^{\mathrm{RWA}}_{n+m,+}\rangle\rangle = \cos\frac{\Theta^{\mathrm{RWA}}_m}{2}|u^0_{n,\uparrow}\rangle\rangle - \operatorname{sign}(\Delta_{-m})\sin\frac{\Theta^{\mathrm{RWA}}_m}{2}|u^0_{n+m,\downarrow}\rangle\rangle, \tag{5.54}$$

with the RWA mixing angle defined by

$$\tan\Theta^{\mathrm{RWA}}_m = \frac{|\Delta_{-m}|}{-\varepsilon+m\omega_{\mathrm{ex}}} \quad \text{for} \quad 0 < \Theta^{\mathrm{RWA}}_m \leq \pi. \tag{5.55}$$

Now we are able to recover the time dependent dynamics of the system (see Appendix B.2). As an example, we give the probability for the TLS starting in the localized state $|\downarrow\rangle$ and returning to it:

$$P^{\mathrm{RWA}}_{\downarrow\to\downarrow}(t) = \cos^2\left(\Omega^{\mathrm{RWA}}_m\frac{t}{2}\right) + \cos^2\Theta^{\mathrm{RWA}}_m\sin^2\left(\Omega^{\mathrm{RWA}}_m\frac{t}{2}\right). \tag{5.56}$$

For the special case of vanishing static bias ($\varepsilon = 0$) and 0-photon resonance,

$$P^{\mathrm{RWA}}_{\downarrow\to\downarrow}(t) = \cos^2\left(|J_0(A/\omega_{\mathrm{ex}})\Delta|\frac{t}{2}\right), \tag{5.57}$$

which agrees with the high-frequency result, $\omega_{\mathrm{ex}} \gg \Delta$, of earlier works [74, 106, 112].

5.2.3 Van Vleck perturbation theory in Δ

As pointed out already in [99, 121], the RWA fails in explaining higher-order effects in Δ such as a shift in the oscillation frequency. Furthermore, we will show that the couplings between the nondegenerate states in (5.46) are needed to get physically correct expressions for the relaxation and dephasing rates. We proceed in the following like in Sec. 2.3.1, where we diagonalized the qubit coupled to a quantized oscillator using Van Vleck perturbation theory (VVP) in Δ. That means we calculate now for the classical oscillator the effective Floquet Hamiltonian, given by $\mathcal{H}_{\mathrm{eff}} = \exp(\mathrm{i}S)\mathcal{H}_{\mathrm{TLS}}\exp(-\mathrm{i}S)$. The transformation matrix S is again determined to second order in Δ and is given in Appendix A.2.2. Like in Sec. 2.3.1

---

[3] The motivation to choose the indices n and $n+m$ of the perturbed eigenstates in this way is that they agree with the ones of the unperturbed states for $\varepsilon > m\omega_{\mathrm{ex}}$. This labeling is arbitrary as long as one stays consistent throughout the calculation.

the effective Hamiltonian for an m-photon resonance again consists of 2×2 blocks of the shape

$$\hbar \begin{pmatrix} E^0_{n,\uparrow} - \frac{1}{4}\sum_{l\neq -m} \frac{\Delta_l^2}{\varepsilon + l\omega_{\rm ex}} & -\frac{1}{2}\Delta_{-m} \\ -\frac{1}{2}\Delta_{-m} & E^0_{n+m,\downarrow} + \frac{1}{4}\sum_{l\neq -m} \frac{\Delta_l^2}{\varepsilon + l\omega_{\rm ex}} \end{pmatrix}. \tag{5.58}$$

The analogy to the qubit-(quantized) oscillator case is obvious when comparing to the effective Hamiltonian (2.34). There we just have to make a few replacements in order to arrive at the effective Floquet Hamiltonian (5.58): First, we replace l by $-m$ and set further $j = n + m$. Instead of a tunneling element dressed by Laguerre polynomials, Eq. (2.33), we have to use the Bessel-function-like dressing of Eq. (5.47): $\Delta_j^{j'} \rightarrow \Delta_{j'-j}$. Further we need to keep in mind that we deal with quasienergies: the Floquet indices n can also become negative, while the oscillator quantum number j is restricted to $j \geq 0$. This yields an infinite sum in the second-order corrections in Eq. (5.58), which will lead to certain cancellations in the following calculations. Diagonalizing the effective Hamiltonian, we get the quasienergies

$$\hbar E_{n,-} = \hbar[(-n - \frac{1}{2}m)\omega_{\rm ex} - \frac{1}{2}\Omega_m^{(2)}], \tag{5.59}$$

$$\hbar E_{n+m,+} = \hbar[(-n - \frac{1}{2}m)\omega_{\rm ex} + \frac{1}{2}\Omega_m^{(2)}], \tag{5.60}$$

with the second-order dressed oscillation frequency[4]

$$\Omega_m^{(2)} = \sqrt{\left(-\varepsilon + m\omega_{\rm ex} - \frac{1}{2}\sum_{l\neq -m} \frac{\Delta_l^2}{\varepsilon + l\omega_{\rm ex}}\right)^2 + \Delta_{-m}^2}. \tag{5.61}$$

This corresponds to formulas (2.37) and (2.38) in Sec. 2.3.1. Compared to the frequency obtained within the RWA, Eq. (5.52), this new frequency is shifted due to the second-order elements in (5.58), and the condition for an m-photon resonance reads now

$$\varepsilon = m\omega_{\rm ex} - \frac{1}{2}\sum_{l\neq -m} \frac{\Delta_l^2}{\varepsilon + l\omega_{\rm ex}}. \tag{5.62}$$

In Fig. 5.2, we compare Eqs. (5.59) and (5.60) for the quasienergies against the eigenenergies we find from a numerical diagonalization of the Floquet matrix (5.46). Whenever the resonance condition, Eq. (5.62), is fulfilled, we notice avoided crossings whose gap distance is determined by Δ_m for an m-photon resonance. The eigenstates $|\Phi^{\rm eff}_{n,\pm}\rangle\rangle$ of the effective Hamiltonian are the same as in (5.53) and (5.54), with the mixing angle $\Theta_m^{\rm RWA}$ replaced by

$$\Theta_m = \arctan\left(\frac{|\Delta_{-m}|}{-\varepsilon + m\omega_{\rm ex} - \frac{1}{2}\sum_{l\neq -m} \frac{\Delta_l^2}{\varepsilon + l\omega_{\rm ex}}}\right). \tag{5.63}$$

To get the eigenstates of $\mathcal{H}_{\rm TLS}$, we calculate $|\Phi_{n,\pm}\rangle\rangle = \exp(-{\rm i}S)|\Phi^{\rm eff}_{n,\pm}\rangle\rangle$ and, following Appendix B.2, we determine the survival probability $P_{\downarrow\rightarrow\downarrow}(t)$. In Fig. 5.3, we visualize the results for the survival probability close to a 2-photon resonance obtained from the RWA

---

[4] We perform the calculation of the effective Hamiltonian (5.58) and the corresponding transformation matrix only to second order in Δ, whereas for the frequency [Eq. (5.61)], the mixing angle [Eq. (5.63)], and the calculation of the survival probability, we retain also higher orders.

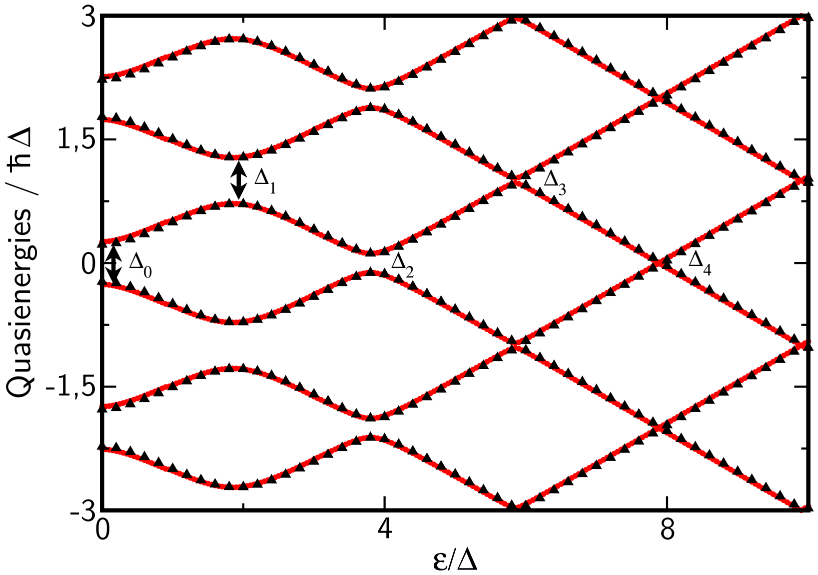

Figure 5.2: Quasienergies against static bias ε. The upward triangles result from numerical diagonalization of the Floquet matrix (5.46), while the solid lines correspond to the analytical formulas (5.59) and (5.60). Parameters are $\omega_{\mathrm{ex}}/\Delta = 2.0$, $A/\Delta = 3.0$. At an m-photon resonance, we find avoided crossings with a gap distance of Δ_m.

approach and first- and second-order Van Vleck perturbation theory. We notice that by applying the RWA the fast oscillations in the first-order Van Vleck result are averaged out. When we compare first- and second-order predictions, the shift of the oscillation frequency is striking. But also the amplitude of the oscillations changes, which is due to the corrected mixing angle, Eq. (5.63). Inserting the second-order mixing angle and frequency into the RWA formula (5.56) results in averaging over the fast oscillations of the second-order Van Vleck graph. To cover also the fast driving-induced oscillations, it is essential to use the eigenstates $|\Phi_{n,\pm}\rangle\rangle$ instead of the effective ones, which leads to a more complicated formula for $P_{\downarrow\to\downarrow}(t)$, see Appendix B.2.

5.2.4 Validity of the Van Vleck approach

We close this section with an overview of the parameter regime in which our approach is valid. To apply Van Vleck perturbation theory at all, a requirement for the Floquet Hamiltonian is that it has for finite Δ a similar doublet structure as in the unperturbed case ($\Delta = 0$). This means that the off-diagonal elements in (5.46) connecting different doublets with each other must be much smaller than the distance between those doublets [28]:

$$|\langle\langle u^0_{n,\uparrow}|\Delta\sigma_x|u^0_{l+m+n,\downarrow}\rangle\rangle| \ll |E^0_{n,\uparrow} - E^0_{l+m+n,\downarrow}| \tag{5.64}$$

for any $l \neq 0$. Using Eqs. (5.47) and (5.49), this becomes

$$|\Delta_{-l-m}| \ll |\varepsilon - (l+m)\omega_{\mathrm{ex}}|. \tag{5.65}$$

Because $|\Delta_{-l-m}| \leq \Delta$, this condition can be even fulfilled for frequencies $\omega_{\mathrm{ex}} < \Delta$. Once Eq. (5.65) is satisfied, we still have to check at which order one can stop the perturbative expansion in Δ. We will distinguish now between two situations: the case of being close to or at an m-photon resonance and the regime far from resonance.

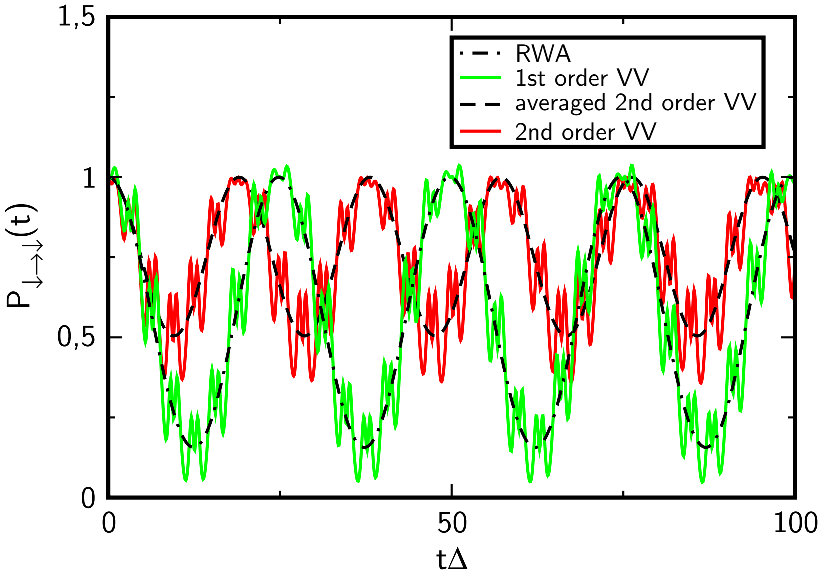

Figure 5.3: Survival probability $P_{\downarrow\to\downarrow}(t)$ close to a 2-photon resonance. The parameters are $\varepsilon/\Delta = 4.1$, $\omega_{\mathrm{ex}}/\Delta = 2.0$, $A/\Delta = 3.0$. We compare results obtained from a RWA and the first- and second-order VVP. Furthermore, we show the averaged second-order Van Vleck dynamics, which correspond to Eq. (5.56) with the Van Vleck frequency [Eq. (5.61)] and second-order mixing angle [Eq. (5.63)].

Dynamics close to or at resonance

Using $\varepsilon \sim m\omega_{\mathrm{ex}}$, Eq. (5.65) becomes simply

$$\omega_{\mathrm{ex}} \gg \frac{|\Delta_{-l-m}|}{|l|}. \tag{5.66}$$

Note that the right-hand side of (5.66) still depends on A/ω_{ex}. Thus, while being surely fulfilled in the RWA case, $\omega_{\mathrm{ex}} \gg \Delta$, condition (5.66) is in general less restrictive. To show this, we examine the following two limiting cases. First, the limit $A/\omega_{\mathrm{ex}} \ll 1$ is considered. For arguments with $0 < x \ll \sqrt{n+1}$, the nth-order Bessel function becomes approximately [77]

$$|J_n(x)| \approx \frac{x^{|n|}}{2^{|n|}|n|!}. \tag{5.67}$$

Thus, for $A/\omega_{\mathrm{ex}} \ll 1$, we find that

$$|\Delta_n| \approx \frac{(A/\omega_{\mathrm{ex}})^{|n|}}{2^{|n|}|n|!}\Delta \tag{5.68}$$

and (5.66) becomes

$$\omega_{\mathrm{ex}} \gg \Delta \frac{(A/\omega_{\mathrm{ex}})^{|-l-m|}}{2^{|-l-m|}|l||-l-m|!}. \tag{5.69}$$

Because $A/\omega_{\mathrm{ex}} \ll 1$, Eq. (5.69) is fulfilled for any $l \neq 0$ if it is satisfied for $l = -m$; i.e., if

$$\omega_{\mathrm{ex}} \gg \frac{\Delta}{|m|}. \tag{5.70}$$

In the case of a 1-photon resonance, this leaves us with the RWA condition, $\omega_{\text{ex}} \gg \Delta$, as then nearest-neighbor doublets are connected by a Δ_0 element in the Floquet matrix which approaches Δ for small A/ω_{ex}. All other perturbative off-diagonal entries in (5.46) are vanishingly small. In the case of an m-photon resonance with $m \neq \pm 1$, the dressed element Δ_0 connects more distant doublets, so that the Van Vleck condition (5.66) can be realized according to (5.70) for frequencies smaller than the ones demanded by the RWA. In the opposite limit of $A/\omega_{\text{ex}} \gg 1$, an upper bound for the dressed Bessel function is [77]

$$|\Delta_n| \leq \Delta\sqrt{\omega_{\text{ex}}/A}. \tag{5.71}$$

Using this, we find that (5.66) is verified if

$$\omega_{\text{ex}} \gg \frac{\Delta^2}{A}. \tag{5.72}$$

Since $A \gg \omega_{\text{ex}}$, it follows that $\Delta^2 \ll A\omega_{\text{ex}} < A^2$ and thus $A \gg \Delta$. Hence, Eq. (5.72) represents an improvement to the RWA condition.

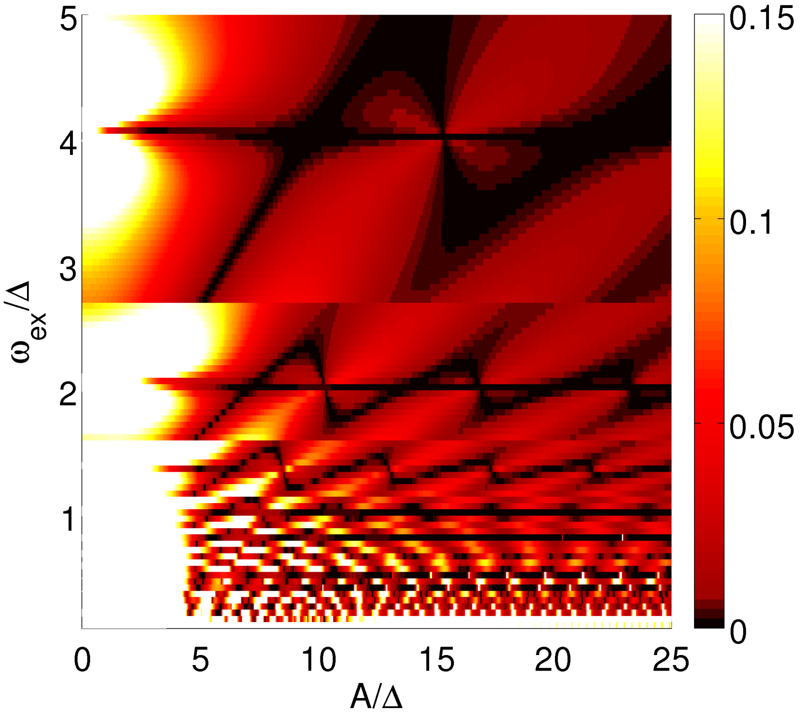

Figure 5.4: Comparison of the main oscillation frequency Ω_m^{RWA} obtained by the RWA and second-order Van Vleck frequency $\Omega_m^{(2)}$ for a fixed static bias, $\varepsilon = 4.0\Delta$. The relative mistake performing the RWA is shown against the driving frequency $\omega_{\text{ex}}/\Delta$ and driving amplitude A/Δ. The darkest areas show regions in parameter space of small or no deviations between the two approaches, whereas the lightest areas show a deviation of 15 % or more.

Further, being close to an m-photon resonance, one single frequency will dominate the system's behavior, and thus neglecting the remaining fast-oscillating terms will already give a good picture of the coarse-grained dynamics. This dominating frequency is represented by Ω_m^{RWA} and by $\Omega_m^{(2)}$ in the case of the RWA and the second-order VVP, respectively. To obtain those frequencies, it is enough to diagonalize the corresponding effective Hamiltonian, without yet considering any modification of the eigenstates of the effective Hamiltonian. As shown in the previous subsection, Ω_m^{RWA} corresponds to the main frequency of the system obtained by applying VVP to first order in Δ. Naturally the question arises as to how good these approximations are, or which orders in Δ are necessary depending on the parameter regime.

In a first step, we examine the improvement obtained by using second-order VVP compared to the RWA; that is, we consider

$$\epsilon^{\mathrm{RWA}} = \frac{|\Omega_m^{\mathrm{RWA}} - \Omega_m^{(2)}|}{\Omega_m^{(2)}}, \tag{5.73}$$

and plot it in Fig. 5.4 against the driving frequency ω_{ex} and amplitude A at a fixed value of the static bias ε. The deviations are visualized through different shades of color. The lightest areas stand for a relative mistake of 15 % or more. We can tell from Fig. 5.4 that the RWA fails for low driving frequencies and/or weak driving amplitudes. The darkest areas determine regions in the parameter space where almost no difference between the RWA and second-order VVP can be found. Of course this is no indication that the results are reliable in those areas, but rather that second-order perturbation theory yields no improvement to the RWA.

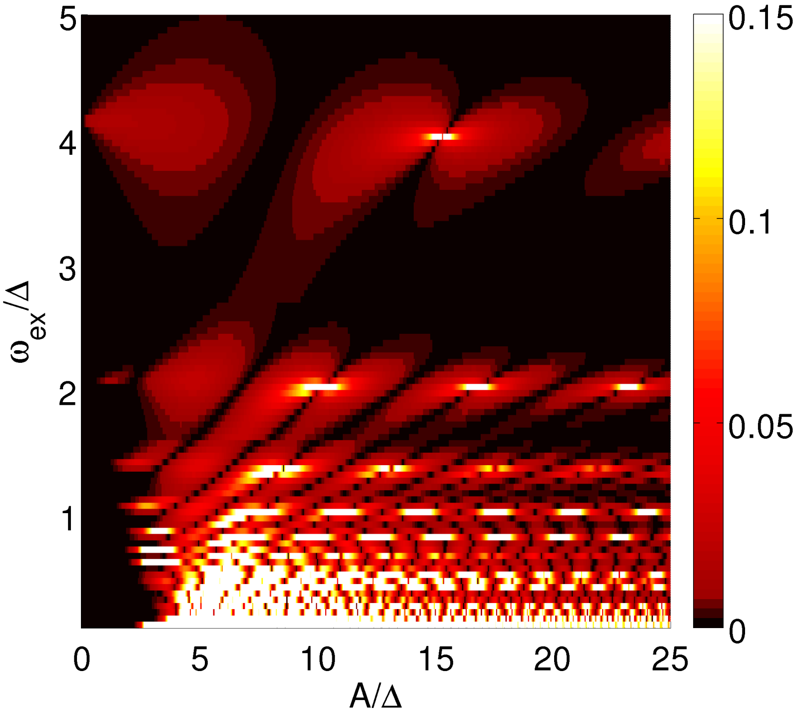

Figure 5.5: Comparison of the main oscillation frequency Ω_m obtained by second-order and third-order VVP for a fixed static bias, $\varepsilon = 4.0\Delta$. The relative mistake performing second-order perturbation theory is shown against the driving frequency $\omega_{\mathrm{ex}}/\Delta$ and driving amplitude A/Δ. Color scale is the same as in Fig. 5.4.

To check the accuracy of the second-order Van Vleck frequency $\Omega_m^{(2)}$, we calculate the deviation

$$\epsilon^{(2)} = \frac{|\Omega_m^{(2)} - \Omega_m^{(3)}|}{\Omega_m^{(3)}} \tag{5.74}$$

from the frequency $\Omega_m^{(3)}$ obtained applying VVP to third order [121]. Results for $\epsilon^{(2)}$ are shown in Fig. 5.5. Again we only consider mistakes up to 15 %. We find strong deviations in the region of low driving frequencies and intermediate driving amplitudes. In the remaining parameter space, the agreement between second- and third-order VVP is quite good apart from small islands. Those islands are located at values of ω_{ex} and A where the second-order condition for coherent destruction of tunneling (CDT) is fulfilled, see discussion in Sec. 5.3.3. For example, for $\varepsilon/\Delta = 4.0$ and $\omega_{\text{ex}}/\Delta = 2.0$, they occur at the zeros of the Bessel function $J_2(A/\omega_{\text{ex}})$. Since at those points the second-order frequency $\Omega_m^{(2)}$ vanishes, even small third-order contributions yield a significant correction. This behavior visualizes nicely the findings of Barata et al. [127] and Frasca [128], who proved analytically that Ω_m does not completely vanish at the zeros of the Bessel function if third-order contributions in Δ are taken into account. On the contrary, both the RWA and second-order VVP predict a vanishing frequency at those points and therefore agree perfectly with each other in Fig. 5.4. We want to emphasize again that, as can be seen from Fig. 5.5, our approach also yields good results for low driving frequencies, $\omega_{\text{ex}} < \Delta$, and small driving amplitudes, $A \sim \Delta$.
In Fig. 5.6, we show the survival probability $P_{\downarrow\to\downarrow}(t)$ and its Fourier transform

$$F(\nu) := \int_{-\infty}^{\infty} dt\, P_{\downarrow\to\downarrow}(t) \mathrm{e}^{\mathrm{i}\nu t} \tag{5.75}$$

at resonance $\varepsilon = \omega_{\text{ex}}$ but for a driving amplitude with $|J_1(A/\omega_{\text{ex}})| \neq 0$. One clearly sees that one frequency, namely, Ω_1, is dominating, and already the RWA conveys a good impression of the dynamics.

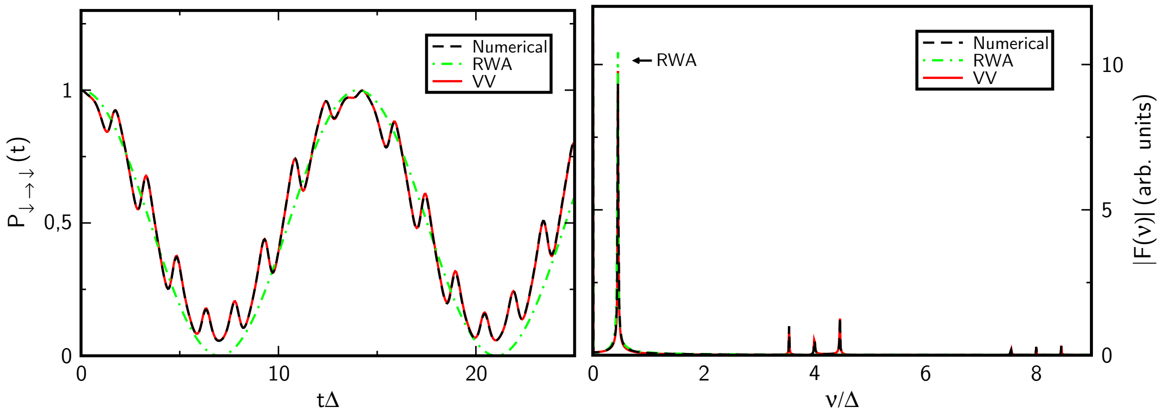

Figure 5.6: Survival probability $P_{\downarrow\to\downarrow}(t)$ and the absolute value of its Fourier transform $F(\nu)$ for $\varepsilon/\Delta = 4.0$, $\omega_{\text{ex}}/\Delta = 4.0$, and $A/\Delta = 4.1$. The oscillation frequency corresponding to $\Omega_1 = 0.45\Delta$ is dominating and is also predicted by the RWA approach. Notice, that there is exact agreement between the second-order VVP and the numerical results.

Dynamics away from resonance

The situation changes when we are away from a resonance. Already intuitively it becomes clear that the dynamics will not be governed anymore by a single frequency. Therefore, by looking only at the coarse-grained dynamics of the system and averaging out the driving-induced oscillations, significant information is lost. This case is presented in Fig. 5.7, where we are in the region between the 1- and 2-photon resonances. In contrast to Fig. 5.6 we find that several frequencies are dominating and determine the dynamics of the system. Second-order VVP reflects this behavior almost perfectly because the driving-induced oscillations are accounted for. However, the RWA shows only one single oscillation since the others are averaged out. It depends on the choice of m in the formula for the RWA, Eq. (5.52), which of the frequencies is taken. This explains also the cuts in Fig. 5.4; see, for example, the horizontal line just below $\omega_{\mathrm{ex}}/\Delta \approx 3$. At these values of the frequency we change m in our analytical calculation. In Fig. 5.5 those cuts are barely visible. Being away from the resonance point, the modifications of the external driving on the system's eigenstates must not be neglected.

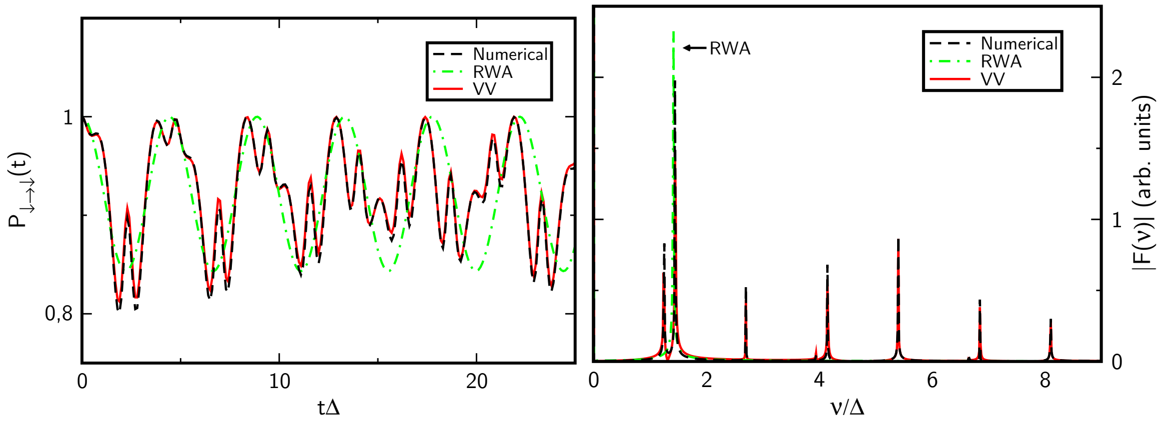

Figure 5.7: Survival probability $P_{\downarrow\to\downarrow}(t)$ and the absolute value of its Fourier transform $F(\nu)$ for $\varepsilon/\Delta = 4.0$, $\omega_{\mathrm{ex}}/\Delta = 2.7$, and $A/\Delta = 4.1$. The numerical and the second-order Van Vleck graph clearly show several dominating oscillation frequencies, while the RWA only shows one of them. Note also the different scale of the y axis of the right graph compared to Fig. 5.6

Off-resonance, the requirement (5.65) for VVP is surely fulfilled for a large enough static bias,

$$|\Delta_{-l-m}| \ll \varepsilon. \tag{5.76}$$

5.3 The dissipative system

To include dissipative effects on our system, we consider the time dependent spin-boson Hamiltonian [1, 74, 112]

$$H(t) = H_{\mathrm{TLS}}(t) + H_{\mathrm{B}} + H_{\text{S-B}}, \tag{5.77}$$

introduced in Sec. 3.5.2, Eq. (3.51). As a reminder: The environmental degrees of freedom are modeled by an infinite set of harmonic oscillators, $H_{\mathrm{B}} = \sum_k \hbar\omega_k b_k^\dagger b_k$, which are bilinearly coupled to the TLS by the coupling Hamiltonian

$$H_{\text{S-B}} = \tilde{X} \sum_k \hbar\nu_k (b_k^\dagger + b_k) + \tilde{X}^2 \sum_k \hbar \frac{\nu_k^2}{\omega_k}. \tag{5.78}$$

We define $\tilde{X} = \sigma_z/2$ as the position of the TLS and omit the tilde in the following discussion. We saw in Sec. 5.1.3 how the Floquet-Born-Markov master equation is derived from the spin-boson Hamiltonian (5.77). For the driven TLS it reads

$$\dot{\rho}_{\alpha\beta}(t) = -\mathrm{i}(E_\alpha - E_\beta)\rho_{\alpha\beta}(t) + \pi \sum_{\alpha',\beta'} \mathcal{L}_{\alpha\beta,\alpha'\beta'}(t)\rho_{\alpha'\beta'}(t), \tag{5.79}$$

where the density matrix is expressed in the basis of the energy eigenstates of the TLS:

$$\rho_{\alpha\beta}(t) = \langle \Phi_\alpha(t)|\rho(t)|\Phi_\beta(t)\rangle, \qquad \alpha,\beta = \pm. \tag{5.80}$$

Notice that $E_\alpha \equiv E_{0,\alpha}$ and $|\Phi_\alpha(t)\rangle \equiv |\Phi_{0,\alpha}(t)\rangle$. The first part of (5.79) describes the nondissipative dynamics as treated in Sec. 5.2. The influence of the bath is fully characterized by the time dependent rate coefficients

$$\begin{aligned}\mathcal{L}_{\alpha\beta,\alpha'\beta'}(t) = \sum_{n,n'} \mathrm{e}^{\mathrm{i}(n+n')\omega_{\mathrm{ex}}t}\Big\{&(N_{n,\alpha\alpha'} + N_{-n',\beta\beta'})X_{n,\alpha\alpha'}X_{n',\beta'\beta}\\ &- \delta_{\beta\beta'}\sum_{\beta''} X_{n',\alpha\beta''}N_{n,\beta''\alpha'}X_{n,\beta''\alpha'} - \delta_{\alpha\alpha'}\sum_{\alpha''} N_{-n,\alpha''\beta'}X_{n,\beta'\alpha''}X_{n',\alpha''\beta}\Big\}\end{aligned} \tag{5.81}$$

with $N_{n,\alpha\beta} = N(E_\alpha - E_\beta + n\omega_{\mathrm{ex}})$, $N(\omega) = G(\omega)n_{\mathrm{th}}(\omega)$, and $n_{\mathrm{th}}(\omega) = \frac{1}{2}\left[\coth(\hbar\beta\omega/2) - 1\right]$.

5.3.1 Position matrix elements

As also the matrix elements of the position operator $X = \sigma_z/2$ are periodic in time, we express them in a Fourier series, $\langle\Phi_\alpha(t)|X|\Phi_\beta(t)\rangle = \sum_n \mathrm{e}^{\mathrm{i}n\omega_{\mathrm{ex}}t}X_{n,\alpha\beta}$. According to Sec. 5.1.1, the Fourier coefficients $X_{n,\alpha\beta}$, which also appear in the rate equations (5.81), can be calculated by

$$X_{n,\alpha\beta} = \frac{1}{T}\int_0^T dt\, \mathrm{e}^{-\mathrm{i}n\omega_{\mathrm{ex}}t}\langle\Phi_\alpha(t)|X|\Phi_\beta(t)\rangle = \langle\langle\Phi_{n,\alpha}|X|\Phi_{n,\beta}\rangle\rangle. \tag{5.82}$$

From this we find that $X_{-n,\alpha\beta} = X^*_{n,\beta\alpha}$ and that we can use the Floquet eigenstates (A.24) and (A.25) to calculate the Fourier coefficients to second order in Δ. We get

$$X^{(2)}_{n,-+} = X^{(1)}_{n,-+}(\Theta_m) + \frac{\sin\Theta_m}{8}\sum_{k\neq n,m}\frac{\Delta_{n-k-m}\Delta_{-k}}{[\varepsilon + (n-k-m)\omega_{\mathrm{ex}}][-\varepsilon + k\omega_{\mathrm{ex}}]}, \tag{5.83}$$

$$X^{(2)}_{n,--} = X^{(1)}_{n,--}(\Theta_m) - \frac{\cos\Theta_m}{8}\sum_{k\neq n+m,m}\frac{\Delta_{n-k}\Delta_{-k}}{[\varepsilon + (n-k)\omega_{\mathrm{ex}}][-\varepsilon + k\omega_{\mathrm{ex}}]}, \tag{5.84}$$

with

$$X^{(1)}_{n,-+}(\xi) = \frac{\sin\xi}{2}\delta_{n,m} - \frac{\mathrm{sign}\,(\Delta_{-m})}{2}\left[\sin^2\frac{\xi}{2}\frac{\Delta_{-n}}{-\varepsilon + n\omega_{\mathrm{ex}}} + \cos^2\frac{\xi}{2}\frac{\Delta_{n-2m}}{\varepsilon + (n-2m)\omega_{\mathrm{ex}}}\right](1-\delta_{n,m}), \tag{5.85}$$

$$X^{(1)}_{n,--}(\xi) = -\frac{\cos\xi}{2}\delta_{n,0} + \frac{\mathrm{sign}\,(\Delta_{-m})}{4}\sin\xi\left[\frac{\Delta_{-m-n}}{-\varepsilon + (m+n)\omega_{\mathrm{ex}}} - \frac{\Delta_{n-m}}{\varepsilon + (n-m)\omega_{\mathrm{ex}}}\right](1-\delta_{n,0}), \tag{5.86}$$

where for ξ either the mixing angle Θ^{RWA}_m or Θ_m is used. Further, we find that $X^{(2)}_{n,++} = -X^{(2)}_{n,--}$. Within the RWA, we would get

$$X^{\mathrm{RWA}}_{n,-+} = \frac{1}{2}\sin\Theta^{\mathrm{RWA}}_m\delta_{n,m} \quad \text{and} \quad X^{\mathrm{RWA}}_{n,--} = -\frac{1}{2}\cos\Theta^{\mathrm{RWA}}_m\delta_{n,0}. \tag{5.87}$$

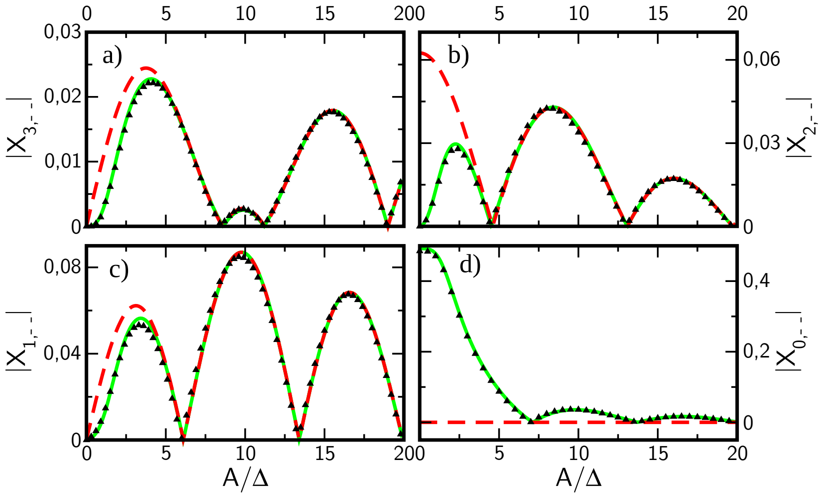

Figure 5.8: Fourier coefficient $|X_{n,--}|$ for various values of n against driving amplitude A. We examine the case $\varepsilon = 2\omega_{\text{ex}} = 4.0\Delta$. The black triangles show data points from numerical diagonalization of the Floquet matrix; the red dashed curve is obtained from first-order perturbation in Δ [Eq. (5.86)], whereas the green solid curve is obtained by going to second order in Δ, see Eq. (5.84).

From this we notice that, in the case of a simple RWA, $X_{n,-+}^{\text{RWA}}$ would be nonzero for $n = m$ and $X_{n,--}^{\text{RWA}}$ for $n = 0$ only. An improvement to that can already be achieved by using VVP to first order in Δ, yielding $X_{n,\alpha\beta}^{(1)}(\Theta_m^{\text{RWA}})$. It contains next to the RWA results additionally first-order corrections for any index n in $X_{n,\alpha\beta}$. Figures 5.8 and 5.9 show the absolute value of the coefficients $X_{n,--}$ and $X_{n,-+}$, respectively. We find a good agreement between the results obtained by a numerical diagonalization of the Floquet matrix (5.46) and second-order VVP, Eqs. (5.83) and (5.84). Concerning Figs. 5.8 (b) and (d) we see a qualitative improvement by going from first to second order in Δ. While in Fig. 5.8 (b) the first-order result approaches a nonvanishing coefficient $X_{2,--}$ for $A \to 0$, Eq. (5.84) corresponds to the numerical calculation very well even in the region of low driving amplitude and meets our expectation that all Fourier coefficients except for $X_{0,\alpha\beta}$ vanish at zero driving. The problem of the first-order results at low driving strength is caused by the definition of the first-order mixing angle Θ_m^{RWA}, Eq. (5.55), which is $\pi/2$ for $\varepsilon = m\omega_{\text{ex}}$. When $n \neq \pm m$ in $X_{n,--}^{(1)}(\Theta_m^{\text{RWA}})$, the coefficient approaches zero for $A \to 0$ because of the term

$$\left[\frac{\Delta_{-m-n}}{-\varepsilon + (m+n)\omega_{\text{ex}}} - \frac{\Delta_{n-m}}{\varepsilon + (n-m)\omega_{\text{ex}}}\right] \tag{5.88}$$

in Eq. (5.86). However, for $n = \pm m$ a zeroth-order Bessel function occurs in that part which does not vanish for $A \to 0$. A second-order improvement of the mixing angle as done in Eq. (5.63) solves this problem. In Fig. 5.8 (d) the first-order solution predicts a coefficient $X_{0,--}^{(1)}(\Theta_m^{\text{RWA}})$ which is constantly zero.

Also, in Fig. 5.9 a noticeable improvement between first- and second-order perturbation theory can be seen. In 5.9 (c) the first-order solution shows a constant coefficient $X_{2,-+}^{(1)}(\Theta_m^{\text{RWA}}) = 0.5$. We see from the numerics and second-order results that indeed this constant value is reached asymptotically for high driving amplitudes; however, for small driving amplitudes, we find a vanishing coefficient. In Fig. 5.9 (h) we can observe a behavior like in 5.8 (b), namely, that $X_{4,-+}^{(1)}(\Theta_m^{\text{RWA}})$ does not approach zero for $A \to 0$. The explanation is similar to

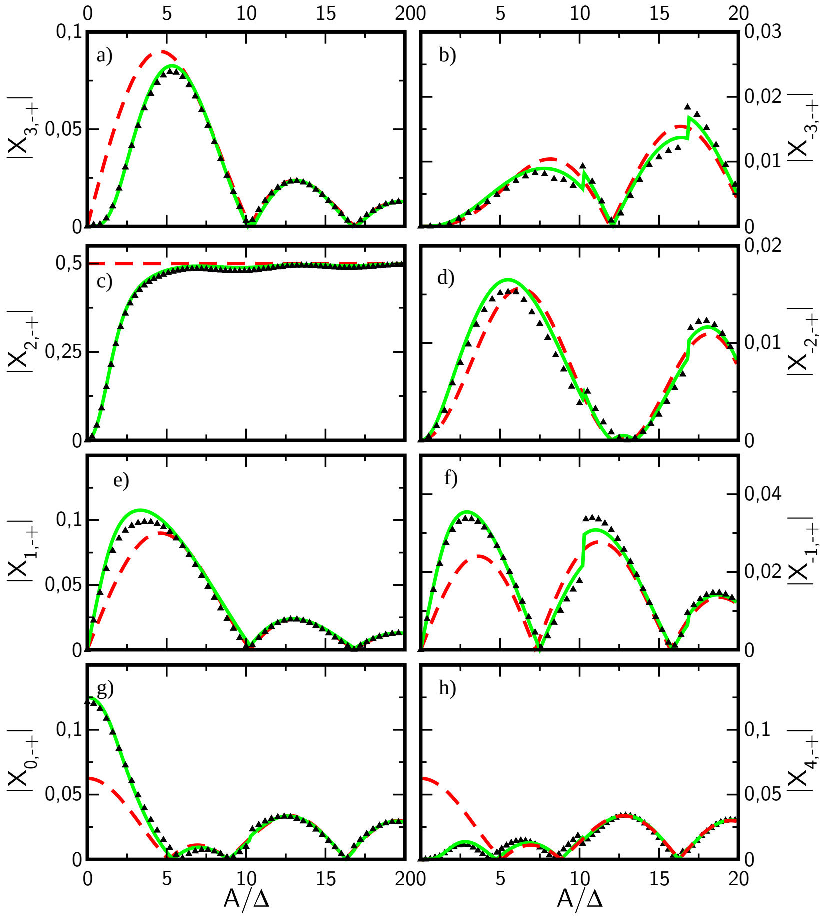

Figure 5.9: Fourier coefficient $|X_{n,-+}|$ for various values of n against driving amplitude A. The parameters are the same as in Fig. 5.8.

the above case.

5.3.2 Moderate rotating-wave approximation

Having calculated the position matrix elements, our rate coefficients $\mathcal{L}_{\alpha\beta,\alpha'\beta'}(t)$ are fully determined. What remains to do is to solve the Floquet-Born-Markov master equation (5.79) for the density matrix ρ. For an analytical calculation, there is, however, still a difficulty: the time dependence of the coefficients. To get rid of this, we perform a moderate rotating-wave approximation (MRWA) [125]; i.e., we neglect fast-oscillatory terms in (5.81), which amounts to selecting only the terms with $n' = -n$, and obtain

$$\mathcal{L}^{\mathrm{MRWA}}_{\alpha\beta,\alpha'\beta'} = \sum_n \Big\{ (N_{n,\alpha\alpha'} + N_{n,\beta\beta'}) X_{n,\alpha\alpha'} X_{-n,\beta'\beta} \\ - \delta_{\beta\beta'} \sum_{\beta''} X_{-n,\alpha\beta''} N_{n,\beta''\alpha'} X_{n,\beta''\alpha'} - \delta_{\alpha\alpha'} \sum_{\alpha''} N_{-n,\alpha''\beta'} X_{n,\beta'\alpha''} X_{-n,\alpha''\beta} \Big\}. \tag{5.89}$$

We observe that $\mathcal{L}^{\mathrm{MRWA}}_{\alpha\alpha,-+} = \mathcal{L}^{\mathrm{MRWA}}_{\alpha\alpha,+-}$, $\mathcal{L}^{\mathrm{MRWA}}_{-+,\alpha\alpha} = \mathcal{L}^{\mathrm{MRWA}}_{+-,\alpha\alpha}$, $\mathcal{L}^{\mathrm{MRWA}}_{\alpha\beta,\alpha\beta} = \mathcal{L}^{\mathrm{MRWA}}_{\beta\alpha,\beta\alpha}$, and $\mathcal{L}^{\mathrm{MRWA}}_{\alpha\beta,\beta\alpha} = \mathcal{L}^{\mathrm{MRWA}}_{\beta\alpha,\alpha\beta}$. Moreover, $\rho_{--}(t) + \rho_{++}(t) = 1$ and $\rho_{+-}(t) = \rho^*_{-+}(t)$. This yields simple expressions for the reduced density matrix elements to first order in the coupling κ to the bath:

$$\rho_{--}(t) = \pi \frac{\mathcal{L}^{\mathrm{MRWA}}_{--,++}}{\gamma_{\mathrm{rel}}} + c_{\mathrm{rel}} \frac{\mathrm{i}}{\pi}(m\omega_{\mathrm{ex}} + \Omega^{(2)}_m)\mathrm{e}^{-\gamma_{\mathrm{rel}}t} + 2\mathcal{L}^{\mathrm{MRWA}}_{--,-+}\mathrm{Re}\{c_{\mathrm{deph}}\mathrm{e}^{-\mathrm{i}(m\omega_{\mathrm{ex}}+\Omega^{(2)}_m)t}\}\mathrm{e}^{-\gamma_{\mathrm{deph}}t}, \tag{5.90}$$

$$\begin{aligned}\rho_{-+}(t) = {}& c_{\mathrm{rel}}(\mathcal{L}^{\mathrm{MRWA}}_{-+,++} - \mathcal{L}^{\mathrm{MRWA}}_{-+,--})\mathrm{e}^{-\gamma_{\mathrm{rel}}t} + \frac{1}{2}\mathcal{L}^{\mathrm{MRWA}}_{-+,+-} c_{\mathrm{deph}}\mathrm{e}^{-\mathrm{i}(m\omega_{\mathrm{ex}}+\Omega^{(2)}_m)t}\mathrm{e}^{-\gamma_{\mathrm{deph}}t} \\ & + c^*_{\mathrm{deph}}\frac{\mathrm{i}}{\pi}(m\omega_{\mathrm{ex}} + \Omega^{(2)}_m)\mathrm{e}^{\mathrm{i}(m\omega_{\mathrm{ex}}+\Omega^{(2)}_m)t}\mathrm{e}^{-\gamma_{\mathrm{deph}}t}.\end{aligned} \tag{5.91}$$

The constants c_{rel} and c_{deph} are fully determined by the initial conditions, Eq. (B.11). The expressions for the relaxation and dephasing rates are

$$\gamma_{\mathrm{rel}} = \pi\left(\mathcal{L}^{\mathrm{MRWA}}_{--,++} - \mathcal{L}^{\mathrm{MRWA}}_{--,--}\right), \quad \gamma_{\mathrm{deph}} = -\pi\mathcal{L}^{\mathrm{MRWA}}_{-+,-+}. \tag{5.92}$$

With (5.89) we can express them in terms of the position matrix elements, yielding

$$\gamma_{\mathrm{rel}} = 4\pi\sum_n \left[N_{n,-+} + \frac{1}{2}\kappa(E_- - E_+ + n\omega_{\mathrm{ex}})\right] X^2_{n,-+}, \tag{5.93}$$

$$\gamma_{\mathrm{deph}} = \frac{1}{2}\gamma_{\mathrm{rel}} + 4\pi\sum_n N_{n,--}X^2_{n,--}. \tag{5.94}$$

With (5.83) and (5.84) we arrive finally at one major result:

$$\gamma_{\mathrm{rel}} = \gamma^0_{\mathrm{rel}} + \sum_{n\neq 0}\gamma^n_{\mathrm{rel}} \quad \text{and} \quad \gamma_{\mathrm{deph}} = \gamma^0_{\mathrm{deph}} + \sum_{n\neq 0}\gamma^n_{\mathrm{deph}} \tag{5.95}$$

with the contributions

$$\gamma^0_{\mathrm{rel}} = \pi G\left(\frac{\Omega^{(2)}_m}{2}\right)\coth\left(\frac{\hbar\beta}{2}\Omega^{(2)}_m\right)\sin^2\Theta_m\left[1 - \frac{1}{2}\sum_{k\neq m}\frac{\Delta^2_{-k}}{(\varepsilon - k\omega_{\mathrm{ex}})^2}\right], \tag{5.96}$$

$$\begin{aligned}\gamma^n_{\mathrm{rel}} = {}& \pi G\left[\frac{1}{2}(\Omega^{(2)}_m - n\omega_{\mathrm{ex}})\right]\coth\left[\frac{\hbar\beta}{2}\left(\Omega^{(2)}_m - n\omega_{\mathrm{ex}}\right)\right] \\ & \times\left[\cos^2\frac{\Theta_m}{2}\frac{\Delta_{n-m}}{\varepsilon + (n-m)\omega_{\mathrm{ex}}} - \sin^2\frac{\Theta_m}{2}\frac{\Delta_{-(n+m)}}{\varepsilon - (n+m)\omega_{\mathrm{ex}}}\right]^2\end{aligned} \tag{5.97}$$

and

$$\gamma^0_{\mathrm{deph}} = \frac{1}{2}\gamma_{\mathrm{rel}} + \pi N(0)\cos^2\Theta_m\left[1 - \frac{1}{2}\sum_{k\neq m}\frac{\Delta^2_{-k}}{(\varepsilon - k\omega_{\mathrm{ex}})^2}\right], \tag{5.98}$$

$$\gamma^n_{\mathrm{deph}} = \frac{\pi}{8}G(n\omega_{\mathrm{ex}})\left[\coth\left(\frac{\hbar\beta}{2}n\omega_{\mathrm{ex}}\right) - 1\right]\sin^2\Theta_m\left[\frac{\Delta_{-m-n}}{-\varepsilon + (m+n)\omega_{\mathrm{ex}}} - \frac{\Delta_{n-m}}{-\varepsilon + (n-m)\omega_{\mathrm{ex}}}\right]^2. \tag{5.99}$$

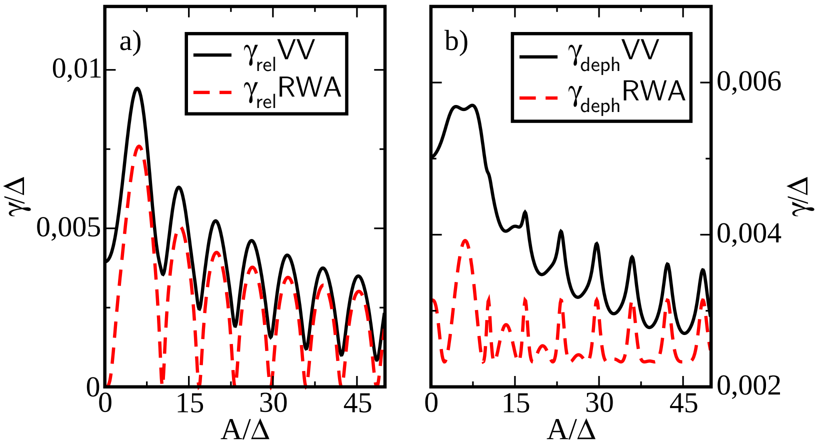

Figure 5.10: Relaxation (a) and dephasing rate (b) against driving amplitude A for $\omega_{\mathrm{ex}}/\Delta = 2.0$, $\varepsilon/\Delta = 4.1$, $\hbar\beta\Delta = 10$, and $\kappa = 0.01$. Results obtained within second-order VVP are compared with RWA calculations. Notice that the RWA predicts an unphysical vanishing of the relaxation rates at the zeros of Δ_2.

For zero temperature, an instructive interpretation of those rates in terms of a dressed energy level diagram is given in [75]. Within the RWA, on the contrary, the corresponding rates read

$$\gamma_{\mathrm{rel}}^{\mathrm{RWA}} = \pi G\left(\frac{\Omega_m^{\mathrm{RWA}}}{2}\right)\coth\frac{\beta\hbar}{2}\Omega_m^{\mathrm{RWA}}\sin^2\Theta_m^{\mathrm{RWA}} \quad \text{and} \quad \gamma_{\mathrm{deph}}^{\mathrm{RWA}} = \frac{1}{2}\gamma_{\mathrm{rel}}^{\mathrm{RWA}} + \pi N(0)\cos^2\Theta_m^{\mathrm{RWA}}. \tag{5.100}$$

The RWA rates correspond to those of an undriven TLS [1] using the dressed energy levels and the RWA mixing angle Θ_m^{RWA}.

In Fig. 5.10, we compare the rates obtained through VVP with the RWA ones for an Ohmic spectral density, $G_{\mathrm{Ohm}}(\omega) = \kappa\omega$. For both the relaxation rate, Fig. 5.10 (a), and the dephasing rate, Fig. 5.10 (b), the RWA approach underestimates the rates. The failing of the RWA becomes especially evident in Fig. 5.10 (a), where a zero relaxation rate is predicted for driving amplitudes A under which Δ_m vanishes. This implies in particular no relaxation at zero driving and $m \neq 0$ simultaneously. Again we see that the higher-order matrix elements in the Floquet matrix (5.46) are necessary in order to correctly describe the dynamics. We find that for certain values of the driving amplitude, namely, whenever $\Delta_m = 0$, γ_{rel}^0 vanishes and thus γ_{rel} becomes minimal. This could be exploited experimentally to minimize relaxation. On the other hand, for higher driving amplitudes, γ_{deph} exhibits peaks at $\Delta_m = 0$ because of the cosine in γ_{deph}^0. For a high driving amplitude, our rates approach asymptotically the ones predicted by an RWA approach. In the opposite regime of small driving amplitudes, however, deviations between the RWA and Van Vleck rates occur, as matrix elements connecting the different doublets in the Floquet matrix play a more important role. Common to both approaches is that the external driving yields a reduction of the rates with increasing strength, a behavior which was already numerically predicted, e.g., in [129].

The failure of the RWA also becomes evident in Fig. 5.11, where we show the dissipative dynamics obtained for an Ohmic environment. Comparing the results for $P_{\downarrow\to\downarrow}(t)$ which we obtain from second-order VVP – formulae (5.90) and (5.91) combined with (B.9) – with the RWA result, we find striking differences. Considering the long-time dynamics (the inset

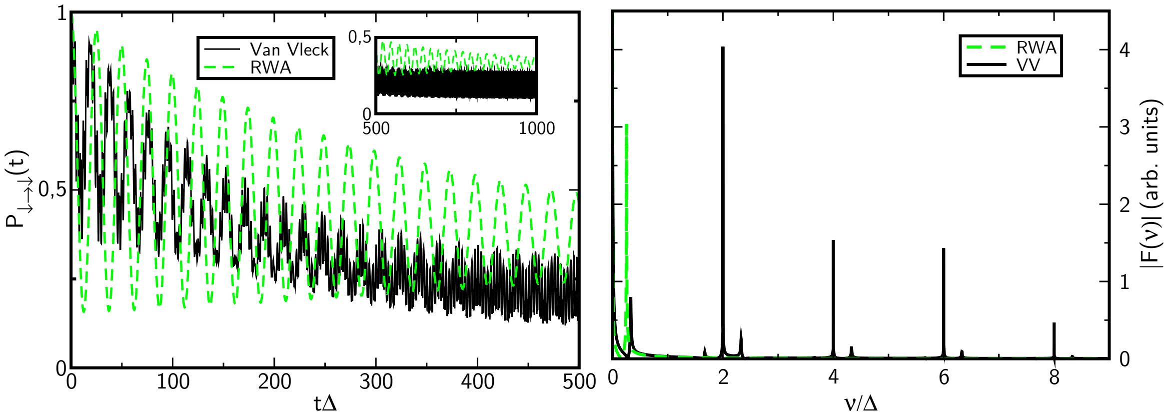

Figure 5.11: Dissipative dynamics close to a 2-photon resonance. The parameters are $\varepsilon/\Delta = 4.1$, $\omega_{\mathrm{ex}}/\Delta = 2.0$, $A/\Delta = 3.0$, $\kappa = 0.01$, and $\hbar\beta\Delta = 10$. Analytical results obtained by second-order VVP are compared with RWA results. Left-hand graph: Survival probability $P_{\downarrow\to\downarrow}(t)$. The inset shows the long-time dynamics and visualizes the deviation of the RWA from the Van Vleck dynamics in the asymptotic limit.
Right-hand graph: Absolute value of the Fourier transform $F(\nu)$ of the survival probability. Next to the relaxation peak at $\nu = 0$ the RWA dynamics are governed by a single frequency $\nu = \Omega_m^{\mathrm{RWA}}$. The second-order dynamics also exhibit the relaxation peak and a main frequency, which, however, is shifted to $\nu = \Omega_m^{(2)}$. Additionally, the higher harmonics of the driving can be seen in the second-order dynamics. For visualization of the δ peaks, appearing at $\nu = n\omega_{\mathrm{ex}}$, a finite width and height have been artificially introduced. Furthermore, broadened peaks appear at $\nu = n\omega_{\mathrm{ex}} \pm \Omega_m^{(2)}$.

in the left graph of Fig. 5.11), we see that the RWA predicts quite a different asymptotic value for $P_{\downarrow\to\downarrow}(t)$. We notice further that the RWA exhibits a single oscillation frequency, which decays completely to a constant value, while within the Van Vleck solution $P_{\downarrow\to\downarrow}(t)$ oscillates for $t \to \infty$ around the equilibrium value. This latter behavior corresponds to the continuous driving of the system through the external field. It is completely missed by the RWA approach. For a further analysis of the dynamics, it is helpful to consider the Fourier transform of $P_{\downarrow\to\downarrow}(t)$, see right-hand graph in Fig. 5.11. Both the RWA and Van Vleck dynamics exhibit a relaxation peak at $\nu = 0$ and the dressed frequency of the system at $\nu = \Omega_m^{\mathrm{RWA}}$ and $\nu = \Omega_m^{(2)}$, respectively. Those latter peaks have a finite width due to the dephasing. Within the RWA Ω_m^{RWA} is the only frequency, while we find additional frequencies for second-order Van Vleck dynamics. They result from the higher harmonics of the driving and are located at integer multiples of the driving frequency, $\nu = n\omega_{\mathrm{ex}}$, and at $\nu = n\omega_{\mathrm{ex}} \pm \Omega_m^{(2)}$. The peaks at $\nu = n\omega_{\mathrm{ex}}$ are δ shaped as they suffer no dephasing, whereas the peaks at $\nu = n\omega_{\mathrm{ex}} \pm \Omega_m^{(2)}$ show the broadening of the main frequency. Already in the nondissipative dynamics, Eq. (B.19), we found the appearance of those multiple frequencies. They result from the beyond-RWA contributions in (B.14) and (B.15) and reflect the external driving. Dephasing only influences the dressed frequency $\Omega_m^{(2)}$ in $\rho_{--}(t)$ and $\rho_{-+}(t)$, see (5.90) and (5.91), and thus for the equilibrium state, the external frequency at $\nu = n\omega_{\mathrm{ex}}$ is dominating. This asymptotic behavior agrees well with the findings in [130–132].

5.3.3 Coherent destruction of tunneling

It has been found in [107, 108] for a driven double-well potential and for a driven TLS in [109] that under certain conditions, coherent destruction of tunneling (CDT) occurs. For a symmetric TLS ($\varepsilon = 0$) and for high enough driving frequencies ($\omega_{\mathrm{ex}} \gg \Delta$) this phenomenon was predicted to happen approximately at the zeros of $J_0(A/\omega_{\mathrm{ex}})$, as can also be seen from Eq. (5.57). For a nonzero static bias and high frequencies, the necessary conditions for CDT are $\varepsilon = m\omega_{\mathrm{ex}}$ and $J_m(A/\omega_{\mathrm{ex}}) = 0$ [133, 134]. In this section, we compare the predictions of the RWA and VVP against exact numerical results.

For the case of an exact m-photon resonance ($\varepsilon = m\omega_{\mathrm{ex}}$) and nonvanishing Δ_m, the RWA mixing angle is $\Theta_m^{\mathrm{RWA}} = \pi/2$, and we get from Eq. (5.56),

$$P_{\downarrow\to\downarrow}^{\mathrm{RWA}}(t) = \cos^2\left(|J_m(A/\omega_{\mathrm{ex}})\Delta|\frac{t}{2}\right). \tag{5.101}$$

Also from this formula, we see that CDT occurs at the zeros of $J_m(A/\omega_{\mathrm{ex}})$. Notice, however, that for $J_m(A/\omega_{\mathrm{ex}}) = 0$, Eq. (5.56) predicts $P_{\downarrow\to\downarrow}^{\mathrm{RWA}}(t) \equiv 1$ even for systems which are not at an m-photon resonance; i.e., within the RWA, the condition $\varepsilon = m\omega_{\mathrm{ex}}$ is not necessary for CDT.

Interestingly, also second-order VVP predicts $\Omega_m^{(2)} = 0$ for $\varepsilon = m\omega_{\mathrm{ex}}$ and $J_m(A/\omega_{\mathrm{ex}}) = 0$, see Eq. (5.61). However, as shown in [127, 128] and discussed in Sec. 5.2.4, this condition holds only to second order in Δ; third-order corrections will cause $\Omega_m^{(3)}$ to be small but finite for $\varepsilon = m\omega_{\mathrm{ex}}$ and $J_m(A/\omega_{\mathrm{ex}}) = 0$. Thus, instead of being localized, the dynamics will oscillate with a large period.

To visualize this behavior, we examine in the following without loss of generality the case of a 3-photon resonance. We choose $\omega_{\mathrm{ex}}/\Delta = 2.0$ and $\varepsilon/\Delta = 6.0$. Then the first zero of $J_3(A/\omega_{\mathrm{ex}})$ occurs at $A/\Delta \approx 12.7603$. Using those parameters in Eq. (5.61), the Van Vleck oscillation frequency $\Omega_3^{(2)}$ is zero. Figure 5.12 shows a comparison between the RWA and Van Vleck dynamics to second order and an exact numerical treatment of the Floquet Hamiltonian for the above parameters. For the RWA, we see a complete destruction of tunneling because the driving-induced oscillations are not accounted for. Also, within the Van Vleck description, the coherent oscillations are strongly suppressed; however, we notice fast oscillations because of the external driving. This becomes especially clear in Fig. 5.12 (b). At $t = (2n+1)\pi/\omega_{\mathrm{ex}}$ with $n = 0, 1, 2, 3...$, we find sharp dips. The plateaus in between show weak oscillations whose number changes with m. The situation changes strongly for the numerical graph: instead of a localization, a complete inversion of the population occurs; CDT seems to have vanished completely, as Ω_m is not zero. Considering, however, the time scale in Fig. 5.12 (a), we notice that the period of $2\pi/\Omega_m$ is rather large. For short times, see figure 5.12 (b), also the numerical dynamics appear to be localized. Note that this observation also holds for the high-frequency case examined in [109]: considering the dynamics at long times the localization will also be destroyed there due to higher-order effects.

In Fig. 5.13, CDT under the influence of dissipation is examined. As in Fig. 5.12, we investigate a 3-photon resonance with vanishing frequencies Ω_3^{RWA} and $\Omega_3^{(2)}$. We compare the dynamics obtained by a numerical solution of the Floquet-Born-Markov master equation (5.79) using the exact eigenstates of the Floquet Hamiltonian, the analytical Van Vleck-MRWA approach, Eqs. (5.90) and (5.91), and the RWA. While the Van Vleck and RWA solutions relax incoherently to a stationary state, the numerical solution exhibits two full oscillations with Ω_m. As in the nondissipative case, the exact oscillation frequency Ω_m is nonzero. For stronger damping those slow oscillations disappear. Both the numerical and Van Vleck oscillations show fast driving-induced oscillations which survive also in the stationary state. While for short time scale, Fig. 5.13 (b), both approaches agree quite well, one finds that in the long time limit the amplitude of the fast oscillations predicted by the

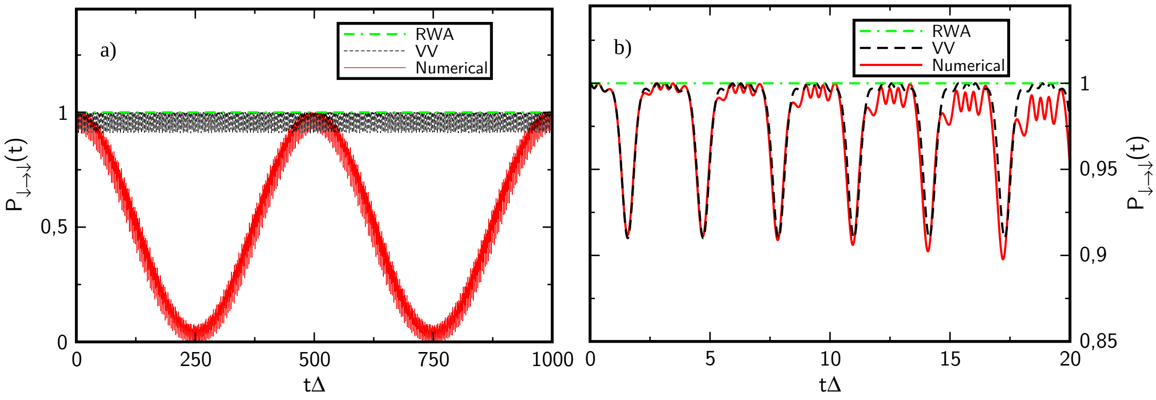

Figure 5.12: Coherent destruction of tunneling for the nondissipative case ($\kappa = 0$). The survival probability $P_{\downarrow\to\downarrow}(t)$ is shown at a 3-photon resonance. The parameters are $\varepsilon/\Delta = 6.0$, $\omega_{\rm ex}/\Delta = 2.0$, and $A/\Delta = 12.7603$. The Van Vleck solution is compared with the RWA and a numerical diagonalization of the Floquet Hamiltonian. Within the RWA, a complete destruction of tunneling can be observed, whereas the analytic Van Vleck solution exhibits driving-induced oscillations. The numerical solution predicts, on the contrary, complete population inversion with low but nonvanishing frequency Ω_m. Figure (b) is a blowup from figure (a) for a shorter time scale. There, the numerical and Van Vleck solutions agree well, and one can nicely see the small oscillations resulting from a 3-photon absorption or emission.

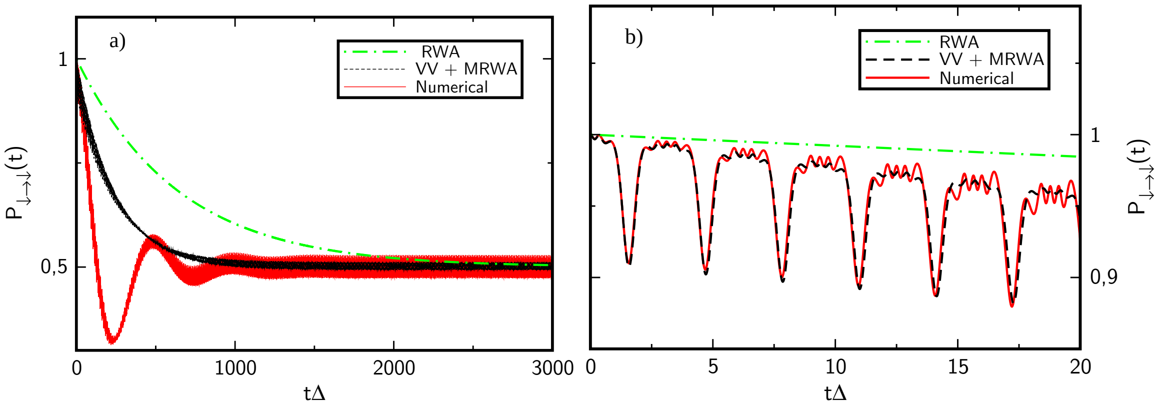

Figure 5.13: Coherent destruction of tunneling for the dissipative case ($\kappa = 0.01$, $\hbar\beta\Delta = 10$). The remaining parameters are the same as in Fig. 5.12. A comparison between the numerical solution of the Floquet Hamiltonian and the full master equation (5.79), the Van Vleck combined with the MRWA approach, and RWA results is provided. The RWA approach predicts a slower relaxation than the numerical one and Van Vleck solution. Deviations between the numerical and Van Vleck solutions can be seen especially in the long time limit. As in Fig. 5.12, the numerical result predicts oscillations with a nonvanishing frequency Ω_m. For short times, see figure (b), the numerical and Van Vleck results agree well.

analytical solution is smaller than the exact numerical one. Compared to the RWA solution, where the equilibrium value is reached after longer time and the fast oscillations are averaged out, VVP is clearly an improvement.

5.3.4 Driving-induced tunneling oscillations

An effect contrary to CDT are driving-induced tunneling oscillations (DITO). It has been predicted in [110–112] and experimentally shown in [70] that for a high static energy bias, $\varepsilon \gg \Delta$, and for high driving frequency, $\omega_{\mathrm{ex}} \gg \Delta$, coherent oscillations with frequency $\Delta|J_m(A/\omega_{\mathrm{ex}})|$ and large amplitude are induced if $\varepsilon \approx m\omega_{\mathrm{ex}}$. The DITO are often also named Rabi oscillations even though in the original problem of Rabi [135] a circularly polarized driving field couples to the TLS. As a consequence, the obtained frequency of the oscillations is linear in A.

In this section, we are going to investigate the effect in the regime of moderate energy bias and driving frequency. First, we examine again the nondissipative case ($\kappa = 0$), see Fig. 5.14. As parameters, we choose a moderate driving amplitude and frequency: $A/\Delta = 3.0$ and $\omega_{\mathrm{ex}}/\Delta = 2.0$. For an exact 3-photon resonance, condition (5.62) must be fulfilled and thus $\varepsilon/\Delta \approx 5.9011$. Note that the RWA resonance condition (5.49), $\varepsilon = 3\,\omega_{\mathrm{ex}}$, is only valid in the case of high frequencies $\omega_{\mathrm{ex}} \gg \Delta$. With condition (5.62) used, VVP results in the oscillation frequency $\Omega_3^{(2)} = \Delta|J_3(A/\omega_{\mathrm{ex}})|$, and for times $t = (2n+1)\pi/\Omega_3^{(2)}$ with $n = 0, 1, 2, 3...$, one finds a complete population inversion, see the Van Vleck graph in Fig. 5.14 (a). Furthermore, in Fig. 5.14 (b), one can nicely see the modifications resulting from the external driving: three small oscillations corresponding to a 3-photon resonance. The exact numerical solution shows a slightly shifted main oscillation frequency Ω_3. The RWA approach exhibits the oscillation frequency Ω_3^{RWA}, which is strongly out of phase compared to the numerical and Van Vleck one, and also has a smaller amplitude, so that a complete population inversion is not reached. When changing the driving frequency to be slightly out of resonance, the driving-induced tunneling oscillations are strongly suppressed, and the system is almost completely localized in the initial state. This behavior originates – contrary to the CDT – not in a zero oscillation frequency $\Omega_3^{(2)}$ but rather in a vanishing amplitude of the $\Omega_3^{(2)}$ oscillation. Also the RWA at $\omega_{\mathrm{ex}} = 1.9\Delta$ is suppressed.

In Fig. 5.15, we consider the influence of the environment. At exact resonance, we observe within the numerical solution and the Van Vleck-MRWA approach coherent oscillations decaying to an equilibrium value. Before reaching the equilibrium value, the dynamics are dominated by the frequency Ω_3, while in the long time limit the coherent oscillations die out; faster ones with the driving frequency ω_{ex} and its higher harmonics around a static equilibrium value are found. The agreement between the numerical and analytical calculations is quite good. Also, in the RWA approach, the coherent oscillation of frequency Ω_3^{RWA} dies out to a stationary state. However, apart from the frequency shift already observed in the nondissipative case and the smaller amplitude, the equilibrium value also differs strongly from the one obtained within the Van Vleck solution. Furthermore, since fast oscillations are completely neglected, the stationary state is constant. Considering the Van Vleck solution for a slightly shifted driving frequency, $\omega_{\mathrm{ex}}/\Delta = 1.9$, we notice an almost incoherent decay to an equilibrium value which is much lower than the one of the dynamics with $\omega_{\mathrm{ex}}/\Delta = 2.0$. Thus, dissipation leads here to an almost complete inversion of the population.

We observe that our analytical methods are also able to recover the findings for the population difference in Chapter 3.2 of [112] in the high-frequency limit ($\omega_{\mathrm{ex}} \gg \Delta$) and even

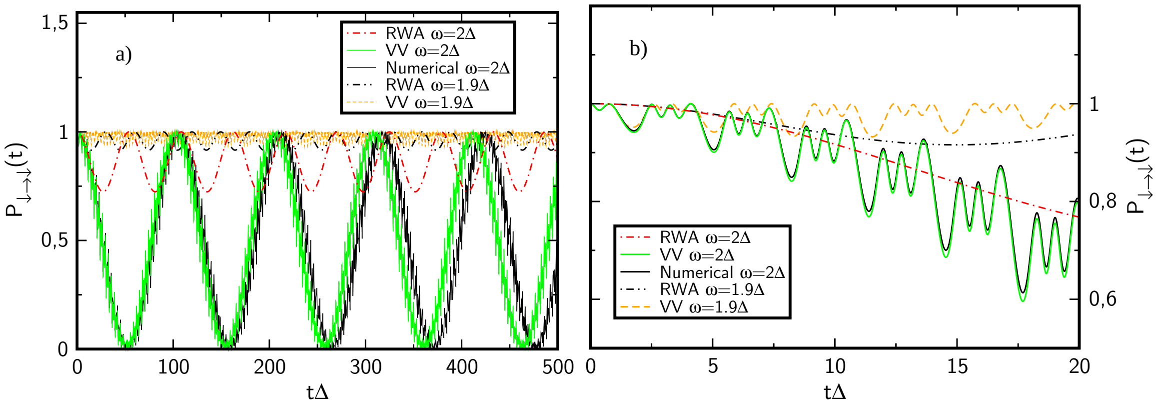

Figure 5.14: Driving-induced tunneling oscillations for the nondissipative case ($\kappa = 0$). The survival probability $P_{\downarrow\to\downarrow}(t)$ is shown for $A/\Delta = 3.0$, $\omega_{\mathrm{ex}}/\Delta = 2.0$, and $\varepsilon/\Delta = 5.9011$ (exact 3-photon resonance). Three approaches are compared: a complete numerical solution of the Floquet Hamiltonian, second-order VVP, and the RWA approach. For the first two approaches, complete population inversion is predicted, and for the Van Vleck dynamics we find the main oscillation frequency $\Omega_3^{(2)} = \Delta|J_3(A/\omega_{\mathrm{ex}})|$. Besides, the numerical and Van Vleck approaches exhibit small driving-induced oscillations, see especially figure (b). The RWA predicts a strongly shifted oscillation frequency. Moreover, population inversion is incomplete. For further comparison, the RWA and the Van Vleck approaches are shown for a slightly shifted external frequency, $\omega_{\mathrm{ex}}/\Delta = 1.9$. The dynamics in this case are almost completely localized.

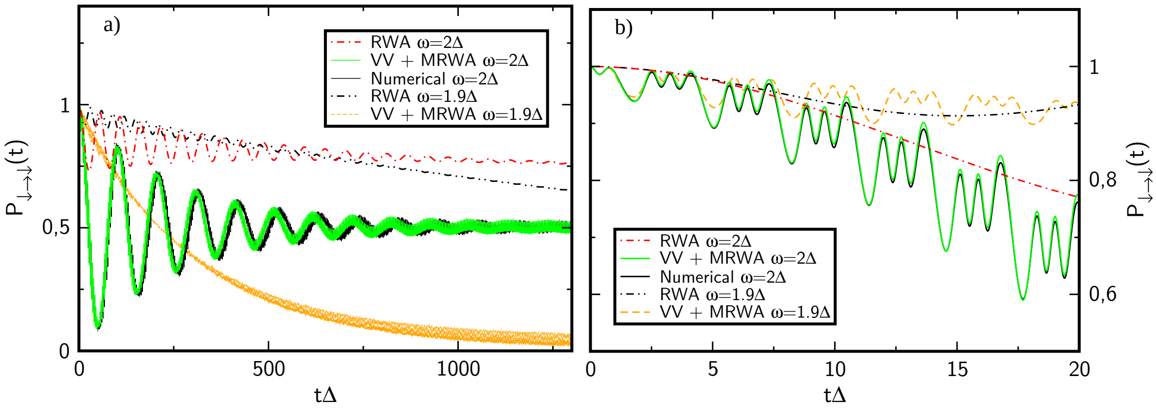

Figure 5.15: Driving-induced tunneling oscillations for the dissipative case ($\kappa = 0.01$ and $\hbar\beta\Delta = 10$). Remaining parameters are the same as in Fig. 5.14. The numerical solution of the master equation (5.79), the analytical Van Vleck-MRWA solution, and the RWA solution for $\omega_{\mathrm{ex}}/\Delta = 2.0$ are compared. Good agreement between the numerical and the Van Vleck solutions can be observed on both long (a) and short (b) time scales. Within the RWA, not only are the main frequency and amplitude changed and the driving-induced oscillations missed, but also the equilibrium value lies far above the Van Vleck prediction. The RWA and the Van Vleck-MRWA solution for $\omega_{\mathrm{ex}}/\Delta = 1.9$ show an almost incoherent decay, and their long time limits differ strongly from the corresponding ones for $\omega_{\mathrm{ex}}/\Delta = 2.0$.

can reproduce the small modulations which are found there by a numerical treatment of the dynamics. Furthermore, we are able to go beyond the assumption of a high driving frequency.

5.4 Summary

In conclusion, we discussed the dynamics of the spin-boson system exposed to an external ac driving. For zero qubit-bath coupling, our investigations in this chapter can be seen as an extension of the work on the qubit-oscillator system done in the previous chapters, in the sense that the oscillator is now in the high-photon limit and thus can be treated classically. Indeed, we could use Van Vleck perturbation theory in Δ just as we did in Sec. 2.3 to find an effective Floquet Hammiltonian. We could show in Sec 5.2.3 that this effective Hamiltonian is equivalent to the one found in the case of a quantized oscillator, where now the dressing of the tunneling matrix element by Laguerre polynomials is replaced by a dressing with Bessel functions.

We found corrections to the renormalized Rabi frequency Ω_m^{RWA} [Eq. (5.52)] also leading to a shift of the resonance condition for an m-photon resonance [Eq. (5.62)]. The so calculated quasienergy spectrum is in very good agreement with results found by a numerical diagonalization of the Floquet Hamiltonian for all values of the static bias ε. Upon investigation of the survival probability $P_{\downarrow\to\downarrow}(t)$, we could recover the shifted oscillation frequency reported already in [121]. We included also the second-order modifications to the Floquet states in our calculation, which account for the higher harmonics induced through the external driving and lead to fast oscillations in $P_{\downarrow\to\downarrow}(t)$, see Figs. 5.3 and 5.11. Our results are at the same time valid for the whole range of the driving amplitude A and for moderate to high driving frequencies ω_{ex}, see the discussion in Sec. 5.2.4.

Assuming weak coupling between TLS and bath, we arrived at a closed analytical expression for the time evolution of the system. In contrast to the NIBA, we are able to treat both an unbiased and a biased TLS for low temperatures and weak damping, applying the Born-Markov and moderate rotating-wave approximation in Sec. 5.3.2. In Sec. 5.3.1, we visualized the good agreement between our analytical formulas for the position matrix elements and a numerical calculation even for low driving amplitudes. This turned out to be essential to arriving at a physically realistic result for the relaxation and dephasing rates given in Sec. 5.3.2. Comparing RWA to Van Vleck results, we found strong deviations and even unphysical predictions for the former one at low driving amplitudes. We remark that our rates agree very well with the zero-temperature results derived recently in [75] via the dressed state approach. In this work, a charge qubit is strongly driven by a microwave field and connected to a dc-SQUID. The higher-order corrections to the rates prove to be important to correctly reflecting the physical findings in this experiment. From this we are encouraged that our results provide a realistic picture of relaxation and dephasing processes in a driven two-level system and, due to the generality of the model, are of interest to a wide range of physical applications.

In Sec. 5.3.3, we performed a detailed analysis of the TLS at an exact 3-photon resonance and for a vanishing third-order Bessel function, which is known to lead to coherent destruction of tunneling in the high-frequency limit. For moderate driving frequencies, we found second-order modifications to the RWA solution. While the latter predicts a complete localization of the TLS in the initial state, the Van Vleck solution shows that driving-induced oscillations survive. Furthermore, for the dissipative case we found an incoherent decay to a quasistationary value.

In Sec. 5.3.4, we examined an effect opposite to the coherent destruction of tunneling: for an appropriately chosen driving amplitude, coherent tunneling oscillations with frequency Ω_m, Eq. (5.61), can be observed at an m-photon resonance. By slightly changing the driving frequency out of resonance, these oscillations are almost completely suppressed and the system shows an incoherent behavior.

6

The driven qubit coupled to an oscillator

Parts of this chapter have been published in collaboration with M. Grifoni in [136].

In the previous chapters, we examined the qubit-oscillator system in two different limits. On the one hand, we assumed the oscillator to be quantized, Chapters 2 and 4, on the other hand in the limit of high photon numbers we chose a semiclassical treatment, where the oscillator was represented by a sinusoidal modulation, Chapter 5. In this chapter, we are interested in the combination of those two viewpoints and therefore will consider the qubit being coupled to two fields, a classical and a quantized one, leading to the Hamiltonian

$$H_{\text{TLS-osc}}(t) = H_{\text{TLS}}(t) + H_{\text{osc}} + H_{\text{int}}. \tag{6.1}$$

We know already its individual parts: it consists of the qubit-oscillator Hamiltonian given in Eq. (1.15), with the TLS being subject to a time dependent external driving just as in Eq. (5.43), namely

$$H_{\text{TLS}}(t) = -\frac{\hbar}{2}\left[\Delta\sigma_x + (\varepsilon + A\cos\omega_{\text{ex}}t)\sigma_z\right]. \tag{6.2}$$

Such a model is not only of mere academical interest. It describes the probing of the qubit-oscillator system by an external radiation as done, for instance, in experiments on the strong coupling regime [35, 43]. For its numerical and analytical treatment usually the driven Jaynes-Cummings model is invoked [137]. It is obtained from Eq. (6.1), following the lines in Sec. 2.1: In the energy basis and for zero static bias ($\varepsilon = 0$), the driving term in Eq. (6.2) translates to

$$\frac{\hbar}{2}\sigma'_x A\cos\omega_{\text{ex}}t = \frac{\hbar}{2}(\sigma'_+ + \sigma'_-)A\cos\omega_{\text{ex}}t. \tag{6.3}$$

Also here counter-rotating terms are neglected, so that we get in the end,

$$H^{\text{JCM}}(t) = -\hbar\frac{\Delta}{2}\sigma'_z + \frac{\hbar}{4}A\left(\sigma'_+\mathrm{e}^{-\mathrm{i}\omega_{\text{ex}}t} + \sigma'_-\mathrm{e}^{\mathrm{i}\omega_{\text{ex}}t}\right) + \hbar\Omega B^\dagger B - \hbar g(\sigma'_+ B + \sigma'_- B^\dagger), \tag{6.4}$$

As we saw already in Section 2.1, the JCM is not valid for a biased qubit and at strong detuning. In particular, it fails in the ultrastrong coupling regime. Furthermore, even in the regime where the undriven JCM works well, the underlying RWA breaks down for extreme driving ($A \gg E_{\text{qb}}$) [138]. Therefore, we will go beyond the driven JCM and avoid the RWA by applying the techniques, introduced in Secs. 2.3 and 5.2: we use the displaced oscillator states together with Floquet and perturbation theory in Δ. There will be only one perturbative parameter in our discussion, and thus we will be able to treat ultrastrong coupling and extreme driving simultaneously. We will investigate the nondissipative dynamics of the qubit and also provide a short discussion on the effect of coherent destruction of tunneling in those systems.

6.1 Dressed Floquet states

For a vanishing tunneling matrix element ($\Delta = 0$), we found already the eigenstates for the undriven qubit-oscillator system and the driven TLS in the previous chapters, namely Eqs. (2.29), (2.30) and (5.45). We combine these states to arrive at the *dressed Floquet state* basis,

$$|\widetilde{n, K, \uparrow / \downarrow}\rangle\rangle = \exp\left\{\pm\frac{g(B - B^\dagger)}{\Omega}\right\}|u^0_{n,\uparrow/\downarrow}\rangle\rangle|K\rangle. \tag{6.5}$$

The lower-case letters stand for the Floquet modes, while the upper-case ones give the oscillator quantum numbers. The dressed Floquet states are eigenstates of (6.1) with the quasienergies

$$\hbar E^0_{n,K,\uparrow/\downarrow} = \mp\frac{\hbar}{2}\varepsilon - \hbar n\omega_{\text{ex}} + \hbar K\Omega - \hbar\frac{g^2}{\Omega}. \tag{6.6}$$

This result is analytically exact and treats the problem for arbitrary coupling strength g. Thus, it provides a good test base for a direct numerical diagonalization of the Floquet Hamiltonian. The latter consists of an infinite-dimensional Hilbert space. If the undriven system is represented by a finite number of degrees of freedom, a usual numerical approach for the driven system is to consider only a finite number $n_{\max}$ of Floquet modes and thus to deal with a truncated Hilbert space. This was also the way we proceeded in Chapter 5 for numerical calculations on the driven TLS. There, the undriven system consisted only of two degrees of freedom, and usually a truncation concerning the Floquet modes converges for a high enough number $n_{\max}$. In this chapter, already the undriven system lives in an infinite Hilbert space, that we additionally have to truncate to a certain maximum number $K_{\max}$. In Fig. 6.1, the exact analytical solution is compared to a numerical diagonalization of the Floquet Hamiltonian, and we can see that a truncation of the oscillator can be problematic already for small values of g. In the example the oscillator is truncated at $K_{\max} = 5$. The closer the index K of the quasienergies $E^0_{n,K,\uparrow/\downarrow}$ comes to $K_{\max}$, the earlier with respect to g the numerics deviate from the exact result. We find better numerical results concerning the lower levels for a higher maximum oscillator number $K_{\max}$ (not shown), while increasing the maximum number of Floquet modes $n_{\max}$ yields no improvement. For numerical investigations of ultrastrong coupling cases, i.e., of $g/\Omega \gtrsim 1$, values of $K_{\max} \geq 30$ are needed to reach converging results.

Another peculiarity can be seen in Fig. 6.1: always two levels are degenerate, namely $E^0_{n+2,K,\downarrow}$ and $E^0_{n,K,\uparrow}$. This degeneracy occurs because we chose $\varepsilon = 2\omega_{\text{ex}}$, the condition for a 2–photon resonance known already from the considerations on the driven TLS. In Figure 6.2, the energy spectrum Eq. (6.6) is shown against the static bias ε for $\Delta = 0$ (green diamonds). We find that further degeneracies occur for

$$\varepsilon = m\omega_{\text{ex}} - L\Omega. \tag{6.7}$$

At this bias value, the energy levels $E^0_{n+m,K+L,\downarrow}$ and $E^0_{n,K,\uparrow}$ cross each other, where we set $K + L = 0, 1, \ldots, \infty$ and $m, n = -\infty, \ldots, \infty$. Those crossings are crucial for a perturbative calculation of the spectrum at finite Δ. Just like in the undriven case, for $L \neq 0$ there are always L nondegenerate levels. For $L > 0$ those are the first L spin-down states (positive slope), while for $L < 0$ the first L spin-up states (negative slope). Thus, for $\varepsilon = m\omega_{\text{ex}} \pm |L|\Omega$ the qubit-oscillator states $|\widetilde{\uparrow / \downarrow, n, K}\rangle\rangle$ for $K < L$ are nondegenerate and thus can be distinguished from the other states in the spectrum at this bias point.

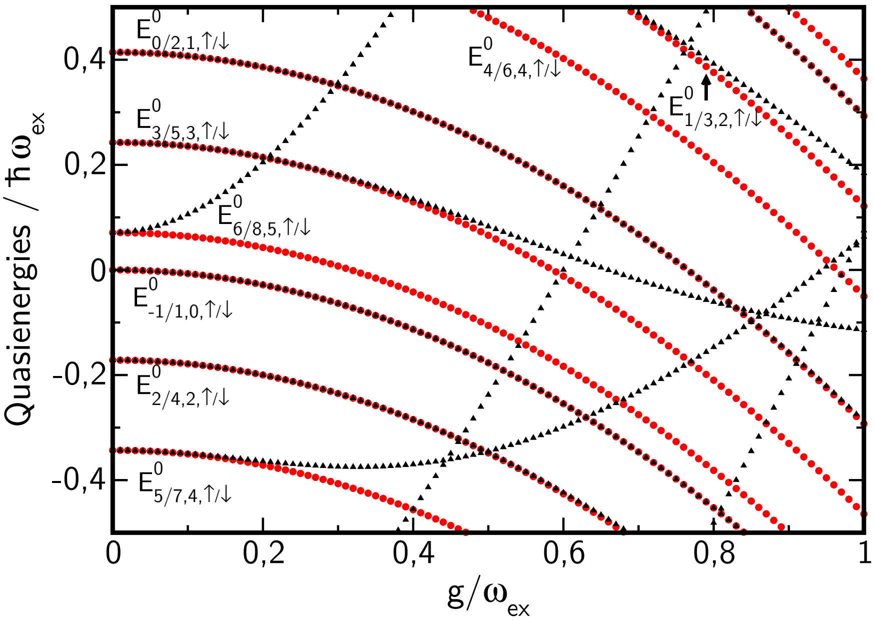

Figure 6.1: The quasienergy spectrum for $\Delta = 0$, Eq. (6.6), within the interval $\{-\omega_{\mathrm{ex}}/2, \omega_{\mathrm{ex}}/2\}$ against coupling g. The parameters are $\Omega/\omega_{\mathrm{ex}} = \sqrt{2}$, $K_{\max} = 5$. We consider the special case of a 2-photon resonance, $\varepsilon/\omega_{\mathrm{ex}} = 2.0$. Furthermore, exact analytical results (red circles) are compared to a numerical diagonalization (black triangles) with the Floquet Hamiltonian truncated at $n_{\max} = 30$.

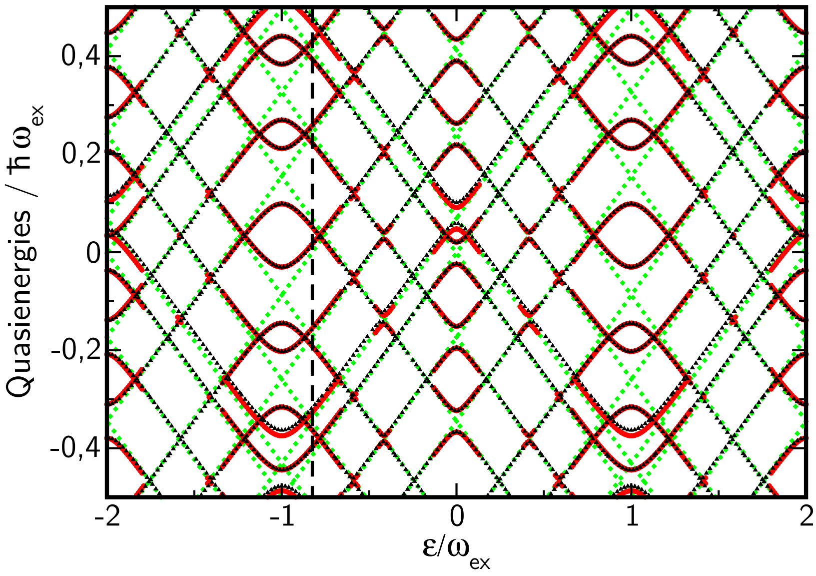

Figure 6.2: Quasienergy spectrum of the qubit and the TLS for finite $\Delta = 0.2$ against the static bias ε for weak qubit-oscillator coupling $g/\omega_{\mathrm{ex}} = 0.05$. Remaining parameters are $\Omega/\omega_{\mathrm{ex}} = \sqrt{2}$, $A/\omega_{\mathrm{ex}} = 2$, $n_{\max} = 30$, and $K_{\max} = 5$. Numerical calculations are shown by black triangles, analytical results in the region of avoided crossings by red solid lines. A good agreement between the analytics and the numerics is found. Only for energy levels with $K = 5$ the numerics yield deviating results due to the truncation. The green diamonds represent the unperturbed case ($\Delta = 0$). The dashed line indicates the bias point $\varepsilon = 2\omega_{\mathrm{ex}} - 2\Omega$.

Additional crossings occur independently of ε if the frequency of the external driving and the oscillator are commensurable, $\Omega/\omega_{\mathrm{ex}} = j/N$ for j and N being positive integers. In this case the levels $E^0_{n,K,\uparrow/\downarrow}$, $E^0_{n+j,K+N,\uparrow/\downarrow}$, $E^0_{n+2j,K+2N,\uparrow/\downarrow}$ etc. are degenerate. Then, the spectrum can be divided into manifolds, where each single one includes an infinite number of degenerate states, which is problematic concerning quasidegenerate perturbation theory. We can avoid such a situation by either choosing incommensurable frequencies or large values for j and N so that only high-photon processes are involved, which we will neglect in the further discussion.

6.2 Quasienergy spectrum for finite Δ

After having found the eigenstates and quasienergies for the unperturbed case, $\Delta = 0$, we calculate now the spectrum for finite Δ. For this, we proceed again like in Sections 2.3 and 5.2. First, the off-diagonal elements of the full Floquet Hamiltonian represented in dressed Floquet states, Eq. (6.5), are determined. We find:

$$\tilde{\Delta}^{n',K'}_{n,K} \equiv \langle\langle \widetilde{n,K,\downarrow} | \Delta\sigma_x | \widetilde{n',K',\uparrow} \rangle\rangle = \left[\mathrm{sign}\left(K'-K\right)\right]^{|K'-K|} \Delta_{n'-n} \Xi^{|K'-K|}_{\mathrm{Min}\{K,K'\}}(\alpha). \tag{6.8}$$

This is a combination of the Bessel function dressing

$$\Delta_m = \Delta J_m\left(A/\omega_{\mathrm{ex}}\right), \tag{6.9}$$

resulting from the classical driving of the TLS, and the dressing by Laguerre polynomials

$$\Xi^L_K(\alpha) = \alpha^{L/2}\sqrt{K!/(K+L)!}\,\mathsf{L}^L_K(\alpha)\mathrm{e}^{-\frac{\alpha}{2}} \tag{6.10}$$

due to the coupling to the quantized oscillator. These off-diagonal elements give raise to avoided crossings in the energy spectrum in Fig. 6.2. They are located around the resonances, Eq. (6.7), and their width is determined to first order by the dressed tunneling matrix element $\tilde{\Delta}^{n,K}_{n+m,K+L}$. Thus, the most dominant crossings are the ones where the static bias is an integer multiple of the driving frequency, $\varepsilon = m\omega_{\mathrm{ex}}$ (an m–photon process), with $L = 0$. The latter means that energy levels which cross each other at this point for $\Delta = 0$ belong to the same oscillator quantum K, and that the dressing contains a Laguerre polynomial of the kind $\mathsf{L}^0_K(\alpha)$. Those gaps are wider than the ones belonging to levels of different oscillator quanta and can even cover them. For instance, one would expect gaps to open for $\varepsilon = 2\omega_{\mathrm{ex}} - 2\Omega$, see the dashed line in Fig. 6.2. Indeed, the spectrum exhibits crossings along this line for $\Delta = 0$. However, there are the gaps of $\varepsilon = -\omega_{\mathrm{ex}}$ in direct neighborhood, which completely cover the small gaps characterized by $\tilde{\Delta}^{n,K}_{n+2,K+2}$. Therefore, care has to be taken when choosing the resonances determining the spectrum and consequently the dynamics.

In Fig. 6.2 we show also a numerical calculation of the energy spectrum and see indeed the gaps open.[1] We can give an analytical description of the quasienergy spectrum by identifying again degenerate subspaces. For a static bias according to Eq. (6.7) there is a two-fold degeneracy, and from the discussions before we readily obtain an effective Hamiltonian to second order in Δ:[2]

$$\hbar\begin{pmatrix} E^0_{n,K,\uparrow} - \frac{1}{4}\varepsilon^{(2)}_{n,K,\uparrow} & -\frac{1}{2}\tilde{\Delta}^{n,K}_{n+m,K+L} \\ -\frac{1}{2}\tilde{\Delta}^{n,K}_{n+m,K+L} & E^0_{n+m,K+L,\downarrow} + \frac{1}{4}\varepsilon^{(2)}_{n+m,K+L,\downarrow} \end{pmatrix}, \tag{6.11}$$

---

[1] In order to obtain reliable numerical results for a low value of K_{max}, we keep Δ and g small in this example.

[2] Without loss of generality we assume $L \geq 0$.

with

$$\varepsilon^{(2)}_{n,K,\uparrow/\downarrow} \equiv \sum_{\substack{p=-\infty \\ \{p,P\}\neq\{-m,\pm L\}}}^{\infty} \sum_{P=-K}^{\infty} \frac{\left(\tilde{\Delta}^{n,K}_{n-p,K+P}\right)^2}{\varepsilon + p\omega_{\mathrm{ex}} \pm P\Omega}. \tag{6.12}$$

The eigenvalues of Eq. (6.11) are found as

$$\hbar E^{m,L}_{n,K,\mp} = \frac{\hbar}{2}\left[-(2n+m)\omega_{\mathrm{ex}} + (2K+L)\Omega + \frac{1}{4}(\varepsilon^{(2)}_{n+m,K+L,\downarrow} - \varepsilon^{(2)}_{n,K,\uparrow}) - \frac{2g^2}{\Omega} \mp \Omega^{m,L}_{n,K}\right] \tag{6.13}$$

with the dressed oscillation frequency

$$\Omega^{m,L}_{n,K} = \sqrt{\left[\varepsilon - m\omega_{\mathrm{ex}} + L\Omega + \frac{1}{4}(\varepsilon^{(2)}_{n+m,K+L,\downarrow} + \varepsilon^{(2)}_{n,K,\uparrow})\right]^2 + \left[\Delta_{-m}\Xi^{L}_{K}(\alpha)\right]^2}. \tag{6.14}$$

The corrected energies

$$E^0_{n,K,\downarrow} + \frac{1}{4}\varepsilon^{(2)}_{n,K,\downarrow} \tag{6.15}$$

of the L nondegenerate spin-down states build together with the eigenvalues of Eq. (6.13) the quasienergy spectrum. The eigenstates are to first order in Δ:

$$|\Phi^{m,L}_{n,K,\downarrow}\rangle\rangle = |\widetilde{n,K,\downarrow}\rangle\rangle \tag{6.16}$$

$$|\Phi^{m,L}_{n,K,-}\rangle\rangle = -\sin\left(\Theta^{m,L}_{n,K}/2\right)|\widetilde{n,K,\uparrow}\rangle\rangle - \mathrm{sign}\left(\tilde{\Delta}^{n,K}_{n+m,K+L}\right)\cos\left(\Theta^{m,L}_{n,K}/2\right)|\widetilde{n+m,K+L,\downarrow}\rangle\rangle, \tag{6.17}$$

and

$$|\Phi^{m,L}_{n,K,+}\rangle\rangle = \cos\left(\Theta^{m,L}_{n,K}/2\right)|\widetilde{n,K,\uparrow}\rangle\rangle - \mathrm{sign}\left(\tilde{\Delta}^{n,K}_{n+m,K+L}\right)\sin\left(\Theta^{m,L}_{n,K}/2\right)|\widetilde{n+m,K+L,\downarrow}\rangle\rangle, \tag{6.18}$$

with the mixing angle

$$\tan\Theta^{m,L}_{n,K} = \frac{|\tilde{\Delta}^{m,L}_{n,J}|}{-\varepsilon + m\omega_{\mathrm{ex}} - L\Omega - \frac{1}{4}(\varepsilon^{(2)}_{n+m,K+L,\downarrow} + \varepsilon^{(2)}_{n,K,\uparrow})}. \tag{6.19}$$

To keep the discussion simple, we neglect in this chapter the higher-order corrections to the states coming from the transformation between the effective Hamiltonian and the original one. Note, however, that already second-order corrections to the diagonal elements of the unperturbed Hamiltonian yield a small shift in the resonance condition, so that the latter becomes,

$$\varepsilon = m\omega_{\mathrm{ex}} - L\Omega - \frac{1}{4}(\varepsilon^{(2)}_{n+m,K+L,\downarrow} + \varepsilon^{(2)}_{n,K,\uparrow}). \tag{6.20}$$

Just like we saw before, this second-order shift vanishes in the case of an unbiased qubit. The quasienergy spectrum obtained from Eqs. (6.13) and (6.15) is shown in Fig. 6.2 around the resonances. Away from a resonance it is given by the unperturbed spectrum, Eq. (6.6). We see a very good agreement with the numerical calculation. Only for levels with $K = K_{\mathrm{max}}$, the numerics slightly deviate from the analytical results due to the already mentioned truncation effects. By increasing K_{max} this deviations will vanish, but also the spectrum will become more dense and harder to interpret. For couplings as weak as used in Fig. 6.2,

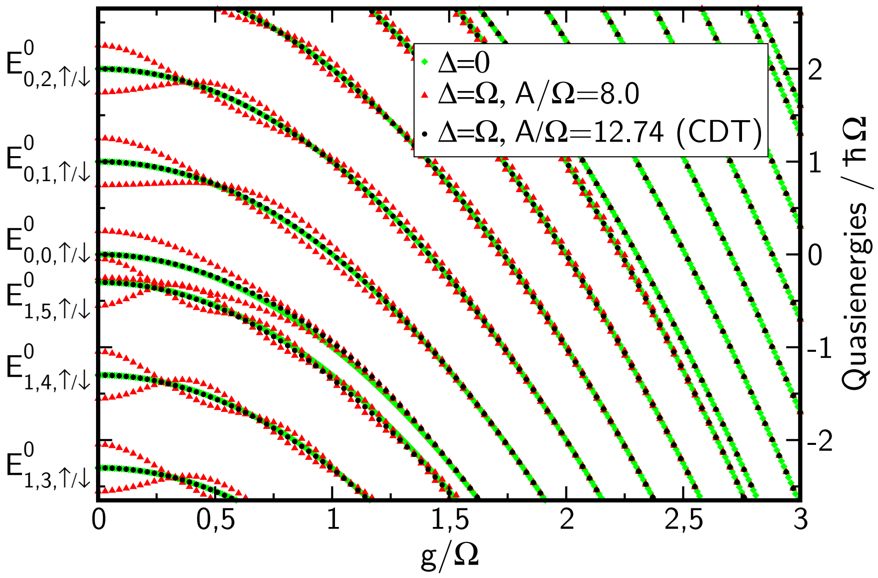

Figure 6.3: Quasienergy spectrum against the coupling strength g in the unbiased case $\varepsilon = 0$. Further, we set $\omega_{\text{ex}}/\Omega = 5.3$ and $\Delta/\Omega = 1.0$. The spectrum is examined for $A/\Omega = 8.0$ (red triangles) and $A/\Omega = 12.74$ (black dots). For the former, avoided crossings of amplitude Ω_K occur, which vanish at values of g yielding zeros of the Laguerre polynomials. For the latter, all Ω_K vanish simultaneously for all values of g, since the CDT condition $J_0(A/\omega_{\text{ex}}) = 0$ is fullfilled independent of the coupling strength g. As a reference the green curves show the unperturbed case $\Delta = 0$.

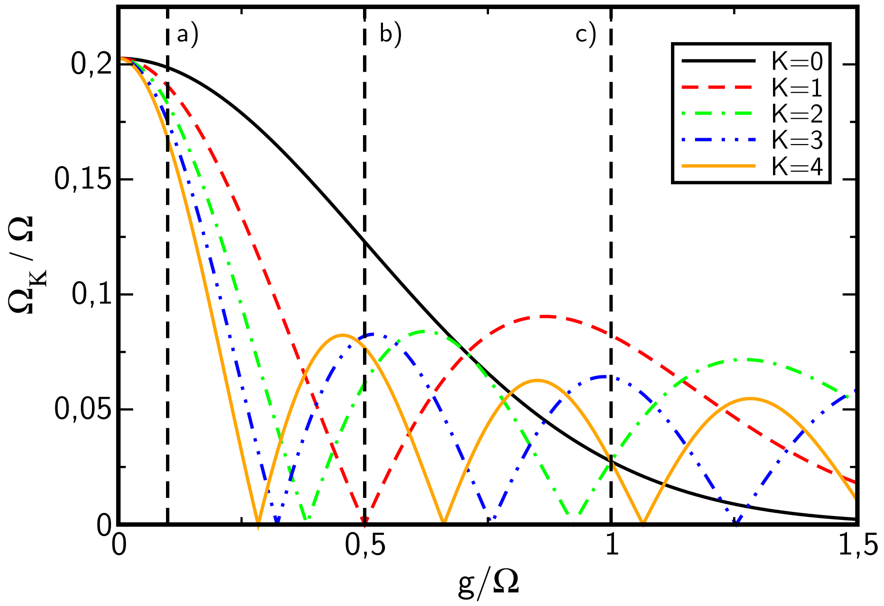

Figure 6.4: Size of the avoided crossing Ω_K against the dimensionless coupling strength g/Ω for an unbiased qubit ($\varepsilon = 0$). Further, $\Delta/\Omega = 0.4$, $\omega_{\text{ex}}/\Omega = 5.3$ and $A/\Omega = 8.0$. Ω_K vanishes at the zeros of the Laguerre polynomial $\mathsf{L}^0_K(\alpha)$. The dashed lines a), b), c) represent $g/\Omega = 0.1, 0.5, 1.0$, respectively, as considered in Fig. 6.5.

the width of the gaps at resonances which fullfill $\varepsilon = m\omega_{\mathrm{ex}}$ is almost the same for different oscillator quanta K, because the dressing by Laguerre polynomials Ξ^0_K approaches one for $\alpha \to 0$. For stronger coupling g, the width varies with K.

In Fig. 6.3, the quasienergy spectrum against the coupling strength g is shown for finite Δ. We examine the unbiased case $\varepsilon = 0$, which implies $m = L = 0$ and hence gaps with $\Omega^{0,0}_{n,K} = |\Delta_0 \mathsf{L}_K(\alpha)\mathrm{e}^{-\frac{\alpha}{2}}| \equiv \Omega_K$. For $g = 0$ and $\Delta \neq 0$, the twofold degeneracy of the unperturbed case is lifted by a gap of width Δ_0. For $g \neq 0$, the gap is further determined by the dressing Ξ^0_K, so that additional degeneracies occur at the roots of the Laguerre polynomials. In Fig. 6.4, the dressed oscillation frequencies corresponding to the avoided crossings in Fig. 6.3, but for a weaker tunneling matrix element Δ, are plotted against the dimensionless coupling strength g/Ω.[3] Next to an exponential decay, they depend through the Laguerre polynomial characteristically on the oscillator quantum number K and exhibit zeros for certain values of g. This changes when choosing the driving amplitude A in such a way that A/ω_{ex} hits a root of the Bessel function in Δ_0. Under this condition coherent destruction of tunneling occurred in the case of the driven TLS [74, 107, 108]. For the latter being coupled to a quantum oscillator, two levels with the same quantum number K in Fig. 6.3 stay degenerate for any value of g, since the dressing by the Bessel function does *not* depend on g or the oscillator level. This leads to the conclusion that CDT also occurs in the case of the extended model discussed in this chapter. We will examine this in the next section, where the dynamics of the qubit-oscillator system is determined.

6.3 Dynamics

In this section, we want to determine the survival probability of the qubit $P_{\downarrow\to\downarrow}(t) = \langle\downarrow|\rho_{\mathrm{red}}(t)|\downarrow\rangle$. From the eigenstates in the extended Hilbert space representation, Eqs. (6.16) – (6.18), and using that[4]

$$|\Phi^{m,L}_{n,K,\alpha}(t)\rangle = \sum_{k,\gamma} \mathrm{e}^{\mathrm{i}k\omega_{\mathrm{ex}}t} \langle\langle -k,\gamma|\Phi^{m,L}_{n,K,\alpha}\rangle\rangle |\gamma\rangle, \tag{6.21}$$

where $|\gamma\rangle \epsilon \{|K', \uparrow / \downarrow\rangle\}$ is a basis state of the unperturbed ($\Delta = 0$), undriven ($A = 0$) and uncoupled ($g = 0$) system, we find the time dependent Floquet states,

$$\begin{aligned} |\Phi^{m,L}_{n,K,\downarrow}(t)\rangle = &-\sum_{K'} \left[\mathrm{sign}\left(K' - K - L\right)\right]^{|K+L-K'|} \Xi^{|K+L-K'|}_{\mathrm{Min}\{K+L,K'\}}\left(\frac{\alpha}{4}\right) \\ &\times \mathrm{e}^{\mathrm{i}\left[\frac{A}{2\omega_{\mathrm{ex}}}\sin\omega_{\mathrm{ex}}t + m\omega_{\mathrm{ex}}t\right]} |K', \downarrow\rangle, \end{aligned} \tag{6.22}$$

---

[3] Note, that in Fig. 6.3 we choose $\Delta/\Omega = 1$ for a better visibility of the oscillations. In Fig. 6.4 and the following graphs, we use instead $\Delta/\Omega = 0.4$ in order to be able to compare to numerical results. The qualitative behavior remains unchanged.

[4] See Eq. (5.15) in Section 5.1.1.

$$
\begin{aligned}
|\Phi^{m,L}_{n,K,-}(t)\rangle = \mathrm{e}^{\mathrm{i}n\omega_{\mathrm{ex}}t} \sum_{K'} \Bigg\{ & -\left[\mathrm{sign}\left(K-K'\right)\right]^{|K'-K|} \sin\left(\frac{\Theta^{m,L}_{n,K}}{2}\right) \Xi^{|K'-K|}_{\mathrm{Min}\{K,K'\}}\left(\frac{\alpha}{4}\right) \\
& \times \mathrm{e}^{-\mathrm{i}\frac{A}{2\omega_{\mathrm{ex}}}\sin\omega_{\mathrm{ex}}t}|K',\uparrow\rangle \\
- \mathrm{sign}\left(\tilde{\Delta}^{n,K}_{n+m,K+L}\right) & \left[\mathrm{sign}\left(K'-K-L\right)\right]^{|K+L-K'|} \cos\left(\frac{\Theta^{m,L}_{n,K}}{2}\right) \Xi^{|K+L-K'|}_{\mathrm{Min}\{K+L,K'\}}\left(\frac{\alpha}{4}\right) \\
& \times \mathrm{e}^{\mathrm{i}[\frac{A}{2\omega_{\mathrm{ex}}}\sin\omega_{\mathrm{ex}}t+m\omega_{\mathrm{ex}}t]}|K',\downarrow\rangle \Bigg\}
\end{aligned}
\tag{6.23}
$$

and

$$
\begin{aligned}
|\Phi^{m,L}_{n,K,+}(t)\rangle = \mathrm{e}^{\mathrm{i}n\omega_{\mathrm{ex}}t} \sum_{K'} \Bigg\{ & \left[\mathrm{sign}\left(K-K'\right)\right]^{|K'-K|} \cos\left(\frac{\Theta^{m,L}_{n,K}}{2}\right) \Xi^{|K'-K|}_{\mathrm{Min}\{K,K'\}}\left(\frac{\alpha}{4}\right) \\
& \times \mathrm{e}^{-\mathrm{i}\frac{A}{2\omega_{\mathrm{ex}}}\sin\omega_{\mathrm{ex}}t}|K',\uparrow\rangle \\
- \mathrm{sign}\left(\tilde{\Delta}^{n,K}_{n+m,K+L}\right) & \left[\mathrm{sign}\left(K'-K-L\right)\right]^{|K+L-K'|} \sin\left(\frac{\Theta^{m,L}_{n,K}}{2}\right) \Xi^{|K+L-K'|}_{\mathrm{Min}\{K+L,K'\}}\left(\frac{\alpha}{4}\right) \\
& \times \mathrm{e}^{\mathrm{i}[\frac{A}{2\omega_{\mathrm{ex}}}\sin\omega_{\mathrm{ex}}t+m\omega_{\mathrm{ex}}t]}|K',\downarrow\rangle \Bigg\}.
\end{aligned}
\tag{6.24}
$$

For the dynamics, we need to determine the matrix elements of the qubit-oscillator density operator, which we define as

$$
\rho^{m,L}_{K,\alpha;K',\beta}(t) = \langle\Phi^{m,L}_{K,\alpha}(t)|\rho(t)|\Phi^{m,L}_{K',\beta}(t)\rangle = \rho^{m,L}_{K,\alpha;K',\beta}(0)\,\mathrm{e}^{-\mathrm{i}\omega^{m,L}_{K,\alpha;K',\beta}t} \tag{6.25}
$$

with

$$
\omega^{m,L}_{K,\alpha;K',\beta} = E^{m,L}_{K,\alpha} - E^{m,L}_{K',\beta}. \tag{6.26}
$$

Here, we set $\{\alpha,\beta\}\,\epsilon\,\{-,+,\downarrow\}$ and dropped the index n as it just leads to an overall phase and, thus, does not effect the dynamics. From Eq. (6.25), one expects two main oscillatory contributions, namely $\omega^{m,L}_{\mp K;\pm K} = \pm\Omega^{m,L}_{K}$ and $\omega^{m,L}_{\alpha K;\alpha K'} = (K-K')\Omega$. Also sums of both can occur.

As starting conditions we assume the qubit to be in the spin-down state and the oscillator obeying a Boltzmann distribution, so that

$$
\rho(0) = |\downarrow\rangle\langle\downarrow| \otimes \sum_K \frac{1}{Z}\mathrm{e}^{-\hbar\beta K\Omega}|K\rangle\langle K|. \tag{6.27}
$$

In Fig. 6.5, we plot the dynamics for zero bias and three different coupling strengths, indicated by the dashed lines in Fig. 6.4. For a weak coupling of $g/\Omega = 0.1$ (a), the analytical calculation shows oscillations between the states $|\downarrow\rangle$ and $|\uparrow\rangle$ with the single frequency Ω_0. The higher oscillator levels seem to play no role. This is confirmed by the numerical calculation. For stronger coupling $g/\Omega = 0.5$ (b), a second peak in the Fourier spectrum occurs, the dressed frequency Ω_2. The amplitude of this latter frequency is very small so that its effect on the survival probability is almost not visible. The peak at Ω_1 is absent, because the corresponding Laguerre polynomial vanishes at this value exactly, see Fig. 6.4. Correspondingly, we observe a tunneling *reduction* compared to case (a).

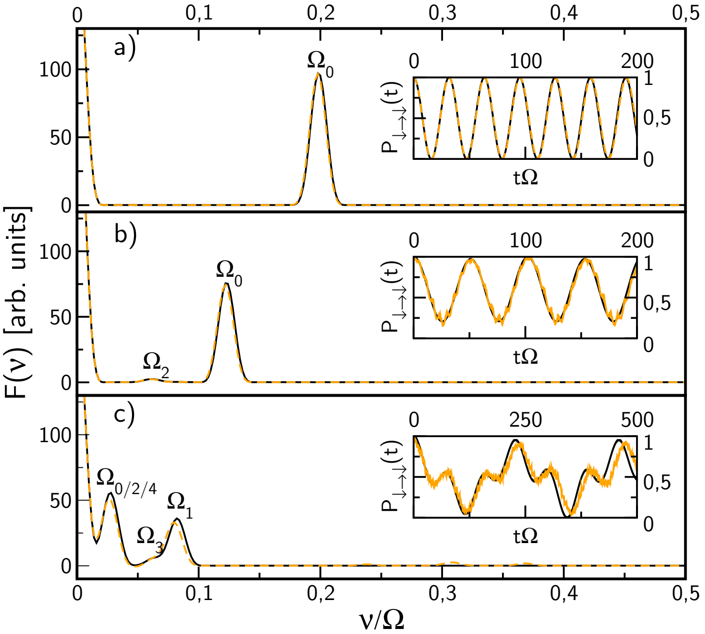

Figure 6.5: Dynamics of the qubit for $\varepsilon = 0$, $\Delta/\Omega = 0.4$, $\omega_{\text{ex}}/\Omega = 5.3$, $A/\Omega = 8.0$ and $\hbar\beta\Omega = 10$. Analytical calculations (black) are compared to numerical results (orange). The graphs show the Fourier transform $F(\nu)$ of the survival probability $P_{\downarrow\rightarrow\downarrow}(t)$ (see the insets). We investigate the different coupling strengths indicated in Fig. 6.4, namely $g/\Omega = 0.1$ (a), 0.5 (b) and 1.0 (c).

Thus, by varying g, so that $\alpha = 2g/\Omega$ hits the root of a Laguerre polynomial, one can make certain oscillatory contributions disappear. This is in analogy to CDT, only that there a zero of a Bessel function leads to complete localization in the high-frequency limit $\Delta \ll \omega_{\text{ex}}$. Considering the numerics, we additionally see fast oscillation in the graph of $P_{\downarrow\rightarrow\downarrow}(t)$. They result from the external frequency ω_{ex} and the oscillator frequency Ω. The corresponding peaks are out of the plotted range in Fig. 6.5 and are not covered by the analytical results. We saw already in Chapter 5 that, in order to include also the influence of this fast oscillations, one needs to take into account the Van Vleck back-transformation. Still, our analytical results give a faithful picture of the coarse-grained dynamics. In graph (c) of Fig. 6.5 we are with $g/\Omega = 1.0$ already deep in the ultrastrong coupling regime. The frequency Ω_1 is now different from zero, and additionally Ω_3 appears. The lowest peak belongs to the frequencies Ω_0, Ω_2 and Ω_4, which are equal for $g/\Omega = 1.0$, see Fig. 6.4. A complete population inversion again takes place. For the numerics, the frequency Ω_1 in graph (c) is shifted slightly to the left in the spectrum so that, concerning the survival probability, the numerical and analytical curve get out of phase for longer times t. Furthermore, we see again fast oscillations overlaid.

As a last point, we want to examine if CDT survives in a TLS which is coupled to an oscillator. We noticed already in Fig. 6.3 that the criteria for CDT is independent of the coupling strength g. For an unbiased qubit, we choose A/ω_{ex} in Fig. 6.6 so that the zeroth order Bessel function in Δ_0 and therefore the dressed frequencies Ω_K vanish. The analytical results predict independently of the coupling strength g complete localization of the survival probability. Also the numerics show strong localization, which is just slightly lifted due to the fast oscillatory contributions coming from ω_{ex} and Ω. However, for long time scale, this localization completely vanishes. The situation is shown in the inset of graph (a) in Fig.

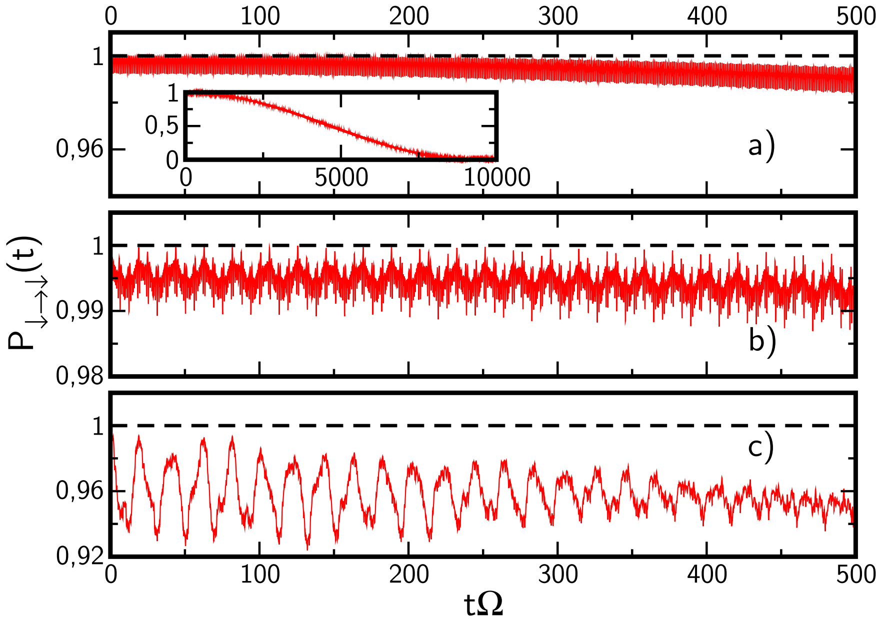

Figure 6.6: Coherent destruction of tunneling in a driven qubit-oscillator system. The survival probability is shown for the same parameters as in Fig. 6.5 except for the amplitude $A/\Omega = 12.7$, which leads to $\Delta_0 = 0$. Three different coupling strengths are examined: $g/\Omega = 0.1$ (a), 0.5 (b) and 1.0 (c). The analytical calculations (black, dashed curves) predict complete localization for all three cases. Also the numerics (red curves) show strong localization for short time scales with fast oscillations overlaid. For long times this localization vanishes (see inset in (a)).

6.6 and is similar also for stronger coupling. We have encountered this behavior already in Section 5.3.3, where we investigated CDT for a driven TLS. The explanation is the same: due to higher-order contributions Ω_0 is not completely zero even with the conditions for CDT being fullfilled. The resulting oscillations have a large period, and the analytics represent a good approximation on a short time scale and for high frequencies $\omega_{\mathrm{ex}} \gg \Delta$. The numerical curves, especially in graph (c), lead to the assumption that localization gets less stable for stronger couplings. However, for such strong couplings, the effects due to the truncation of the Hilbert space become stronger, and higher K-values have to be taken into account in order to reach convergent results, which makes a numerical calculation less feasible. Because of computational restrictions we chose as maximum value $K_{\max} = 30$, which might still not be high enough for $g/\Omega = 1.0$ in the case of CDT.

The behavior of the dynamics of the biased qubit ($\varepsilon \neq 0$) is analogous and provided as well by the above equations. We will not further discuss it here. Besides, we investigated also higher values of Δ, in particular the resonant case $\Delta = \Omega$. There the behavior is qualitatively the same as in Fig. 6.5, but, especially for strong couplings like treated in graph (c) of Fig. 6.5, the dephasing between the analytical and the numerical curve becomes stronger, and higher-order elements in Δ become more important.

6.4 Summary

In this chapter, we combined the approaches used in Chapters 2 and 5 for the qubit-oscillator system and the driven TLS to obtain the dressed Floquet state basis. The latter represents a starting point for a perturbative treatment of the driven qubit-oscillator system beyond the rotating-wave approximation and thus for parameter regimes where the driven Jaynes-Cummings model fails, in particular for extreme driving and ultrastrong coupling. Separately, these two situations have already been realized experimentally [71, 75] or are close to be reached [46, 48]. We showed that the appearance of avoided crossings in the energy spectrum at certain bias values can be modelled by a dressing of the tunneling matrix element by both Bessel functions and Laguerre polynomials, where the former result from the classical and the latter from the quantized oscillator. Thus, the tunneling oscillations in the dynamics can be modulated by a variation of the external driving or the qubit-oscillator coupling parameter. Both approaches are strongly related as also the quantized oscillator is described in the high-photon limit as classical oscillator. However, also differences exist: the Bessel function dressing can be completely suppressed by a suitable choice of driving amplitude A and external frequency ω_{ex} - coherent destruction of tunneling occurs. We can show that this CDT is robust against the oscillator coupling, at least to first order in Δ. A numerical analysis reveals a small but nonvanishing dressed frequency which leads to large-period oscillations between the two qubit states. This had already been observed in the previous chapter on the driven TLS. Nevertheless, also the numerics predict a strong localization on the short timescale. Contrary to the dressing coming from the external driving, the dressing by Laguerre polynomials depends on the coupling strength g. Moreover, there exists a dressed frequency for each oscillator quantum number K, and the corresponding Laguerre polynomials do not vanish for the same value of g. For low g/Ω only the dressing Ω_0 is of importance which exhibits no zero.

In the above discussion, we calculated second-order corrections only for the diagonal elements of the effective Hamiltonian. In order to cover also the driving-induced fast oscillations a higher-order treatment of the states would be necessary. This could be achieved by applying Van Vleck perturbation theory as introduced in Sections 2.3 and 5.2.3 to the dressed Floquet states. Concerning the validity of the above approach, we refer to the discussion of the RWA used for the driven TLS and the adiabatic approximation of the qubit-oscillator system. In particular, high-frequency driving $\omega_{\text{ex}} \gg \Delta$ and negative detuning between qubit and oscillator $\Delta < \Omega$ assures reliable results, while we saw already in Chapter 5.2.4 that even second-order corrections in Δ are not sufficient for exactly determining the disappearing of the dressed oscillation frequency. Our discussion is also valid for the biased case.

7

Summary and open questions

At the end we want to give a short overview of the major findings in this thesis. More detailed summaries can be found in Chapters 2, 4, 5 and 6.

When we started this project three years ago its working title was "Spin-boson dynamics in characteristic environments". It was based on a diploma project where we tried to generalize the investigations of Nesi et al. on the dynamics of an unbiased qubit in presence of a structured environment [139] to the biased case [140]. In that project we used the Feynman-Vernon real-time path-integral formalism to solve the spin-boson problem. One of its advantages is that one starts from an *exact*, non-Markovian master equation. However, the resulting formulae can still be rather complicated and hard to interpret. Therefore, in order to get a more intuitive understanding, we decided to use in this thesis as central setup the qubit-oscillator system coupled to an *Ohmic* bath for which an exact mapping to the spin-boson problem with a structured environment exists [20, 22, 85].

The first difficulty we faced was the diagonalization of the Hamiltonian of the nondissipative system. Apart from including the bias of the TLS, we wanted to avoid a rotating-wave approximation (RWA) and go beyond the Jaynes-Cummings model. In chapter 2, we introduced two methods to circumvent this difficulty.

First, in Sec. 2.2, Van Vleck perturbation theory (VVP) with respect to the coupling strength g was used. It takes nicely advantage of the doublet structure of the qubit-oscillator system's energy spectrum at resonance and works also for slightly detuned systems, see Sec. 2.2. We included second-order corrections in g, and thereby could also account for the Bloch-Siegert shift.

We used this approach also in Chapter 4 to determine the nondissipative dynamics. Thereby, we assumed a weak coupling between oscillator and bath, and calculated the density matrix of the qubit-oscillator system by applying the Bloch-Redfield master equations. Invoking further approximations, we were able to give analytical expressions for the relaxation and dephasing rates of the qubit, which we checked by a comparison to numerical results. In contrast to previous works where the model was treated by a perturbative approach with respect to the coupling between TLS and *structured* bath, we could correctly include the influence of the oscillator on the rates. To our knowledge, this work provided for the first time closed analytical expressions for the dissipative qubit-oscillator system for both the biased and unbiased, resonant and detuned case. A comparison to the dissipative Jaynes-Cummings model in Section 4.4 showed that for a slightly detuned system an inclusion of counter-rotating terms is necessary to obtain a correct picture of the relaxation and dephasing behavior. An understanding of the rates is crucial in experimental situations as introduced in Chapter 1, where the qubit suffers from dissipation and decoherence induced from the surrounding circuitry. However, analytical expressions for the dynamics and the rates do not come for free: Because of the Born approximation we were limited to small system bath couplings, $\kappa \ll 1$, which corresponds to an oscillator of small linewidth $\Gamma/2\pi\Omega \ll 1$. Furthermore, for too low bath temperatures the Markov approximation becomes questionable. In this work we assumed temperatures corresponding to frequencies being one order of magnitude smaller than the qubit's energy splitting. Together with the used values for the damping the resulting relaxation times are at the lower limit for the Markov approximation to be justified. Stronger damping or lower bath temperatures (larger thermal correlation time) ask for a non-Markovian treatment as provided, e.g., by the path-integral formalism. Despite all these limitations, the model seems to be suited to mimic realistic, experimental situations [20, 22].

Another limitation concerned the qubit-oscillator coupling: The perturbative treatment with respect to g restricted our considerations to intermediate coupling strengths. Nevertheless, by the time doing the above calculations this was only a minor concern, because dimensionless coupling strengths of more than a few percent seemed to be beyond the experimental reach, and effects like the Bloch-Siegert shift were unlikely to be observed. The situation changed dramatically within an astonishingly short time: fabrication techniques of circuit QED devices experienced an enormous boost, and ultrastrong coupling became more than just a theoretical concept, see Chapter 1. The break-down of the Jaynes-Cummings Hamiltonian has been demonstrated and the Bloch-Siegert shift has been measured. As even coupling strengths of $g/\Omega \geq 1$ seem possible, nonperturbative treatments in g became necessary. Therefore, we used in Sec. 2.3 as our second analytical approach to diagonalize the qubit-oscillator system a combination of the polaron transformation and Van Vleck perturbation theory in the qubit tunneling matrix element Δ. We compared this approach to the generalized rotating-wave approximation (GRWA) and the so-called adiabatic approximation, where we extended the latter to the biased case. Numerical calculations showed that our analytics yield reliable results for $\Delta < \Omega$ and for certain coupling strengths even for resonance and positive detuning, see discussion in Sec. 2.3.

In Chapter 5 we investigated – motivated by the experiment by Wilson et al. [71] – the qubit coupled to an oscillator in the high-photon limit. In contrast to Chapter 2, we did not use the dressed state picture to describe the dynamics of the system, but rather chose a semiclassical treatment in which the oscillator is described by a classical driving term acting on the bias of the qubit. In order to diagonalize the underlying Floquet Hamiltonian we applied Van Vleck perturbation theory with respect to Δ. There is a strong analogy to the approach used in Sec. 2.3: The coupling to the quantized oscillator with coupling strength g and frequency Ω becomes a sinusoidal driving of amplitude A and external frequency ω_{ex}. The dressing of the tunneling matrix element by Laguerre polynomials is replaced by a dressing with Bessel functions and the adiabatic approximation corresponds to a rotating-wave approximation with respect to Δ in the Floquet Hamiltonian. We went beyond this RWA and included also second-order corrections which become especially important away from an m–photon resonance $\varepsilon = m\omega_{\text{ex}}$ and, furthermore, are necessary to take into account fast driving-induced oscillations in the dynamics. Coupling the driven TLS to an Ohmic bath led us to the driven spin-boson model, which we solved using the Floquet-Born-Markov master equation. We found that we had to go beyond the RWA for an accurate description of the relaxation and dephasing rates. For both cases of a TLS with and without bath we examined coherent destruction of tunneling and driving-induced tunneling oscillations, where also strong differences between the RWA and VVP treatment were found.

Finally, in Chapter 6, we used both the dressed state picture of Sec. 2.3 and Floquet theory to treat the classically driven qubit-oscillator system. Remarkably, our approach is perturbative neither in the coupling strength g nor in the driving amplitude A and thus clearly

goes beyond previous approaches like the driven Jaynes-Cummings model. Owing to the complexity of the problem, we only treated the spectrum of the Floquet Hamiltonian up to second order in Δ, while using first-order states. Still, the coarse-grained dynamics obtained from the analytics exhibits a good agreement with the numerics, and we were able to explain the appearance or vanishing of certain oscillation frequencies, in particular proving the existence of CDT also for the qubit-oscillator system.
The field of quantum circuit QED evolves at an incredible speed. Only a bit more than 10 years passed between the first proof of microscopic quantum coherence in superconducting circuits and the advance into the ultrastrong coupling regime. Today, simple gate operations are performed with superconducting qubits, and transmission lines are used as quantum buses. We hope that we can give with this thesis a small contribution to the further development. There are still many open questions left. We will list a few of them which are directly related to this work and give suggestions for further proceeding:

Open questions

- In this thesis we included dissipative effects for the case of the qubit-oscillator system treated within Van Vleck perturbation theory with respect to g and for the driven TLS. It should be straightforward to use the methods introduced there also for the displaced oscillator basis and the driven qubit-oscillator system. For $g \ll \Delta$ the dependence of the dephasing on g is found to be rather weak [86]. It will be interesting to see if this behavior changes in the ultrastrong coupling regime.

- Although a bit tedious, a calculation of the eigenstates of the Floquet Hamiltonian of the driven qubit-oscillator system to second order follows the same lines as in Secs. 2.3 and 5.2.3. It will allow us to use larger tunneling matrix elements, $\Delta \gtrsim \Omega$, and give in combination with a master equation approach a realistic picture of the rates.

- In Chapter 6, the driving was assumed to couple to the TLS. Also the contrary case of the oscillator being driven promises to be interesting and has been so far only examined within the driven Jaynes-Cummings model [137]. The basis for this project is already given in the Bachelor thesis of Johannes Kleiner [141].

- We also used the approach of Sec. 2.2 for a qubit coupled to a nonlinear oscillator [36]. This work could also be extended to the ultrastrong coupling and extreme driving regime.

A Van Vleck perturbation theory

Let us consider the Hamiltonian

$$H = H_0 + V \tag{A.1}$$

consisting of the free Hamiltonian H_0 and a small perturbation V. Additionally we assume that the energy levels $E_{j,\alpha}$ of H_0 are grouped into manifolds, with α being the index of the manifold and j is used to distinguish between different energy levels within the same manifold. The energy levels $E_{j,\alpha}$ are eigenenergies of H_0:

$$H_0|j,\alpha\rangle = E_{j,\alpha}|j,\alpha\rangle. \tag{A.2}$$

Through the perturbation V different manifolds are coupled together. As long as the perturbation is small, namely $|\langle j,\alpha|V|j,\beta\rangle| \ll |E_{j,\alpha} - E_{j,\beta}|$ for $\alpha \neq \beta$, also the energy levels of the total Hamiltonian H are clustered into manifolds. Using the transformation $H_{\text{eff}} = \mathrm{e}^{\mathrm{i}S} H \mathrm{e}^{-\mathrm{i}S}$, we construct an effective Hamiltonian H_{eff} which acts only within the individual manifolds; i.e., $\langle j,\alpha|H_{\text{eff}}|j,\beta\rangle = 0$ for $\alpha \neq \beta$, and has the same eigenvalues as H within the manifolds. We expand S and H_{eff} in terms of the small parameter V up to second order:

$$S = S^{(1)} + S^{(2)} + \mathcal{O}(V^3) \quad \text{and} \quad H_{\text{eff}} = H_{\text{eff}}^{(0)} + H_{\text{eff}}^{(1)} + H_{\text{eff}}^{(2)} + \mathcal{O}(V^3) \tag{A.3}$$

For calculating $S^{(1/2)}$ and $H_{\text{eff}}^{(1/2)}$ we use that $\langle j,\alpha|H_{\text{eff}}^{(1/2)}|j,\beta\rangle = 0$ for $\alpha \neq \beta$ and furthermore choose that S has no matrix elements within a manifold, namely $\langle j,\alpha|iS^{(1/2)}|j,\alpha\rangle = 0$. Now, one can iteratively calculate S and H_{eff} order by order. For details see [28]. Here, we give only the results. For the transformation one has

$$\langle j,\alpha|iS^{(1)}|j,\beta\rangle = \frac{\langle j,\alpha|V|j,\beta\rangle}{E_{j,\alpha} - E_{j,\beta}}, \quad \text{for} \quad \alpha \neq \beta, \tag{A.4}$$

and

$$\begin{aligned}\langle j,\alpha|iS^{(2)}|j,\beta\rangle =& \frac{1}{2}\sum_{k,\gamma\neq\alpha,\beta} \frac{\langle j,\alpha|V|k,\gamma\rangle\langle k,\gamma|V|j,\beta\rangle}{E_{j,\beta} - E_{j,\alpha}} \left[\frac{1}{E_{k,\gamma} - E_{j,\alpha}} + \frac{1}{E_{k,\gamma} - E_{j,\beta}}\right] \\ &+ \sum_k \frac{1}{E_{j,\beta} - E_{j,\alpha}} \frac{\langle j,\alpha|V|k,\beta\rangle\langle k,\beta|V|j,\beta\rangle}{E_{k,\beta} - E_{j,\alpha}} \\ &+ \sum_k \frac{1}{E_{j,\beta} - E_{j,\alpha}} \frac{\langle j,\alpha|V|k,\alpha\rangle\langle k,\alpha|V|j,\beta\rangle}{E_{k,\alpha} - E_{j,\beta}}, \quad \text{for} \quad \alpha \neq \beta. \end{aligned} \tag{A.5}$$

The effective Hamiltonian is up to second order

$$\begin{aligned}\langle i,\alpha|H_{\text{eff}}|j,\alpha\rangle =& E_{j,\alpha}\delta_{ij} + \langle i,\alpha|V|j,\alpha\rangle \\ &+ \frac{1}{2}\sum_{k,\gamma\neq\alpha} \langle i,\alpha|V|k,\gamma\rangle\langle k,\gamma|V|j,\alpha\rangle \left[\frac{1}{E_{i,\alpha} - E_{k,\gamma}} + \frac{1}{E_{j,\alpha} - E_{k,\gamma}}\right] + \mathcal{O}(V^3). \end{aligned} \tag{A.6}$$

Finally, we get the transformation up to second order in V:

$$e^{\pm\mathrm{i}S} = \mathbb{1} \pm \mathrm{i}S^{(1)} \pm \mathrm{i}S^{(2)} + \frac{1}{2}\mathrm{i}S^{(1)}\mathrm{i}S^{(1)} + \mathcal{O}(V^3). \tag{A.7}$$

A.1 Perturbation in g

In this section, we give the transformation matrix elements of S for Van Vleck perturbation theory performed on the qubit-oscillator Hamiltonian with respect to the coupling strength, g, see Sec. 2.2. The first-order matrix elements are

$$\mathrm{i}S^{(1)}_{\mathrm{e}_{j-1}\mathrm{e}_j} = \sqrt{j}\frac{\varepsilon}{E_{\mathrm{qb}}\Omega}g, \tag{A.8a}$$

$$\mathrm{i}S^{(1)}_{\mathrm{g}_j\mathrm{g}_{j+1}} = -\sqrt{j+1}\frac{\varepsilon}{E_{\mathrm{qb}}\Omega}g, \tag{A.8b}$$

$$\mathrm{i}S^{(1)}_{\mathrm{g}_j\mathrm{e}_{j+1}} = \sqrt{j+1}\frac{\Delta}{E_{\mathrm{qb}}(E_{\mathrm{qb}}+\Omega)}g, \tag{A.8c}$$

and for the second-order contributions

$$\mathrm{i}S^{(2)}_{\mathrm{e}_j\mathrm{g}_{j+2}} = 2\sqrt{(j+1)(j+2)}\frac{\varepsilon\Delta}{E^2_{\mathrm{qb}}\Omega(2\Omega - E_{\mathrm{qb}})}g^2, \tag{A.9a}$$

$$\mathrm{i}S^{(2)}_{\mathrm{e}_j\mathrm{e}_{j+2}} = -\sqrt{(j+1)(j+2)}\frac{\Delta^2}{2E^2_{\mathrm{qb}}\Omega(E_{\mathrm{qb}}+\Omega)}g^2, \tag{A.9b}$$

$$\mathrm{i}S^{(2)}_{\mathrm{g}_j\mathrm{e}_j} = -\frac{1}{2}(2j+1)\frac{\varepsilon\Delta}{E^2_{\mathrm{qb}}\Omega(E_{\mathrm{qb}}+\Omega)}g^2, \tag{A.9c}$$

$$\mathrm{i}S^{(2)}_{\mathrm{g}_j\mathrm{g}_{j+2}} = \frac{1}{2}\sqrt{(j+1)(j+2)}\frac{\Delta^2}{E^2_{\mathrm{qb}}\Omega(\Omega+E_{\mathrm{qb}})}g^2, \tag{A.9d}$$

$$\mathrm{i}S^{(2)}_{\mathrm{g}_j\mathrm{e}_{j+2}} = -\sqrt{(j+1)(j+2)}\frac{\varepsilon\Delta}{E_{\mathrm{qb}}\Omega(E_{\mathrm{qb}}+\Omega)(E_{\mathrm{qb}}+2\Omega)}g^2, \tag{A.9e}$$

where, e.g.,

$$S^{(1)}_{\mathrm{e}_{j-1}\mathrm{e}_j} = \langle (j-1), \mathrm{e}|S|j, \mathrm{e}\rangle. \tag{A.10}$$

These matrix elements change sign under index transposition and all other matrix elements vanish.

A.2 Perturbation in Δ

We calculate the matrix element of the transformation matrix S obtained by Van Vleck perturbation theory with respect to Δ for the qubit-oscillator system, where the latter is either in the quantized (Sec. 2.3) or in the classical regime (Sec. 5.2.3). Both situations are analogous and can be derived from each other. For clearness we show both cases.

A.2.1 The quantized oscillator

We examine the TLS coupled to a quantized harmonic oscillator, Sec. 2.3. As basis states we use $\{|\widetilde{j,\uparrow}\rangle, |\widetilde{j,\downarrow}\rangle\}$, Eqs. (2.29) and (2.30). To first order the matrix elements are:

$$\langle \widetilde{j,\downarrow/\uparrow}|\mathrm{i}S^{(1)}|\widetilde{j',\uparrow/\downarrow}\rangle = -\frac{(\pm)^{|j'-j|}}{2}\frac{\Delta^{j'}_{j}}{\varepsilon \mp (j'-j)\Omega}(1-\delta_{j\pm l,j'}). \tag{A.11}$$

To second order we get,

$$\begin{aligned}\langle \widetilde{j,\uparrow}|\mathrm{i}S^{(2)}|\widetilde{j',\uparrow}\rangle =&\frac{1}{4(j'-j)\Omega}\Bigg\{ \sum_{\substack{k=0\\ k\neq\{j-l,j'-l\}}}^{\infty} \frac{\Delta_k^j\Delta_k^{j'}}{2}\left[\frac{1}{\varepsilon+(k-j)\Omega}+\frac{1}{\varepsilon+(k-j')\Omega}\right]\\ &+\frac{\Delta^j_{j'-l}\Delta^{j'}_{j'-l}}{\varepsilon+(j'-l-j)\Omega}+\frac{\Delta^j_{j-l}\Delta^{j'}_{j-l}}{\varepsilon+(j-l-j')\Omega}\Bigg\}(1-\delta_{j,j'}),\end{aligned} \tag{A.12}$$

$$\begin{aligned}\langle \widetilde{j,\downarrow}|\mathrm{i}S^{(2)}|\widetilde{j',\downarrow}\rangle =&\frac{1}{4(j'-j)\Omega}\Bigg\{ \sum_{\substack{k=0\\ k\neq\{j+l,j'+l\}}}^{\infty} \frac{\Delta_j^k\Delta_{j'}^{k}}{2}\left[\frac{1}{-\varepsilon+(k-j)\Omega}+\frac{1}{-\varepsilon+(k-j')\Omega}\right]\\ &+\frac{\Delta_j^{j'+l}\Delta_{j'}^{j'+l}}{-\varepsilon+(j'+l-j)\Omega}+\frac{\Delta_j^{j+l}\Delta_{j'}^{j+l}}{-\varepsilon+(j+l-j')\Omega}\Bigg\}(1-\delta_{j,j'}).\end{aligned} \tag{A.13}$$

Using the above expressions, we find the eigenstates of H to second order in Δ as

$$|\Phi_{j,\pm}\rangle = |\Phi^{(0)}_{j,\pm}\rangle + |\Phi^{(1)}_{j,\pm}\rangle + |\Phi^{(2)}_{j,\pm}\rangle \tag{A.14}$$

with

$$|\Phi^{(1)}_{j,-}\rangle = \sin\frac{\Theta_j^l}{2}\sum_{j'=0}^{\infty}|\widetilde{j',\uparrow}\rangle\langle\widetilde{j',\uparrow}|\mathrm{i}S^{(1)}|\widetilde{j,\downarrow}\rangle + \mathrm{sign}\left(\Delta_j^{j+l}\right)\cos\frac{\Theta_j^l}{2}\sum_{j'=0}^{\infty}|\widetilde{j',\downarrow}\rangle\langle\widetilde{j',\downarrow}|\mathrm{i}S^{(1)}|\widetilde{j+l,\uparrow}\rangle \tag{A.15}$$

and

$$\begin{aligned}|\Phi^{(2)}_{j,-}\rangle =&\sin\frac{\Theta_j^l}{2}\sum_{j'=0}^{\infty}|\widetilde{j',\downarrow}\rangle\langle\widetilde{j',\downarrow}|\mathrm{i}S^{(2)}|\widetilde{j,\downarrow}\rangle + \mathrm{sign}\left(\Delta_j^{j+l}\right)\cos\frac{\Theta_j^l}{2}\sum_{j'=0}^{\infty}|\widetilde{j',\uparrow}\rangle\langle\widetilde{j',\uparrow}|\mathrm{i}S^{(2)}|\widetilde{j+l,\uparrow}\rangle\\ &-\frac{1}{2}\sin\frac{\Theta_j^l}{2}\sum_{j'=0,k'=0}^{\infty}|\widetilde{j',\downarrow}\rangle\langle\widetilde{j',\downarrow}|\mathrm{i}S^{(1)}|\widetilde{k',\uparrow}\rangle\langle\widetilde{k',\uparrow}|\mathrm{i}S^{(1)}|\widetilde{j,\downarrow}\rangle\\ &-\frac{1}{2}\mathrm{sign}\left(\Delta_j^{j+l}\right)\cos\frac{\Theta_j^l}{2}\sum_{j'=0,k'=0}^{\infty}|\widetilde{j',\uparrow}\rangle\langle\widetilde{j',\uparrow}|\mathrm{i}S^{(1)}|\widetilde{k',\downarrow}\rangle\langle\widetilde{k',\downarrow}|\mathrm{i}S^{(1)}|\widetilde{j+l,\uparrow}\rangle.\end{aligned} \tag{A.16}$$

For $|\Phi^{(i)}_{j,+}\rangle$ one just replaces $\sin\frac{\Theta_j^l}{2}\rightarrow -\cos\frac{\Theta_j^l}{2}$ and $\cos\frac{\Theta_j^l}{2}\rightarrow\sin\frac{\Theta_j^l}{2}$.

A.2.2 The classical oscillator

Here, we give the matrix elements of the transformation matrix S to second order in Δ expressed in the eigenstates (5.45) of the unperturbed Hamiltonian of the classically driven system in Sec. 5.2.3. Its elements are [28]

$$\langle\langle u^0_{n,\uparrow}|\mathrm{i}S^{(1)}|u^0_{l,\downarrow}\rangle\rangle = \frac{1}{2}\frac{\Delta_{n-l}}{\varepsilon+\omega(n-l)}(1-\delta_{l-n,m}), \tag{A.17}$$

$$\langle\langle u^0_{l,\downarrow}|\mathrm{i}S^{(1)}|u^0_{n,\uparrow}\rangle\rangle = -\frac{1}{2}\frac{\Delta_{n-l}}{\varepsilon+\omega(n-l)}(1-\delta_{l-n,m}). \tag{A.18}$$

For the second-order elements, we find

$$\langle\langle u^0_{n,\uparrow}|\mathrm{i}S^{(2)}|u^0_{j,\uparrow}\rangle\rangle = \frac{1}{4(n-j)\omega}\Bigg\{\sum_{\substack{k\neq n+m\\ k\neq j+m}}\frac{\Delta_{n-k}\Delta_{j-k}}{2}\left[\frac{1}{\varepsilon+(n-k)\omega}+\frac{1}{\varepsilon+(j-k)\omega}\right] + \frac{\Delta_{n-j-m}\Delta_{-m}}{\varepsilon+(n-j-m)\omega}+\frac{\Delta_{j-n-m}\Delta_{-m}}{\varepsilon+(j-n-m)\omega}\Bigg\}(1-\delta_{j,n}), \tag{A.19}$$

$$\langle\langle u^0_{n,\downarrow}|\mathrm{i}S^{(2)}|u^0_{j,\downarrow}\rangle\rangle = \frac{1}{4(n-j)\omega}\Bigg\{\sum_{\substack{k\neq n-m\\ k\neq j-m}}\frac{\Delta_{k-n}\Delta_{k-j}}{2}\left[\frac{1}{-\varepsilon+(n-k)\omega}+\frac{1}{-\varepsilon+(j-k)\omega}\right] + \frac{\Delta_{j-m-n}\Delta_{-m}}{-\varepsilon+(n-j+m)\omega}+\frac{\Delta_{n-m-j}\Delta_{-m}}{-\varepsilon+(j-n+m)\omega}\Bigg\}(1-\delta_{j,n}), \tag{A.20}$$

$$\langle\langle u^0_{n,\uparrow}|\mathrm{i}S^{(2)}|u^0_{j,\downarrow}\rangle\rangle = \langle\langle u^0_{j,\downarrow}|\mathrm{i}S^{(2)}|u^0_{n,\uparrow}\rangle\rangle = 0. \tag{A.21}$$

These matrix elements correspond to the ones of the qubit coupled to the quantized oscillator, Eqs. (A.11) – (A.13). By applying the transformation now on the eigenstates of the effective Hamiltonian $|\Phi^{\mathrm{eff}}_{n,\mp}\rangle\rangle$, see Sec. 5.2.3, we get the eigenstates of the Floquet Hamiltonian $\mathcal{H}_{\mathrm{TLS}}$ to first order in Δ,

$$|\Phi^{(1)}_{n,-}\rangle\rangle = |\Phi^{\mathrm{eff}}_{n,-}\rangle\rangle + \frac{1}{2}\sum_{j\neq -m}\frac{\Delta_j}{\varepsilon+j\omega}\left\{\mathrm{sign}\,(\Delta_{-m})\cos\frac{\Theta_m}{2}|u^0_{j+n+m,\uparrow}\rangle\rangle - \sin\frac{\Theta_m}{2}|u^0_{n-j,\downarrow}\rangle\rangle\right\}, \tag{A.22}$$

$$|\Phi^{(1)}_{n,+}\rangle\rangle = |\Phi^{\mathrm{eff}}_{n,+}\rangle\rangle + \frac{1}{2}\sum_{j\neq -m}\frac{\Delta_j}{\varepsilon+j\omega}\left\{\mathrm{sign}\,(\Delta_{-m})\sin\frac{\Theta_m}{2}|u^0_{j+n,\uparrow}\rangle\rangle + \cos\frac{\Theta_m}{2}|u^0_{n-m-j,\downarrow}\rangle\rangle\right\}. \tag{A.23}$$

And to second order,

$$\begin{aligned}|\Phi^{(2)}_{n,-}\rangle\rangle = |\Phi^{(1)}_{n,-}\rangle\rangle &+ \sum_{j\neq 0}\left\{\sin\frac{\Theta_m}{2}|u^0_{j+n,\uparrow}\rangle\rangle + \mathrm{sign}\,(\Delta_{-m})\cos\frac{\Theta_m}{2}|u^0_{-j+n+m,\downarrow}\rangle\rangle\right\}\\ &\times\Bigg\{\frac{\Delta_{-m}}{4j\omega}\left[\frac{\Delta_{j-m}}{\varepsilon+(j-m)\omega}+\frac{\Delta_{-j-m}}{\varepsilon-(j+m)\omega}\right]\\ &\quad+\sum_{\substack{p\neq -j-m\\ p\neq -m}}\frac{1}{4j\omega}\frac{\Delta_{j+p}\Delta_p}{2}\left[\frac{1}{\varepsilon+(j+p)\omega}+\frac{1}{\varepsilon+p\omega}\right]\Bigg\}\\ &+\frac{1}{8}\sum_{k\neq -m}\sum_{j\neq -m}\frac{\Delta_k\Delta_j}{(\varepsilon+k\omega)(\varepsilon+j\omega)}\left\{\sin\frac{\Theta_m}{2}|u^0_{k+n-j,\uparrow}\rangle\rangle + \mathrm{sign}\,(\Delta_{-m})\cos\frac{\Theta_m}{2}|u^0_{k+n+m-j,\downarrow}\rangle\rangle\right\},\end{aligned} \tag{A.24}$$

$$\begin{aligned}
|\Phi^{(2)}_{n,+}\rangle\rangle = |\Phi^{(1)}_{n,+}\rangle\rangle - \sum_{j\neq 0} &\left\{ \cos\frac{\Theta_m}{2}|u^0_{j+n-m,\uparrow}\rangle\rangle - \operatorname{sign}(\Delta_{-m})\sin\frac{\Theta_m}{2}|u^0_{-j+n,\downarrow}\rangle\rangle \right\} \\
\times &\left\{ \frac{1}{4j\omega}\left[\frac{\Delta_{j-m}\Delta_{-m}}{\varepsilon+(j-m)\omega} + \frac{\Delta_{-j-m}\Delta_{-m}}{\varepsilon-(j+m)\omega}\right] \right. \\
&\left. + \sum_{\substack{p\neq -j-m \\ p\neq -m}} \frac{1}{4j\omega}\frac{\Delta_{j+p}\Delta_p}{2}\left[\frac{1}{\varepsilon+(j+p)\omega} + \frac{1}{\varepsilon+p\omega}\right]\right\} \\
- \frac{1}{8}\sum_{k\neq -m}\sum_{j\neq -m} &\frac{\Delta_k\Delta_j}{(\varepsilon+k\omega)(\varepsilon+j\omega)}\left\{\cos\frac{\Theta_m}{2}|u^0_{k+n-j-m,\uparrow}\rangle\rangle - \operatorname{sign}(\Delta_{-m})\sin\frac{\Theta_m}{2}|u^0_{j+n-k,\downarrow}\rangle\rangle\right\} .
\end{aligned} \tag{A.25}$$

B Dynamics

In this appendix, we derive expressions for the population difference and survival probability, starting from the density operator of the system under observation.

B.1 Dynamics of the qubit-oscillator system

Here, we show how to derive Eq. (2.21) given in Sec. 2.2.2. In order to trace out the oscillator degrees of freedom we transform $\rho_{nm}(t)$ into the basis $\{|j,\mathrm{g}\rangle;|j,\mathrm{e}\rangle\}$ and by using $\rho_{nm}=\rho^*_{mn}$ we find

$$\rho_{j\mathrm{g},j\mathrm{g}}(t)=\langle j,\mathrm{g}|\rho(t)|j,\mathrm{g}\rangle=\sum_n\langle j,\mathrm{g}|n\rangle^2\rho_{nn}(t)+\sum_{\substack{n,m\\n\neq m}}\mathrm{Re}\{\rho_{nm}(t)\}\langle j,\mathrm{g}|n\rangle\langle m|j,\mathrm{g}\rangle \tag{B.1a}$$

$$\rho_{j\mathrm{e},j\mathrm{e}}(t)=\langle j,\mathrm{e}|\rho(t)|j,\mathrm{e}\rangle=\sum_n\langle j,\mathrm{e}|n\rangle^2\rho_{nn}(t)+\sum_{\substack{n,m\\n\neq m}}\mathrm{Re}\{\rho_{nm}(t)\}\langle j,\mathrm{e}|n\rangle\langle m|j,\mathrm{e}\rangle. \tag{B.1b}$$

Performing the trace over the oscillator

$$\rho_{\mathrm{red;gg}}(t)=\langle \mathrm{g}|\rho_{\mathrm{red}}(t)|\mathrm{g}\rangle=\sum_{j=0}^{\infty}\sum_n\langle j,\mathrm{g}|n\rangle^2\rho_{nn}(t)+\sum_{j=0}^{\infty}\sum_{\substack{n,m\\n\neq m}}\mathrm{Re}\{\rho_{nm}(t)\}\langle j,\mathrm{g}|n\rangle\langle m|j,\mathrm{g}\rangle, \tag{B.2a}$$

$$\rho_{\mathrm{red;ee}}(t)=\langle \mathrm{e}|\rho_{\mathrm{red}}(t)|\mathrm{e}\rangle=\sum_{j=0}^{\infty}\sum_n\langle j,\mathrm{e}|n\rangle^2\rho_{nn}(t)+\sum_{j=0}^{\infty}\sum_{\substack{n,m\\n\neq m}}\mathrm{Re}\{\rho_{nm}(t)\}\langle j,\mathrm{e}|n\rangle\langle m|j,\mathrm{e}\rangle. \tag{B.2b}$$

Similarily, we find for the off-diagonal elements of the reduced density matrix

$$\begin{aligned}\rho_{\mathrm{red;eg}}(t)=&\sum_{j=0}^{\infty}\sum_n\langle j,\mathrm{e}|n\rangle\rho_{nn}(t)\langle n|j,\mathrm{g}\rangle\\&+\frac{1}{2}\sum_{j=0}^{\infty}\sum_{\substack{n,m\\n\neq m}}\left[\langle j,\mathrm{e}|n\rangle\rho_{nm}(t)\langle m|j,\mathrm{g}\rangle+\langle j,\mathrm{e}|m\rangle\rho^*_{nm}(t)\langle j,\mathrm{g}|n\rangle\right],\end{aligned} \tag{B.3a}$$

$$\begin{aligned}\rho_{\mathrm{red;ge}}(t)=&\sum_{j=0}^{\infty}\sum_n\langle j,\mathrm{g}|n\rangle\rho_{nn}(t)\langle n|j,\mathrm{e}\rangle\\&+\frac{1}{2}\sum_{j=0}^{\infty}\sum_{\substack{n,m\\n\neq m}}\left[\langle j,\mathrm{g}|n\rangle\rho_{nm}(t)\langle m|j,\mathrm{e}\rangle+\langle j,\mathrm{g}|m\rangle\rho^*_{nm}(t)\langle j,\mathrm{e}|n\rangle\right].\end{aligned} \tag{B.3b}$$

With this we can express the population difference $P(t)$ in the energy basis, yielding

$$\begin{align}
P(t) =& \cos\Theta\left[\rho_{\mathrm{red;gg}}(t) - \rho_{\mathrm{red;ee}}(t)\right] + \sin\Theta\left[\rho_{\mathrm{red;ge}}(t) + \rho_{\mathrm{red;eg}}(t)\right] \notag\\
=& \cos\Theta\Bigg(\sum_{j=0}^{\infty}\sum_{n}\left[\langle j\mathrm{g}|n\rangle^2 - \langle j,\mathrm{e}|n\rangle^2\right]\rho_{nn}(t) \notag\\
&+ \sum_{j=0}^{\infty}\sum_{\substack{n,m\\ n\neq m}}\left[\langle j,\mathrm{g}|n\rangle\langle m|j,\mathrm{g}\rangle - \langle j,\mathrm{g}|n\rangle\langle m|j,\mathrm{g}\rangle\right]\mathrm{Re}\{\rho_{nm}(t)\}\Bigg) \notag\\
&+ \sin\Theta\Bigg(2\sum_{j=0}^{\infty}\sum_{n}\langle j,\mathrm{e}|n\rangle\rho_{nn}(t)\langle n|j,\mathrm{g}\rangle \tag{B.4}\\
&+ \sum_{j=0}^{\infty}\sum_{\substack{n,m\\ n\neq m}}\left[\langle j,\mathrm{e}|n\rangle\langle m|j,\mathrm{g}\rangle + \langle j,\mathrm{e}|m\rangle\langle j,\mathrm{g}|n\rangle\right]\mathrm{Re}\{\rho_{nm}(t)\}\Bigg). \tag{B.5}
\end{align}$$

With Eq. (2.23) we can write

$$P(t) = \sum_{n} p_{nn}(t) + \sum_{\substack{n,m\\ n>m}} p_{nm}(t)\cos\omega_{nm}t, \tag{B.6}$$

where

$$\begin{align}
p_{nn}(t) =& \sum_{j}\left\{\cos\Theta\left[\langle j,\mathrm{g}|n\rangle^2 - \langle j,\mathrm{e}|n\rangle^2\right] + 2\sin\Theta\langle j,\mathrm{g}|n\rangle\langle j,\mathrm{e}|n\rangle\right\}\rho_{nn}(t), \tag{B.7a}\\
p_{nm}(t) =& 2\sum_{j}\Bigg\{\cos\Theta\left[\langle j,\mathrm{g}|n\rangle\langle m|j,\mathrm{g}\rangle - \langle j,\mathrm{e}|n\rangle\langle m|j,\mathrm{e}\rangle\right] \notag\\
&+ \sin\Theta\left[\langle j,\mathrm{e}|n\rangle\langle m|j,\mathrm{g}\rangle + \langle j,\mathrm{e}|m\rangle\langle n|j,\mathrm{g}\rangle\right]\Bigg\}\mathrm{Re}\{\rho_{nm}(t)\}. \tag{B.7b}
\end{align}$$

B.2 Dynamics of the driven TLS

To calculate the survival probability of the system, $P_{\gamma\to\gamma}(t)$, where $\gamma =\uparrow,\downarrow$, we start with the density operator $\rho(t)$ of the TLS, fulfilling the condition that $\rho(0) = |\gamma\rangle\langle\gamma|$. By diagonalization of the Floquet matrix (5.46) or by solving the master equation (5.79), we obtain the density matrix in energy basis with the matrix elements

$$\rho_{\alpha\beta}(t) = \langle\Phi_\alpha(t)|\rho(t)|\Phi_\beta(t)\rangle \qquad \alpha,\beta = \pm. \tag{B.8}$$

Using that $\rho_{--}(t) + \rho_{++}(t) = 1$ and $\rho_{-+}(t) = \rho^{*}_{+-}(t)$, we get

$$\begin{align}
P_{\gamma\to\gamma}(t) =& 2\mathrm{Re}\left\{\langle\gamma|\Phi_-(t)\rangle\langle\Phi_+(t)|\gamma\rangle\rho_{-+}(t)\right\} + |\langle\gamma|\Phi_+(t)\rangle|^2 \notag\\
&+ \left(|\langle\gamma|\Phi_-(t)\rangle|^2 - |\langle\gamma|\Phi_+(t)\rangle|^2\right)\rho_{--}(t). \tag{B.9}
\end{align}$$

The corresponding transition probability is just $P_{\gamma\to\delta}(t) = 1 - P_{\gamma\to\gamma}(t)$, where $\delta\neq\gamma$. We get the components $\langle\gamma|\Phi_\alpha(t)\rangle$ of the Floquet states in Eq. (B.9) using formula (5.26).

B.2.1 Survival probability in the nondissipative case

For the Hamiltonian of the nondissipative TLS, Eq. (5.43), the master equation is simply

$$\dot{\rho}_{\alpha\beta}(t) = -\mathrm{i}(\varepsilon_\alpha - \varepsilon_\beta)\rho_{\alpha\beta}(t), \tag{B.10}$$

so that $\rho_{--}(t) = \rho_{--}(0)$ and $\rho_{-+}(t) = \rho_{-+}(0)\exp\left[\mathrm{i}\left(m\omega_{\mathrm{ex}} + \Omega_m^{(2)}\right)t\right]$, where we used the general expression for the quasienergies at an m-photon resonance found in Sec. 5.2. The starting conditions are calculated through

$$\rho_{\alpha\beta}(0) = \langle\Phi_\alpha(0)|\gamma\rangle\langle\gamma|\Phi_\beta(0)\rangle. \tag{B.11}$$

Combing this, one gets

$$\begin{aligned} P_{\gamma\to\gamma}(t) = {} & \left(|\langle\gamma|\Phi_-(t)\rangle|^2 - |\langle\gamma|\Phi_+(t)\rangle|^2\right)|\langle\gamma|\Phi_-(0)\rangle|^2 + |\langle\gamma|\Phi_+(t)\rangle|^2 \\ & + 2\mathrm{Re}\left\{\langle\gamma|\Phi_-(t)\rangle\langle\Phi_+(t)|\gamma\rangle\langle\Phi_-(0)|\gamma\rangle\langle\gamma|\Phi_+(0)\rangle \mathrm{e}^{\mathrm{i}\left(m\omega_{\mathrm{ex}}+\Omega_m^{(2)}\right)t}\right\}. \end{aligned} \tag{B.12}$$

RWA survival probability

Using in this general expression the eigenstates (5.53) and (5.54), we arrive at the survival probability in the RWA,

$$P^{\mathrm{RWA}}_{\downarrow\to\downarrow}(t) = \cos^2\left(\Omega_m^{\mathrm{RWA}}\frac{t}{2}\right) + \cos^2\Theta_m^{\mathrm{RWA}}\sin^2\left(\Omega_m^{\mathrm{RWA}}\frac{t}{2}\right). \tag{B.13}$$

Van Vleck survival probability

To get the survival probability to second order in Δ, we use (A.22) – (A.25) in (5.26) and obtain

$$\begin{aligned} \langle\downarrow|\Phi_-^{(2)}(t)\rangle = {} & \exp\left(-\mathrm{i}\frac{A}{2\omega_{\mathrm{ex}}}\sin\omega_{\mathrm{ex}}t\right)\left\{-\mathrm{sign}\,(\Delta_{-m})\cos\frac{\Theta_m}{2}\mathrm{e}^{-\mathrm{i}m\omega_{\mathrm{ex}}t} - \frac{1}{2}\sin\frac{\Theta_m}{2}A(t)\right. \\ & \left. + \,\mathrm{sign}\,(\Delta_{-m})\cos\frac{\Theta_m}{2}\mathrm{e}^{-\mathrm{i}m\omega_{\mathrm{ex}}t}\left[B(t)+C(t)\right]\right\}, \end{aligned} \tag{B.14}$$

$$\begin{aligned} \langle\downarrow|\Phi_+^{(2)}(t)\rangle = {} & \exp\left(-\mathrm{i}\frac{A}{2\omega_{\mathrm{ex}}}\sin\omega_{\mathrm{ex}}t\right)\left\{-\mathrm{sign}\,(\Delta_{-m})\sin\frac{\Theta_m}{2} + \frac{1}{2}\cos\frac{\Theta_m}{2}\mathrm{e}^{\mathrm{i}m\omega_{\mathrm{ex}}t}A(t)\right. \\ & \left. + \,\mathrm{sign}\,(\Delta_{-m})\sin\frac{\Theta_m}{2}\left[B(t)+C(t)\right]\right\}, \end{aligned} \tag{B.15}$$

where we defined

$$A(t) \equiv \sum_{n\neq -m}\mathrm{e}^{\mathrm{i}n\omega_{\mathrm{ex}}t}\frac{\Delta_n}{\varepsilon + n\omega_{\mathrm{ex}}}, \tag{B.16}$$

$$B(t) = \sum_{n\neq 0} \mathrm{e}^{\mathrm{i}n\omega_{\mathrm{ex}}t} \frac{1}{4n\omega_{\mathrm{ex}}} \left[\frac{\Delta_{n-m}\Delta_{-m}}{\varepsilon + (n-m)\omega_{\mathrm{ex}}} + \frac{\Delta_{-m-n}\Delta_{-m}}{\varepsilon - (n+m)\omega_{\mathrm{ex}}} \right] + \frac{1}{8}|A(t)|^2, \tag{B.17}$$

$$C(t) = \sum_{n\neq 0} \sum_{\substack{p\neq -m \\ p\neq -n-m}} \frac{\Delta_p \Delta_{p+n}}{8n\omega_{\mathrm{ex}}} \mathrm{e}^{\mathrm{i}n\omega_{\mathrm{ex}}t} \left[\frac{1}{\varepsilon + p\omega_{\mathrm{ex}}} + \frac{1}{\varepsilon + (p+n)\omega_{\mathrm{ex}}} \right] \tag{B.18}$$

Using those expressions in (B.12), we obtain the survival probability

$$P_{\downarrow\to\downarrow}(t) = P^{\mathrm{RWA}'}_{\downarrow\to\downarrow}(t) + P^{(1)}_{\downarrow\to\downarrow}(t) + P^{(2)}_{\downarrow\to\downarrow}(t). \tag{B.19}$$

We distinguish three different parts. The first one corresponds to the averaged second-order Van Vleck approach:

$$P^{\mathrm{RWA}'}_{\downarrow\to\downarrow}(t) = \cos^2\left(\Omega^{(2)}_m \frac{t}{2}\right) + \cos^2\Theta_m \sin^2\left(\Omega^{(2)}_m \frac{t}{2}\right). \tag{B.20}$$

Then we have additional contributions from Van Vleck perturbation theory to first order in Δ:

$$\begin{aligned} P^{(1)}_{\downarrow\to\downarrow}(t) = & -\frac{1}{2}\mathrm{sign}\,(\Delta_m)\sin\Theta_m\,\sin\Omega^{(2)}_m t \sum_{n\neq -m} \frac{\Delta_n}{\varepsilon + n\omega_{\mathrm{ex}}} \sin[(n+m)\omega_{\mathrm{ex}}t] \\ & + \mathrm{sign}\,(\Delta_m)\sin 2\Theta_m\,\sin^2\left(\Omega^{(2)}_m \frac{t}{2}\right) \left[\sum_{n\neq -m} \frac{1}{2}\frac{\Delta_n}{\varepsilon + n\omega_{\mathrm{ex}}} \cos(n+m)\omega_{\mathrm{ex}}t + \frac{1}{2}A(0) \right]. \end{aligned} \tag{B.21}$$

And finally the second-order part:

$$\begin{aligned} P^{(2)}_{\downarrow\to\downarrow}(t) = & -\mathrm{sign}\,(\Delta_m)\sin 2\Theta_m\,\sin^2\left(\Omega^{(2)}_m \frac{t}{2}\right) \sqrt{\frac{1}{4}A(0)^2 - 2[B(0) + C(0)\cos\Theta_m]} \\ & + \frac{1}{4}\sin^2\Theta_m \sin^2\left(\Omega^{(2)}_m \frac{t}{2}\right) \left[\left(\sum_{n\neq -m} \frac{\Delta_n}{\varepsilon + n\omega_{\mathrm{ex}}} \sin(n+m)\omega_{\mathrm{ex}}t \right)^2 + A(0)^2 \right. \\ & \left. + \left(\sum_{n\neq -m} \frac{\Delta_n}{\varepsilon + n\omega_{\mathrm{ex}}} \cos(n+m)\omega_{\mathrm{ex}}t \right)^2 \right] \\ & + \sum_{n\neq -m} \frac{A(0)\Delta_n}{2(\varepsilon + n\omega_{\mathrm{ex}})} \left[\cos(n+m)\omega_{\mathrm{ex}}t\cos^2\left(\Omega^{(2)}_m \frac{t}{2}\right) + \cos\Theta_m \sin(n+m)\omega_{\mathrm{ex}}t\sin\Omega^{(2)}_m t \right. \\ & \left. - \cos(n+m)\omega_{\mathrm{ex}}t\cos^2\Theta_m \sin^2\left(\Omega^{(2)}_m \frac{t}{2}\right) \right] \end{aligned}$$

$$
\begin{aligned}
&-\left[\cos^2\left(\Omega_m^{(2)}\frac{t}{2}\right)+\cos^2\Theta_m\sin^2\left(\Omega_m^{(2)}\frac{t}{2}\right)\right]\\
&\qquad\times\left\{-\frac{1}{4}\sum_{j\neq -m}\sum_{k\neq -m}\frac{\Delta_j\Delta_k}{(\varepsilon+k\omega_{\mathrm{ex}})(\varepsilon+j\omega_{\mathrm{ex}})}\cos(j-k)\omega_{\mathrm{ex}}t\right.\\
&\qquad\quad+\sum_{n\neq 0}\frac{1}{2n\omega_{\mathrm{ex}}}\left[\frac{\Delta_{n-m}\Delta_{-m}}{\varepsilon+(n-m)\omega_{\mathrm{ex}}}+\frac{\Delta_{-m-n}\Delta_{-m}}{\varepsilon-(n+m)\omega_{\mathrm{ex}}}\right]\cos n\omega_{\mathrm{ex}}t\\
&\qquad\quad\left.+\sum_{n\neq 0}\sum_{\substack{p\neq -m\\ p\neq -n-m}}\frac{\Delta_p\Delta_{p+n}}{4n\omega_{\mathrm{ex}}}\left[\frac{1}{\varepsilon+p\omega_{\mathrm{ex}}}+\frac{1}{\varepsilon+(p+n)\omega_{\mathrm{ex}}}\right]\cos\Theta_m\cos n\omega_{\mathrm{ex}}t\right\}\\
&-\frac{1}{4}A(0)\left[\cos^2\left(\Omega_m^{(2)}\frac{t}{2}\right)+\cos^2\Theta_m\sin^2\left(\Omega_m^{(2)}\frac{t}{2}\right)-\sin\Theta_m\cos^2\left(\Omega_m^{(2)}\frac{t}{2}\right)\right].
\end{aligned}
\tag{B.22}
$$

C

Dissipative qubit-oscillator system

In this appendix, we give the ingredients necessary to solve the Bloch-Redfield master equation (4.7) in Chapter 4.

C.1 Oscillator matrix elements

The position matrix elements X_{nm} defined in Sec. 4.2.1 are

$$
\begin{aligned}
X_{2j+1,2j+1} =& -2L_0\cos\alpha_j + \sqrt{j+1}L^-_{\mathrm{q,osc}}\sin\alpha_j,\\
X_{2j+1,2j+2} =& 2L_0\sin\alpha_j + \sqrt{j+1}L^-_{\mathrm{q,osc}}\cos\alpha_j,\\
X_{2j+1,2j+3} =& L_{\mathrm{q}}\cos(\alpha_j/2)\sin(\alpha_{j+1}/2) + \sqrt{j+2}(1+L_{\mathrm{osc}})\cos(\alpha_j/2)\cos(\alpha_{j+1}/2)\\
&+ \sqrt{j+1}(1-L_{\mathrm{osc}})\sin(\alpha_j/2)\sin(\alpha_{j+1}/2),\\
X_{2j+1,2j+4} =& L_{\mathrm{q}}\cos(\alpha_j/2)\cos(\alpha_{j+1}/2) - \sqrt{j+2}(1+L_{\mathrm{osc}})\cos(\alpha_j/2)\sin(\alpha_{j+1}/2)\\
&+ \sqrt{j+1}(1-L_{\mathrm{osc}})\sin(\alpha_j/2)\cos(\alpha_{j+1}/2),\\
X_{2j+1,2j+5} =& \sqrt{j+2}L^+_{\mathrm{q,osc}}\cos(\alpha_j/2)\sin(\alpha_{j+2}/2),\\
X_{2j+1,2j+6} =& \sqrt{j+2}L^+_{\mathrm{q,osc}}\cos(\alpha_j/2)\cos(\alpha_{j+2}/2),\\
X_{2j+2,2j+2} =& 2L_0\cos\alpha_j - \sqrt{j+1}L^-_{\mathrm{q,osc}}\sin\alpha_j,\\
X_{2j+2,2j+3} =& -L_{\mathrm{q}}\sin(\alpha_j/2)\sin(\alpha_{j+1}/2) - \sqrt{j+2}(1+L_{\mathrm{osc}})\sin(\alpha_j/2)\cos(\alpha_{j+1}/2)\\
&+ \sqrt{j+1}(1-L_{\mathrm{osc}})\cos(\alpha_j/2)\sin(\alpha_{j+1}/2),\\
X_{2j+2,2j+4} =& -L_{\mathrm{q}}\sin(\alpha_j/2)\cos(\alpha_{j+1}/2) + \sqrt{j+2}(1+L_{\mathrm{osc}})\sin(\alpha_j/2)\sin(\alpha_{j+1}/2)\\
&+ \sqrt{j+1}(1-L_{\mathrm{osc}})\cos(\alpha_j/2)\cos(\alpha_{j+1}/2),\\
X_{2j+2,2j+5} =& -\sqrt{j+2}L^+_{\mathrm{q,osc}}\sin(\alpha_j/2)\sin(\alpha_{j+2}/2),\\
X_{2j+2,2j+6} =& -\sqrt{j+2}L^+_{\mathrm{q,osc}}\sin(\alpha_j/2)\cos(\alpha_{j+2}/2).
\end{aligned}
$$

Matrix elements including the groundstate are given separately because of the special shape of $|0\rangle$:

$$
\begin{aligned}
X_{0,0} =& -2L_0,\\
X_{0,1} =& \sin(\alpha_0/2)L_{\mathrm{q}} + \cos(\alpha_0/2)(1+L_{\mathrm{osc}}),\\
X_{0,2} =& \cos(\alpha_0/2)L_{\mathrm{q}} - \sin(\alpha_0/2)(1+L_{\mathrm{osc}}),\\
X_{0,3} =& \sin(\alpha_1/2)L^+_{\mathrm{q,osc}},\\
X_{0,4} =& \cos(\alpha_1/2)L^+_{\mathrm{q,osc}}.
\end{aligned}
$$

All other matrix elements are zero.

C.2 Rate coefficients for the off-diagonal density matrix elements

The dephasing coefficients of the Bloch-Redfield tensor as needed in Eq. (4.17) are:

$$
\begin{aligned}
\mathcal{L}_{01,01} =& \frac{4\kappa}{\hbar\beta} L_0^2 (2\cos\alpha_0 - \cos^2\alpha_0 - 1) - \frac{1}{2}\mathcal{L}_{00,11}, && \text{(C.1)}\\
\mathcal{L}_{02,02} =& \frac{4\kappa}{\hbar\beta} L_0^2 (-2\cos\alpha_0 - \cos^2\alpha_0 - 1) - \frac{1}{2}\mathcal{L}_{00,22}, && \text{(C.2)}\\
\mathcal{L}_{03,03} =& \frac{4\kappa}{\hbar\beta} L_0^2 (2\cos\alpha_1 - \cos^2\alpha_1 - 1) - \frac{1}{2}\mathcal{L}_{11,33} - \frac{1}{2}\mathcal{L}_{22,33}, && \text{(C.3)}\\
\mathcal{L}_{04,04} =& \frac{4\kappa}{\hbar\beta} L_0^2 (-2\cos\alpha_1 - \cos^2\alpha_1 - 1) - \frac{1}{2}\mathcal{L}_{11,44} - \frac{1}{2}\mathcal{L}_{22,44}, && \text{(C.4)}\\
\mathcal{L}_{12,12} =& -\frac{16\kappa}{\hbar\beta} L_0^2 \cos^2\alpha_0 - \frac{1}{2}\mathcal{L}_{00,11} - \frac{1}{2}\mathcal{L}_{00,22}, && \text{(C.5)}\\
\mathcal{L}_{13,13} =& -\frac{4\kappa}{\hbar\beta} L_0^2 (\cos\alpha_0 - \cos\alpha_1)^2 - \frac{1}{2}\mathcal{L}_{00,11} - \frac{1}{2}\mathcal{L}_{11,33} - \frac{1}{2}\mathcal{L}_{22,33}, && \text{(C.6)}\\
\mathcal{L}_{14,14} =& -\frac{4\kappa}{\hbar\beta} L_0^2 (\cos\alpha_0 + \cos\alpha_1)^2 - \frac{1}{2}\mathcal{L}_{00,11} - \frac{1}{2}\mathcal{L}_{11,44} - \frac{1}{2}\mathcal{L}_{22,44}, && \text{(C.7)}\\
\mathcal{L}_{23,23} =& -\frac{4\kappa}{\hbar\beta} L_0^2 (\cos\alpha_0 + \cos\alpha_1)^2 - \frac{1}{2}\mathcal{L}_{00,22} - \frac{1}{2}\mathcal{L}_{11,33} - \frac{1}{2}\mathcal{L}_{22,33}, && \text{(C.8)}\\
\mathcal{L}_{24,24} =& -\frac{4\kappa}{\hbar\beta} L_0^2 (\cos\alpha_0 - \cos\alpha_1)^2 - \frac{1}{2}\mathcal{L}_{00,22} - \frac{1}{2}\mathcal{L}_{11,44} - \frac{1}{2}\mathcal{L}_{22,44}, && \text{(C.9)}\\
\mathcal{L}_{12,12} =& -\frac{16\kappa}{\hbar\beta} L_0^2 \cos^2\alpha_1 - \frac{1}{2}\mathcal{L}_{11,33} - \frac{1}{2}\mathcal{L}_{22,33} - \frac{1}{2}\mathcal{L}_{11,44} - \frac{1}{2}\mathcal{L}_{22,44}, && \text{(C.10)}\\
& && \text{(C.11)}
\end{aligned}
$$

$$
\begin{aligned}
\mathcal{L}_{01,02} = \frac{4\kappa}{\hbar\beta}(X_{00}X_{12} - X_{12}X_{22}) - G(\omega_{02})N_{02}X_{01}X_{02} - G(\omega_{12})N_{12}X_{11}X_{12}\\
-G(\omega_{32})N_{32}X_{13}X_{23} - G(\omega_{42})N_{42}X_{14}X_{24},
\end{aligned}
\tag{C.12}
$$

$$
\begin{aligned}
\mathcal{L}_{02,01} = \frac{4\kappa}{\hbar\beta}(X_{00}X_{12} - X_{12}X_{11}) - G(\omega_{01})N_{01}X_{01}X_{02} - G(\omega_{21})N_{21}X_{22}X_{12}\\
-G(\omega_{31})N_{31}X_{13}X_{23} - G(\omega_{41})N_{41}X_{14}X_{24},
\end{aligned}
\tag{C.13}
$$

$$
\begin{aligned}
\mathcal{L}_{13,23} = \frac{4\kappa}{\hbar\beta}(X_{33}X_{12} - X_{12}X_{22}) - G(\omega_{12})N_{12}(X_{11}X_{12} - X_{12}X_{33})\\
-G(\omega_{02})N_{02}X_{01}X_{02} - G(\omega_{32})N_{32}X_{13}X_{23} - G(\omega_{42})N_{42}X_{14}X_{24},
\end{aligned}
\tag{C.14}
$$

$$
\begin{aligned}
\mathcal{L}_{23,13} = \frac{4\kappa}{\hbar\beta}(X_{33}X_{12} - X_{12}X_{11}) - G(\omega_{21})N_{21}(X_{22}X_{12} - X_{12}X_{33})\\
-G(\omega_{01})N_{01}X_{01}X_{02} - G(\omega_{31})N_{31}X_{13}X_{23} - G(\omega_{41})N_{41}X_{14}X_{24},
\end{aligned}
\tag{C.15}
$$

$$\mathcal{L}_{14,24} = \frac{4\kappa}{\hbar\beta}(X_{44}X_{12} - X_{12}X_{22}) - G(\omega_{12})N_{12}(X_{11}X_{12} - X_{12}X_{44})$$
$$-G(\omega_{02})N_{02}X_{01}X_{02} - G(\omega_{32})N_{32}X_{13}X_{23} - G(\omega_{42})N_{42}X_{14}X_{24}, \tag{C.16}$$

$$\mathcal{L}_{24,14} = \frac{4\kappa}{\hbar\beta}(X_{44}X_{12} - X_{12}X_{11}) - G(\omega_{21})N_{21}(X_{22}X_{12} - X_{12}X_{33})$$
$$-G(\omega_{01})N_{01}X_{01}X_{02} - G(\omega_{31})N_{31}X_{13}X_{23} - G(\omega_{41})N_{41}X_{14}X_{24}. \tag{C.17}$$

C.3 Diagonal reduced density matrix elements

The solutions of the FSA master equation Eq. (4.21) for the diagonal elements reads:

$$\begin{aligned}
\sigma_{00}(t) &= \sigma^0_{00} + \sigma^0_{11} + \sigma^0_{22} + \sigma^0_{33} + \sigma^0_{44} \\
&- \mathrm{e}^{-\pi\mathcal{L}_{00,11}t}\left(\sigma^0_{11} + \sigma^0_{33}\frac{\mathcal{L}_{11,33}}{-\mathcal{L}_{00,11}+\mathcal{L}_{11,33}+\mathcal{L}_{22,33}} + \sigma^0_{44}\frac{\mathcal{L}_{11,44}}{-\mathcal{L}_{00,11}+\mathcal{L}_{11,44}+\mathcal{L}_{22,44}}\right) \\
&- \mathrm{e}^{-\pi\mathcal{L}_{00,22}t}\left(\sigma^0_{22} + \sigma^0_{33}\frac{\mathcal{L}_{22,33}}{-\mathcal{L}_{00,22}+\mathcal{L}_{11,33}+\mathcal{L}_{22,33}} + \sigma^0_{44}\frac{\mathcal{L}_{22,44}}{-\mathcal{L}_{00,22}+\mathcal{L}_{11,44}+\mathcal{L}_{22,44}}\right) \\
&+ \mathrm{e}^{-\pi(\mathcal{L}_{11,33}+\mathcal{L}_{22,33})t}\sigma^0_{33}\left(\frac{\mathcal{L}_{00,22}-\mathcal{L}_{11,33}}{-\mathcal{L}_{00,22}+\mathcal{L}_{11,33}+\mathcal{L}_{22,33}} + \frac{\mathcal{L}_{11,33}}{-\mathcal{L}_{00,11}+\mathcal{L}_{11,33}+\mathcal{L}_{22,33}}\right) \\
&+ \mathrm{e}^{-\pi(\mathcal{L}_{11,44}+\mathcal{L}_{22,44})t}\sigma^0_{44}\left(\frac{\mathcal{L}_{00,22}-\mathcal{L}_{11,44}}{-\mathcal{L}_{00,22}+\mathcal{L}_{11,44}+\mathcal{L}_{22,44}} + \frac{\mathcal{L}_{11,44}}{-\mathcal{L}_{00,11}+\mathcal{L}_{11,44}+\mathcal{L}_{22,44}}\right),
\end{aligned} \tag{C.18}$$

$$\begin{aligned}
\sigma_{11}(t) = &- \mathrm{e}^{-\pi\mathcal{L}_{00,11}t}\sigma^0_{11} - \mathrm{e}^{-\pi(\mathcal{L}_{00,11}+\mathcal{L}_{11,33}+\mathcal{L}_{22,33})t}\sigma^0_{33}\frac{\mathcal{L}_{11,33}}{-\mathcal{L}_{00,11}+\mathcal{L}_{11,33}+\mathcal{L}_{22,33}} \\
&- \mathrm{e}^{-\pi(\mathcal{L}_{00,11}+\mathcal{L}_{11,44}+\mathcal{L}_{22,44})t}\sigma^0_{44}\frac{\mathcal{L}_{11,44}}{-\mathcal{L}_{00,11}+\mathcal{L}_{11,44}+\mathcal{L}_{22,44}},
\end{aligned} \tag{C.19}$$

$$\begin{aligned}
\sigma_{22}(t) = &- \mathrm{e}^{-\pi\mathcal{L}_{00,22}t}\sigma^0_{22} - \mathrm{e}^{-\pi(\mathcal{L}_{00,22}+\mathcal{L}_{11,33}+\mathcal{L}_{22,33})t}\sigma^0_{33}\frac{\mathcal{L}_{22,33}}{-\mathcal{L}_{00,22}+\mathcal{L}_{11,33}+\mathcal{L}_{22,33}} \\
&- \mathrm{e}^{-\pi(\mathcal{L}_{00,22}+\mathcal{L}_{11,44}+\mathcal{L}_{22,44})t}\sigma^0_{44}\frac{\mathcal{L}_{22,44}}{-\mathcal{L}_{00,22}+\mathcal{L}_{11,44}+\mathcal{L}_{22,44}},
\end{aligned} \tag{C.20}$$

$$\sigma_{33}(t) = \mathrm{e}^{-\pi(\mathcal{L}_{11,33}+\mathcal{L}_{22,33})t}\sigma^0_{33}, \tag{C.21}$$

$$\sigma_{44}(t) = \mathrm{e}^{-\pi(\mathcal{L}_{11,44}+\mathcal{L}_{22,44})t}\sigma^0_{44}. \tag{C.22}$$

References

[1] U. Weiss, *Quantum dissipative systems*, World Scientific, Singapore, third edition, 2008.

[2] J. B. Hartle, *Gravity: an introduction to Einstein's general relativity*, Addison Wesley, San Francisco, 2003.

[3] E. Schrödinger, Naturwiss. **35**, 807 (1935).

[4] C. Jönsson, Z. Phys. **161**, 454 (1961).

[5] A. Tonomura, J. Endo, T. Matsuda, T. Kawasaki, and H. Ezawa, Am. J. Phys. **57**, 117 (1989).

[6] A. J. Leggett, Prog. Theor. Phys. (Suppl.) **69**, 80 (1980).

[7] A. J. Leggett, Contemporary Physics **25**, 583 (1984).

[8] B. D. Josephson, Phys. Lett. **1**, 251 (1962).

[9] M. H. Devoret and J. M. Martinis, Quantum Information Processing **3**, 163 (2004).

[10] M. Tinkham, *Introduction to Superconductivity*, McGraw-Hill, New York, second edition, 1996.

[11] A. O. Caldeira and A. J. Leggett, Ann. Phys., NY **149**, 374 (1983).

[12] Y. Makhlin, G. Schön, and A. Shnirman, Rev. Mod. Phys. **73**, 357 (2001).

[13] Y. Nakamura, Y. A. Pashkin, and J. S. Tsai, Nature **398**, 786 (1999).

[14] M. A. Nielsen and I. L. Chang, *Quantum Computation and Quantum Information*, Cambridge University Press, Cambridge, 2000.

[15] V. Bouchiat, D. Vion, P. Joyez, D. Esteve, and M. H. Devoret, Physica Scripta **T76**, 165 (1998).

[16] M. Büttiker, Phys. Rev. B **36**, 3548 (1987).

[17] J. R. Friedman, V. Patel, W. Chen, S. K. Tolpygo, and J. E. Lukens, Nature **406**, 43 (2000).

[18] I. Chiorescu, Y. Nakamura, C. J. P. M. Harmans, and J. E. Mooij, Science **299**, 1869 (2003).

[19] J. E. Mooij et al., Science **285**, 1036 (1999).

[20] C. H. van der Wal et al., Science **290**, 773 (2000).

[21] T. P. Orlando et al., Phys. Rev. B **60**, 15398 (1999).

[22] L. Tian, S. Lloyd, and T. P. Orlando, Phys. Rev. B **65**, 144516 (2002).

[23] C. H. van der Wal, F. K. Wilhelm, C. J. P. M. Harmans, and J. E. Mooij, Eur. Phys. J. B **31**, 111 (2003).

[24] L.-M. Duan, M. D. Lukin, J. I. Cirac, and P. Zoller, Nature **414**, 413 (2001).

[25] J. M. Raimond, M. Brune, and S. Haroche, Rev. Mod. Phys. **73**, 565 (2001).

[26] H. Mabuchi and A. C. Doherty, Science **298**, 1372 (2002).

[27] P. Lambropoulos and D. Petrosyan, *Fundamentals of Quantum Optics and Quantum Information*, Springer, Berlin, 2007.

[28] C. Cohen-Tannoudji, J. Dupont-Roc, and G. Grynberg, *Atom-Photon Interactions: Basic Processes and Applications*, Wiley, Weinheim, 2004.

[29] A. Blais, R.-S. Huang, A. Wallraff, S. M. Girvin, and R. J. Schoelkopf, Phys. Rev. A **69**, 062320 (2004).

[30] M. Devoret, S. Girvin, and R. Schoelkopf, Ann. Phys. (Leipzig) **16**, 767 (2007).

[31] A. Wallraff et al., Nature **431**, 162 (2004).

[32] D. I. Schuster et al., Nature **445**, 515 (2007).

[33] R. J. Schoelkopf and S. M. Girvin, Nature **451**, 664 (2008).

[34] J. Majer et al., Nature **449**, 443 (2007).

[35] I. Chiorescu et al., Nature **431**, 159 (2004).

[36] C. Vierheilig, J. Hausinger, and M. Grifoni, Phys. Rev. A **80**, 052331 (2009).

[37] Y. Makhlin, G. Schön, and A. Shnirman, Nature **431**, 138 (2004).

[38] J. Johansson et al., Phys. Rev. Lett **96**, 127006 (2006).

[39] A. A. Houck et al., Nature **449**, 328 (2007).

[40] M. A. Sillanpää, J. I. Park, and R. W. Simmonds, Nature **449**, 438 (2007).

[41] E. T. Jaynes and F. W. Cummings, IEEE Proc. **51**, 90 (1963).

[42] J. M. Fink et al., Nature **454**, 315 (2008).

[43] F. Deppe et al., Nature Physics **4**, 686 (2008).

[44] L. S. Bishop et al., Nature Physics **5**, 105 (2009).

[45] J. Bourassa et al., Phys. Rev. A **80**, 032109 (2009).

[46] T. Niemczyk et al., Nature Physics **6**, 772 (2010).

[47] P. Forn-Díaz et al., arXiv:1005.1559 (2010).

[48] A. Fedorov et al., Phys. Rev. Lett. **105**, 060503 (2010).

[49] C. Ciuti, G. Bastard, and I. Carusotto, Phys. Rev. B **72**, 115303 (2005).

[50] G. Günter et al., Nature Physics **458**, 178 (2009).

[51] A. A. Anappara et al., Phys. Rev. B **79**, 201303 (2009).

[52] E. K. Irish, J. Gea-Banacloche, I. Martin, and K. C. Schwab, Phys. Rev. B **72**, 195410 (2005).

[53] J. Hausinger and M. Grifoni, New J. Phys. **10**, 115015 (2008).

[54] J. Hausinger and M. Grifoni, arXiv:1007.5437 (2010).

[55] J. H. Van Vleck, Phys. Rev. **33**, 467 (1929).

[56] B. Kirtman, J. Chem. Phys. **49**, 3890 (1968).

[57] P. R. Certain and J. O. Hirschfelder, J. Chem. Phys. **52**, 5977 (1970).

[58] I. Shavitt and L. T. Redmon, J. Chem. Phys. **73**, 5711 (1980).

[59] B. Kirtman, J. Chem. Phys. **75**, 798 (1981).

[60] E. C. Kemble, *The Fundamental Principles of Quantum Mechanics*, McGraw-Hill, New York, 1937.

[61] S. Ashhab and F. Nori, Phys. Rev. A **81**, 042311 (2010).

[62] B. W. Shore and P. L. Knight, J. Mod. Opt. **40**, 1195 (1993).

[63] F. Bloch and A. Siegert, Phys. Rev. **57**, 522 (1940).

[64] E. K. Irish, Phys. Rev. Lett. **99**, 173601 (2007).

[65] F. Nesi, M. Grifoni, and E. Paladino, New J. Phys. **9**, 316 (2007).

[66] D. Zueco, G. M. Reuther, S. Kohler, and P. Hänggi, Phys. Rev. A **80**, 033846 (2009).

[67] F. Brito, D. P. DiVincenzo, R. H. Koch, and M. Steffen, New J. Phys. **10**, 033027 (2008).

[68] J. Plata and J. M. Gomez Llorente, Phys. Rev. A **48**, 782 (1993).

[69] P. Neu and R. J. Silbey, Phys. Rev. A **54**, 5323 (1996).

[70] Y. Nakamura, Y. A. Pashkin, and J. S. Tsai, Phys. Rev. Lett. **87**, 246601 (2001).

[71] C. M. Wilson et al., Phys. Rev. Lett. **98**, 257003 (2007).

[72] H. Breuer and M. Holthaus, Z. Phys. D **11**, 1 (1989).

[73] A. Eckardt and M. Holthaus, J. Phys.: Conf. Ser. **99**, 012007 (2008).

[74] M. Grifoni and P. Hänggi, Phys. Rep. **304**, 229 (1998).

[75] C. M. Wilson et al., Phys. Rev. B **81**, 024520 (2010).

[76] J. Hausinger and M. Grifoni, Phys. Rev. A **81**, 022117 (2010).

[77] G. B. Arfken and H. J. Weber, *Mathematical Methods for Physicists*, Academic Press, San Diego, fifth edition, 2001.

[78] W. T. Coffey, Y. P. Kalmykov, and J. T. Waldron, *The Langevin Equation, With Applications in Physics, Chemistry and Electrical Engineering*, World Scientific, Singapore, 1996.

[79] A. O. Caldeira and A. J. Leggett, Physica A **121**, 587 (1983).

[80] P. Ullersma, Physica (Utrecht) **32**, 27, 56, 74, 90 (1966).

[81] R. Zwanzig, J. Stat. Phys. **9**, 215 (1973).

[82] C. W. Gardiner and P. Zoller, *Quantum Noise. A Handbook of Markovian and Non-Markovian Quantum Stochastic Methods with Applications to Quantum Optics*, Springer, Berlin Heidelberg, third edition, 2004.

[83] H.-P. Breuer and F. Petruccione, *The theory of open quantum systems*, Oxford University Press, New York, 2002.

[84] A. Leggett et al., Rev. Mod. Phys. **59**, 1 (1987).

[85] A. Garg, J. N. Onunchic, and V. Ambegaokar, J. Chem. Phys **83**, 4491 (1985).

[86] M. Thorwart, E. Paladino, and M. Grifoni, Chem. Phys. **296**, 333 (2004).

[87] F. K. Wilhelm, S. Kleff, and J. von Delft, Chem. Phys. **296**, 345 (2004).

[88] M. C. Goorden, M. Thorwart, and M. Grifoni, Phys. Rev. Lett. **93**, 267005 (2004).

[89] M. C. Goorden, M. Thorwart, and M. Grifoni, Eur. Phys. J. B **45**, 405 (2005).

[90] S. Kleff, S. Kehrein, and J. von Delft, Physica E **18**, 343 (2003).

[91] S. Kleff, S. Kehrein, and J. von Delft, Phys. Rev. B **70**, 014516 (2004).

[92] P. Huang and H. Zheng, J. Phys.: Condens. Matter **20**, 395233 (2008).

[93] N. Makri and D. E. Makarov, J. Chem. Phys. **102**, 4600 (1995).

[94] N. Makri and D. E. Makarov, J. Chem. Phys. **102**, 4611 (1995).

[95] F. Brito and A. O. Caldeira, New J. Phys. **10**, 115014 (2008).

[96] S. Saito et al., Phys. Rev. Lett. **93**, 037001 (2004).

[97] S. Saito et al., Phys. Rev. Lett. **96**, 107001 (2006).

[98] A. Izmalkov et al., Europhys. Lett. **65**, 844 (2004).

[99] W. D. Oliver et al., Science **310**, 1653 (2005).

[100] D. M. Berns et al., Phys. Rev. Lett. **97**, 150502 (2006).

[101] M. Sillanpää, T. Lehtinen, A. Paila, Y. Makhlin, and P. Hakonen, Phys. Rev. Lett. **96**, 187002 (2006).

[102] D. M. Berns et al., Nature **455**, 51 (2008).

[103] M. S. Rudner et al., Phys. Rev. Lett. **101**, 190502 (2008).

[104] X. Wen and Y. Yu, Phys. Rev. B **79**, 094529 (2009).

[105] M. Baur et al., Phys. Rev. Lett. **102**, 243602 (2009).

[106] J. H. Shirley, Phys. Rev. **138**, 979 (1965).

[107] F. Grossmann, T. Dittrich, P. Jung, and P. Hänggi, Phys. Rev. Lett. **67**, 516 (1991).

[108] F. Grossmann, P. Jung, T. Dittrich, and P. Hänggi, Z. Phys. B **84**, 315 (1991).

[109] F. Grossmann and P. Hänggi, Europhys. Lett. **18**, 571 (1992).

[110] L. Hartmann, M. Grifoni, and P. Hänggi, J. Chem. Phys. **109**, 2635 (1998).

[111] L. Hartmann, I. Goychuk, M. Grifoni, and P. Hänggi, Phys. Rev. E **61**, R4687 (2000).

[112] I. Goychuk and P. Hänggi, Adv. Phys. **54**, 525 (2005).

[113] Y. Dakhnovskii, Phys. Rev. B **49**, 4649 (1994).

[114] Y. Dakhnovskii, Ann. Phys. (N.Y.) **230**, 145 (1994).

[115] Y. Dakhnovskii, J. Chem. Phys. **100**, 6492 (1994).

[116] Y. Dakhnovskii and R. D. Coalson, J. Chem. Phys. **103**, 2908 (1995).

[117] H. Wang, V. N. Freire, and X.-G. Zhao, Phys. Rev. E **58**, 2632 (1998).

[118] M. Thorwart, L. Hartmann, I. Goychuk, and P. Hänggi, J. Mod. Opt. **47**, 2905 (2000).

[119] M. C. Goorden and F. K. Wilhelm, Phys. Rev. B **68**, 012508 (2003).

[120] H. Sambe, Phys. Rev. A **7**, 2203 (1973).

[121] S.-K. Son, S. Han, and S.-I. Chu, Phys. Rev. A **79**, 032301 (2009).

[122] S. Ashhab, J. R. Johansson, A. M. Zagoskin, and F. Nori, Phys. Rev. A **75**, 063414 (2007).

[123] P. K. Aravind and J. O. Hirschfelder, J. Phys. Chem. **88**, 4788 (1984).

[124] G. F. Simmons, *Introduction to Topology and Modern Analysis*, McGraw–Hill, New York, 1963.

[125] S. Kohler, T. Dittrich, and P. Hänggi, Phys. Rev. E **55**, 300 (1997).

[126] M. Abramowitz and I. A. Stegun, *Handbook of Mathematical Functions with Formulas, Graphs, and Mathematical Tables*, Dover, New York, nineth edition, 1964.

[127] J. C. A. Barata and W. F. Wreszinski, Phys. Rev. Lett. **84**, 2112 (2000).

[128] M. Frasca, Phys. Rev. B **71**, 073301 (2005).

[129] D. E. Makarov and N. Makri, Phys. Rev. E **52**, 5863 (1995).

[130] M. Grifoni, M. Sassetti, P. Hänggi, and U. Weiss, Phys. Rev. E **52**, 3596 (1995).

[131] M. Grifoni, M. Winterstetter, and U. Weiss, Phys. Rev. E **56**, 334 (1997).

[132] M. Grifoni, L. Hartmann, and P. Hänggi, Chem. Phys. **217**, 167 (1997).

[133] H. Wang and X.-G. Zhao, J. Phys. Condens. Matter **7**, L89 (1995).

[134] H. Wang and X.-G. Zhao, Phys. Lett. A **217**, 225 (1996).

[135] I. I. Rabi, Phys. Rev. **51**, 652 (1937).

[136] J. Hausinger and M. Grifoni, arXiv:1009.1485 (2010).

[137] P. Alsing, D.-S. Guo, and H. J. Carmichael, Phys. Rev. A **45**, 5135 (1992).

[138] G. Berlín and J. Aliaga, J. Opt. B **6**, 231 (2004).

[139] F. Nesi, *Characterization of a qubit in presence of dissipation and external driving*, PhD thesis, Universität Regensburg, 2007.

[140] J. Hausinger, *Quantum Dissipation in Flux Qubits*, Diplomarbeit, Universität Regensburg, 2007.

[141] J. Kleiner, *Dissipative dynamics of a driven quantum oscillator-qubit system*, Bachelor thesis, Universität Regensburg, 2010.

Nomenclature

In the following we give a list of the abbreviations and symbols most frequently used in this thesis.

Abbreviations

CDT	Coherent destruction of tunneling.
DITO	Driving-induced tunneling oscillations.
FSA	Full secular approximation.
GRWA	Generalized rotating wave approximation.
JCM	Jaynes-Cummings model.
MQC	Macroscopic quantum coherence.
MQT	Macroscopic quantum tunneling.
MRWA	Moderate rotating-wave approximation.
NIBA	Non-interacting blip approximation.
PSA	Partial secular approximation.
QED	Quantum electrodynamics.
QUAPI	Quasiadiabatic propagator path-integral method.
RWA	Rotating-wave approximation.
SQUID	Superconducting quantum interference device.
TLS	Two-level system.
VVP	Van Vleck perturbation theory.
WDA	Weak damping approximation.

States

$\lvert\cdot\rangle\rangle$	Dirac notation in the extended Hilbert space $\mathcal{H}\otimes\mathcal{T}$, see page 87.
$\lvert\cdot)$	Dirac notation in the Hilbert space $\mathcal{T}$ of the time-periodic functions, see page 87.
$\lvert\uparrow/\downarrow\rangle$	Logical states of the qubit; localized basis states of the TLS.
$\lvert\Phi_{j,\pm}\rangle$	Eigenstates of the qubit-oscillator Hamiltonion obtained by perturbation theory in Δ, see page 35.
$\lvert\Phi_{n,\mp}\rangle\rangle$	Eigenstates of the Floquet Hamiltonian of the driven TLS, see page 95.
$\lvert\Phi^{m,L}_{n,K,\alpha}\rangle\rangle$	Eigenstates of the Floquet Hamiltonian of the driven qubit-oscillator system, see page 119.
$\lvert\mathrm{g/e}\rangle$	Groundstate and excited state of the qubit, see Eq. (2.3).
$\lvert j\rangle$	Fock-number states of the harmonic oscillator.
$\lvert\widetilde{j,\uparrow/\downarrow}\rangle$	Displaced-oscillator states for the undriven qubit-oscillator system, see page 33.
$\lvert n,\widetilde{K,\uparrow/\downarrow}\rangle\rangle$	Dressed Floquet states for the driven qubit-oscillator system, see Eq. (6.5).
$\lvert n\rangle$	Eigenstates of the qubit oscillator system obtained by perturbation theory in g, see Eq. (2.18).
$\lvert n\rangle^{\mathrm{JCM}}$	Eigenstates of the Jaynes-Cummings Hamiltonian, see page 23.
$\lvert u^{0}_{n,\uparrow/\downarrow}\rangle\rangle$	Eigenstates of the Floquet Hamiltonian of the driven TLS for $\Delta=0$, see Eq. (5.45).

Greek Letters

α	Dimensionless coupling constant $\alpha=(2g/\Omega)$, see page 33.
α_j	Mixing angle of the qubit-oscillator Hamiltonian (perturbation theory in g), see page 25.
β	Inverse temperature $(k_BT)^{-1}$ of the harmonic oscillator, page 21, and the heat bath, page 57.
Δ	Tunneling element of the TLS, see page 11.
$\tilde{\Delta}$	Dressed tunneling matrix element of the qubit-oscillator system (perturbation theory in g), see page 25.
$\Delta_j^{j'}$	Dressed tunneling matrix element of the qubit-oscillator system (perturbation theory in Δ), see Eq. (2.33).
Δ_n	Dressed tunneling matrix element of the driven TLS, see Eq. (5.47).

$\tilde{\Delta}_{n,K}^{n',K'}$	Dressed tunneling matrix element of the driven qubit-oscillator system, see Eq. (6.8).
ε	Static bias of the TLS, see page 11.
$\varepsilon_{j,\downarrow/\uparrow}^{(2)}$	Second-order corrections to the effective Hamiltonian of the qubit-oscillator system, see Eq. (2.35).
$\varepsilon_{n,K,\uparrow/\downarrow}^{(2)}$	Second-order corrections to the effective Hamiltonian of the driven qubit-oscillator system, see Eq. (6.12).
Γ_{r}	Relaxation rate of the qubit-oscillator system, see page 70.
Γ_{nm}	Dephasing rate of the qubit-oscillator system, see page 69.
γ_{rel}	Relaxation rate of the driven TLS, see Eq. (5.93).
γ_{deph}	Dephasing rate of the driven TLS, see Eq. (5.94).
κ	Dimensionless damping constant, see Eq. (3.72).
ρ	Density operator of the qubit-oscillator system, see page 21.
ρ_{red}	Reduced density operator of the TLS, see page 21.
σ_i	Pauli-spin matrix, see page 11.
Θ	Qubit mixing angle, see page 22.
Θ_j^l	Mixing angle of the qubit-oscillator system (perturbation theory in Δ), see Eq. (2.41).
Θ_m	Mixing angle of the driven TLS, see Eq. (5.63).
$\Theta_{n,K}^{m,L}$	Mixing angle of the driven qubit-oscillator system, see Eq. (6.19).
ω_c	High-frequency cutoff in the spectral density $J(\omega)$, see Eq. (3.34).
ω_{ex}	External driving frequency, see page 86.
ω_{nm}	Transition frequency between energy level E_n and E_m of the qubit-oscillator system, see page 28.
$\omega_{K,\alpha;K',\beta}^{m,L}$	Transition frequencies of the driven qubit-oscillator system, see Eq. (6.26).
Ω	Frequency of the harmonic oscillator, see page 15.
Ω_j^l	Dressed oscillation frequency of the qubit-oscillator system, see Eq. (2.38).
Ω_m	Dressed oscillation frequency of the driven TLS, see Eq. (5.61).
$\Omega_{n,K}^{m,L}$	Dressed oscillation frequency of the driven qubit-oscillator system, see Eq. (6.14).
Ξ_j^l	Modified Laguerre polynomial, see Eq. (2.31).

Latin letters

A	Driving amplitude for the driven TLS, see page 92.
$B, B^\dagger$	Annihilation and creation operator of the harmonic oscillator, see page 15.
E_{qb}	Qubit transition frequency, see page 22.
E_n	Eigenenergies of the qubit-oscillator system obtained by perturbation theory in g, see Eq. (2.17).
E_n^{JCM}	Eigenenergies of the Jaynes-Cummings Hamiltonian, see Eq. (2.9).
$E^0_{j,\uparrow/\downarrow}$	Eigenenergies of the qubit-oscillator Hamiltonian for $\Delta = 0$, see Eq. (2.32).
$E_{j,\mp}$	Eigenenergies of the qubit-oscillator system obtained by perturbation in Δ, see Eq. (2.37).
$E^0_{n,\uparrow/\downarrow}$	Quasienergies of the driven TLS for $\Delta = 0$, see page 92.
$E_{n,\pm}$	Quasienergies of the driven TLS, see page 96.
$E^0_{n,K,\uparrow/\downarrow}$	Quasienergies of the driven qubit-oscillator system for $\Delta = 0$, see Eq. (6.6).
$E^{m,L}_{n,K,\mp}$	Quasienergies of the driven qubit-oscillator system, see Eq. (6.13).
g	Coupling strength between qubit and oscillator, see page 15.
$G(\omega)$	Spectral density of the bath, see Eq. (3.59).
H_{eff}	Effective Hamiltonian, see Eq. (2.10).
$\mathcal{H}_{\mathrm{eff}}$	Effective Floquet Hamiltonian, see page 95.
H_{int}	Interaction Hamiltonian between qubit and oscillator, see page 15.
H^{JCM}	Jaynes-Cummings Hamiltonian, see Eq. (2.6).
H_{osc}	Hamiltonian of the harmonic oscillator, see page 15.
H_{SB}	Spin-boson Hamiltonian, see Eq. (4.1).
H_{TLS}	Hamiltonian of the TLS, see Eq. (1.9).
$\mathcal{H}_{\mathrm{TLS}}$	Floquet Hamiltonian of the driven TLS, see Eq. (5.46).
$H_{\text{TLS-osc}}$	Qubit-oscillator Hamiltonian, see Eq. (1.15), see page 15.
$J_k(x)$	Bessel function of oder k, see page 92.
$\mathcal{L}_{\mathrm{Diss}}(t)$	Kernel of the dissipative environment, see Eq. (3.60).
$\mathcal{L}_{nm,kl}$	Bloch-Redfield tensor, see Eq. (3.70).
$P_{\downarrow\to\downarrow}(t)$	Survival or returning probability of a TLS starting in the state $\mid\downarrow\rangle$, see Eq. (5.56).

$P(t)$	Population difference between the localized states of the qubit, see Eq. (2.1).
S	Transformation matrix of Van Vleck perturbation theory.
W_0, W_1	Second-order contributions in g, see page 25.
$\tilde{X}_{n,\alpha\beta}$	Fourier coefficients of the position matrix element $\tilde{X}_{\alpha\beta}(t)$, see Eq. (5.36).
Z	Partition function of the harmonic oscillator, see page 21.

Acknowledgements

My first and special thanks go to my supervisor Milena Grifoni. Thank you very much, Milena, that you gave me the opportunity to work in your group, for the motivation, encouragement and guidance during the last years. I appreciate it very much that despite your various obligations you always found so much time for intensive discussions in order to solve problems concerning this work. You gave me a lot of freedom concerning the evolution of this project but also were there to lead me into the right direction.

Parts of this work are motivated by the PhD thesis of Francesco Nesi who also gave me much support during my diploma thesis. Thank you, Francesco!

I want to thank Carmen Vierheilig for the collaboration and especially for the many helpful and critical remarks on the qubit-oscillator part and the driven systems.

Further, I enjoyed the short but fruitful time I could work with Johannes Kleiner while he was doing his Bachelor thesis on dissipative driven oscillator-qubit systems.

I am thankful to the “Augsburg people” Georg Reuther, David Zueco and Sigmund Kohler for several interesting discussions.

Many thanks also to the Walther-Meißner-Institute in Garching, in particular to Frank Deppe, for their time and the detailed lab tour. It was very impressive to see how real qubits are fabricated and operated.

The excursion into the field of quantum ratchets and to learn how the Floquet formalism can be applied there was a very pleasant change for me. I want to thank Milena Grifoni and Sergey Smirnov for their patience concerning my lack of knowledge about the σ-DVR basis and other methods used there. Furthermore, I am grateful to Dario Bercioux for the long discussions on the Mathematica codes and especially his hospitality in Freiburg.

When I was in Brazil, Amir Caldeira gave me the opportunity to visit him and his group several times – also very spontaneously. Thank you very much! At this point many thanks also to Felipe Fanchini for the nice discussions and time in Brazil. Good luck in Ouro Preto!

Very important for me was to work in a nice environment. For that I thank my office mates. In particular, I want to mention Georg Begemann, who I shared the office with for a long period and who also became a good friend during various adventures. Thank you very much, Georg, for the nice time! A lot of fun I had also with Alexander Lopez and Sergey Smirnov, who filled perfectly the open chairs in 3.1.23. I appreciate it very much that you even went to German classes in order to communicate with me. In that sense: Vielen Dank und viel Erfolg im A2!

Concerning excursions and a nice time in Regensburg and beyond I am also especially thinking of my colleague and friend Dana Darau. Dana, vielen Dank auch für die vielen interessanten Diskussionen!

I say thank you to Andrea Donarini for always finding time to answer my short questions on various topics.

A big contribution to this work was also provided by Lizy Lazar. Vielen Dank, Lizy, für die Hilfe und Unterstützung in zahlreichen Dingen nicht nur administrativer Art!

For proofreading parts of this thesis I am very grateful to Matthias Kronschnabl and Marta

Gutiérrez.
Another very important person during the last years was Michael Hartung, who I could contact whenever there were any problems with the computers. Danke für Deine Hilfe und Deine Geduld. I also thank all of the sysadmins of the particle physics group and the Richter chair (special thanks to Timo Hartmann) for their help concerning the computer administration. Thanks to Andreas Scholz who took over the system administration in our group a couple of weeks ago and thereby helped me to fully concentrate on writing this thesis. I appreciated a lot the support by Fritz Wünsch and Rudi Holzer who also always had their doors open in case of computer and printer problems.
Thanks also to my friends, Raquel and Marcus Bonanca, for the nice time here in Regensburg. Unfortunately you left too early, but I was very happy that I could celebrate your big day with you.
I also want to thank a lot Daiane Cavalheiro for her support and friendship.
In general, many people contributed to this work in many different ways. Direct support came through discussions, criticism, helpful remarks etc.. Equally important was the moral support of friends accompanying me during the last three years. Many did both and it would be impossible to name all of you. Therefore I end this last page with a general “Thank you!” to all my friends and colleagues, especially to the group Quantum Transport and Spintronics with all its nice present and former members.

I am very grateful to my family, in particular to my parents, who supported me always in any imaginable kind.

Financial support through the SFB 631: *Solid-State Based Quantum Information Processing* is gratefully acknowledged.